

# Modelling Viscous Flow and Elastic Deformation in Fold-Thrust Belts and Magmatic Intrusions



**Thomasina Verity Ball**

Supervisor: Dr Jerome A. Neufeld

Department of Earth Sciences  
University of Cambridge

This dissertation is submitted for the degree of  
*Doctor of Philosophy*



## Declaration

---

This thesis is the result of my own work and includes nothing which is the outcome of work done in collaboration except as declared in the Preface and specified in the text. It is not substantially the same as any that I have submitted, or, is being concurrently submitted for a degree or diploma or other qualification at the University of Cambridge or any other University or similar institution except as declared in the Preface and specified in the text. I further state that no substantial part of my thesis has already been submitted, or, is being concurrently submitted for any such degree, diploma or other qualification at the University of Cambridge or any other University or similar institution except as declared in the Preface and specified in the text. It does not exceed the prescribed word limit for the relevant Degree Committee.

Thomasina Verity Ball  
May 2019



# **Modelling Viscous Flow and Elastic Deformation in Fold-Thrust Belts and Magmatic Intrusions** *by Thomasina Verity Ball*

Fluid dynamics governs many phenomena on the Earth's surface and interior, from the emplacement of fluid magma, to the viscous deformation of mountain ranges on the longest time scales. Understanding these processes presents a challenge to traditional modelling techniques. However, simplifying models of the leading-order features of the flow can give insight into the dominant physical balances at play. In this dissertation I use theoretical analysis, numerical simulations, and laboratory experiments to address two geophysical processes: the formation of fold-thrust belts and the dynamics of shallow magmatic intrusions. Although geophysically distinct, these two problems both involve the interplay between viscous flow and elastic deformation and so inform the modelling of one another.

Fold-thrust belts are formed at convergent margins, where accretion of weak sediments to the front of the overriding plate results in continued flexural subsidence of the underthrusting plate. In this dissertation I build a new dynamic model to investigate both the role of the thickness and material properties of the incoming sediment, and the flexure in the underthrusting plate in controlling the behaviour and evolution of fold-thrust belts. The analysis shows that the evolution of fold-thrust belts can be dominated by either gravitational spreading or vertical thickening. I apply the model to the Makran accretionary prism and the Indo-Burman Ranges, and show that for the Makran flexure is important, while in the Indo-Burman Ranges the incoming sediment thickness has a first-order control on topography.

The propagation of shallow magmatic intrusions is governed by the interplay between elastically deforming sedimentary layers, the viscous flow of magma beneath, and the requirement to fracture at the front. In this dissertation I describe this process by extending the model for elastic-plated gravity currents to an axisymmetric geometry and show that adhesion (or fracture toughness) gives rise to two dynamical regimes of spreading; viscosity dominant spreading and adhesion dominant spreading. Experiments using clear, PDMS elastic sheets enable new, direct measurements of the vapour tip, and confirm the existence of spreading regimes controlled by viscosity and adhesion. I extend this laminar model of magma propagation to large mafic sills, which are thought to exhibit turbulent flow. Using a hybrid laminar-turbulent flow model I examine the transition to turbulence and show that volume fluxes several orders of magnitude above the average are required to reproduce the aspect ratios of large mafic sills measured in the field. Finally, I explore the role topographic gradients may play in driving magmatic intrusions by carrying out further experiments where the elastic sheets are inclined at an angle to the horizontal. Experimental observations show the formation of a transient head and a static tail structure with good first order comparisons to the deformation patterns of the Piton de la Fournaise flank sill intrusion.



## Publications arising from this dissertation

### Chapter 2

Ball, T. V., Penney, C. E., Neufeld, J. A., and Copley, A. C. (2019b). Controls on the geometry and evolution of thin-skinned fold-thrust belts, and applications to the Makran accretionary prism and Indo-Burman Ranges. *Geophys. J. Int.*, 218(1):247–267

### Chapter 3

Ball, T. V. and Neufeld, J. A. (2018). Static and dynamic fluid-driven fracturing of adhered elastica. *Phys. Rev. Fluids*, 3(7):074101

## Publications not arising from this dissertation

Ball, T. V., Balmforth, N. J., and Hewitt, I. J. (2019a). Indentation into a plastic fluid layer. *Proc. Roy. Soc. A*, 475:20180747

Ball, T. V., Huppert, H. E., Lister, J. R., and Neufeld, J. A. (2017). The relaxation time for viscous and porous gravity currents following a change in flux. *J. Fluid Mech.*, 821:330–342



*“Nature does not consist entirely, or even largely, of problems designed by a Grand Examiner to come out neatly in finite terms, and whatever subject we tackle the first need is to overcome timidity about approximating.”*

Sir Harold Jeffreys  
Bertha Swirles Jeffreys  
in *Methods of Mathematical Physics*, 1946



## Acknowledgements

---

I would like to start by thanking Jerome Neufeld for his unwavering guidance and patience during the course of my PhD. Jerome's tireless enthusiasm to understand fluid dynamical problems has made the past four years a thoroughly enjoyable experience. Thanks also go to Camilla Penney and Alex Copley for their knowledge and expertise on all aspects of the fold-thrust belt research.

Much of my time has been spent beavering away in the BPI labs, which would not have been possible without Andrew Pluck's excellent handy work in making my experimental setups (and everything else I could possibly need!), the safety and care of Lotty Gladstone, and the supervision of Finn Box. Thanks to all for your support.

The fluids and tectonics groups at Bullard have been a great environment to work in during my PhD. Thanks to Chunendra Sahu, Adam Butler, Aisling O'Kane, Zhong Zheng, Laurence Cowton and Andrew Gilbert for their academic input and interesting discussions in both fields. Thanks also to office mates Kieran Gilmore and Sam Wimpenny for putting up with me.

I would also like to thank Ian Frame and Dave Lyness for their computer support, to Joyce and Gill, without whom Bullard would not be able to operate, and to Sarah Humbert for her library support in finding those hidden papers.

To Girtonians Catherine, Alice, Carly and Alex who have been there since the beginning of my Cambridge adventure, thanks for a wonderful eight years of laughter and unforgettable memories. It wouldn't have been the same otherwise.

Finally, I'd like to thank my family, Mum, for listening to my endless worries, Dad, for his continuing encouragement in everything, Tamara and Orianna, for keeping me sane, and Tarek, Orlin and Octavia, for supporting me throughout. And last but not least, thanks to Sid for dancing through the last stretch with me. I'm not sure how I could have done it otherwise, it certainly wouldn't have been anywhere near as fun!



# Table of contents

---

<b>List of figures</b>	<b>xvii</b>
<b>List of tables</b>	<b>xix</b>
<b>1 Introduction</b>	<b>1</b>
1.1 Fold-thrust belts . . . . .	2
1.2 Magmatic intrusions . . . . .	5
1.3 Outline of dissertation . . . . .	8
<b>2 Geometry and evolution of fold-thrust belts</b>	<b>11</b>
2.1 Introduction . . . . .	11
2.2 Model setup . . . . .	12
2.3 Model results . . . . .	16
2.3.1 Overview of regimes of wedge evolution . . . . .	17
2.3.2 Flexural subsidence of the underthrusting plate . . . . .	18
2.3.3 Height of topography . . . . .	20
2.3.4 Numerical solutions . . . . .	25
2.4 Discussion and applications . . . . .	29

---

2.4.1	Makran accretionary prism . . . . .	31
2.4.2	Indo-Burman Ranges . . . . .	35
2.4.3	Comparison with Coulomb wedge theory . . . . .	39
2.5	Conclusion . . . . .	41
<b>3</b>	<b>Modelling shallow magmatic intrusions</b>	<b>43</b>
3.1	Introduction . . . . .	43
3.1.1	Magmatic intrusions . . . . .	43
3.1.2	Fluid-driven fracturing . . . . .	44
3.2	Theoretical model . . . . .	46
3.2.1	Static shapes . . . . .	46
3.2.2	Dynamic spreading . . . . .	50
3.3	Experimental methods . . . . .	54
3.4	Results . . . . .	56
3.4.1	Viscosity dominant spreading . . . . .	58
3.4.2	Adhesion dominant spreading . . . . .	62
3.5	Discussion . . . . .	65
3.6	Concluding remarks . . . . .	66
<b>4</b>	<b>Turbulent fluid-driven fracturing</b>	<b>69</b>
4.1	Introduction . . . . .	69
4.2	Model setup . . . . .	72
4.2.1	Turbulent–laminar model recap . . . . .	72
4.2.2	Transition to laminar control . . . . .	73

---

4.2.3	Similarity solutions for turbulent flow . . . . .	75
4.3	Laminar control . . . . .	78
4.3.1	Pre-wetted film model . . . . .	80
4.3.2	Fluid lag model, viscosity dominant . . . . .	82
4.3.3	Fluid lag model, adhesion dominant . . . . .	84
4.4	Discussion . . . . .	86
4.4.1	Summary of models . . . . .	86
4.4.2	Mafic sills comparison . . . . .	90
4.5	Concluding remarks . . . . .	94
<b>5</b>	<b>Downslope shallow magmatic intrusions</b>	<b>95</b>
5.1	Introduction . . . . .	95
5.2	Theoretical model . . . . .	97
5.2.1	Model setup . . . . .	97
5.2.2	Transient dynamics . . . . .	101
5.2.3	Steady state . . . . .	101
5.3	Experiments . . . . .	106
5.3.1	Experimental setup . . . . .	106
5.3.2	Calibration . . . . .	107
5.3.3	Results . . . . .	107
5.4	Discussion and future work . . . . .	120
5.5	Concluding remarks . . . . .	123
<b>6</b>	<b>Conclusions and future work</b>	<b>125</b>

6.1	Conclusions . . . . .	125
6.1.1	Fold-thrust belts . . . . .	125
6.1.2	Magmatic intrusions . . . . .	126
6.2	Future work . . . . .	127
6.2.1	Fold-thrust belts . . . . .	127
6.2.2	Magmatic intrusions . . . . .	127
	<b>References</b>	<b>129</b>
	<b>Appendix A Numerical methods</b>	<b>141</b>
	<b>Appendix B Optimisation method</b>	<b>143</b>
	Makran . . . . .	143
	Indo-Burman Ranges . . . . .	144

# List of figures

---

2.1	Schematic of the theoretical model for a fold-thrust belt . . . . .	13
2.2	Regime plot of the evolution of a fold-thrust belt . . . . .	19
2.3	Numerical solutions for a fold-thrust belt with $H_\infty = 3.2$ , $\lambda = 3.0$ . . . . .	27
2.4	Numerical solutions for a fold-thrust belt with $H_\infty = 0.4$ , $\lambda = 3.0$ . . . . .	28
2.5	Changing the sediment thickness and the elastic thickness . . . . .	30
2.6	Location and geometry of the Makran accretionary prism . . . . .	32
2.7	Best-fitting Makran geometry . . . . .	34
2.8	Location and geometry of the Indo-Burman Ranges . . . . .	36
2.9	Best-fitting Indo-Burman Ranges geometry . . . . .	40
3.1	Schematic and photograph of a fracturing experiment . . . . .	47
3.2	Static blister profiles and length scales . . . . .	49
3.3	Experimental images and fluid lag length evolution . . . . .	55
3.4	Measuring adhesion curvature . . . . .	57
3.5	Experimental results of the cross-section . . . . .	59
3.6	Experimental results for viscosity dominant spreading . . . . .	61
3.7	Experimental results for adhesion dominant spreading . . . . .	63

---

3.8	Measured curvature in adhesion dominant regime . . . . .	64
4.1	Figure adapted from Cruden et al. (2017) (their figure 1a) . . . . .	70
4.2	Similarity solutions for the turbulent model . . . . .	78
4.3	Turbulent model plotted against mafic sills data . . . . .	92
5.1	Diagram of the theoretical and experimental setup . . . . .	98
5.2	Schematic of the transient head and the steady-state channel . . . . .	102
5.3	Calibrating dye attenuation . . . . .	108
5.4	Images of experiment 1 (table 5.1) . . . . .	110
5.5	Surface plots of experiment 1 (table 5.1) . . . . .	111
5.6	Downslope extent of the transient head . . . . .	113
5.7	Downslope geometry of the transient head . . . . .	114
5.8	Extent of the transient head . . . . .	116
5.9	Evolution of length scales of the transient head . . . . .	117
5.10	Upslope extent . . . . .	118
5.11	Steady-state experiment . . . . .	121
5.12	Figure adapted from Froger et al. (2015) (their figure 2). . . . .	123
5.13	Figure adapted from Froger et al. (2015) (their figure 4). . . . .	124

# List of tables

---

3.1	Experimental parameters for horizontal experiments . . . . .	58
4.1	Aspect ratios and timescale for transition to laminar flow . . . . .	87
4.2	Aspect ratios for varying flux $Q = Q_0(t/T_0)^a(V_f/V_0)^b$ . . . . .	89
5.1	Experimental parameters for downslope experiments . . . . .	107



# Chapter 1

## Introduction

---

Mathematical modelling is an integral tool for interpreting field observations of geophysical phenomena. Theoretical, numerical and experimental techniques aim to better understand geophysical processes by quantifying how they evolve spatially and temporally. The models produced are simplified versions of these processes, acknowledging the dominant contributions and neglecting any parameters that have a minor impact. In contrast to more traditional modelling techniques, the aim of using simplified models is not to replicate every detail but to describe the first-order features of these processes. This approach means the effect of changing one parameter in the system can easily be identified. In addition, non-dimensional parameters can be defined which demonstrate possible trade-offs between physical characteristics.

Geophysical processes act over timescales of seconds to millions of years, and over length scales of microns to thousands of kilometres. The modelling approach taken depends on the time and length scales of the geophysical process being considered. Taking rheology as an example, on short timescales over the length of individual faults, deformation may be elastic up to the point of brittle failure. In contrast, over geological timescales and over the length scale of mountain ranges, a continuum approach can be taken with deformation due to viscous or plastic flow. Observations of folding, particularly in sedimentary rocks, demonstrate the ductile behaviour of rocks, which can be explained by thermally-activated creep mechanisms. At low temperatures and stress levels, deformation of a crystalline solid is due to a diffusion of ions and vacancies through the crystal lattice. This process of diffusion relaxes the stress in the material and produces strain. This is known as diffusion creep, and results in a Newtonian behaviour in sedimentary rocks, where the strain rate is proportional to the stress. Hence, the modelling details depend on the scale of response to forcing (Carey, 1962; Price, 1973), and the time period of the response to forcing (Watts et al., 2013).

Fold-thrust belts are an example of where deformation can be explained predominantly by ductile processes. These tectonic structures are formed at convergent margins where the accretion of sediments at the front of the overriding plate results in crustal thickening and continued subsidence of the underthrusting plate. They are known to evolve over millions of years and hundreds of kilometres and form through the coupling of the elastic deformation of the underthrusting plate to the viscous flow of the accumulated sediment. Magmatic intrusions are an example of a geophysical process where the behaviour of near-surface rocks is predominantly elastic. Magmatic intrusions describe the emplacement of magma between sedimentary strata in the crust. Intrusions evolve over days to years, with a time scale that is primarily dependent on the magma viscosity, and their evolution couples the elastic deformation of the crust to the viscous flow of magma underneath.

These two phenomena evolve over different length and time scales, and hence require contrasting rheological descriptions of the lithosphere. However, the overall geophysical process in each involves a balance between viscous flow and elastic deformation. The similar underlying physical principles mean common mathematical modelling techniques can be used to describe both phenomena. In this dissertation I aim to demonstrate this simplifying approach by modelling both fold-thrust belts and magmatic intrusions within the same fluid dynamical framework. In both cases I use simplified theoretical, numerical and experimental techniques to understand key features of geophysical phenomena. In sections 1.1 and 1.2, I introduce the topics of fold-thrust belts and magmatic intrusions in detail, and how the problems studied in this dissertation build upon advances in the respective fields thus far.

## 1.1 Fold-thrust belts

Fold-thrust belts are mountain ranges along convergent margins made of highly deformed sedimentary rocks. A lot of natural variation exists among fold-thrust belts and the submarine equivalent of accretionary wedges. However, there are several characteristics which are common among all of them: (i) they have a sediment-basement interface below which there is negligible deformation; (ii) horizontal compression and deformation is accommodated in the fold-thrust belt above the sediment basement; and (iii) they form in front of a region of relatively undeformable rock on the overriding plate, with a geometry that tapers towards the incoming subducting plate. These common features suggest there are underlying physical principles that control the large-scale evolution and geometry of fold-thrust belts, and therefore that a simplified model could be used to investigate these processes in a wide range of locations.

Modelling approaches to fold-thrust belts initially aimed to describe the wedge-like geometry observed in the field. Price (1973) was the first to model a wedge-like fold-thrust belt using a continuum plastic rheology with a depth independent yield strength. In Price's model, flow is driven by horizontal pressure gradients associated with surface slopes. The continuum plastic model was revisited by Elliot (1976) and Chapple (1978). By setting the strength of the interface between the wedge and the rigid underthrusting plate to be that of the wedge, Elliot (1976) showed that the gravitational force provided by the weight of the accreted sediment dominated the deformation. Conversely, by introducing a weaker interface between the wedge and the underthrusting plate, Chapple (1978) highlighted that horizontal compression associated with shortening can contribute to overcoming the resisting shear stress at the base of the wedge without the requirement of a surface slope. The analysis of Elliot (1976) and Chapple (1978) was then expanded by Stockmal (1983) using slipline theory to calculate the stress and velocity field within the wedge.

These models do not account for the material strength in a fold-thrust belt increasing with depth due to the increasing effective overburden stress and lithification. Dahlen et al. (1984); Davis et al. (1983) and Dahlen (1984, 1990) used a Coulomb rheology, where the yield strength increases with depth and is set by the internal friction angle, in cases of a non-cohesive (Davis et al., 1983) or a cohesive (Dahlen et al., 1984) thrust belt. Extensions to these models have considered the effect of pore fluid pressures and changes in cohesion due to compaction and lithification (Zhao et al., 1986). In particular, Dahlen (1984) presented an exact solution for the stress state in a non-cohesive wedge.

The Coulomb wedge described by Davis et al. (1983) and others relies on the hypothesis that the interior of the wedge is everywhere on the verge of failure (Mandl, 1988). Hence, this model does not account for the possibility that deformation may be confined to a narrow zone, as observed in many fold-thrust belts where deformation is dominated by large slip on a few major faults (Suppe, 1980). Numerical models have been developed by others to allow for inhomogeneous deformation with more complex rheologies, including plastic (Borja and Dreiss, 1989; Willett, 1992), elasto-plastic (Simpson, 2011), and elasto-visco-plastic (Ruh et al., 2012; Stockmal et al., 2007) rheologies, as well as for time-dependent stress states (e.g. Wang and Hu, 2006).

Alongside these studies, fold-thrust belts have been described with more simplified rheologies. In thick layers of sediment, deformation is thought to be associated with diffusion creep due to water assisted transport of material via diffusion at the grain scale, and is known to occur at low temperatures (Rutter, 1983). Such a deformation mechanism would result in a viscous fluid rheology at large scales. Emerman and Turcotte (1983) first considered the geometry of a fold-thrust belt with a purely viscous rheology. By using lubrication theory (flow in

a thin viscous layer), they described a quasi-steady profile due to the balance of advection of the incoming sediment layer and gravitational spreading within the wedge. Applying the model to bathymetric profiles across the Kurile, Ryukyu and Aleutian accretionary prisms, Emerman and Turcotte inferred sediment viscosities of between  $10^{17} - 10^{18}$  Pa s. A viscous rheology has also been used to investigate the asymmetry of doubly vergent orogens (Medvedev, 2002), and to understand the length scales over which coupling to the kinematics of the underlying mantle is important (Ellis et al., 1995). More recently, Perazzo and Gratton (2010) demonstrated that the growth of fold-thrust belts is self-similar and showed good comparisons to locally averaged profiles of a variety of mountain ranges.

Much of these analyses have either focused on a prescribed taper of the underthrusting plate (Dahlen et al., 1984; Davis et al., 1983) or assumed isostatic compensation (Ellis et al., 1995). However, over smaller length scales of 10's to 100's km, flexure of the underthrusting plate plays an important role in determining the geometry of the resultant deformation (Forsyth, 1985; McKenzie and Fairhead, 1997), and should therefore be included for a full description of the fold-thrust belt evolution. Many studies have demonstrated that the patterns of gravity anomalies in the forelands of mountain ranges reveal the elastic flexure of the underthrusting plate in response to the load imposed by the mountain range (e.g. Burov et al., 1990; Haddad and Watts, 1999; Jordan and Watts, 2005; Karner and Watts, 1983; Lyon-Caen and Molnar, 1983; Snyder and Barazangi, 1986; Watts et al., 1995). These studies have been concerned with using the present-day pattern of gravity anomalies to infer the flexural properties of the lithosphere. More recently, numerical models have been used to consider the growth and evolution of the coupled system of flexure in the underthrusting plate overlain by shortening and thickening to form a fold-thrust belt. In particular, studies have focused on coupling flexure with complex rheologies such as an elasto-visco-plastic wedge (Simpson, 2006, 2010; Stockmal et al., 2007) and a Coulomb wedge (Wang, 2001). However, a simplified model combining wedge deformation with flexure in the underthrusting plate is yet lacking.

In chapter 2, I build on this previous work by considering the growth of a fold-thrust belt in which the underthrusting plate deforms elastically in response to the evolving overlying fold-thrust belt. I consider a purely viscous rheology to model the long wavelength topography associated with fold-thrust belts on length scales much larger than individual faults (England and McKenzie, 1982). This rheology is chosen for its simplicity, and ability to accommodate distributed and spatially variable deformation, and is appropriate if a large proportion of the deformation is by fluid-activated or thermally-activated creep mechanisms (Rutter, 1983). The low to absent rates of seismicity in the regions to which I apply my model may support this assumption.

## 1.2 Magmatic intrusions

Describing the processes involved in the transport of magma through the lithosphere is important for understanding the make-up of the continental crust, and the activity of volcanic regions. In particular, magmatic intrusion is more frequent than magmatic extrusion (Crisp, 1984). Therefore, determining the physics behind the emplacement of magma in the crust is important for understanding volcanic systems as a whole. Magmatic intrusions come in a variety of geometries, from dykes, sills and cone sheets (Kuenen, 1937; Rubin, 1995) with very low aspect ratios, to laccoliths (Corry, 1988) and plutons with much higher aspect ratios.

Many of these intrusions are emplaced in sedimentary basins, where they either cross-cut or intrude between sedimentary strata. Magma begins by ascending through the crust in the form of a dyke, utilising fractures and structural weaknesses (e.g. crustal heterogeneities, joints, rheological contrasts). In the case of magmatic intrusions, there is a transition to lateral flow (Menand, 2011). This has classically been thought of as occurring at the level of neutral buoyancy (Corry, 1988), however much field evidence contradicts this mechanism (e.g. Johnson and Pollard, 1973). Instead, the transition from dykes to sills (lateral flow) has been shown to be either due to rigidity contrasts between softer and stiffer layers of rock (Parsons et al., 1992), rheology contrasts where emplacement occurs in weak ductile zones (Holness and Humphreys, 2003), or due to the rotation of the deviatoric stress when the minimum compressive stress becomes vertical (Anderson, 1951). Laterally spreading magmatic intrusions form sills and laccoliths, with larger magmatic bodies such as plutons shown to be amalgamations of smaller intrusions (Cruden and McCaffrey, 2001; Glazner et al., 2004). As the building blocks of volcanic systems, it is important to understand the geometry and evolution of sills and laccoliths.

The process of modelling magmatic intrusions has taken a variety of different approaches. Classically the geometry of magmatic intrusions, in particular laccoliths, has been modelled theoretically as the deflection of a thin-elastic plate due to a fixed driving pressure (Corry, 1988; Johnson and Pollard, 1973), inspired by observations in the Henry Mountains, Utah (Gilbert, 1877). In this model the sedimentary strata are assumed to deform elastically, where the overburden pressure in the fluid and the elastic pressure exerted by the walls are in balance, and the intrusion occurs at a depth sufficiently shallow to feel the effects of the free surface above. Crucially these models produce a static geometry for a given length intrusion and ignore any coupling to the viscous flow of magma in the interior. However, it has been shown for dykes that the viscous pressure drop along a dyke has a controlling influence on its propagation (Lister, 1990). As such, more recently modelling has moved towards considering the coupling of viscous flow and elastic deformation in the emplacement of

magmatic intrusions together with the time evolution of emplacement (Bunger and Cruden, 2011; Michaut, 2011).

The study of viscous flow underneath an elastic sheet is a complex fluid dynamics problem. Near the front, a large negative pressure gradient is required to drive the viscous fluid into the narrowing gap. This causes viscous stresses to diverge and gives rise to theoretical predictions of an immobile contact line; the elastic equivalent of the problem of a moving droplet considered by Huh and Scriven (1971). Physically, the low pressures at the front cause the formation of a vapour tip, where volatiles in the magma such as water and carbon dioxide are exsolved (Anderson, 1978; Lister, 1990). This vapour tip mathematically provides a regularisation at the front allowing the contact line to advance. Hewitt et al. (2015) demonstrated this regularisation for a two-dimensional elastic-plated gravity current. The related problem of a penny-shaped crack in an extensive elastic medium often invokes the formation of a vapour tip (e.g. Garagash and Detournay, 1999).

The vapour tip separates the fluid front and fracture front of the intrusion. At the fracture front there is a requirement to overcome the surface energy that holds the sedimentary strata together. In fracture mechanics, this is referred to as the fracture toughness. Lister (1990) showed that the fracture resistance of crustal rocks is negligible for dykes, where a balance between buoyancy forces and a viscous pressure drop along the dyke governs the propagation. This is not the case for lateral intrusions, where, as for penny-shaped cracks, fracture toughness can play a leading order role in the propagation of intrusions (Bunger and Cruden, 2011; Detournay, 2016). However, the coupling between a vapour tip and a fracture criterion at the front, when the flow is dominated by fracture toughness in lateral intrusions, has yet to be explored in detail. In chapter 3, I consider this problem by studying the axisymmetric fluid-driven fracturing of an elastic sheet adhered to a substrate. I explore the evolution of the vapour tip formed at the front and when viscosity of the fluid and the fracture toughness at the fracture front play a leading order role in the propagation.

This simplified model of a magmatic intrusion relies on the assumption that the sedimentary strata deform elastically, and that the spreading magma can be modelled as a Newtonian, isoviscous fluid. However, intrusions are influenced by the rheological properties and stress field in the host rock, and the physical properties of the intruding magma. In the setting of laccoliths and sills, this model has been developed to deal with temperature dependent rheologies of the magma (Thorey and Michaut, 2016), and plastic deformation at the fracture front (Scheibert et al., 2017). However, there are numerous other outstanding extensions of this model. For example, field evidence suggests that mafic sills may exhibit turbulent flow when emplaced (Holness and Humphreys, 2003; Kille et al., 1986). However, as described, current theoretical models assume a viscous, laminar flow everywhere in the intrusion. In

chapter 4 I address this by building a turbulent-laminar hybrid model to explore the influence of turbulence and the transition from turbulent to laminar flow. In addition, the sedimentary strata and bedding planes along which magma intrude are assumed to be horizontal. The influence of topographic gradients has only been explored theoretically for the horizontal propagation of dykes (Townsend et al., 2017), despite being a suspected key control on measured intrusions of sills in the field (Froger et al., 2015). In chapter 5 I consider the influence of topographic gradients on magmatic intrusions by looking at the downslope evolution of an adhered, elastic-plated gravity current.

As the modelling of magmatic intrusions progresses, comparison with field measurements is vital to understand which physical processes are playing a first-order role. However, these comparisons often only have the solidified remains of intrusions as constraints. In chapter 4 this problem is discussed when considering the length versus thickness field data for mafic sills. Advances in monitoring techniques mean in situ measurements of magmatic intrusions are becoming more regular. For example, monitoring of the 2014 dyke intrusion from the Bárðabunga volcanic system in Iceland (Sigmundsson et al., 2014) has produced a dataset following a dyke laterally for  $\sim 45$  km. In general these detailed time-dependent measurements of magmatic intrusions are sparse so other approaches are required.

Analogue modelling using laboratory experiments sits between theoretical modelling and field observations as an alternative approach to understanding magmatic intrusions. Gelatine is often used as an analogue for the deforming host rock (Kavanagh et al., 2013), with a viscous fluid injected into either a small crack to model the propagation of buoyant dykes, or into a pre-existing weakness between two horizontal gelatine layers to model lateral intrusions. These gelatine type experiments have been used to investigate the different physical properties of the intruding magma, for example the influence of solidification (Chanceaux and Menand, 2016), and the possibility of turbulent emplacement (Kavanagh et al., 2006). In addition, the versatility of gelatine means the host rock properties can be altered to consider changes to the stress field due to a pressurised reservoir (Pansino and Taisne, 2019) or to topographic gradients (Urbani et al., 2017). Smaller scale features of fracturing at the front of magmatic intrusions can also be investigated (O’Keeffe et al., 2018; Tanaka et al., 2000) demonstrating intricate scalloped features on the fractured surfaces.

These gelatine experiments provide an excellent qualitative and quantitative description of the impact of the physical properties of the magma and the rheological properties of the host rock on the propagation of magmatic intrusions. For shallow magmatic intrusions, most of the deformation is accommodated by roof-lifting processes rather than deformation of the sedimentary strata below. This lends itself to a further simplification of the analogue experiments, more in line with the theoretical model considered, where the overburden

deforms elastically but the substrate below the intrusion is rigid. Lister et al. (2013) performed experiments injecting a viscous fluid beneath an elastic sheet with a pre-wetting film between the elastic sheet and the rigid horizontal substrate beneath. However, the pre-wetting film has no physical analogue in the case of magmatic intrusions. Instead, a surface energy should be considered between the elastic sheet and the rigid substrate. In chapter 3, I describe a new set of experiments where a viscous fluid is injected beneath an elastic sheet adhered to a horizontal substrate. The surface energy is due to an adhesive film between the two layers. This new setup allows for repeatable results which can be compared with the theoretical model and allows observation of the vapour tip, previously only seen experimentally in the fracturing of gelatine blocks (e.g. Medlin and Massé, 1984). The simplicity of the setup means that it can easily be adapted to consider more complex systems. In chapter 5 the experiments are extended to consider the influence of topographic gradients on magmatic intrusions by looking at the downslope evolution of adhered, elastic-plated gravity currents.

### 1.3 Outline of dissertation

**Chapter 2 - Geometry and evolution of thin-skinned fold-thrust belts: applications to the Makran accretionary prism and the Indo-Burman Ranges.** Chapter 2 describes a theoretical and numerical model for the formation of fold-thrust belts. The analysis shows that the evolution of a fold-thrust belt can either be dominated by gravitational spreading or vertical thickening depending on the thickness and material properties of the incoming sediment, and the flexure in the underthrusting plate. Good comparisons are made with the topography and sediment-basement interface of the Makran accretionary prism and the Indo-Burman Ranges. In the Makran, flexure is shown to be necessary to explain the geometry of the sediment basement interface. In the Indo-Burman Ranges, sediment thickness is shown to play a leading order role in controlling the topography observed in the north and south.

**Chapter 3 - Modelling shallow magmatic intrusions: fluid-driven fracturing of adhered elastica.** Chapter 3 describes a theoretical model of fluid-driven fracturing of adhered elastica. Propagation can be split into two regimes: viscosity dominant spreading where viscous dissipation at the front limits the propagation, or adhesion dominant spreading where the requirement to overcome adhesion at the fracture front limits the propagation. Laboratory experiments are conducted where a viscous fluid is injected underneath an elastic sheet, adhered to a horizontal substrate. Comparisons with theoretical results confirm the

existence of two regimes of spreading and demonstrate the formation of a vapour tip, or fluid lag, between the fluid front and fracture front.

**Chapter 4 - Turbulent fluid-driven fracturing.** Chapter 4 describes a theoretical model for an elastic-plated gravity current incorporating the possibility of both turbulent and laminar flow. The time and length scale of the transition from turbulent to laminar flow is determined for different physical processes at the fracture front: either a pre-wetting film, a fluid lag dominated by viscous dissipation, or a fluid lag dominated by fracture toughness at the front. Comparisons are made with field observations of the thickness versus length of mafic sills, suggesting a volume flux several orders of magnitude above the average is required to reproduce the data. Other physical mechanisms that might be at play, dominating the aspect ratios of intrusions measured in the field, are also discussed.

**Chapter 5 - Influence of topographic gradients on shallow magmatic intrusions: downslope evolution of an adhered, elastic-plated gravity current.** Chapter 5 describes a theoretical model for the downslope evolution of an adhered, elastic-plated gravity current motivated by the influence of topographic gradients on magmatic intrusions. Laboratory experiments are conducted where a viscous fluid is injected underneath an elastic sheet adhered to a rigid substrate, and both the elastic sheet and substrate are inclined at an angle to the horizontal. Experiments show the formation of a transient head that propagates downslope, with a steady state structure formed in the wake of the head. Leading order comparisons are made with observations of inclined magmatic intrusions observed in the field.

**Chapter 6 - Conclusions and future work.** Chapter 6 summarises the findings of the dissertation and describes future work.



## Chapter 2

# Geometry and evolution of thin-skinned fold-thrust belts: applications to the Makran accretionary prism and the Indo-Burman Ranges<sup>†</sup>

---

### 2.1 Introduction

Plate convergence forms a wide range of mountain belts with varying geometry and structure. Due to the dependence on pressure and time, the sizes and thermal structures of these ranges control their rheology, and therefore their deformation and evolution. At one extreme, the largest ranges on Earth (e.g. the Tibetan Plateau and the Andes) involve the entire thickness of the lithosphere, are bounded by rigid plates that are many hundreds of kilometres apart, and involve a range of deformation mechanisms including seismic failure in earthquakes and thermally-activated creep (e.g. Brace and Kohlstedt, 1980; Chen and Molnar, 1983). Opinion is divided in terms of the relative dynamical importance of brittle deformation on faults and the more distributed deformation in the underlying ductile lithosphere, and in the choice of boundary conditions used on the base and lateral edges for models of mountain ranges (e.g. Beaumont et al., 2001; England and McKenzie, 1982; Flesch et al., 2018; Meade, 2007; Molnar and Tapponnier, 1975). In this chapter I examine the behaviour of smaller ranges over length scales spanning 100's of km. At some convergent margins weak sediments on an underthrusting plate are deformed during accretion to the front of a relatively rigid

---

<sup>†</sup>This chapter is adapted from Ball, T. V., Penney, C. E., Neufeld, J. A., and Copley, A. C. (2019b). Controls on the geometry and evolution of thin-skinned fold-thrust belts, and applications to the Makran accretionary prism and Indo-Burman Ranges. *Geophys. J. Int.*, 218(1):247–267.

‘backstop’, which represents a region of the overlying plate that is stronger than the incoming sediments. This leads to the formation of a fold-thrust belt, or an accretionary wedge, which is my focus here.

I examine a coupled system of deformation of the incoming sediment pile and flexure of the underthrusting plate. By developing new dynamic models, I am able to address the role that is played by the thickness and material properties of the incoming sediments, and by the elastic properties of the underthrusting plate, in the behaviour and evolution of fold-thrust belts. First I describe the effects of changing these physical parameters on the geometry and deformation of the resulting fold-thrust belts. I then describe applications to specific regions that demonstrate the geological implications of the effects studied. In particular, I consider the Makran accretionary prism in order to demonstrate the necessity of including flexure in the model. I then investigate how changing the sediment thickness affects the geometry of fold-thrust belts by considering the Indo-Burman Ranges.

This chapter is laid out as follows. In section 2.2 I describe the theoretical model of a fold-thrust belt. In section 2.3 I describe the analytical and numerical results of this model. Finally, in section 2.4 I discuss applications of the model to the Makran accretionary prism and the Indo-Burman Ranges.

## 2.2 Model setup

Consider a two-dimensional model of a fold-thrust belt as shown in figure 2.1. Incoming sediment is modelled as a viscous fluid with density  $\rho$ , and viscosity  $\mu$ , and the underlying mantle below as an inviscid fluid with density  $\rho_m$ . For a submarine wedge,  $\rho$  should be replaced by  $\bar{\rho} = \rho - \rho_w$ , where  $\rho_w$  is the density of water. An initial configuration of the wedge at time  $t = 0$  consists of a uniform layer of sediment of thickness  $T_s$ . The height  $h(x, t)$  is the portion of the wedge above  $z = 0$ , and  $s(x, t)$  is the depth of the interface below  $z = 0$ , defined as negative in the model. The underthrusting plate is modelled as a thin-elastic beam translating horizontally with speed  $U$  towards the backstop, with elastic thickness  $T_e$ , Young’s modulus  $E$ , Poisson’s ratio  $\nu$ , and hence bending stiffness  $B = T_e^3 E / 12(1 - \nu^2)$ . Due to elasticity, there is a rapidly decay response out to infinity. However, for practical purposes a lateral extent  $x_N$  is defined as the length of the topography above a threshold value as described in section 2.3.4. For distances along the  $x$ -axis much greater than  $x_N$ , the layer is in isostatic balance with the mantle beyond the nose of the thrust belt (see figure 2.1). The viscous sediment layer is advected with this plate towards the backstop. The convergence velocity  $U$  is defined as the total rate of motion between the incoming plate and the backstop. The backstop, which is fixed at  $x = 0$ , represents a region of overlying plate that is stronger

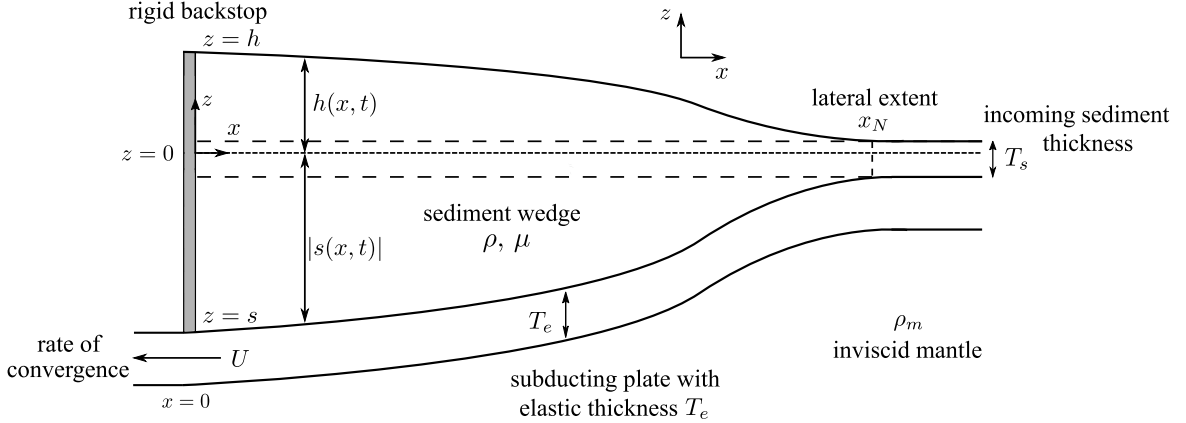


**Figure 2.1: Schematic of the theoretical model for a fold-thrust belt.** The physical parameters in the system are defined as topographic height  $h$ , plate deflection  $s$ , lateral extent  $x_N$ , incoming sediment thickness  $T_s$ , sediment and mantle densities  $\rho$  and  $\rho_m$ , and viscosity  $\mu$ , and underthrusting plate with elastic thickness  $T_e$  and convergence velocity  $U$ .

than the incoming sediments. Here, the backstop remains undeformed during the evolution of the thrust belt and prevents any flow of sediment out of the model domain.

Geological and geophysical observations show that the typical vertical thickness of a thrust belt is much smaller than the across-strike width, therefore lubrication theory (flow in a thin viscous layer) can be used to model deformation in the wedge (Schlichting, 1979). The rate of change of the thickness of the wedge ( $h - s$ ) due to advection of sediment and strain within the wedge can be written as an advection-diffusion equation (e.g. Perazzo and Gratton, 2008),

$$\frac{\partial}{\partial t} (h - s) = \frac{\rho g}{3\mu} \frac{\partial}{\partial x} \left[ (h - s)^3 \frac{\partial h}{\partial x} \right] + U \frac{\partial}{\partial x} (h - s). \quad (2.1)$$

Across the wedge there is a balance between the flexural subsidence of the plate due to the mass of the overlying wedge and the hydrostatic restoring force of the underlying mantle as a result of this subsidence. This balance is defined by the Euler-Bernoulli beam equation (Timoshenko and Woinowsky-Krieger, 1959),

$$B \frac{\partial^4 s}{\partial x^4} + \rho_m g s = -\rho g (h - s). \quad (2.2)$$

Boundary conditions are applied by first imposing no flow of sediment through the backstop at  $x = 0$ ,

$$-\frac{\rho g}{3\mu} (h - s)^3 \frac{\partial h}{\partial x} \Big|_{x=0} = U (h - s) \Big|_{x=0}. \quad (2.3)$$

It is assumed that loading behind the backstop does not affect the deformation of the underthrusting plate and therefore a mechanical break is imposed in the plate at  $x = 0$  by

setting the bending moment and shear force to be zero,

$$\left. \frac{\partial^2 s}{\partial x^2} \right|_{x=0} = \left. \frac{\partial^3 s}{\partial x^3} \right|_{x=0} = 0, \quad (2.4)$$

respectively. A uniform sediment layer thickness is imposed in the far field, which is in isostatic balance with the underlying mantle below,

$$h \rightarrow h_\infty, \quad s \rightarrow s_\infty = -\frac{\rho}{\rho_m - \rho} h_\infty \quad \text{as } x \rightarrow \infty, \quad (2.5)$$

such that  $h_\infty - s_\infty = T_s$  is the far-field sediment layer thickness. Finally, far from the loading in the wedge the underthrusting plate is undeformed so that deflections decay,

$$\frac{\partial s}{\partial x} \rightarrow 0 \quad \text{as } x \rightarrow \infty. \quad (2.6)$$

There are several natural length and time scales in the problem, with which a universal, non-dimensional problem may be determined. In the horizontal, the length scale at which the weight of the wedge begins to dominate over the strength of the plate is defined as the elastogravity length scale (also known as the flexural parameter), which has units of length,

$$l_{eg} = \left( \frac{B}{\Delta \rho g} \right)^{1/4}, \quad (2.7)$$

where  $\Delta \rho = \rho_m - \rho > 0$  is the density difference between the mantle and the sediment in the wedge. By balancing the evolution of the thickness of the wedge with the advection of sediment and strain within the wedge, as described by equation (2.1), characteristic vertical height and time scales may be written as

$$H = \left( \frac{3\mu U l_{eg}}{\rho g} \right)^{1/3}, \quad T = \frac{l_{eg}}{U}. \quad (2.8)$$

Hence non-dimensional variables are defined as

$$\tilde{h} = \frac{h}{H} \equiv h \left( \frac{\rho g}{3\mu U l_{eg}} \right)^{1/3}, \quad \tilde{s} = \frac{s}{H}, \quad \tilde{x} = \frac{x}{l_{eg}} \quad \text{and} \quad \tilde{t} = \frac{t}{T} \equiv t \frac{U}{l_{eg}}. \quad (2.9)$$

The non-dimensional equations are therefore functions of only two parameters,

$$\lambda = \frac{\rho}{\rho_m - \rho} \equiv \frac{\rho}{\Delta \rho} \quad \text{and} \quad H_\infty = T_s \left( \frac{\rho g}{3\mu U l_{eg}} \right)^{1/3}. \quad (2.10)$$

The density ratio  $\lambda = \rho/\Delta\rho$  describes the proportion of the wedge thickness accommodated by downwards deflection of the underthrusting plate in isostatic balance. The parameter  $H_\infty$  is the ratio of buoyancy forces to the compressive forces, over the elastogravity length scale.  $H_\infty$  is therefore equivalent to the Argand number (often expressed as the ratio between the stress from buoyancy to the stress needed to deform the material; England and McKenzie, 1982), with the addition of flexural effects.

Dropping the hat decoration, the non-dimensional equations can be written as

$$\frac{\partial}{\partial t}(h-s) = \frac{\partial}{\partial x} \left[ (h-s)^3 \frac{\partial h}{\partial x} \right] + \frac{\partial}{\partial x}(h-s), \quad (2.11)$$

$$\frac{\partial^4 s}{\partial x^4} + s = -\lambda h, \quad (2.12)$$

with boundary conditions

$$(h-s)^2 \frac{\partial h}{\partial x} = -1, \quad \frac{\partial^2 s}{\partial x^2} = \frac{\partial^3 s}{\partial x^3} = 0 \quad \text{at } x=0, \quad (2.13)$$

$$h \rightarrow \frac{H_\infty}{1+\lambda}, \quad s \rightarrow -\frac{\lambda H_\infty}{1+\lambda}, \quad \frac{\partial s}{\partial x} \rightarrow 0 \quad \text{as } x \rightarrow \infty. \quad (2.14)$$

The total volume accumulated in the wedge due to advection is given by

$$H_\infty t = \int_0^\infty (h-s-H_\infty) dx. \quad (2.15)$$

This statement of global mass conservation is a direct consequence of local mass conservation and the requirement of zero flow of sediment through the backstop and out of the model domain, given by equation (2.3). By varying  $\lambda$  and  $H_\infty$ , the full parameter space can be explored for any properties of the incoming sediment and underthrusting plate.

In deriving this model, several assumptions have been made in order to reduce the number of unknown parameters. Firstly, the underthrusting plate is modelled as a thin-elastic beam resting on an inviscid fluid mantle. Here the timescale over which the wedge evolves is assumed to be much longer than the viscous relaxation time of the underlying mantle, and hence there is no viscous resistance to deflection, and shorter than the viscous relaxation of the lithosphere (Walcott, 1970; Watts et al., 2013). Secondly, by modelling the sediment as a viscous fluid the viscosity of the sediment is assumed to be much smaller than that of the underthrusting plate (Brace and Kohlstedt, 1980). Ellis et al. (1995) included the viscosity of the underlying mantle in their analysis when considering crustal thickening at convergent margins, and showed that the coupling to the mantle can be neglected when the wedge is weakly coupled to its base, or when thickness of the underlying mantle is large compared with the deflection of the underthrusting plate, as assumed in the model described above. A

basally driven model can then be used, where the underlying mantle is inviscid in comparison to the sedimentary wedge and only provides a hydrostatic restoring force to the wedge.

At the backstop the boundary condition that there is no flow of sediment out of the wedge is imposed. It would be relatively straightforward to include the subduction of deformable sediment in the model (Shreve and Cloos, 1986). Doing so would not change the qualitative results of the model but would make the analysis more complex. In the analysis to follow the bottom of the wedge is referred to as the underthrusting plate but this should be thought of as the base of the deformable sediment, where lithified sediment mechanically coupled to the underthrusting plate is treated as part of the plate. In addition, any erosion of the topography is neglected, which would generally smooth the topographic surface, but again have no impact on the qualitative results described.

Finally, a Newtonian viscous rheology is assumed for the sediment in the thrust belt, meaning that the stress is linearly related to the strain rate. The aim is to model the long wavelength topography associated with fold-thrust belts on length scales much larger than individual faults (England and McKenzie, 1982). This rheology is chosen for its simplicity, and ability to accommodate distributed and spatially variable deformation. This model can be extended to a power-law rheology. For a power-law rheology the stress is proportional to some power of the strain rate, allowing effective viscosities to reduce with increased shear stress. It is anticipated that, as for a convergent Newtonian viscous gravity current on a horizontal non-deforming base (Gratton and Perazzo, 2009), a power-law rheology would give fold-thrust belts with steeper surface gradients and hence imply larger bulk viscosities than the Newtonian equivalent. However, because fluid-activated or thermally-activated creep results in a Newtonian rheology (Rutter, 1983), a Newtonian viscous fluid is used in the model described above.

## 2.3 Model results

In this section the different regimes of wedge evolution are described due to the competition between elastic deformation of the underthrusting plate, advection of sediment, and strain within the wedge. A brief overview of the key results and regimes of wedge evolution is given in section 2.3.1. Then, in sections 2.3.2 and 2.3.3, analytical results underpinning these model regimes are derived along with examples of the shapes and vertical and horizontal length scales of wedges in each regime. Finally, in section 2.3.4 the numerical solutions of the fully coupled system are described to investigate the transition between these regimes.

### 2.3.1 Overview of regimes of wedge evolution

The wedge evolves from early to late time depending on the vertical and horizontal length scales. ‘Early time’ is defined as when the lateral extent of the wedge is much less than the elastogravity length scale  $l_{eg}$  (non-dimensional extent  $x_N \ll 1$ ) and the vertical thickness of the wedge is much less than the incoming non-dimensional sediment height  $H_\infty/(1 + \lambda) = T_s(\rho g/3\mu U l_{eg})^{1/3}/(1 + \lambda)$ , where the density ratio  $\lambda = \rho/\Delta\rho$ . ‘Late time’ is defined as when the lateral extent of the wedge is much greater than the elastogravity length scale (non-dimensional extent  $x_N \gg 1$ ) and the vertical thickness of the wedge is much greater than the incoming non-dimensional sediment height  $H_\infty/(1 + \lambda)$ . By balancing the sediment flux due to strain within the wedge with the flux due to advection of sediment on the underthrusting plate, a critical non-dimensional parameter  $\Lambda_C = \pi^{1/2} H_\infty^3/(1 + \lambda)$  is defined. The evolution of the wedge from early to late time depends on the value of this parameter, and describes whether lateral spreading due to strain within the wedge or vertical thickening due to advection of sediment is the dominant mechanism for growth. From now on, lateral spreading due to strain within the wedge is referred to as ‘gravitational spreading’, where the lateral extent increases due to gravity acting on topography. For a wedge with a low viscosity, high density and thick incoming sediment layer, and an underthrusting plate with a small elastic thickness and convergence velocity (i.e. large critical non-dimensional parameter  $\Lambda_C \gg 1$ ), the initial evolution is predominantly through gravitational spreading, with little vertical thickening due to advection of sediment. In contrast, for a wedge with a high viscosity, low density and thin incoming sediment layer, and an underthrusting plate with a large elastic thickness and convergence velocity (i.e. small  $\Lambda_C \ll 1$ ), the initial evolution is predominantly through vertical thickening due to advection of sediment, with little gravitational spreading.

Figure 2.2 plots the lateral extent of the wedge  $x_N$  against the normalised maximum topographic height at the backstop,  $h_0 = h(0, t)$ . The points are calculated numerically as described below in section 2.3.4, where different symbols represent different values of the non-dimensional parameters  $H_\infty$  and  $\lambda$ , and hence  $\Lambda_C$ , with increasing time going from the bottom left to the top right of the graph. Figure 2.2 is split into four quadrants, as shown by the vertical and horizontal dashed lines, to indicate the four regimes: early-time; intermediate time, gravitational spreading dominant; intermediate time, vertical thickening dominant; and late-time. The schematics i–iv in figure 2.2 demonstrate the key scalings for the vertical and horizontal length scales of the wedge for these regimes from the theoretical analysis described below. The early- and late-time regimes occur in the bottom left and top right-hand quadrants, with scalings represented by schematics i and iv respectively. When  $\Lambda_C$  is large ( $\Lambda_C \gg 1$ ) the wedge grows predominantly by gravitational spreading, hereafter referred to as Path 1. Evolving through this intermediate regime, the numerical solution passes

through the bottom right-hand quadrant with scalings represented by schematic figure 2.2ii. However, when the parameter  $\Lambda_C$  is small ( $\Lambda_C \ll 1$ ) the wedge grows predominantly by vertical thickening due to advection of sediment, referred to as Path 2. Evolving through this intermediate regime, the numerical solution passes through the top left-hand quadrant with scalings represented by schematic figure 2.2iii. In sections 2.3.2–2.3.3, the analytical results underpinning these model regimes are described along with examples of the size of wedges in each regime.

### 2.3.2 Flexural subsidence of the underthrusting plate

The deformation of the underthrusting plate due to the mass of the overlying wedge is dependent on the lateral extent of the sediment load. For small lateral extents, where the sediment has not spread to lengths greater than the elastogravity length scale  $l_{eg}$  (non-dimensional extent  $x_N \ll 1$ ), the loading due to the wedge can be approximated as a point force localised at the position of the backstop  $x = 0$ . Assuming also that the increase in the thickness of sediment is small compared with the total incoming sediment thickness,  $(h - s) - H_\infty \ll H_\infty$ , equation (2.12), describing the flexural subsidence of the plate, reduces to

$$\frac{\partial^4 s}{\partial x^4} + (1 + \lambda)s \simeq -\lambda H_\infty. \quad (2.16)$$

Boundary conditions at the backstop and in the far field can now be applied (equations (2.13) and (2.14)) with the condition of zero shear force being replaced by the approximation of a point loading force,

$$\left. \frac{\partial^3 s}{\partial x^3} \right|_{x=0} = -\lambda H_\infty t. \quad (2.17)$$

Hence the deflection of the underthrusting plate for  $x_N \ll 1$  is given by

$$s = -\frac{\lambda H_\infty}{1 + \lambda} \left[ 1 + \sqrt{2}(1 + \lambda)^{1/4} t e^{-mx} \cos mx \right], \quad (2.18)$$

where  $m = (1 + \lambda)^{1/4}/\sqrt{2}$ . The maximum deflection is  $\sqrt{2}\lambda H_\infty t/(1 + \lambda)^{3/4}$  with oscillations that decay to the far-field deflection  $-\lambda H_\infty/(1 + \lambda)$ , with decay rate and wavelength  $1/m$ .

When the lateral extent of the sediment load is much greater than the elastogravity length scale ( $x_N \gg 1$ ), the underthrusting plate can no longer support the topography. The pressure due to the deflection of the plate is now dominated by a balance between the loading of the wedge and the hydrostatic restoring force of the underlying mantle. For large lateral extents, the wedge therefore transitions into isostatic balance where

$$s(x, t) = -\lambda h(x, t), \quad (2.19)$$

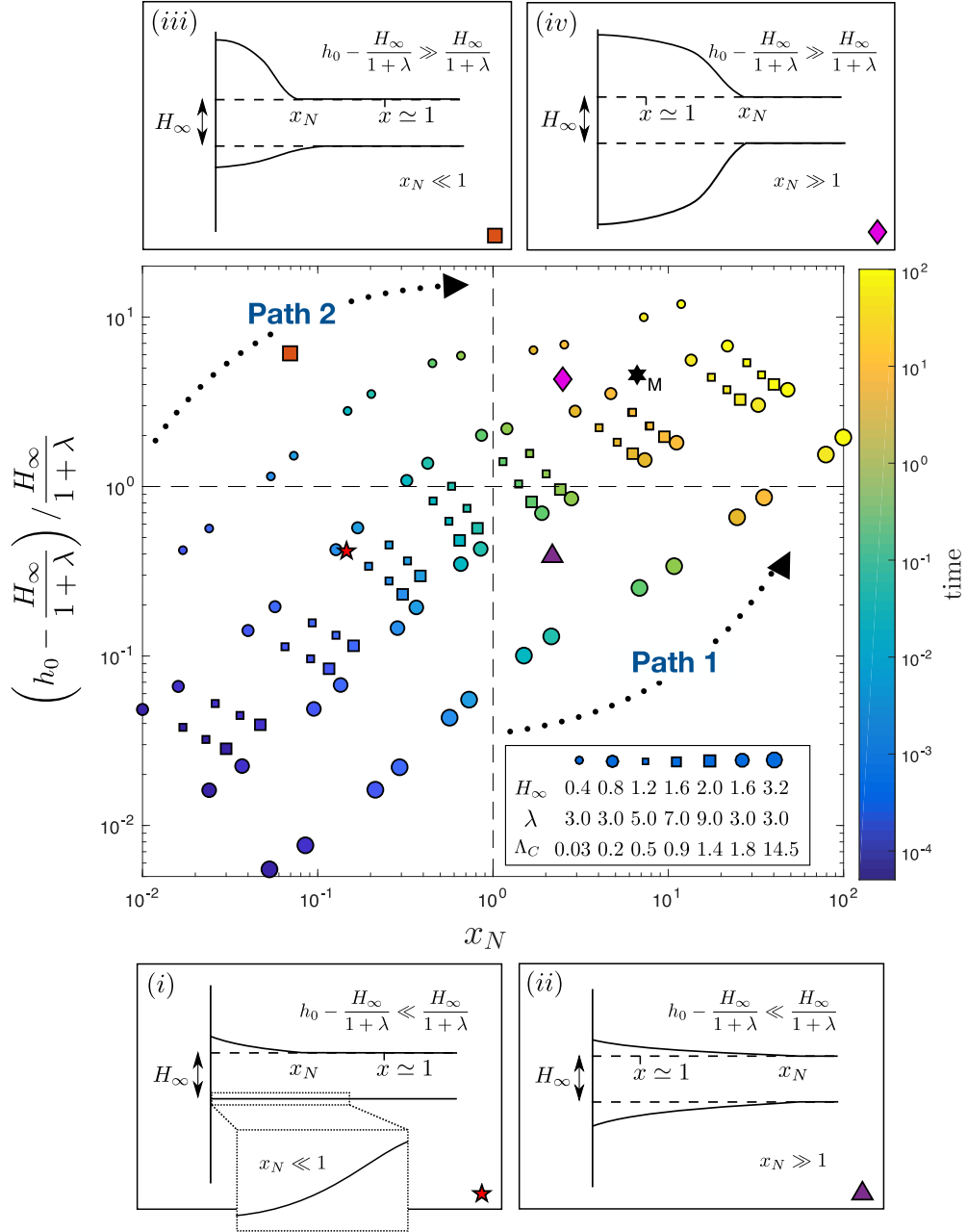


**Figure 2.2: Regime plot of the evolution of a fold-thrust belt.** Graph of horizontal extent  $x_N$  plotted against maximum vertical topographic height  $h_0$  normalised by the sediment thickness above  $z = 0$ ,  $H_\infty/(1 + \lambda)$ , for seven different numerical simulations for different values of parameters  $H_\infty$  and  $\lambda$ , and hence  $\Lambda_C$ , see legend. (i-iv) Schematics of different regimes of propagation: (i) Early-time regime, (ii) intermediate regime along Path 1, where gravitational spreading dominates, (iii) intermediate regime along Path 2, where vertical thickening due to advection of sediment dominates, and (iv) late-time regime. The red star, purple triangle, orange square and pink diamond refer to specific examples of wedges in each regime as described in section 2.3.3. The black hexagon labelled ‘M’ refers to the Makran accretionary prism, see section 2.4.1.

except near the nose region, where flexure of the plate remains important on length scales comparable to the elastogravity length scale.

### 2.3.3 Height of topography

#### Early time

The evolution of the height of the wedge  $h$  depends on the relative height of the wedge compared with incoming non-dimensional sediment height  $H_\infty/(1+\lambda)$  above  $z = 0$ . Initially, the height of the wedge is small compared with the height of the advected sediment layer,  $h_0 - H_\infty/(1+\lambda) \ll H_\infty/(1+\lambda)$ . In addition, the added load of the wedge acts as a point force (equation (2.18)) but is initially insufficient to significantly deform the plate and hence the underthrusting plate remains relatively undeformed with  $s \simeq -\lambda H_\infty/(1+\lambda)$ . The governing equation for the height of the wedge can therefore be linearised about the far-field sediment height. A scaling of equation (2.11) suggests that initially thickening due to advection is small,

$$\frac{h}{t} \sim \frac{H_\infty^3 h}{x^2} \gg \frac{h}{x} \quad \text{provided} \quad x_N \ll H_\infty^3, \quad (2.20)$$

giving height and extent scales  $h - H_\infty/(1+\lambda) \sim H_\infty^{-1/2} t^{1/2}$  and  $x_N \sim H_\infty^{3/2} t^{1/2}$ . In this limit the topography of the wedge is self-similar. Hence, the similarity variable  $\zeta = x/(4H_\infty^3 t)^{1/2}$  may be defined with the height written as  $h = H_\infty/(1+\lambda) + t^{1/2} f(\zeta)$ ,  $s \simeq -\lambda H_\infty/(1+\lambda)$ , where  $f$  is a solution to the non-linear ordinary differential equation

$$\frac{\partial^2 f}{\partial \zeta^2} + 2\zeta \frac{\partial f}{\partial \zeta} - 2f = 0 \quad \Rightarrow \quad f = c_1 \zeta + c_2 \left[ \pi^{1/2} \zeta \operatorname{erfc}(\zeta) - \exp(-\zeta^2) \right], \quad (2.21)$$

and  $c_1, c_2$  are constants of integration that need to be determined by applying boundary conditions at the backstop and in the far field. Linearising the boundary conditions (equations (2.13) and (2.14)),

$$H_\infty^2 \frac{\partial h}{\partial x} \Big|_{x=0} = -1 \quad \text{and} \quad h(x \rightarrow \infty) \rightarrow \frac{H_\infty}{1+\lambda}, \quad (2.22)$$

and applying these to the general solution for  $f$  (equation (2.21)), then gives an expression for the topographic height of an accretionary wedge in the early-time regime,

$$h = \frac{H_\infty}{1+\lambda} + \frac{2t^{1/2}}{(\pi H_\infty)^{1/2}} \left[ \exp\left(-\frac{x^2}{4H_\infty^3 t}\right) - \frac{\pi^{1/2} x}{2(H_\infty^3 t)^{1/2}} \operatorname{erfc}\left(\frac{x}{2(H_\infty^3 t)^{1/2}}\right) \right]. \quad (2.23)$$

This analytical result is shown by Perazzo and Gratton (2008) for a viscous convergent gravity current on a horizontal, non-deformable base. The maximum topographic height is

$H_\infty/(1+\lambda) + 2t^{1/2}/(\pi H_\infty)^{1/2}$  which decays monotonically to the far-field sediment layer height  $H_\infty/(1+\lambda)$ , with lateral extent given by  $x_N \sim 2H_\infty^{3/2}t^{1/2}$ . Equation (2.23) for the topographic height along with equation (2.18) for the deflection of the underlying plate defines the early-time regime where lateral extent of the wedge is much less than the elastogravity length scale  $l_{eg}$  and the vertical height is much less than the non-dimensional incoming sediment height  $H_\infty/(1+\lambda)$ . Applying these bounds ( $x_N \ll 1$  and  $h_0 - H_\infty/(1+\lambda) \ll H_\infty/(1+\lambda)$ ) to the scalings from equation (2.23) gives a timescale for the early-time regime,

$$2H_\infty^{3/2}t^{1/2} \ll 1 \quad \text{and} \quad \frac{2t^{1/2}}{(\pi H_\infty)^{1/2}} \ll \frac{H_\infty}{1+\lambda} \quad \Rightarrow \quad t \ll \min \left\{ \frac{\pi H_\infty^3}{4(1+\lambda)^2}, \frac{1}{4H_\infty^3} \right\}. \quad (2.24)$$

To indicate when the early-time regime may be appropriate in nature, consider a wedge with common values of parameters of sediment thickness, viscosity and density  $T_s = 4$  km,  $\mu = 10^{20}$  Pa s and  $\rho = 2400$  kg m<sup>-3</sup> respectively, where the underthrusting plate has an elastic thickness of  $T_e = 20$  km, Young's modulus  $E = 10^{11}$  Pa, Poisson's ratio  $\nu = 0.25$ , and convergence velocity  $U = 4$  mm yr<sup>-1</sup>, with an underlying mantle of density  $\rho_m = 3300$  kg m<sup>-3</sup> ( $H_\infty = 0.91$ ,  $\lambda = 2.7$ ). For an age of  $t = 0.1$  Myr, this gives a maximum topographic height of  $\sim 450$  m above the far-field sediment height, with lateral extent of  $\sim 8$  km. From equation (2.18), the maximum deflection of the plate is  $\sim 43$  m with decay rate and wavelength  $\sim 54$  km. Substituting these parameters into timescale given in equation (2.24) shows that the conditions for early-time regime behaviour are satisfied provided  $t \ll 1$  Myr. Hence these behaviours are not expected to be observed except in the very early stages of wedge growth. On figure 2.2 this early-time regime represents the bottom left-hand quadrant where  $x_N \ll 1$  and  $h_0 - H_\infty/(1+\lambda) \ll H_\infty/(1+\lambda)$ . This example is marked as a red star in the bottom left-hand quadrant of figure 2.2, and is demonstrated by the schematic i.

### Intermediate time: gravitational spreading dominant

After this early-time regime the wedge can either grow by gravitational spreading or vertical thickening. If the wedge spreads laterally more rapidly than it thickens vertically, referred to as Path 1 (figure 2.2), it can reach an intermediate regime where the lateral extent of the wedge is much greater than the elastogravity length scale  $l_{eg}$  but the vertical height of the wedge is still much less than the non-dimensional sediment height  $H_\infty/(1+\lambda)$ . Applying these bounds ( $x_N \gg 1$  and  $h_0 - H_\infty/(1+\lambda) \ll H_\infty/(1+\lambda)$ ) to the solution for the early-time topographic height, equation (2.23), gives a condition for evolution along Path 1,

$$2H_\infty^{3/2}t^{1/2} \sim 1 \quad \text{and} \quad \frac{2t^{1/2}}{(\pi H_\infty)^{1/2}} \ll \frac{H_\infty}{1+\lambda} \quad \Rightarrow \quad \Lambda_C \equiv \frac{\pi^{1/2}H_\infty^3}{1+\lambda} \gg 1, \quad (2.25)$$

where  $\Lambda_C$  is the critical non-dimensional parameter defined above, the effect of which is described below.

Since the lateral extent of the wedge is much greater than the elastogravity length scale ( $x_N \gg 1$ ), the wedge is in isostatic balance and the deflection of the plate is linearly proportional to the topographic height, given by equation (2.19). Substituting this expression for the deflection  $s$  into equation (2.11), and carrying out a similar analysis to above, gives an expression for the topography of a wedge in the intermediate regime evolving along Path 1,

$$h = \frac{H_\infty}{1 + \lambda} + \frac{2t^{1/2}}{(\pi(1 + \lambda)H_\infty)^{1/2}} \left[ \exp\left(-\frac{(1 + \lambda)x^2}{4H_\infty^3 t}\right) - \frac{(\pi(1 + \lambda))^{1/2} x}{2(H_\infty^3 t)^{1/2}} \operatorname{erfc}\left(\frac{(1 + \lambda)^{1/2} x}{2(H_\infty^3 t)^{1/2}}\right) \right]. \quad (2.26)$$

The maximum topographic height is  $H_\infty/(1 + \lambda) + 2t^{1/2}/(\pi(1 + \lambda)H_\infty)^{1/2}$  which decays monotonically to the far-field sediment layer height  $H_\infty/(1 + \lambda)$ , with lateral extent given by  $x_N \sim 2H_\infty^{3/2}t^{1/2}/(1 + \lambda)^{1/2}$ . To demonstrate evolution of a wedge along Path 1, consider a wedge with sediment thickness, viscosity and density  $T_s = 10$  km,  $\mu = 10^{20}$  Pa s and  $\rho = 2400$  kg m<sup>-3</sup> respectively, where the underthrusting plate has an elastic thickness of  $T_e = 20$  km, Young's modulus  $E = 10^{11}$  Pa, Poisson's ratio  $\nu = 0.25$  and convergence velocity  $U = 4$  mm yr<sup>-1</sup>, with an underlying mantle of density  $\rho_m = 3300$  kg m<sup>-3</sup> ( $H_\infty = 2.3$ ,  $\lambda = 2.7$ ). Substituting these values into equation (2.25) gives critical non-dimensional parameter  $\Lambda_C = 5.6 \gg 1$ , hence it is expected for the wedge to evolve along Path 1. Taking a wedge of age  $t = 5$  Myr gives a maximum topographic height of  $\sim 1.1$  km above the far-field sediment height, maximum deflection of the plate of  $\sim 2.8$  km and a lateral extent of  $\sim 120$  km. On figure 2.2 this intermediate regime evolving along Path 1 represents the bottom right-hand quadrant where  $x_N \gg 1$  and  $h_0 - H_\infty/(1 + \lambda) \ll H_\infty/(1 + \lambda)$ . This example is marked as a purple triangle in the bottom right-hand quadrant of figure 2.2, and is demonstrated by the schematic ii. This evolution represents regions where the incoming sediment layer is thick with low viscosity and high density, and the underthrusting plate has a small elastic thickness and small convergence velocity.

### Intermediate time: thickening dominant

If the wedge thickens vertically more rapidly than it spreads laterally, it follows an alternative evolution referred to as Path 2. Along this second trajectory the wedge can reach an intermediate regime where the lateral extent of the wedge is still much less than the elastogravity length scale but the vertical height of the wedge is much greater than the non-dimensional sediment height  $H_\infty/(1 + \lambda)$ . Applying these bounds ( $x_N \ll 1$  and  $h_0 - H_\infty/(1 + \lambda) \gg H_\infty/(1 + \lambda)$ ) to the solution for the early-time topographic height, equation (2.23), gives a condition for

evolution along Path 2,

$$2H_\infty^{3/2}t^{1/2} \ll 1 \quad \text{and} \quad \frac{2t^{1/2}}{(\pi H_\infty)^{1/2}} \sim \frac{H_\infty}{1+\lambda} \Rightarrow \Lambda_C \equiv \frac{\pi^{1/2}H_\infty^3}{1+\lambda} \ll 1. \quad (2.27)$$

Since the vertical height of the wedge is much greater than the non-dimensional incoming sediment height  $H_\infty/(1+\lambda)$ , the height of the wedge reaches a quasi-static balance where strain driven by lateral pressure gradients, which results in gravitational slumping and hence diffusive behaviour, balances the advection of the sediment layer by the underthrusting plate. The governing equation for the thickness of the wedge (equation (2.11)) simplifies to

$$0 = \frac{\partial}{\partial x} \left[ (h-s)^3 \frac{\partial h}{\partial x} \right] + \frac{\partial}{\partial x} (h-s). \quad (2.28)$$

Integrating equation (2.28), assuming the underthrusting plate remains relatively undeformed  $s \simeq -\lambda H_\infty/(1+\lambda)$ , and applying boundary conditions at the backstop (equation (2.13)) and at the nose due to compact support,

$$h = \frac{H_\infty}{1+\lambda} \quad \text{at} \quad x = x_N, \quad (2.29)$$

gives the expression for the topographic height

$$h = -\frac{\lambda H_\infty}{1+\lambda} + \left[ H_\infty^3 + 3(x_N - x) \right]^{1/3}. \quad (2.30)$$

Using the statement of global conservation of mass (equation (2.15)), the lateral extent  $x_N$  is given by the real root of

$$H_\infty \left( \frac{1}{4} H_\infty^3 + x_N + t \right) = \frac{1}{4} (H_\infty^3 + 3x_N)^{4/3}. \quad (2.31)$$

Equation (2.30) describes a cube root profile where the topographic height no longer explicitly depends on time (although there is an implicit time dependence through the lateral extent  $x_N$ ), and hence can be described as quasi-static. For example, consider a wedge with sediment thickness, viscosity and density  $T_s = 1$  km,  $\mu = 10^{20}$  Pa s and  $\rho = 2400$  kg m<sup>-3</sup> respectively, where the underthrusting plate has an elastic thickness of  $T_e = 20$  km, Young's modulus  $E = 10^{11}$  Pa, Poisson's ratio  $\nu = 0.25$  and convergence velocity  $U = 4$  mm yr<sup>-1</sup>, with an underlying mantle of density  $\rho_m = 3300$  kg m<sup>-3</sup> ( $H_\infty = 0.23$ ,  $\lambda = 2.7$ ). Substituting these values into equation (2.27) gives critical non-dimensional parameter  $\Lambda_C = 0.0056 \ll 1$ , hence it is expected for the wedge to evolve along Path 2. Taking a wedge of age  $t = 1$  Myr gives a maximum topographic height of  $\sim 1.7$  km above the far-field sediment height, with lateral extent  $\sim 3.7$  km. From equation (2.18) the maximum deflection of the plate

is  $\sim 110$  m with decay rate and wavelength  $\sim 54$  km. On figure 2.2 this intermediate regime evolving along Path 2 represents the top left-hand quadrant where  $x_N \ll 1$  and  $h_0 - H_\infty/(1 + \lambda) \gg H_\infty/(1 + \lambda)$ . This example is marked as an orange square in the top left-hand quadrant of figure 2.2, and is demonstrated by the schematic iii. This path represents regions where the incoming sediment layer is thin with a high viscosity and low density, and the underthrusting plate has a large elastic thickness and a high convergence rate.

### Late time

Ultimately, the evolution of a wedge along both Path 1 or Path 2 transitions into the late-time regime where the lateral extent of the wedge is much greater than the elastogravity length scale ( $x_N \gg 1$ ) and the height of the wedge is much greater than the non-dimensional sediment height ( $h_0 - H_\infty/(1 + \lambda) \gg H_\infty/(1 + \lambda)$ ). Since the lateral extent is much greater than the elastogravity length scale ( $x_N \gg 1$ ) the wedge is in isostatic balance with deflection given by equation (2.19). As in the intermediate regime along Path 2, the wedge is in a quasi-static state where strain balances the advection of the sediment layer by the underthrusting plate. Substituting the deflection (equation (2.19)) into the governing equation for the quasi-static wedge (equation (2.28)), integrating and applying boundary conditions at the backstop and compact support at the nose (equations (2.13) and (2.29)), the topographic height is given by

$$h = \left[ \frac{H_\infty^3}{(1 + \lambda)^3} + \frac{3(x_N - x)}{(1 + \lambda)^2} \right]^{1/3}. \quad (2.32)$$

Again, using the statement of global conservation of mass (equation (2.15)), the lateral extent  $x_N$  is given by the real root of

$$H_\infty \left[ \frac{H_\infty^3}{4(1 + \lambda)} + x_N + t \right] = \frac{1}{4(1 + \lambda)} \left[ H_\infty^3 + 3(1 + \lambda)x_N \right]^{4/3}. \quad (2.33)$$

Equation (2.32) describes a cube root profile where the topographic height of the wedge no longer explicitly depends on time (although there is an implicit time dependence through the lateral extent  $x_N$ ). For example, consider a wedge with sediment thickness, viscosity and density  $T_s = 2$  km,  $\mu = 10^{19}$  Pa s,  $\rho = 2400$  kg m $^{-3}$  respectively, where the underthrusting plate has an elastic thickness of  $T_e = 20$  km, Young's modulus  $E = 10^{11}$  Pa, Poisson's ratio  $\nu = 0.25$  and convergence velocity  $U = 20$  mm yr $^{-1}$ , with an underlying mantle of density  $\rho_m = 3300$  kg m $^{-3}$  ( $H_\infty = 0.57$ ,  $\lambda = 2.7$ ). For an age of  $t = 20$  Myr, the wedge would have maximum topographic height  $\sim 2.3$  km above the far-field sediment height, maximum deflection of the plate of  $\sim 6.3$  km, with lateral extent  $\sim 130$  km. On

figure 2.2 this late-time regime represents the top right-hand quadrant where  $x_N \gg 1$  and  $h_0 - H_\infty/(1 + \lambda) \gg H_\infty/(1 + \lambda)$ . This example is marked as a pink diamond in the top right-hand quadrant of figure 2.2, and is demonstrated by the schematic iv.

The analytical solutions derived above describe the limiting case in each of the four regimes shown in figure 2.2. However, a given fold-thrust belt lies along an evolutionary transition between these solutions. In order to fully understand how a fold-thrust belt evolves, in the next section this coupled system is solved numerically. In particular, the full evolution of two wedges is described, one evolving along Path 1, and one evolving along Path 2.

### 2.3.4 Numerical solutions

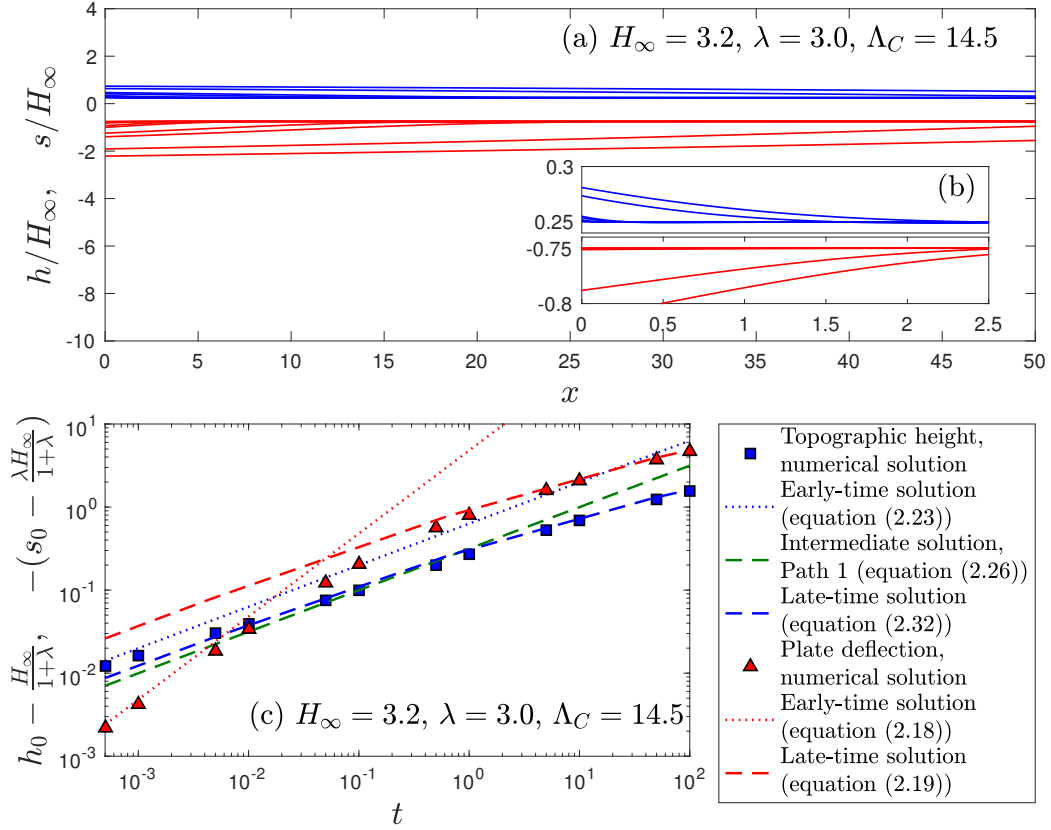
The coupled system of non-dimensional equations for the evolution of the topographic height and the flexural subsidence of the underthrusting plate was solved, as described by equations (2.11) and (2.12), along with boundary conditions at the backstop and in the far field (equations (2.13) and (2.14)), and global mass conservation (equation (2.15)). The numerical scheme uses a finite difference Crank-Nicolson algorithm with an adaptive time and spatial step, and a predictor-corrector scheme to handle the non-linearities (see Appendix A).

Figure 2.2 plots the vertical topographic height against the lateral extent for seven different numerical simulations with different values of non-dimensional parameters  $H_\infty$  and  $\lambda$  (see legend inset). Note that the location of the lateral extent  $x_N$  is determined by considering the width of topography above a threshold value such that  $h(x_N, t) - H_\infty/(1 + \lambda) = 10^{-3}$  at the edge of the wedge, consistent in all simulations. The transition between evolution along Path 1 or Path 2 depends on the critical non-dimensional parameter  $\Lambda_C = \pi^{1/2} H_\infty^3 / (1 + \lambda)$ . Figure 2.2 shows that by decreasing  $\Lambda_C$  the evolution moves from Path 1 to Path 2 with the transition occurring when  $\Lambda_C \sim 1$ . In dimensional form, the transition occurs when  $\Lambda_C = \pi^{1/2} T_s^3 \rho g / [3\mu U l_{eg} (1 + \rho/\Delta\rho)] \sim 1$ . Hence, by decreasing the sediment thickness and density and/or increasing the sediment viscosity and elastic thickness and convergence velocity of the underthrusting plate, evolution moves from predominantly gravitational spreading along Path 1 to predominantly vertical thickening along Path 2.

Figures 2.3 and 2.4 show the two numerical simulations from figure 2.2 with the largest and smallest values of  $\Lambda_C$ , respectively. Figure 2.3a plots the profiles of the topographic height (blue lines) and plate deflection (red lines) with parameters  $H_\infty = 3.2$ ,  $\lambda = 3.0$  and  $\Lambda_C = 14.5 \gg 1$  for times  $t = 5 \times 10^{-4}, 10^{-3}, \dots, 10^2$ , where figure 2.3b (inset) is a zoom of profiles at early times ( $t \leq 10^{-1}$ ). Evolution of the wedge is along Path 1, where gravitational spreading dominates over vertical thickening. Figure 2.3c is a log-log plot of the maximum topographic height (blue squares) and maximum plate deflection (red triangles) against

time. The dotted and dashed lines plot the early- and late-time solutions respectively for the maximum topographic height (blue, equations (2.23) and (2.32)) and the maximum plate deflection (red, equations (2.18) and (2.19)) and show good agreement with the numerical solution for small and large times. The green dashed line plots the solution between the early- and late-times for the height of the topographic wedge, defined as the intermediate solution, for evolution along Path 1 (equation (2.26)). Although it does well to describe the points around  $t \sim 1$ , the intermediate solution largely overlaps the early- and late-time solutions and hence does not provide any further information about the growth of the wedge. However, it is anticipated that this solution would be more useful (i.e. describe the evolution when both the early- and late-time do not apply) when there is a larger separation between the early- and late-time i.e. for larger  $\Lambda_C$ . This evolution describes a wedge with a thick incoming sediment layer of large density and small viscosity, and an underthrusting plate with a small elastic thickness and low convergence velocity.

Figure 2.4a plots the profiles of the topographic height (blue lines) and plate deflection (red lines) with parameters  $H_\infty = 0.4$ ,  $\lambda = 3.0$  and  $\Lambda_C = 0.03 \ll 1$  for times  $t = 5 \times 10^{-4}, 10^{-3}, \dots, 10^2$ , where figure 2.4b (inset) is a zoom of profiles at early times ( $t \leq 1$ ). Evolution of the wedge is along Path 2, where vertical thickening dominates over gravitational spreading. Figure 2.4c is a log-log plot of the maximum topographic height (blue squares) and maximum plate deflection (red triangles) against time. The dotted and dashed lines plot the early- and late-time solutions respectively for the maximum topographic height (blue, equations (2.23) and (2.32)) and the maximum plate deflection (red, equations (2.18) and (2.19)) and again shows good agreement with the numerical solution for small and large times. The green dashed line plots the solution between early- and late-times for the height of the topographic wedge (the intermediate solution) for the evolution along Path 2 (equation (2.30)). This intermediate solution does well to describe the points around  $t \sim 1$  where both the early-time and late-time solution do not apply: the numerical solution given by the blue squares sits in between the blue dot-dashed and dashed lines for the early- and late-time solutions respectively, but sits close to the green dashed line of the intermediate solution. This evolution describes a wedge with a thin incoming sediment layer of small density and large viscosity, and an underthrusting plate with a large elastic thickness and high convergence velocity. Comparing the profiles of the two wedges (figures 2.3a and 2.4a) there is a clear difference in the nose region of the wedge where there is a prominent flexural depression and bulge when  $\Lambda_C = 0.03 \ll 1$  compared with when  $\Lambda_C = 14.5 \gg 1$ . This forms at early times, figure 2.4b, and then propagates as a steady structure at the nose, figure 2.4a. This flexural depression and bulge demonstrates that, even at late times when the wedge is in isostatic balance, flexure remains important on length scales comparable with the elastogravity length scale  $l_{eg}$ . Away from the nose, the general shape of the profiles look similar, however the underlying balance of forces changes significantly between the two



**Figure 2.3: Numerical solutions for a fold-thrust belt with  $H_\infty = 3.2, \lambda = 3.0$ .** (a) Plot of profiles of the topographic height (blue lines) and plate deflection (red lines) for a wedge evolving along Path 1 with parameters  $H_\infty = 3.2, \lambda = 3.0, \Lambda_C = 14.5$  for  $t = 5 \times 10^{-4}, 10^{-3} \dots 10^2$ , where (b) (inset) is a zoom in of profiles at early times for  $t \leq 10^{-1}$ . (c) Log-log plot of the maximum topographic height  $h_0$  (blue squares) and maximum plate deflection  $s_0$  (red triangles) against time for each profile shown in (a–b). The dotted and dashed lines plot the early- and late-time solutions respectively for the maximum topographic height (blue) and the maximum plate deflection (red). The intermediate solution is given by the green dashed line. See legend for more details.

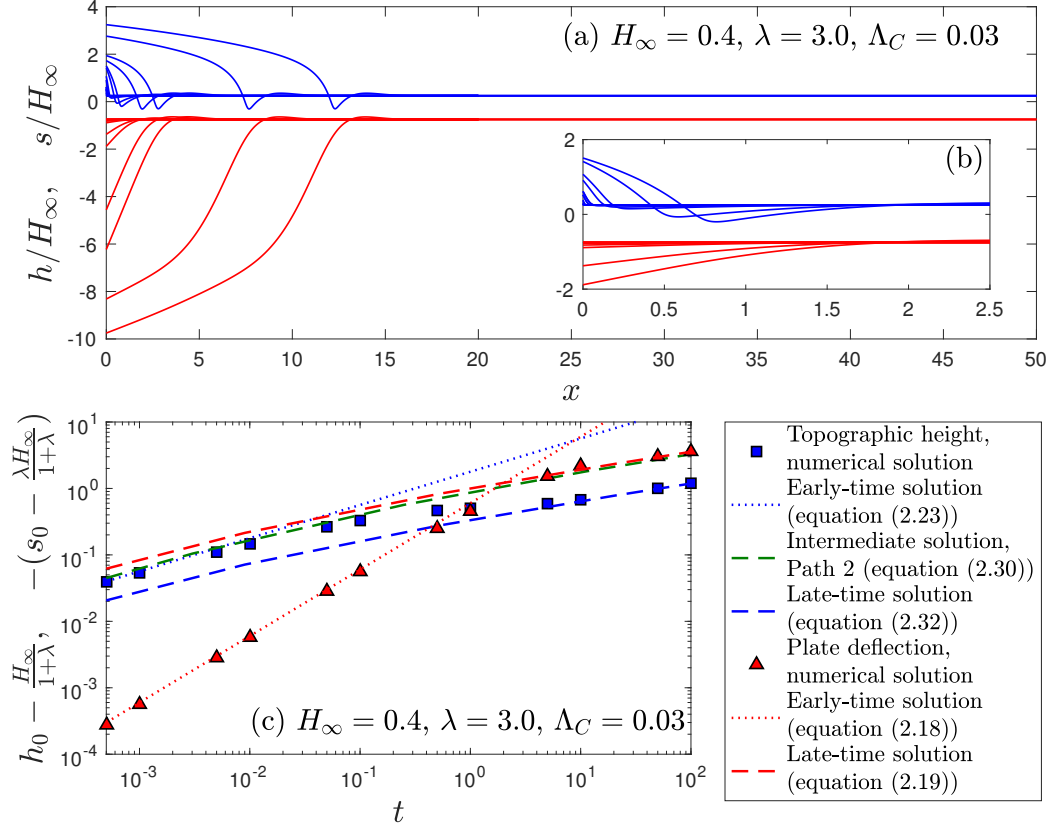


**Figure 2.4: Numerical solutions for a fold-thrust belt with  $H_\infty = 0.4, \lambda = 3.0$ .** (a) Plot of profiles of the topographic height (blue lines) and plate deflection (red lines) for a wedge evolving along Path 1 with parameters  $H_\infty = 0.4, \lambda = 3.0, \Lambda_C = 0.03$  for  $t = 5 \times 10^{-4}, 10^{-3} \dots 10^2$ , where (b) (inset) is a zoom in of profiles at early times for  $t \leq 1$ . (c) Log-log plot of the maximum topographic height  $h_0$  (blue squares) and maximum plate deflection  $s_0$  (red triangles) against time for each profile shown in (a–b). The dotted and dashed lines plot the early- and late-time solutions respectively for the maximum topographic height (blue) and the maximum plate deflection (red). The intermediate solution is given by the green dashed line. See legend for more details.

regimes, from gravitational spreading dominant to advection dominant, which is what defines the ‘regimes’.

## 2.4 Discussion and applications

The model described above considers how changing the properties of the wedge (density, viscosity, age, incoming sediment thickness) and properties of the underthrusting plate (elastic thickness, convergence velocity) affect the evolution of the wedge. In this section, the effects of changing two key parameters (the incoming sediment thickness  $T_s$  and elastic thickness  $T_e$ ) are discussed in more detail.

Figure 2.5 shows the evolution of a wedge in 5 Myr intervals for  $t = 5 - 50$  Myr, convergence velocity  $U = 4 \text{ mm yr}^{-1}$ , viscosity  $\mu = 10^{20} \text{ Pa s}$ , sediment and underlying mantle densities  $\rho = 2400 \text{ kg m}^{-3}$ ,  $\rho_m = 3300 \text{ kg m}^{-3}$  (density ratio  $\lambda = 2.7$ ). Figures 2.5a–c show a wedge in isostatic balance for which the elastic thickness of the plate is neglected ( $T_e = 0 \text{ km}$ ) with increasing sediment thicknesses  $T_s = 2, 4$  and  $10 \text{ km}$ . Figures 2.5d–f show the evolution of an identical series of wedges now resting on a underthrusting plate with an increased elastic thickness of  $T_e = 20 \text{ km}$  (Young’s Modulus  $E = 10^{11} \text{ Pa}$  and Poisson’s ratio  $\nu = 0.25$ ). Substituting these values into the critical non-dimensional parameter  $\Lambda_C$  gives  $\Lambda_C = 0.045, 0.36$  and  $5.6$  for corresponding incoming sediment thicknesses  $T_s = 2, 4$  and  $10 \text{ km}$ . Hence, both figure 2.5 and the values of  $\Lambda_C$  demonstrate that, as described in the previous section, decreasing the incoming sediment thickness, and hence decreasing  $\Lambda_C$ , causes the evolution to transition from Path 1 (figure 2.5f), to Path 2 (figure 2.5d), where vertical thickening dominates over gravitational spreading.

For the smallest sediment thickness,  $T_s = 2 \text{ km}$  in figures 2.5a and 2.5d, increasing the elastic thickness gives profiles with a higher maximum topographic elevation for small lateral extents. This is consistent with a stronger plate providing additional support to topography. In addition, increasing the elastic thickness gives a shallower dip to the deflection of the underthrusting plate behind the nose of the wedge, with a flexural depression and bulge in front of the nose of the wedge (figures 2.5d and 2.5e). This feature is present because flexure becomes important when topography varies on length scales comparable with the elastogravity length scale  $l_{eg}$ , for example near the nose. As the incoming sediment thickness increases, the elastic thickness of the plate has less of an impact on the profiles. This effect is clearly shown in figures 2.5c and 2.5f for  $T_s = 10 \text{ km}$  where the profiles of the wedge for the isostatic and flexural case are almost identical. By increasing the incoming sediment thickness, the critical non-dimensional parameter  $\Lambda_C$  increases causing the transition to

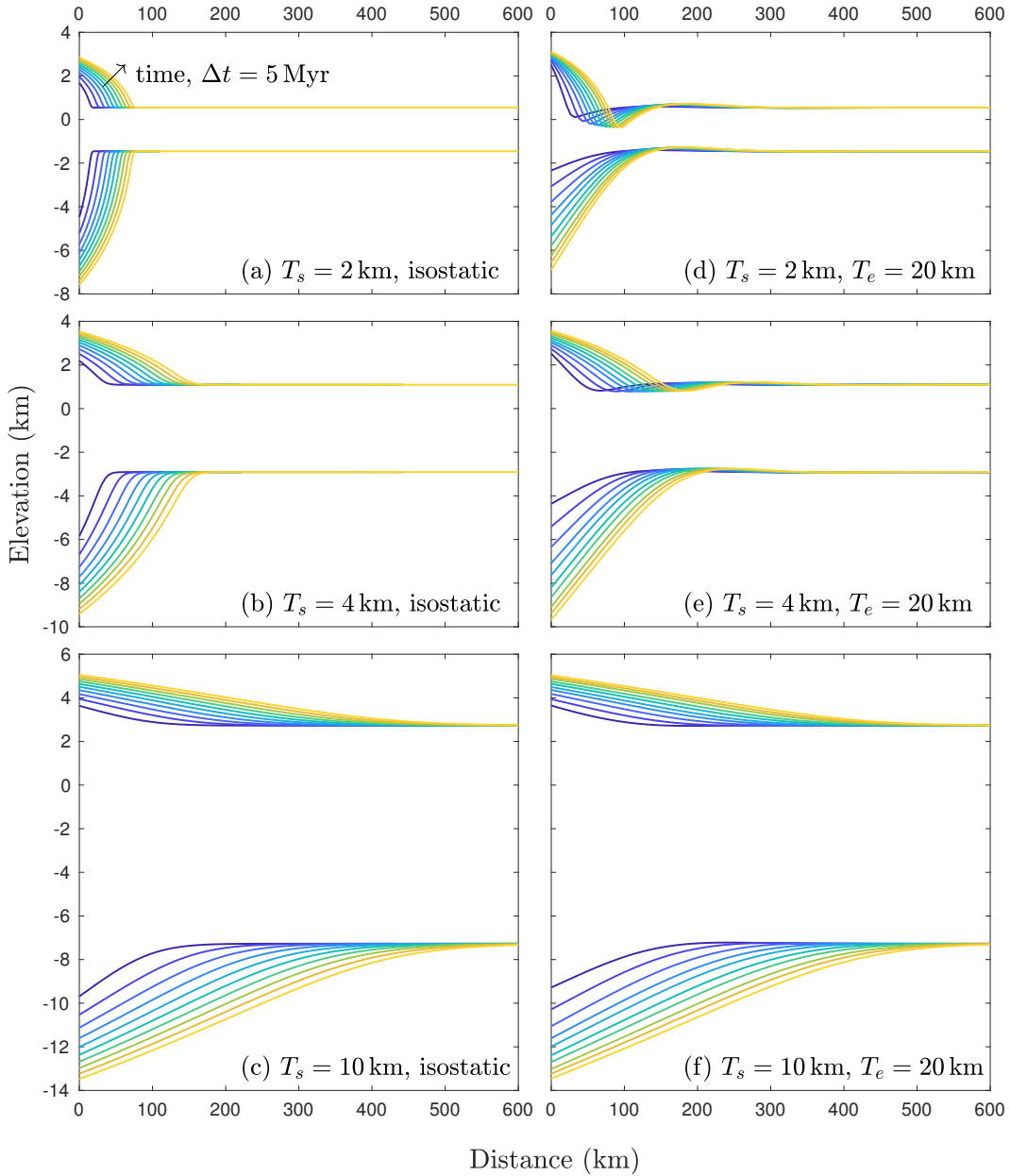


**Figure 2.5: Changing the sediment thickness and the elastic thickness.** Dimensional plot of the growth of a fold-thrust belt considering the effects of increasing the sediment thickness  $T_s$  and the elastic thickness  $T_e$ . (a–c) Evolution of a wedge for  $t = 5 - 50$  Myr and sediment thicknesses  $T_s = 2, 4, 10$  km respectively in isostatic balance with no elastic thickness ( $T_e = 0$  km). (d–f) Evolution of a wedge with the same sediment thicknesses as plots (a–c) but with elastic thickness  $T_e = 20$  km (Young’s modulus  $E = 10^{11}$  Pa, Poisson’s ratio  $\nu = 0.25$ ). In both cases, all other parameters remain the same with convergence velocity  $U = 4$  mm yr $^{-1}$ , viscosity  $\mu = 10^{20}$  Pa s, sediment and underlying mantle densities  $\rho = 2400$  kg m $^{-3}$ ,  $\rho_m = 3300$  kg m $^{-3}$ .

isostatic balance to occur at earlier times. Hence, changing the elastic thickness has less of an impact for wedges with larger sediment thicknesses.

In order to examine the effects described in the model, applications to the Makran accretionary prism and the Indo-Burman Ranges are considered. The analysis refers to specific values of the incoming sediment thickness, viscosity and density, and the elastic properties and convergence velocity of the underthrusting plate. However, the aim is to illustrate the importance of flexure and incoming sediment thickness on the evolution of fold-thrust belts in general, rather than to imply these ranges are particularly unusual.

### 2.4.1 Makran accretionary prism

The Makran accretionary prism, figure 2.6a, is one of the largest accretionary wedges on Earth. With a large sediment thickness on the incoming plate of  $\sim 7$  km (Kopp et al., 2000; White, 1982), the Makran accretionary prism is formed due to the subduction of the Arabian plate beneath southern Iran and Pakistan. The convergence rate between Arabia and eastern Iran/western Pakistan varies from  $19.5 \pm 2$  mm yr<sup>-1</sup> in the west of the Makran to  $27 \pm 2$  mm yr<sup>-1</sup> in the east (Vernant et al., 2004). Accretion of sediment into the wedge is thought to have started in the Eocene (Byrne et al., 1992), however an imbricate zone of upper Cretaceous rocks have been identified in the northern part of the Makran (Dolati, 2010), which may represent the onset of sediment accretion. These observations give a possible age range for the onset of growth of the accretionary wedge of 30 – 90 Myr.

Figure 2.6b shows three topographic profiles across the Makran centered on 59.5°E, 61°E and 63°E (red, green and blue lines respectively). The profiles show a negligible along-strike change in topography suggesting a two-dimensional model is appropriate. Figure 2.6c plots the sediment-basement interface from seismic reflection profiles at 62.9°E (solid black line, Kopp et al., 2000). The blue dots plot the inferred subduction interface at 62°E (Penney et al., 2017) based on the location of earthquakes interpreted as occurring on the subduction interface or within the subducting plate. In the following comparisons, the middle topographic profile at 61°E is taken (as there is negligible along strike variation) along with the sediment-basement and plate interface datasets shown in figure 2.6c. The backstop of the wedge is assumed to be located roughly at 27.5°N based on the location of the Jaz Murian and Maskel depressions, which low elevations and low seismic strain rates suggest are relatively undeformed. However, the position of the backstop only affects the age of the wedge in the numerical simulations, and not the overall conclusions regarding the controls on the evolution of the wedge.

The effects of flexure in the Makran accretionary prism are considered by calculating two models with different elastic thicknesses, but with the same incoming sediment thickness,

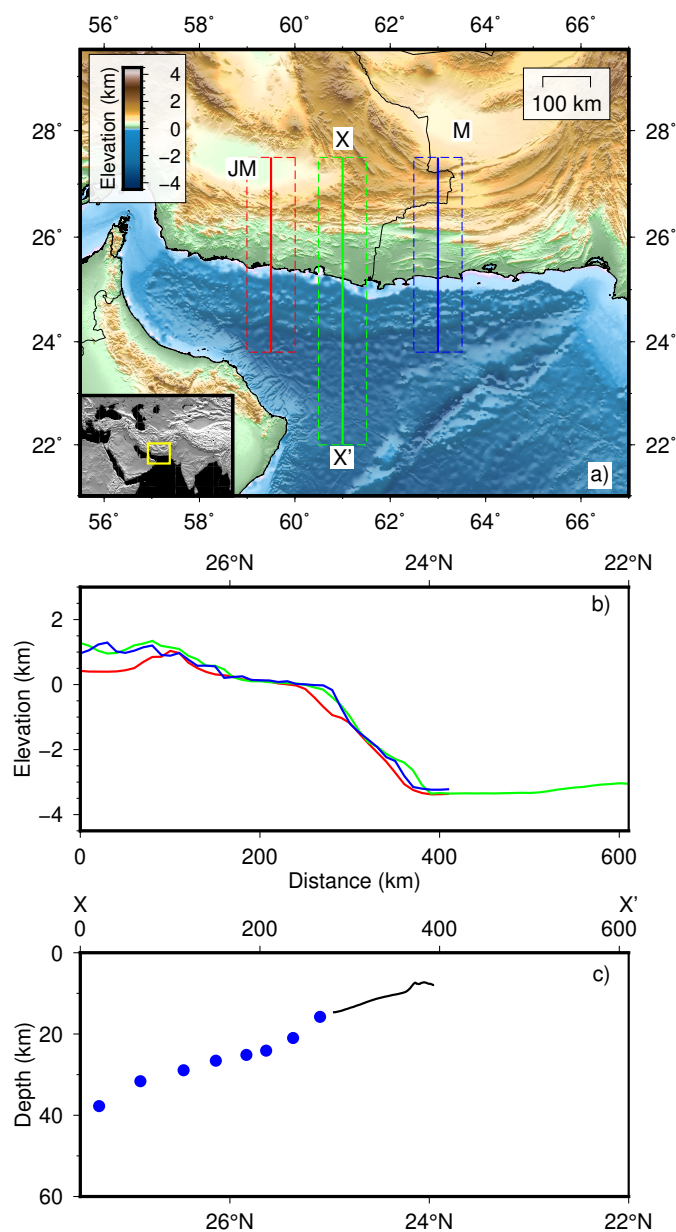


**Figure 2.6: Location and geometry of the Makran accretionary prism.** (a) Map of the Makran with cross sections at  $59.5^{\circ}\text{E}$ ,  $61^{\circ}\text{E}$  and  $63^{\circ}\text{E}$  marked by red, green and blue boxes respectively. Dashed lines indicate the region over which profile is averaged. The Jaz Murian and Maskel depressions are marked by ‘JM’ and ‘M’. (b) Averaged topographic profiles using a 10 km Gaussian filter plotted from north to south. (c) Sediment-basement interface from seismic reflection data at  $62.9^{\circ}\text{E}$  (solid black line, Kopp et al., 2000) and inferred subduction interface at  $62^{\circ}\text{E}$  (Penney et al., 2017) based on the location of earthquakes interpreted as occurring on the subduction interface or within the subducting plate (blue dots).

viscosity and density, underlying mantle density, and underthrusting plate convergence rate. First, consider a flexural model with incoming sediment thickness  $T_s = 7 \pm 1$  km, convergence velocity  $U = 25 \pm 5$  mm yr<sup>-1</sup> and mantle density  $\rho_m = 3300$  kg m<sup>-3</sup>. An elastic thickness, viscosity, density and age that best reproduces the observed topography and sediment-basement interface can then be found from comparisons with numerical simulations for different values of non-dimensional sediment thickness  $H_\infty$  (see appendix B for further details of the optimisation method used). For all input parameters, small sediment densities failed to reproduce observations from the Makran accretionary prism, suggesting significant sediment compaction. Hence, a higher estimate of  $\lambda = 5.0$ ,  $\rho = 2750$  kg m<sup>-3</sup> is taken for the sediment density of the wedge.

For the range of sediment thicknesses and convergence rates, a good fit to the observations is found for an elastic thickness of  $T_e = 18 - 24$  km (elastogravity length scale  $l_e = 56 - 69$  km) with incoming sediment viscosity  $\mu = 0.9 - 1.5 \times 10^{20}$  Pa s and an age of between  $t = 44 - 66$  Myr, given by parameters  $H_\infty = 0.68 - 0.95$ ,  $\Lambda_C = 0.094 - 0.25$ . A comparison between the numerical simulation and the observations for  $T_s = 7$  km and  $U = 25$  mm yr<sup>-1</sup> is plotted in figure 2.7c giving  $T_e = 20$  km,  $\mu = 1.1 \times 10^{20}$  Pa s and  $t = 42$  Myr. The critical non-dimensional parameter  $\Lambda_C = \pi^{1/2} H_\infty^3 / (1 + \lambda) = 0.094 - 0.25 \ll 1$  suggests that the Makran accretionary prism evolved along Path 2 where vertical thickening was the dominant growth mechanism, although testing this hypothesis would require tectonic reconstructions beyond the scope of the present study. The lateral extent and topographic height of the Makran accretionary prism are plotted on the regime plot in figure 2.2 given by the black hexagram labelled ‘M’ and shows that the Makran is now in the late-time regime. As a result, only the nose region of the sediment-basement interface, where flexure is important, can constrain the elastic thickness. Therefore, a wide range of elastic thicknesses,  $T_e = 18 - 24$  km, can fit the observations. Such elastic thicknesses are consistent with previous studies on the elastic thickness of the Arabian plate in the Makran zone (Chen et al., 2015), and with observed elastic thicknesses for oceanic lithosphere elsewhere (Bry and White, 2007; Craig and Copley, 2014). The estimate of the sediment viscosity is slightly higher than estimated previously in some studies (Emerman and Turcotte, 1983; Shreve and Cloos, 1986) but similar to other recent studies of viscous wedges (Copley and McKenzie, 2007; Medvedev, 2002). Finally, the estimated age of  $t = 44 - 66$  Myr is consistent with the geology but is primarily a function of the choice of location of the backstop, and hence volume of sediment accumulated in the wedge. As the wedge is in the late-time regime, the topographic height and plate deflection are given by equations (2.32) and (2.19), which do not explicitly depend on time, although there is an implicit time dependence through lateral extent  $x_N$ . As a result, the choice of backstop location determines the age of the wedge but not any other parameters in the model.

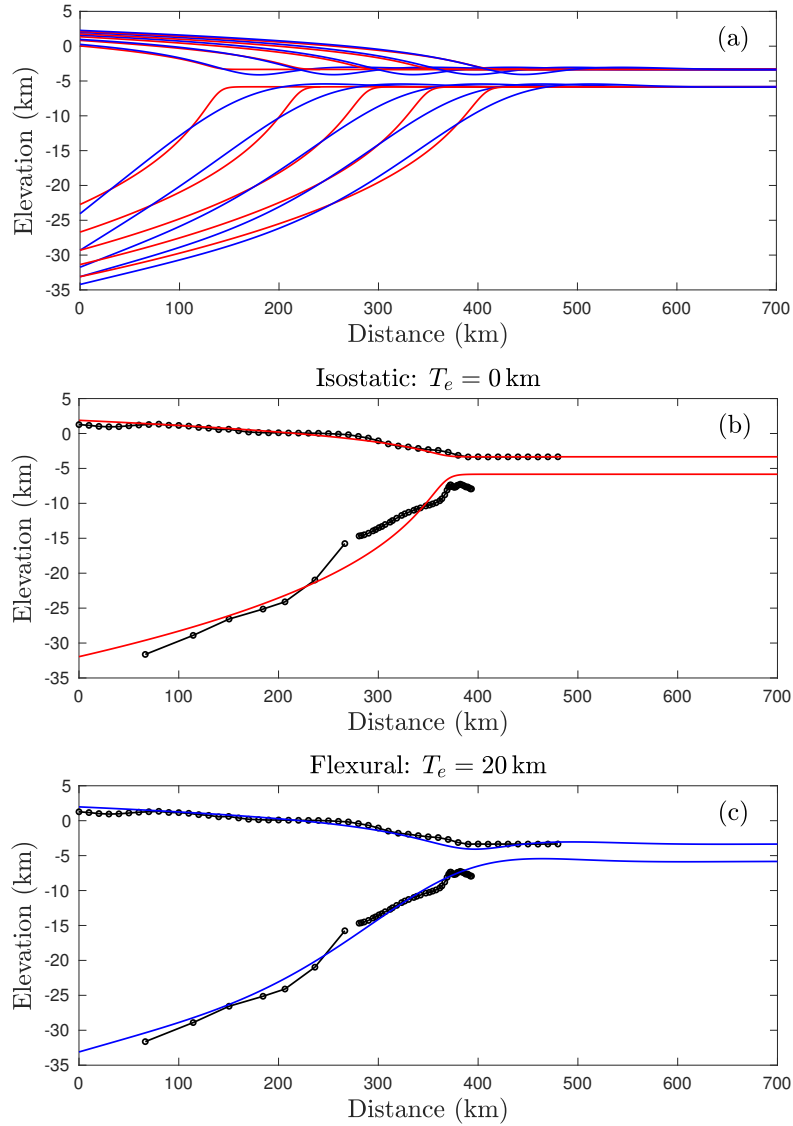


**Figure 2.7: Best-fitting Makran geometry.** (a) Numerical profiles of the topography and sediment-basement interface for isostatic model with  $T_e = 0$  km (red lines) and flexural model with  $T_e = 20$  km (blue lines) for  $t = 10, 20, 30, 40$  and  $50$  Myr. (Sediment thickness  $T_s = 7$  km, convergence velocity  $U = 25$  mm yr $^{-1}$ , viscosity  $\mu = 1.1 \times 10^{20}$  Pa s, and sediment and underlying mantle densities  $\rho = 2750$  kg m $^{-3}$ ,  $\rho_m = 3300$  kg m $^{-3}$ , density ratio  $\lambda = 5.0$ ). (b) Isostatic model with  $T_e = 0$  km for  $t = 42$  Myr (red line) plotted against data for topography and sediment-basement interface (solid black line with open circles). (c) Flexural model with  $T_e = 20$  km for  $t = 42$  Myr (blue line) plotted against data for topography and sediment-basement interface (solid black line with open circles).

The second model considered is in isostatic balance ( $T_e = 0$  km), but otherwise has the same parameter values as the model described above. Figure 2.7a plots the numerical profiles for the topographic height and base of the sediment with elastic thicknesses  $T_e = 0$  km in isostatic balance (solid red lines) and  $T_e = 20$  km (solid blue lines) for  $t = 10, 20, 30, 40$  and 50 Myr. The topography is almost identical in the two models, apart from the flexural depression and bulge at the nose of the wedge observed in the flexural model. However, there is a significant difference between the two models in the depth to the base of the sediment, particularly behind the nose where the dip of the base of the sediment is much more gentle in the flexural model compared with the isostatic model. Figures 2.7b and 2.7c then compare these models for  $t = 42$  Myr in each case, with the data for the topographic height and sediment-basement interface (solid black lines with open circles). The topography agrees well in both cases. When considering the base of the sediment, particularly the comparison with the seismic reflection profiles, a flexural model with elastic thickness  $T_e = 20$  km does a better job at reproducing the observed geometry than the purely isostatic model where the elastic thickness is neglected. This result suggests that flexure is necessary to explain the dip of the sediment-basement interface as observed in seismic reflection profiles, and hence shows the importance of modelling flexure in the underlying plate.

### 2.4.2 Indo-Burman Ranges

The Indo-Burman Ranges were formed by accretion of sediment from the underthrusting Indian plate as it subducts beneath southeast Asia (Ni et al., 1989; Steckler et al., 2016; Stork et al., 2008), see figure 2.8a. The fold-thrust belt is thought to have developed since the late Oligocene (Soibam et al., 2015). Two topographic sections, north and south of the Shillong Plateau (marked as ‘SP’ in figure 2.8a), are shown in figure 2.8 as blue and red lines. The surface geology within the Indo-Burman Ranges is characterised by progressively older rocks from west to east. South of the Shillong Plateau, sedimentary rocks in the central part of the range are composed of an Eocene sequence (‘inner’ Indo-Burman wedge), with a western portion of younger rock composed of Neogene fluvio-deltaic sediments and turbidites (‘outer’ Indo-Burman wedge) (Khin et al., 2014, 2017; Sikder and Alam, 2003). The eastern margin of the Indo-Burman Range is characterised by upper-Cretaceous and Triassic deep water sediments, Mesozoic metamorphics and Jurassic ophiolite assemblages (Brunnschweiler, 1974; Mitchell, 1993). North of the Shillong Plateau, the western portion of the Indo-Burman wedge comprises an Oligocene sedimentary sequence, with a region towards the east of Cretaceous sandstones overlying mafic volcanics of a Jurassic ophiolite suite (Brunnschweiler, 1966; Ghose and Singh, 1980). The region of ophiolites and metamorphics that straddle the length of the range is taken to represent a rigid backstop, which allows the fold-thrust belt to form (marked on figure 2.8a, black dashed line; figures 2.8b–c, grey shaded region).

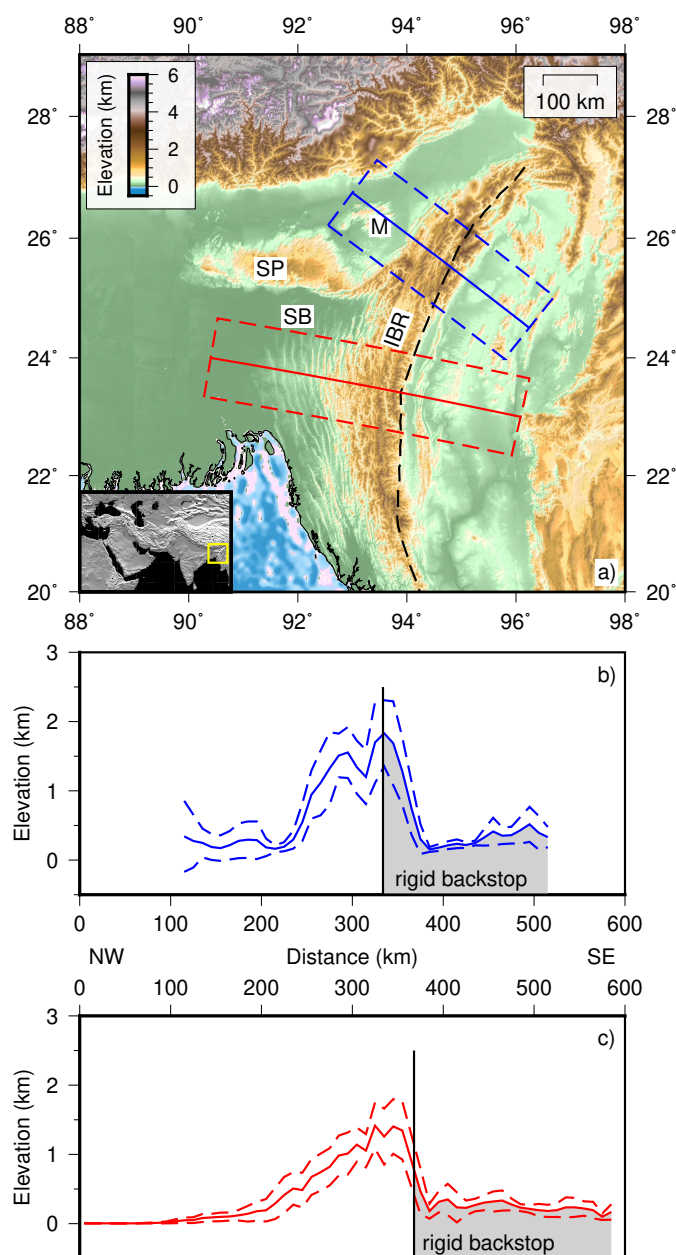


**Figure 2.8: Location and geometry of the Indo-Burman Ranges.** (a) Map of the Indo-Burman Ranges with cross-sections through the northern (blue line) and southern (red line) portion of the range. Dashed lines indicate the region over which the profile is averaged. The Shillong Plateau is marked by ‘SP’, the Mikir Hills by ‘M’, and the Surma Basin by ‘SB’. Estimate of location of the backstop given by the black dashed line. (b) Averaged topographic profile using a 10 km Gaussian filter along the northern cross-section (blue line) with error bar of one standard deviation. Grey shaded area indicates estimate of the backstop. (c) Same as (b) for the southern cross-section.

Along the Indo-Burman Ranges from north to south of the Shillong Plateau there is a significant change in both foreland sediment thickness and the topography of the wedge. In the north, the Indo-Burman Ranges are bounded to the west by the lowlands of Assam. The sediment thickness ranges from zero, where the crystalline basement is exposed at the surface (e.g. Mikir Hills, marked as ‘M’ in figure 2.8a), up to  $\sim 5$  km (Dasgupta et al., 2000) in the northeastern corner of the syntaxis. The average sediment thickness shown by Dasgupta et al. (2000) is  $\sim 2$  km. The topography is characterised by a narrow range width and steep surface slopes near the range front, shown as the blue lines on figure 2.8b. South of the Shillong Plateau, the Indo-Burman Ranges are bounded by the Surma Basin (marked as ‘SB’ in figure 2.8a) and the Bengal Basin, where the sediment thickness in the foreland is significantly larger ( $\sim 15 - 22$  km; Alam et al., 2003; Curray, 1991). The Indo-Burman Range has a larger width and shallower surface slopes than to the north of the Shillong Plateau, shown as red lines on figure 2.8c.

The sedimentary sequences that make up the fold-thrust belt to the west of the backstop in the Indo-Burman Ranges were originally deposited in a series of basins with a common sediment source from the Ganges and Brahmaputra river networks (Govin et al., 2018; Steckler et al., 2008). Hence, the lithology of the sediment in the north and south Indo-Burman wedge is expected to be similar. This similarity suggests that this region may provide insights into the effects of changing sediment thickness on the formation of a fold-thrust belt.

The lower-crustal depth and strike-slip style of earthquakes in the Indo-Burman Ranges suggest they are occurring within the underthrusting Indian plate (Mitra et al., 2005). Hence, the earthquake locations do not constrain the depth of the thrust interface. The analysis to follow focuses therefore on the geometry of topography in the region, rather than the (unknown) geometry of the underthrusting plate.

The Indo-Burman Ranges have shallower surface slopes and larger range widths where the foreland sediment thickness is larger, south of the Shillong Plateau. This observation is consistent with the effect of increasing sediment thickness shown in figure 2.5. To investigate further, consider two models in isostatic balance with different incoming sediment thicknesses, but otherwise the same parameter values. The wedge is assumed to be in isostatic balance as the comparison does not use information about the underthrusting plate needed to constrain the elastic thickness. However, as shown in figure 2.5, the qualitative behaviour of changing sediment thickness is independent of the elastic thickness, and hence this does not affect the conclusions. Consider a range of sediment densities  $\rho = 2400 - 2750 \text{ kg m}^{-3}$ , with mantle density  $\rho_m = 3300 \text{ kg m}^{-3}$  (density ratio  $\lambda = 2.7 - 5.0$ ). The viscosity, convergence velocity and sediment thicknesses in the north and south that best reproduce the observations of topography is then found (see appendix B for further details of the optimisation method used).

From the estimate that the formation of the fold-thrust belt started in the Oligocene (Soibam et al., 2015), an age of  $t = 30 \pm 10$  Myr is taken. However this choice only affects the quantitative parameter values determined, not the qualitative interpretations. For the estimated range of ages and sediment densities, incoming sediment thicknesses are found with  $T_{s(north)} = 2.1 - 2.3$  km in the north and  $T_{s(south)} = 4.7 - 5.0$  km in the south, together with sediment viscosity  $\mu = 3.0 - 8.8 \times 10^{19}$  Pa s and underthrusting plate convergence velocity  $U = 2.8 - 8.8$  mm yr<sup>-1</sup> for both the north and the south.

The estimate of incoming sediment thickness in the north is consistent with the observation that the foreland sediment thickness can range from zero to  $\sim 5$  km in places (Dasgupta et al., 2000) with an average of  $\sim 2$  km. In the south, however, the estimate of  $T_{s(south)} = 4.7 - 5.0$  km is significantly less than the observation  $\sim 15 - 22$  km from seismic data (Alam et al., 2003; Curray, 1991). It has been suggested that temperatures and pressures at large depths in the sediment layer are sufficient for metamorphism to take place (Curray, 1991). If this is the case, only the upper deformable portions of the sediment layer may be playing a role in the growth of the wedge. Given that the model estimates the effective deformable sediment thickness, it is expected to underestimate the true sediment thickness, as the deeper parts will be dewatered, lithified, and effectively part of the rigid Indian plate. Crucially, the models reproduce a thicker sediment sequence to the south than north of the Shillong Plateau, consistent with the observations. Sikder and Alam (2003) observe a detachment in seismic reflection data at around 4s two-way travel time, corresponding with a depth of roughly  $\sim 5$  km, which is consistent with more recent studies (Betka et al., 2018), and hence supports the estimate of the effective deformable sediment thickness. The value of sediment viscosity  $\mu = 3.0 - 8.8 \times 10^{19}$  Pa s is consistent with previous studies on the Indo-Burman Ranges (Copley and McKenzie, 2007) and on sediments under similar conditions (Connolly and Podladchikov, 2000; Gratier et al., 1999; Niño et al., 1998). Finally, the convergence velocity of  $U = 2.8 - 8.8$  mm yr<sup>-1</sup> is consistent with the total rate of convergence of  $5 - 10$  mm yr<sup>-1</sup> in this area from present-day geodetic data (Steckler et al., 2016), but note there is a trade-off with estimating the age of the fold-thrust belt, the sediment volume, and changes in either of these quantities through time.

Figure 2.9a plots numerical profiles for the topographic height of a wedge with sediment thicknesses  $T_{s(north)} = 2.2$  km (solid blue lines) and  $T_{s(south)} = 5.0$  km (solid red lines) for  $t = 10, 20, 30, 40$  and  $50$  Myr, with convergence velocity  $U = 3.8$  mm yr<sup>-1</sup>, viscosity  $\mu = 5.0 \times 10^{19}$  Pa s, and sediment and underlying mantle densities  $\rho = 2400$  kg m<sup>-3</sup>,  $\rho_m = 3300$  kg m<sup>-3</sup>. This comparison again shows that for larger sediment thicknesses, the wedge formed has a larger range width with a shallower topographic slope. Figures 2.9b and 2.9c plot the comparisons between topographic data in the northern and southern part of the Indo-Burman Ranges respectively (solid black lines with open circles) with the numerical

profiles for an age of  $t = 30$  Myr (blue and red solid lines). By increasing the sediment thickness by more than a factor of two going from the north to the south, the difference in surface slopes and range widths can be reproduced. The discrepancy in figure 2.9b between the back of the wedge in the numerical simulation and the backstop inferred from the geology is due to choosing the same age for the fold-thrust belt in the north and south. However, the mismatch between the observations and the model is small given the uncertainties in the location of the backstop. The results therefore suggest that the incoming sediment thickness is playing a first-order role in the development of topography in the Indo-Burman Ranges.

### 2.4.3 Comparison with Coulomb wedge theory

In the model outlined in this chapter a purely viscous rheology is used to describe the incoming sediment. As a result of this choice of rheology, the shear stresses are unbounded. The shear stress can be written as

$$\tau = \mu \frac{\partial u}{\partial z} = -\rho g \frac{\partial h}{\partial x} (h - z), \quad (2.34)$$

which is maximum at the base,  $z = s$ . For example, for the flexural model proposed for the Makran shown in figure 2.7c, the maximum shear stress at the base is  $\sim 8$  MPa, in agreement with that calculated by Penney et al. (2017) of  $\sim 5 - 35$  MPa. For the Indo-Burman Ranges, the maximum shear stress is calculated for the base of northern profile, shown in figure 2.9b, to be  $\sim 1$  MPa. Hence, for both comparisons the shear stress is low, and is consistent with the levels of stress under which rocks can deform at geological strain rates by creep. Unlike Coulomb wedge theory that includes a yield stress, this model does not aim to explain brittle deformation. For a purely viscous rheology, the strain rate,  $\dot{\xi}$ , is linearly proportional to the shear stress,  $\dot{\xi} = \tau/\mu$ . Equation (2.34) shows that the strain rate increases linearly with depth and is proportional to gradients in surface topography. At late-times, the topography of the model wedges exhibit concave-downward profiles with increasing surface gradients towards the toe of the wedge. Hence, the largest strain rates are expected to be seen at depth and towards the toe; a feature analogous to the strain rate pattern for Coulomb wedge theory as described by Willett (1992).

A key feature of Coulomb wedge theory is that in the interior of the wedge everywhere is on the verge of failure by the same mechanism, i.e. thrust faulting at the angle of sliplines. In contrast, this model allows for distributed and spatially variable deformation. The main distinguishing feature between this viscous model and Coulomb wedge theory is the surface topography of wedges produced. Unlike the linear taper from cohesionless Coulomb wedge theory, a viscous rheology produces a range of topographies from concave-upward

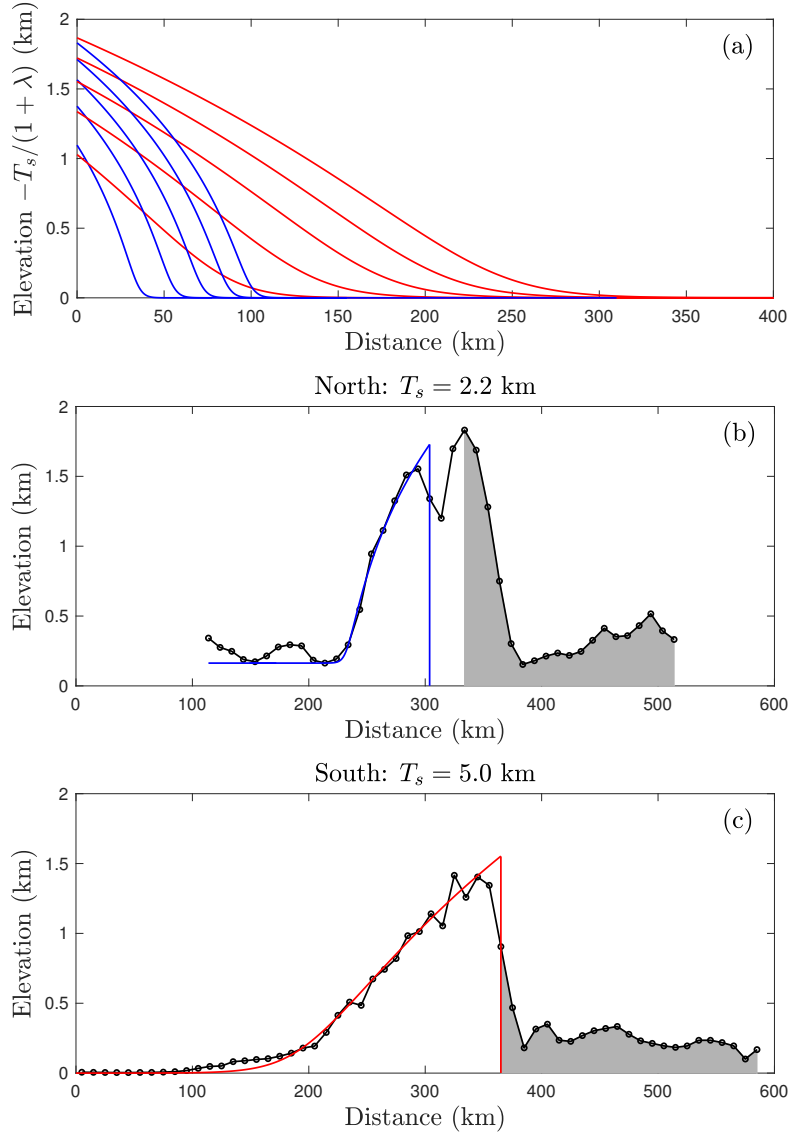


**Figure 2.9: Best-fitting Indo-Burman Ranges geometry.** (a) Numerical profiles of the topography for sediment thicknesses  $T_{s(north)} = 2.2$  km (solid blue lines) and  $T_{s(south)} = 5.0$  km (solid red lines) for  $t = 10, 20, 30, 40$  and  $50$  Myr. (Convergence velocity  $U = 3.8$  mm yr $^{-1}$ , viscosity  $\mu = 5.0 \times 10^{19}$  Pa s, and sediment and underlying mantle densities  $\rho = 2400$  kg m $^{-3}$ ,  $\rho_m = 3300$  kg m $^{-3}$ , density ratio  $\lambda = 2.7$ ). (b) Numerical profile with  $T_{s(north)} = 2.2$  km for  $t = 30$  Myr (solid blue line) plotted against topographic data for northern cross section of Indo-Burman Range (solid black line with open circles). (c) Numerical profile with  $T_{s(south)} = 5.0$  km for  $t = 30$  Myr (solid red line) plotted against topographic data for southern cross section of Indo-Burman Range (solid black line with open circles). All models are in isostatic balance with  $T_e = 0$  km.

to concave-downward as the wedge evolves in time. As seen from the comparisons with the Makran accretionary prism and the Indo-Burman Ranges, these shapes are consistent with observations from a range of locations. However, a clear direction for future work is to examine the extent to which this is globally true.

## 2.5 Conclusion

In this chapter I have presented an analytical and numerical model to describe the growth of fold-thrust belts due to the accretion of sediments from the underthrusting plate. In particular, I have examined a balance between advection of sediment and gravitational spreading within the accretionary wedge coupled to the flexural subsidence of the underthrusting plate. The analysis shows that the evolution of accretionary wedges is dependent on two non-dimensional parameters: the non-dimensional sediment thickness  $H_\infty = T_s(\rho g/3\mu U l_{eg})^{1/3}$  and the density ratio  $\lambda = \rho/\Delta\rho$ , where  $T_s$ ,  $\rho$ ,  $\mu$  are the incoming sediment thickness, density and viscosity,  $U$  is the convergence rate of the incoming plate, and  $l_{eg}$  is the elastogravity length scale, the length scale at which the weight of the wedge begins to dominate over the strength of the plate. I describe early- and late-time regimes of the wedge and demonstrate two paths of evolution between these regimes, where the wedge either grows predominantly through gravitational spreading (Path 1) or through vertical thickening due to advection of sediment (Path 2) depending on the size of the critical non-dimensional parameter  $\Lambda_C = \pi^{1/2} H_\infty^3/(1 + \lambda)$ . In addition, I solve the coupled system numerically to understand the transition between these regimes and explore the parameter space more widely.

The generality of the model allows conclusions to be drawn in a multitude of locations. I have considered the particular examples of the Makran accretionary prism and the Indo-Burman Ranges, to investigate the importance of sediment thickness and elastic thickness (flexure of the underthrusting plate) in the growth of a fold-thrust belt. I have shown that flexure is important in the Makran accretionary prism in order to understand dip in the sediment-basement interface from seismic reflections profiles. In the Indo-Burman Ranges, I have shown that a lateral contrast in sediment thickness plays an important role in generating the different styles of topography north and south of the Shillong Plateau.



# Chapter 3

## Modelling shallow magmatic intrusions: fluid-driven fracturing of adhered elastica<sup>†</sup>

---

### 3.1 Introduction

#### 3.1.1 Magmatic intrusions

The propagation of shallow magmatic intrusions is dominated by a roof lifting process, whereby the overlying sedimentary layers are deformed to make room for the intruding magma to spread (Jackson and Pollard, 1988; Pollard and Johnson, 1973). As described in section 1.2, a lot of work has focused on the static geometry of intrusions rather than the dynamics of emplacement. However, more recently studies such as Michaut (2011) have aimed at coupling the static elastic response of the crust with the evolving fluid response of the magma. This has focussed attention more towards understanding the dynamics of fluid-driven fracturing. The geometry and propagation of fluid-driven fractures is determined by a competition between the flow of the viscous fluid, the elastic deformation of the solid and the energy required to create new surfaces through fracturing. Aside from magmatic intrusions (Rubin, 1995), these processes feature industrially in the hydraulic fracturing of shale (Detournay, 2016), and otherwise in nature in the propagation of cracks at the base of glaciers (Tsai and Rice, 2010).

Following the work of numerous authors (e.g. Bungler and Cruden, 2011; Michaut, 2011), I simplify the propagation of magmatic intrusions to try to understand the key physical

---

<sup>†</sup>This chapter is adapted from Ball, T. V. and Neufeld, J. A. (2018). Static and dynamic fluid-driven fracturing of adhered elastica. *Phys. Rev. Fluids*, 3(7):074101.

mechanisms at play. I model the overlying sedimentary layer or overburden as a thin-elastic beam, where the thickness is much less than the extent and much greater than the thickness of the intrusion. The intruding magma is modelled as a Newtonian, isoviscous fluid. Finally I assume that the two layers of rock, in between which the magma spreads, need to be fractured for propagation of the intrusion to occur. This can be thought of as overcoming a level of adhesion between two layers in order to peel them apart. In the remainder of this chapter I use the terminology adhesion, but this is equivalent to the fracture toughness more commonly used in the literature. The aim of the model developed with these assumptions is to look at the dynamics of the flow by incorporating a fracture condition at the front of the intrusion.

### 3.1.2 Fluid-driven fracturing

The transient spreading of a viscous fluid beneath an adhered, elastic sheet may be controlled by the dynamics at the tip. The physics at the contact line is directly analogous to the capillary-driven spreading of a droplet, where elasticity plays the role of surface tension. Near the front, a large negative pressure gradient is needed to drive the viscous fluid into the narrowing gap of the fracture where the rate of viscous dissipation diverges. This is the elastic equivalent of Huh and Scriven's paradox (Huh and Scriven, 1971), and theoretically leads to the immobility of the contact line. In the context of a spreading droplet, microscopic mechanisms such as a precursor film (Eres et al., 2000) and relaxation of the no-slip conditions at the front (Huh and Scriven, 1971) have been proposed to account for experimental observations. For the problem of a viscous fluid spreading underneath an elastic sheet, a macroscopic precursor film has been used to regularise this contact-line singularity (Lister et al., 2013), but this fails to explain fracturing phenomena, as found in magmatic intrusions, where there is no evidence of a pre-wetted surface.

Through consideration of a simple lubrication model it is shown that a fluid lag, or vapour tip, between the fluid front and the fracture front can be used to regularise the tip, figure 3.1. The large negative pressure gradient at the tip is limited by the vapour pressure of the fluid, and hence the fracture front travels faster (at the elastic wave speed in the solid) while the fluid lags behind. This physical process leads to the emergence of a fluid lag that regularises the dynamics at the tip (Hewitt et al., 2015). In this chapter an experimental system capable of characterising this vapour tip is demonstrated, thereby confirming its presence and role in the transient dynamics. A fluid lag has previously been invoked in other contexts, when modelling penny-shaped cracks (Garagash and Detournay, 1999) and buoyancy-driven fractures (Lister, 1990), and has been observed in laboratory experiments on the fracturing of elastic blocks (Bunger et al., 2005, 2013; Medlin and Massé, 1984) but has not been systematically characterised. The development of a theoretical model and

consistent laboratory experiments using thin elastica lead to a simpler analysis and treatment of fluid-driven fracturing and provides a usefully reduced system in which to understand the dynamics of fluid-driven fracturing.

To delaminate adhered elastica, the energy required to create new surfaces is  $\Delta\gamma = \gamma_{SV}^{(\text{sheet})} + \gamma_{SV}^{(\text{substrate})} - \gamma_{SS}$ , where  $\gamma_{SV}$  is the solid-vapour surface energy and  $\gamma_{SS}$  the solid-solid surface energy. This imposes a curvature at the fracture front, or fracture criterion, given by

$$\kappa = \sqrt{2}/l_{ec}, \quad (3.1)$$

where  $l_{ec} = (B/\Delta\gamma)^{1/2}$  is the elastocapillary length scale, with bending stiffness  $B$ . This curvature condition is obtained from an energy balance at the crack tip where the elastic strain energy in the sheet is balanced by the creation of new surfaces (Glassmaker and Hui, 2004; Wagner and Vella, 2013). The quasi-static condition may be derived by energy minimisation at the crack tip, and assumes a separation of scales between the fast fracturing dynamics and the relatively slow fluid dynamics driving tip propagation. The material strength of adhesion at the crack tip allows for the possibility of static solutions, and controls the long-time behaviour of spreading.

Two dynamical regimes are possible; viscosity dominant spreading controlled by the pressure gradient driving fluid into the vapour tip and adhesion dominant spreading controlled by interfacial adhesion. These two regimes are analogous to the limiting regimes of propagation for a semi-infinite hydraulic crack in an elastic medium (Garagash and Detournay, 1999). In the elastic bending case considered here, an asymptotic model for propagation in the adhesion and viscosity dominated limits is demonstrated by resolving the behaviour of the vapour tip.

Wang and Detournay (2018) present a comparable analysis of the problem of fluid-driven fracturing of adhered thin elastica in which two regimes of propagation are described in the context of near-surface hydraulic fractures. This work complements the mathematical approach taken in this chapter, where in addition the results of these analyses have been tested experimentally, demonstrating the formation of a vapour tip and different regimes of propagation.

This chapter is laid out as follows. In section 3.2, I describe the static blister shapes and a dynamic model demonstrating the transition from viscosity dominant to adhesion dominant spreading within the thin elastica framework. In section 3.3, I describe the experimental setup and methods. The experimental results are analysed and compared with the theoretical model in section 3.4. Finally, in section 3.5, I discuss some implications of the model described.

## 3.2 Theoretical model

To examine the fluid-driven delamination of an adhered elastic sheet (see figure 3.1), a volume of fluid of density  $\rho$  and viscosity  $\mu$  is injected beneath an elastic sheet of thickness  $d$  and density  $\rho_s$  initially adhered to a horizontal substrate with adhesion energy  $\Delta\gamma$ . Here, motivated by laboratory experiments (discussed in section 3.3), axisymmetric spreading and elastic deformation are assumed. In all dynamic cases the fracture front,  $R_N$ , extends beyond the fluid front,  $R_F$ , such that a vapour filled tip exists of length  $L = R_N - R_F$ . The contribution to the pressure due to bending stresses dominates over contributions from tensional forces when the vertical deflection of the sheet is smaller than the thickness,  $h(r, t) \ll d$ . Hence the reduced pressure can be written as  $\tilde{p} = p - p_0 - \rho_s g d = B\nabla^4 h + \rho g(h - z)$ , where tension is neglected,  $p$  is the pressure in the fluid, and  $p_0$  is a reference pressure with bending stiffness  $B = Ed^3/12(1 - \nu^2)$ , where  $E$  and  $\nu$  are the Young's modulus and Poisson's ratio of the sheet respectively.

For large aspect ratios the viscous drag is balanced with the hydrostatic and elastic pressure gradients to describe the deflection of the sheet (Flitton and King, 2004),

$$\frac{\partial h}{\partial t} = \frac{1}{12\mu} \frac{1}{r} \frac{\partial}{\partial r} \left[ rh^3 \frac{\partial}{\partial r} (B\nabla^4 h + \rho gh) \right], \quad (3.2)$$

where global mass conservation gives

$$V(t) = 2\pi \int_0^{R_F} hr \, dr. \quad (3.3)$$

The balance between elastic stresses and gravity acting on the fluid gives rise to a natural horizontal, elastogravity length scale,  $l_{eg} = (B/\rho g)^{1/4}$ , and hence characteristic height and time scales may be defined as  $H_0 = (12\mu Q/\rho g)^{1/4}$  and  $T_0 = H_0 l_{eg}^2/Q$  respectively, where  $Q$  is a typical volume flux.

### 3.2.1 Static shapes

Adhesion of the sheet at the perimeter allows for the possibility of static solutions with no vapour tip,  $R_N = R_F$ , analogous to the capillary sessile drop (Tanner, 1979). The potential energy of the blister is balanced by the energy of adhesion between the elastic sheet and the horizontal substrate. For a constant volume  $V$ , this gives rise to static shapes with uniform pressure  $\tilde{p}$ . The potential energy of the blister has contributions from elastic deformation, and from the gravitational potential. When the radius is smaller than the elastogravity length scale,  $R_F \ll l_{eg}$ , the pressure within the blister is dominated by bending stresses

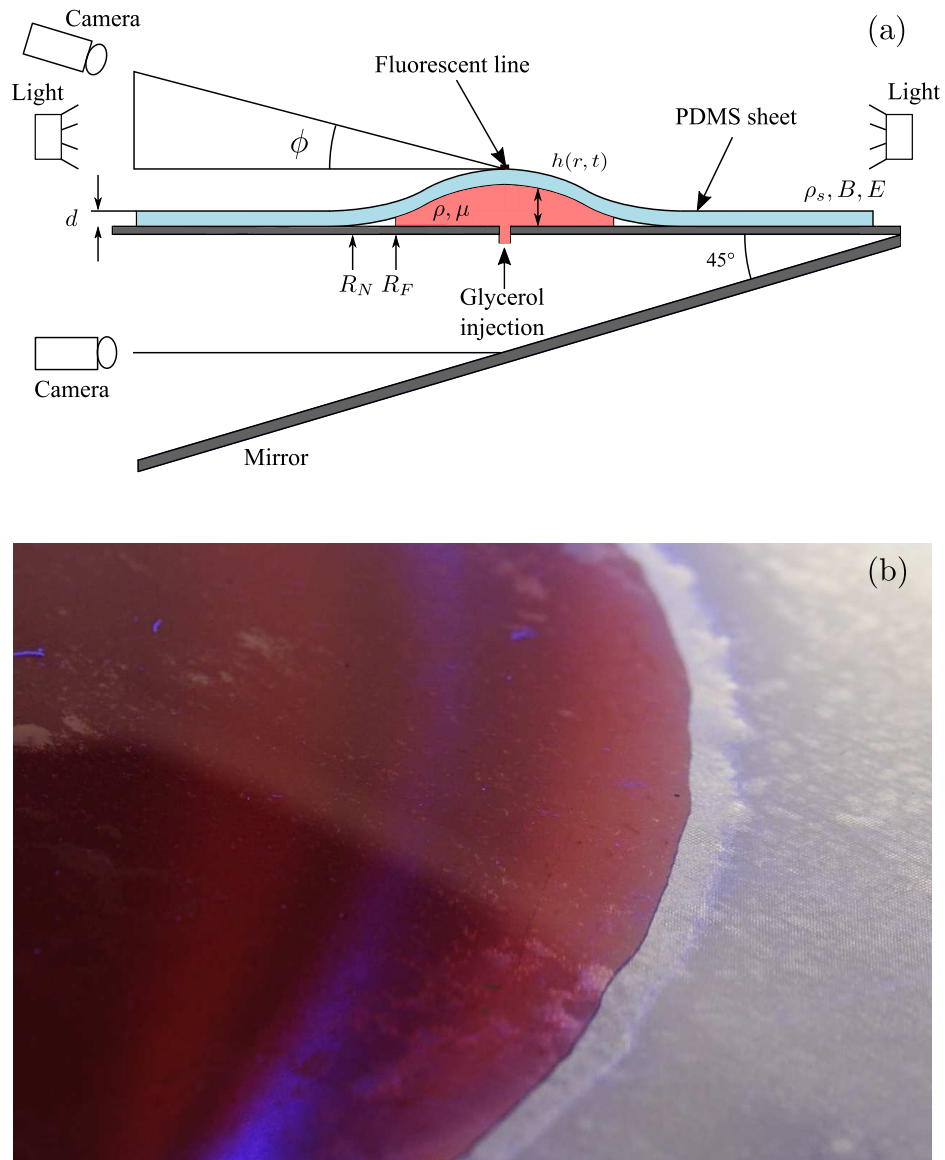


**Figure 3.1: Schematic and photograph of a fracturing experiment.** (a) Schematic diagram of the theoretical model and experimental setup with the physical parameters in the system. (b) Photograph of an experimental fluid front showing the lag between the fluid front and fracture front.

with  $\tilde{p} \simeq B\nabla^4 h$ . At the origin, the imposition of zero slope and bending moment ensure that the mathematical description of the height of the sheet does not diverge as  $r \rightarrow 0$ . For static shapes the fracture and fluid fronts coincide, and continuity with the adjoining adhered regions requires that the height and gradient of the sheet are zero at the front,  $h = \nabla h = 0$  at  $r = R_F$ . The deflection reduces to the classic bell-shaped form (Pollard and Johnson, 1973; Timoshenko and Woinowsky-Krieger, 1959)

$$h(r) = \frac{\tilde{p}R_F^4}{64B} \left(1 - \frac{r^2}{R_F^2}\right)^2, \quad (3.4)$$

see figure 3.2ai (inset). Global mass conservation (3.3) and the curvature condition at the front due to adhesion impose  $V = \pi\tilde{p}R_F^6/192B$  and  $\kappa = \tilde{p}R_F^2/8B$  respectively, where  $\kappa = \sqrt{2}/l_{eg}$  (Wagner and Vella, 2011), and thus determine the radial extent and central deflection,

$$R_F = \left(\frac{24V}{\pi\kappa}\right)^{1/4} \quad \text{and} \quad h_0 = \left(\frac{3\kappa V}{8\pi}\right)^{1/2}. \quad (3.5)$$

In contrast, for larger volumes when the radius is much greater than the elastogravity length scale,  $R_F \gg l_{eg}$ , gravity becomes important and the uniform pressure contains both elastic and hydrostatic contributions,  $\tilde{p} = B\nabla^4 h + \rho gh$ . In the interior, the pressure is nearly hydrostatic and hence the height is uniform,  $h \simeq h_0$ , and the profiles are flat topped. Near the front, on a length scale  $\mathcal{O}(l_{eg})$ , the hydrostatic pressure is balanced by elastic stresses due to bending the elastic sheet over the periphery. Adhesion at the fracture front imposes the curvature of the sheet as it touches down,  $\kappa \sim h_0/l_{eg}^2$ , which thereby determines the height of the static elastic droplet. (Note that for an axisymmetric blister the second radius of curvature,  $\sim 1/R_F$ , does not play a role in fracturing as the tip may be considered roughly two-dimensional for  $R_F \gg h, d$ ). An analytic solution can be found by matching the interior profile of uniform height with the peripheral bending region, where  $p \simeq Bh^{IV} + \rho gh$ . This gives profile

$$h(r) = \kappa l_{eg}^2 \left[1 - e^X (\cos X - \sin X)\right], \quad (3.6)$$

where  $X = (r - R_F)/\sqrt{2}l_{eg}$ , see figure 3.2aii (inset). In this sessile, elastic limit the radial extent and central deflection are

$$R_F = \left(\frac{V}{\pi\kappa l_{eg}^2}\right)^{1/2} \quad \text{and} \quad h_0 = \kappa l_{eg}^2. \quad (3.7)$$

Figures 3.2a–c show the transition from bending dominant to gravitationally dominant profiles, radial extent and central deflection with increasing volume (blue curves) along with asymptotic scaling from equations (3.5) and (3.7), black dot-dashed lines.

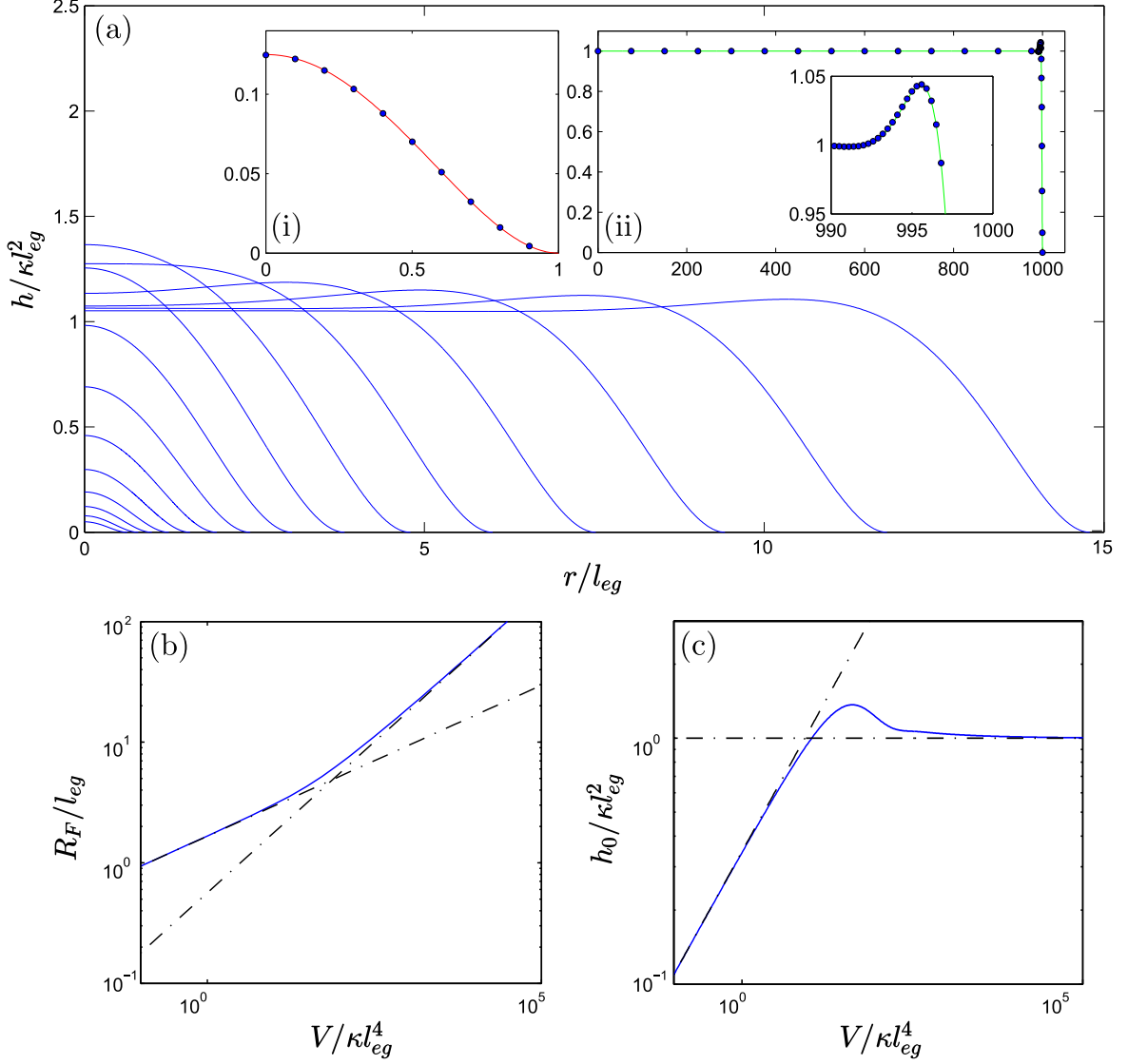


**Figure 3.2: Static blister profiles and length scales.** (a) Plot of the static profiles for a constant volume  $V$  transitioning from bending to gravitationally dominated regimes. Inset (i) shows numerical solution in the pure bending regime (blue dots) plotted on top of theoretical profile equation (3.4) (the red curve), and (ii) the numerical solution in the gravity dominant regime with a bending tip (blue dots) plotted on top of theoretical profile equation (3.6) (the green curve), with axes the same as the main figure (a). (b) Dimensionless radial extent with volume. (c) Dimensionless central deflection with volume.

These static shapes arise due to the balance between adhesion of the elastic sheet and the substrate at the periphery and the hydrostatic and elastic potential energy of the blister. In section 3.2.2, at late times it is shown that the dynamic spreading of the fluid blister transitions through a series of quasi-steady equilibrium states given by these static solutions with  $V = Qt$ .

### 3.2.2 Dynamic spreading

In contrast to the static case, dynamic inflation leads to the emergence of a vapour tip. Viscous stresses diverge at the tip requiring a large pressure gradient to drive viscous fluid to the fracture front. The pressure in the fluid is limited by the vapour pressure, and hence the fracture front travels faster (at the elastic wave speed in the solid) while the fluid lags behind. This physical process regularises the dynamics at the tip by introducing a finite fluid thickness at the fluid front (Hewitt et al., 2015). An examination of the dominant length scales at the tip reveal two possible behaviours when the volume  $V(t) = Qt$ ; either the expansion of the fluid blister is controlled by viscous dissipation, or by the requirement to overcome the energy of adhesion.

#### Vapour tip

At early times,  $R_F \ll l_{eg}$ , the evolution of the blister is slow so that the viscous pressure losses from the fluid input to the fluid front are small, and therefore the interior pressure is nearly constant. The deflection of the sheet in this limit takes the bell-shaped form described in (3.4). The rate at which the blister expands is determined entirely by processes at the fluid front. Assuming that the radial extent of the fluid greatly exceeds the length of the vapour tip,  $R_F \gg L$ , the tip region can be treated as two-dimensional with reduced pressure  $\tilde{p}_T = p_T - p_0 - \rho_s g d = B h^{IV}$ , where  $h^{IV} = \partial^4 h / \partial r^4$  and  $\sigma = -\tilde{p}_T$  is large and the vapour tip pressure  $p_T$  is negligible compared with atmospheric pressure  $p_0$  and the weight of the beam (Detournay, 2016; Hewitt et al., 2015). For large values of  $\sigma$  the regularisation is only felt over a small boundary layer near the fluid front. Hence the interior profile can be given by the static solution, (3.4). As in the static case, continuity at the tip requires the height and gradient to be zero  $h = h' = 0$  with fracture criterion  $h'' = \kappa$  at  $r = R_N$ , where prime denotes differentiation with respect to  $r$ . The deflection of the sheet in the vapour tip may

then be written as

$$\begin{aligned} h(r, t) &= -\frac{\sigma}{24B}(R_N - r)^3(R_N - r - L) \\ &+ \frac{h(R_F, t)}{L^3}(R_N - r)^3 - \frac{\kappa}{2L}(R_N - r)^2(R_N - r - L), \end{aligned} \quad (3.8)$$

for  $R_F, R_N \gg h, d$ , which extends the vapour tip model (Hewitt et al., 2015, their equation (3.5)), to include adhesion at the fracture front. From (3.8), it is apparent that the curvature at the fluid front is imposed by adhesion and the dynamics of the propagating fluid interface,  $\kappa_F \simeq 2h(R_F, t)/L^2 \simeq \kappa + \sigma L^2/8B$ . This defines a natural length scale  $L_C = (B\kappa/\sigma)^{1/2}$  over which the curvature due to adhesion is felt. A comparison of this length scale with the size of the vapour tip,  $L$ , may be used to determine the dominant physics controlling spreading. When  $L \gg L_C$  the curvature at the fluid front is dominated by the viscous fluid dynamics and spreading is in the viscosity dominant regime. In contrast, when  $L \ll L_C$  the curvature at the front is imposed by the adhesion criterion, and spreading is adhesion dominant.

### Travelling wave solution

To determine the length of the lag region  $L$ , and hence the spreading rate, a travelling wave solution is sought near the fluid front of the form  $h = h_F f[\xi \equiv (r - R_F(t))]$ , which satisfies (3.2),

$$-\dot{R}_F h_F f' = \frac{Bh_F^4}{12\mu} (f^3 f^V)' \quad \Rightarrow \quad -\dot{R}_F = \frac{Bh_F^3}{12\mu} f^2 f^V, \quad (3.9)$$

using mass conservation at the fluid front  $\dot{R}_F = \lim_{r \rightarrow R_F} -h^2 p_r / 12\mu$ , where  $f' = \partial f / \partial \xi$ ,  $f^V = \partial^5 f / \partial \xi^5$  and  $p_r = \partial p / \partial r$ . This balance at the fluid front may be used to define a viscous peeling length scale  $l_p = (Bh_F^3 / 12\mu \dot{R}_F)^{1/5}$  (Lister et al., 2013). By writing  $X \equiv \xi / l_p$  and choosing curvature scaling in the viscosity controlled regime,  $2h_F / l_p^2 = \sigma l_p^2 / 8B$ , a fifth-order ODE for  $f$ ,  $-1 = f^2 f^V$  is derived, along with unknown lag length,  $L = \lambda l_p$ , subject to four matching conditions for the deflection of the elastic plate at the fluid-vapour interface,  $X = 0$ ,

$$\begin{aligned} f' &= \frac{2\lambda^3}{3} - \frac{3f}{\lambda} + \frac{\lambda \kappa l_p^2}{2h_F}, & f'' &= -4\lambda^2 + \frac{6f}{\lambda^2} - \frac{2\kappa l_p^2}{h_F}, \\ f''' &= 12\lambda - \frac{6f}{\lambda^3} + \frac{3\kappa l_p^2}{\lambda h_F} & \text{and } f^{IV} &= -16. \end{aligned} \quad (3.10)$$

Closing the system requires the curvature to tend to a constant to match the interior solution,  $f'' \rightarrow \gamma$ , as well as  $f'''$ ,  $f^{IV} \rightarrow 0$  as  $X \rightarrow -\infty$ . To solve numerically the MATLAB function BVP4c is used giving  $\gamma$  and  $\lambda$  in the viscosity and adhesion dominant regimes.

### Viscosity dominant spreading

In the viscosity controlled regime, the curvature is  $\kappa_F \simeq 2h_F/L^2 \simeq \sigma L^2/8B$ , where  $l_p$  is the dominant length scale at the tip and hence  $L \simeq l_p$ . The viscous peeling length scale is then

$$l_p = \left[ \frac{2^{12}(12\mu)B^2\dot{R}_F}{\sigma^3} \right]^{1/7} \quad (3.11)$$

and demonstrates that spreading is viscosity controlled at early times providing  $\dot{R}_F$  is sufficiently large, and hence  $L \simeq l_p \gg L_C$ . The fluid front exhibits a dynamic curvature that can be defined without recourse to adhesion (Flitton and King, 2004),

$$\kappa_F \simeq \frac{2h_F}{L^2} \simeq \frac{\sigma L^2}{8B} \simeq 1.77 \left[ \frac{(12\mu)^2\sigma}{B^3} \right]^{1/7} \dot{R}_F^{2/7}, \quad (3.12)$$

where the prefactor comes from numerically solving (3.9), with non-dimensional lag length  $\lambda = 1.33(2^{-12/7})$ . The factors of 2 in the expression for  $\lambda$  are due to the peeling lengthscale  $l_p$  being defined differently to Hewitt et al. (2015). It is this curvature which initially controls the propagation. Hence, this gives an evolution equation for the fluid front given an interior curvature  $\kappa_{int}$ ,

$$\dot{R}_F \simeq 1.77^{-7/2} \left[ \frac{B^3\kappa_{int}^7}{(12\mu)^2\sigma} \right]^{1/2}. \quad (3.13)$$

Matching onto the interior curvature  $\kappa_{int} = 24Qt/\pi R_F^4$  from (3.4) for a constant flux injection an asymptotic model for the radial extent, central deflection and lag length in the viscosity dominant regime can be found,

$$R_F(t) = 1.52 \left[ \frac{Q^7 B^3}{(12\mu)^2 \sigma} \right]^{1/30} t^{3/10}, \quad (3.14)$$

$$h_0(t) = 0.41 \left[ \frac{(12\mu)^2 \sigma Q^8}{B^3} \right]^{1/15} t^{2/5}, \quad (3.15)$$

$$L(t) = 1.19 \left[ \frac{(12\mu)^4 B^9 Q}{\sigma^{13}} \right]^{1/30} t^{-1/10}. \quad (3.16)$$

It is worth emphasising that these initial solutions are independent of the adhesion at the front.

### Adhesion dominant spreading

At later times,  $t > (12\mu)^{4/3}Q^{1/3}\sigma^{2/3}/B^2\kappa^5$ , the decrease in the velocity  $\dot{R}_F$ , implies that  $l_p \ll L_C$ , and there is therefore a transition to adhesion dominant spreading where the viscous peeling length scale no longer dominates the curvature at the tip. The curvature at the fluid front is predominantly that imposed by adhesion,  $\kappa_F \simeq \kappa$ , and the blister transitions through a series of quasi-static solutions, identical to those described by (3.5), now with  $V = Qt$ ,

$$R_F(t) = \left(\frac{24Q}{\pi\kappa}\right)^{1/4} t^{1/4}, \quad (3.17)$$

$$h_0(t) = \left(\frac{3\kappa Q}{8\pi}\right)^{1/2} t^{1/2}. \quad (3.18)$$

Importantly, these late-time solutions are now independent of the fluid viscosity, as well as the presence (and hence length) of a vapour tip.

The lag length  $L$  may be calculated *a posteriori* by considering mass conservation at the fluid front,  $\dot{R}_F \simeq h_F^2\sigma/12\mu L$ , where there is a jump in pressure of  $\mathcal{O}(\sigma)$  at the fluid-vapour interface, and the curvature due to adhesion,  $2h_F/L^2 \simeq \kappa$ . Hence the lag length is determined by the slow flow of a viscous fluid infilling a wedge whose geometry is governed by adhesion. Numerically solving equation (3.9) gives non-dimensional lag length  $\lambda = 1.10(2^{-4/3})(\kappa l_p^2/h_F)^{-2/3}$ , and hence

$$L(t) = 0.82 \left[ \frac{(12\mu)^4 Q}{\sigma^4 \kappa^9} \right]^{1/12} t^{-1/4}. \quad (3.19)$$

It can be shown that the assumptions of constant interior pressure and pure bending ( $r \ll l_{eg}$  and  $h \ll d$ ) are valid provided  $(12\mu B/Q\sigma^2)^{1/2} \ll t \ll l_{eg}^4\kappa/Q$ ,  $d^2/Q\kappa$  by substituting the scalings for the two regimes into the original time evolution equation for the deflection (3.2). For axisymmetric spreading the transition from viscosity dominant to adhesion dominant spreading occurs at transitional horizontal, height and time scales  $R_C = (12\mu Q)^{1/3}\sigma^{1/6}/B^{1/2}\kappa^{3/2}$ ,  $H_C = (12\mu Q)^{2/3}\sigma^{1/3}/B^{7/15}\kappa^2$ , and  $T_C = (12\mu)^{4/3}Q^{1/3}\sigma^{2/3}/B^2\kappa^5$ , respectively. Note that these may occur before or after the transition to a gravity dominated interior, which occurs at  $R_F \sim (B/\rho g)^{1/4}$ .

In summary, dynamic spreading of a fluid beneath an elastic sheet is governed by a competition between elastic deformation of the sheet and either viscous dissipation or the energy required to overcome adhesion. At early times, the spreading is viscosity dominant, controlled by the pressure gradients driving viscous fluid into the tip, and given by the no-adhesion solution (Hewitt et al., 2015). When  $l_p \ll L_C$ , there is a transition to adhesion control, where the lag length no longer plays a role in the propagation of the fluid front and spreading is independent

of viscosity of the fluid and pressure in the vapour tip. The regimes described here have parallels with those described for a semi-infinite hydraulic fracture evolving from a viscosity dominant to a toughness dominant crack in an elastic half-space (Garagash and Detournay, 1999), and, as shown in the following section, can be readily observed in experiments on thin elastica.

### 3.3 Experimental methods

Experiments conducted to investigate the fluid-driven fracturing of adhered elastica consisted of injecting a viscous fluid beneath an elastic sheet adhered to a horizontal substrate (see figure 3.1). An elastic sheet of polydimethylsiloxane (PDMS) was used with diameter  $917 \pm 1$  mm and thickness  $d = 9.8 \pm 0.3$  mm. The bending stiffness  $B = 0.18 \pm 0.02$  Pa m<sup>3</sup> was measured using loop (Stuart, 1966) and circular blister tests (Malyshev and Salganik, 1965). The PDMS sheet was manually adhered to a horizontal glass table using TUFFBond™ Adhesive Mount Film of thickness  $0.15 \pm 0.01$  mm. Glycerine-water solutions were injected between the glass table and composite PDMS and adhesive sheet. Injection was through a 5.5 mm diameter aperture and the flux was determined by measuring the volume injected on the table from the deflection profiles.

The deformation of the PDMS sheet was measured by imaging a fluorescent line on top of the sheet at a known oblique angle  $\phi$ , as shown in figure 3.1. To improve the contrast between the line and the background, the line was illuminated by a blue light and the blue colour channel was isolated in the digital images acquired. A filtered image taken using this method is shown in figure 3.3b demonstrating the contrast achieved. Deflections of the line are determined by comparing with a reference image of the undeformed PDMS taken prior to injection. A Gaussian was then fit to the intensity profile across the line in a strip of pixels where the central peak was chosen as the centreline. To reduce scatter, an average was taken every 10 pixels. The final profile for this sample snapshot is plotted in figure 3.5 for time  $t = 64$  s, viscosity  $\mu = 2.12$  Pa s and volume flux  $Q = 3.09 \times 10^{-7}$  m<sup>3</sup> s<sup>-1</sup>.

The fluid and fracture fronts were measured by imaging from underneath the glass substrate using a mirror placed at 45° to the base (see figures 3.1 and 3.3a). A high contrast between the fluid and the substrate meant the fluid front could be computed directly from the image using an edge-detection algorithm, as demonstrated in figure 3.3c by the black-dashed line. Due to the small, non-axisymmetric deviations, a circle was fit to the points detected at the fluid front to give radial extent  $R_F$  at each timestep.

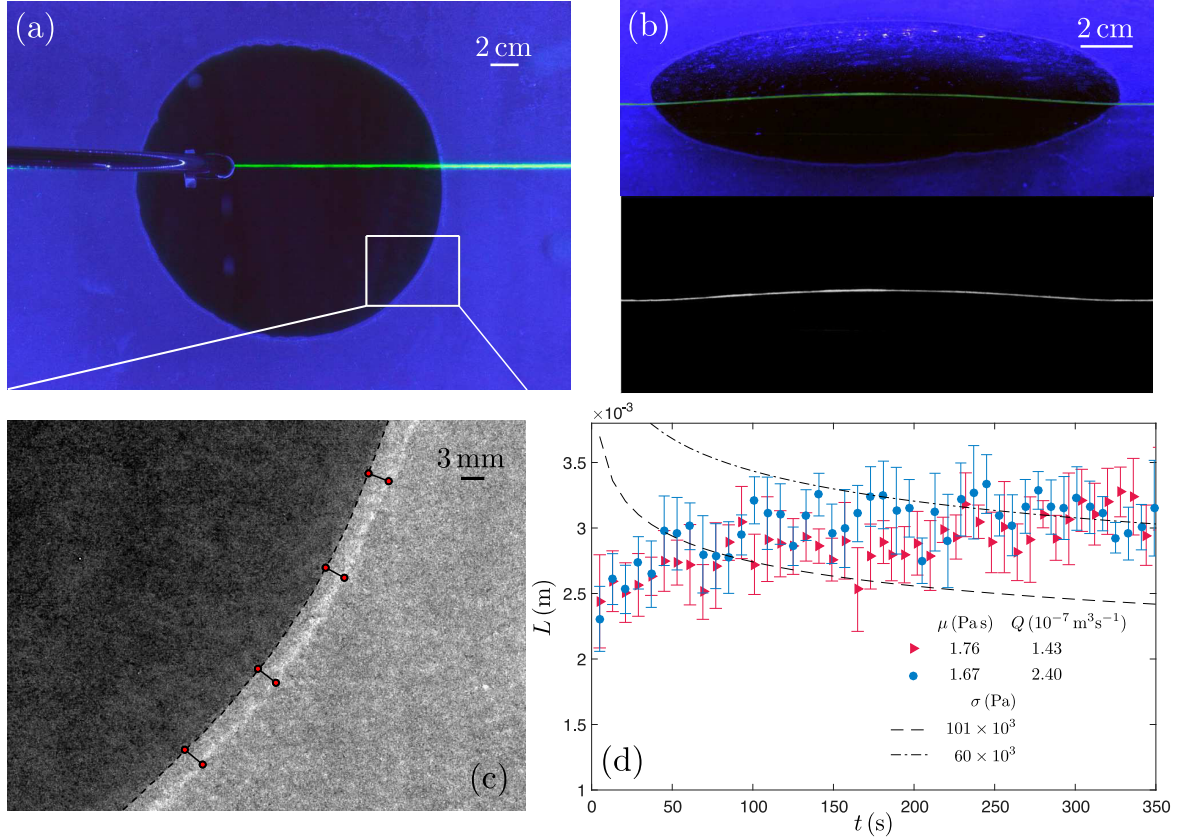


**Figure 3.3: Experimental images and fluid lag length evolution.** Images of an experiment with viscosity and volume flux  $\mu = 2.12 \text{ Pa s}$ ,  $Q = 3.09 \times 10^{-7} \text{ m}^3 \text{ s}^{-1}$  respectively at  $t = 64 \text{ s}$  taken from (a) underneath the experiment showing the radial extent and lag region (N.B. the injection pipe is obscuring the left-hand side of the image), and (b) above at an oblique angle  $\phi$  to the horizontal showing the fluorescent line painted on top of PDMS sheet with a filtered image showing the deflected line. (c) Expanded view of the edge of the experiment shown in (a) filtered to demonstrate intensity contrast between vapour tip and the substrate. Fluid front given by the black-dashed line with lag lengths given by pairs of red dots. (d) Lag length with time for two experiments in the viscosity dominant regime with different viscosities  $\mu$  and volumes fluxes  $Q$ . The dot-dashed and dashed lines plot the theoretical lag length in the viscosity dominant regime (3.16) for  $\sigma = (60, 101) \times 10^3 \text{ Pa}$ , respectively.

Partial internal reflection within the vapour tip allowed for distinction between the fluid front and fracture front. This is demonstrated in figure 3.3c where the blue colour channel is isolated and the contrast increased. The scatter in the brightness of the vapour tip meant the fracture front could not be determined from an edge-detection algorithm. As a result, the fracture front was manually tracked at 10 points around the edge of the blister. The red dots in figure 3.3c show the edge-detected  $R_F$  and manually picked  $R_N$ . The lag length is determined at each pair of points and an average is taken for each timestep. The results of this procedure are shown in figure 3.3d, with the error given by the standard deviation of the 10 points measured at each timestep.

The adhesion energy  $\Delta\gamma$  of the adhesive film was measured using a two-dimensional lift-off experiment. A 30 cm  $\times$  8 cm strip of PDMS was adhered to the glass table with the adhesive film. One end of the strip was uplifted using a micrometer in 0.2 mm increments and the resulting profile at each height determined by imaging a fluorescent line painted along the length of the strip. The profiles for one series of experiments are shown in figure 3.4a for increasing heights  $h_0$ . In figure 3.4b the profiles have been translated such that the fracture positions coincide and collapses the data onto one curve with the same tip structure. The curvature  $\kappa$ , and hence adhesion energy  $\Delta\gamma$ , can then be calculated by fitting a quadratic to the profiles (black-dashed line). From four independent experiments (including the one shown in figure 3.4), the curvature is measured to be  $\kappa = 2.94 \pm 0.15 \text{ m}^{-1}$ , and hence adhesion energy  $\Delta\gamma = 0.78 \pm 0.17 \text{ J m}^{-2}$ . This adhesion energy is comparable to values previously obtained for similar tapes (Wagner and Vella, 2013).

### 3.4 Results

Using the PDMS sheet described above, the elastogravity length scale of  $l_{eg} = 65 \text{ mm}$  restricts the experiments to a short radial range. Hence, the current setup cannot transition from one regime to another without the influence of gravity. As such the viscosity and adhesion regimes are looked at separately. From the measurements of the adhesion energy and taking an estimate of the reduced tip pressure  $\sigma = 101 \times 10^3 \text{ Pa}$  (which is justified later when describing the measured lag length) the transition timescale  $T_C$  can be calculated. Table 3.1 lists the series of experiments carried out in terms of viscosity  $\mu$  and volume flux  $Q$ , where experiments 1–6 have a large transition timescale,  $T_C = 93.0 - 154.1 \text{ s}$ , and experiments 7–12 have a small transition timescale,  $T_C = 0.4 - 5.7 \text{ s}$ . By equating the expressions for the radial extent in the two regimes ((3.14) and (3.17)), the time of transition  $t_C = ((24/\pi)^{1/4}/1.52)^{20} \simeq 6.0T_C$ . Hence, it is anticipated that experiments 1–6 are in the viscosity dominant regime and experiments 7–12 are in the adhesion dominant regime.

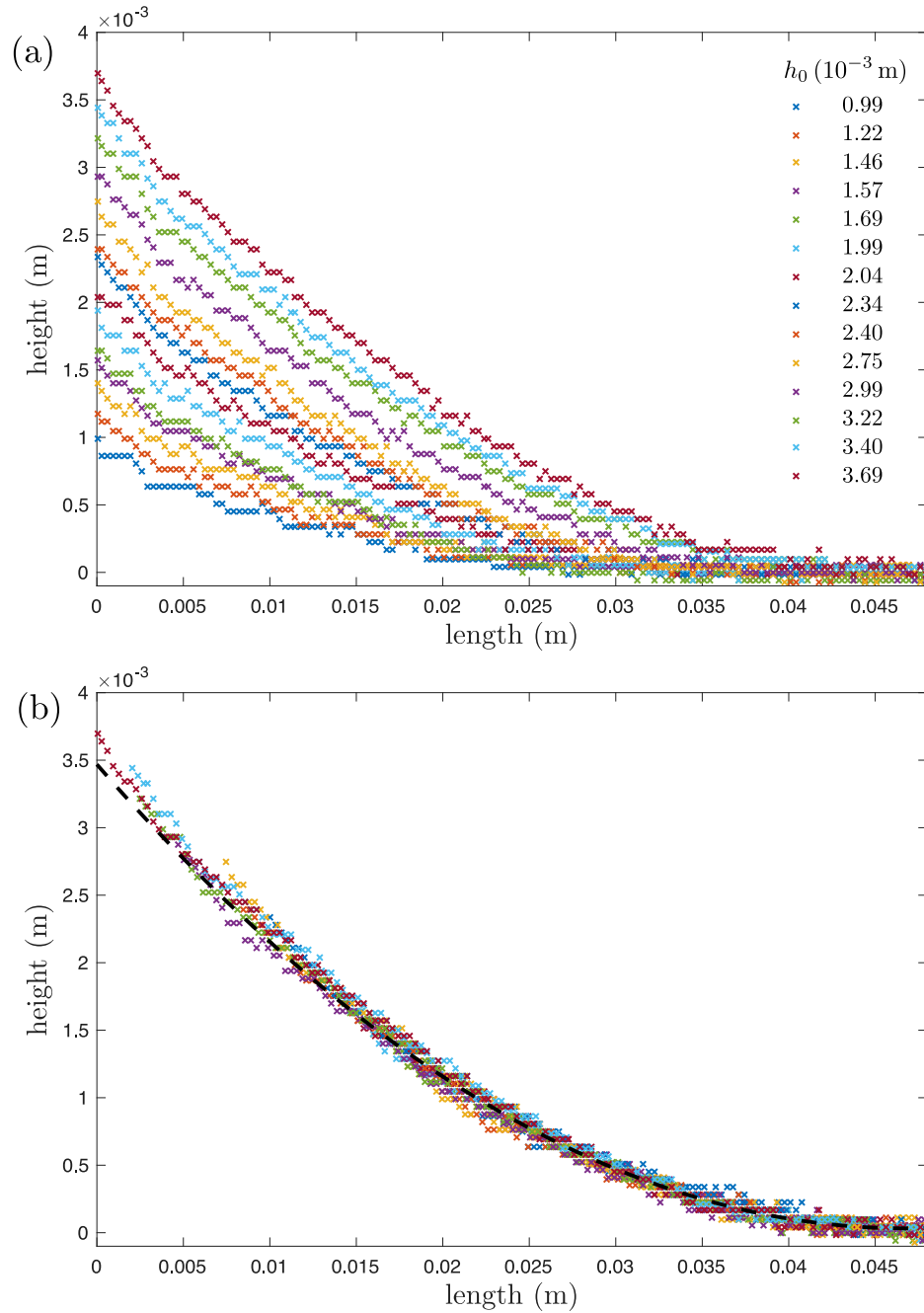


**Figure 3.4: Measuring adhesion curvature.** (a) Plot of profiles for two-dimensional lift-off experiment for increasing heights  $h_0$ . (b) Translated profiles such that the fracture positions coincide. Fitted quadratic curve given by black-dashed line.

Experiment	$\mu$ (Pa s)	$Q$ ( $10^{-7} \text{ m}^3 \text{ s}^{-1}$ )	$T_C$ (s)	$\kappa_{adh}$ ( $\text{m}^{-1}$ )
1	1.76	1.43	93.0	n/a
2	1.76	1.74	99.3	n/a
3	1.69	2.12	100.5	n/a
4	1.67	2.40	103.1	n/a
5	1.78	2.83	118.4	n/a
6	2.12	3.09	154.1	n/a
7	0.17	1.64	4.3	$2.91 \pm 0.25$
8	0.16	4.81	5.7	$3.04 \pm 0.28$
9	0.15	1.58	3.6	$2.53 \pm 0.15$
10	0.11	3.12	3.0	$2.48 \pm 0.26$
11	0.07	1.56	1.3	$2.03 \pm 0.17$
12	0.03	1.60	0.4	$1.42 \pm 0.26$

**Table 3.1: Experimental parameters for 12 experiments with varying viscosities  $\mu$  and volume fluxes  $Q$ .** The transition timescale  $T_C$  is calculated using bending stiffness  $B = 0.18 \text{ Pa m}^3$ , reduced vapour tip pressure  $\sigma = 101 \times 10^3 \text{ Pa}$  and measured curvature  $\kappa = 2.94 \pm 0.15 \text{ m}^{-1}$ .  $\kappa_{adh}$  is the tip curvature measured during experiments in the adhesion dominant regime, and hence is not applicable to experiments 1–6 in the viscosity dominant regime.

### 3.4.1 Viscosity dominant spreading

In experiments 1–6 in the viscosity dominant regime, see table 3.1, pure glycerine was used with viscosities  $\mu = 1.67 - 2.12 \text{ Pa s}$  and volume fluxes  $Q = (1.43 - 3.09) \times 10^{-7} \text{ m}^3 \text{ s}^{-1}$ . Figure 3.5 shows the measured deflection for an experiment with viscosity  $\mu = 2.12 \text{ Pa s}$  and volume flux  $Q = 3.09 \times 10^{-7} \text{ m}^3 \text{ s}^{-1}$  for  $t = 64 - 130 \text{ s}$ , with profiles plotted every  $\Delta t = 6 \text{ s}$ . From section 3.2, equations (3.14) and (3.15) describe the radius and central deflection at time  $t$  in the viscosity dominant regime. By scaling the radius and height of the profiles in figure 3.5a by these expressions for  $R_F$  and  $h_0$ , the profiles collapse on to a universal curve described by (3.5), see figure 3.5b. The black-dashed line shows the theoretical profile given by equation (3.4) demonstrating agreement with the collapsed dataset. This confirms that in the dynamic spreading case the shape of the blister remains unchanged from the classic bell-shaped profile.

Because the pressure within the central blister was quasi-static, the position of the blister with respect to the injection hole was only weakly constrained and hence was very sensitive to initial experimental conditions. For example, the differing angle the injection pipe made to the horizontal substrate, or small differences in the adhesion energy in the immediate vicinity of the injection hole resulted in migration of the blister off-centre, see figure 3.3a. At the start of each experiment, the fluorescent line on the PDMS sheet was aligned with the injection hole, and hence for the same experiments the detected deflection profile is of

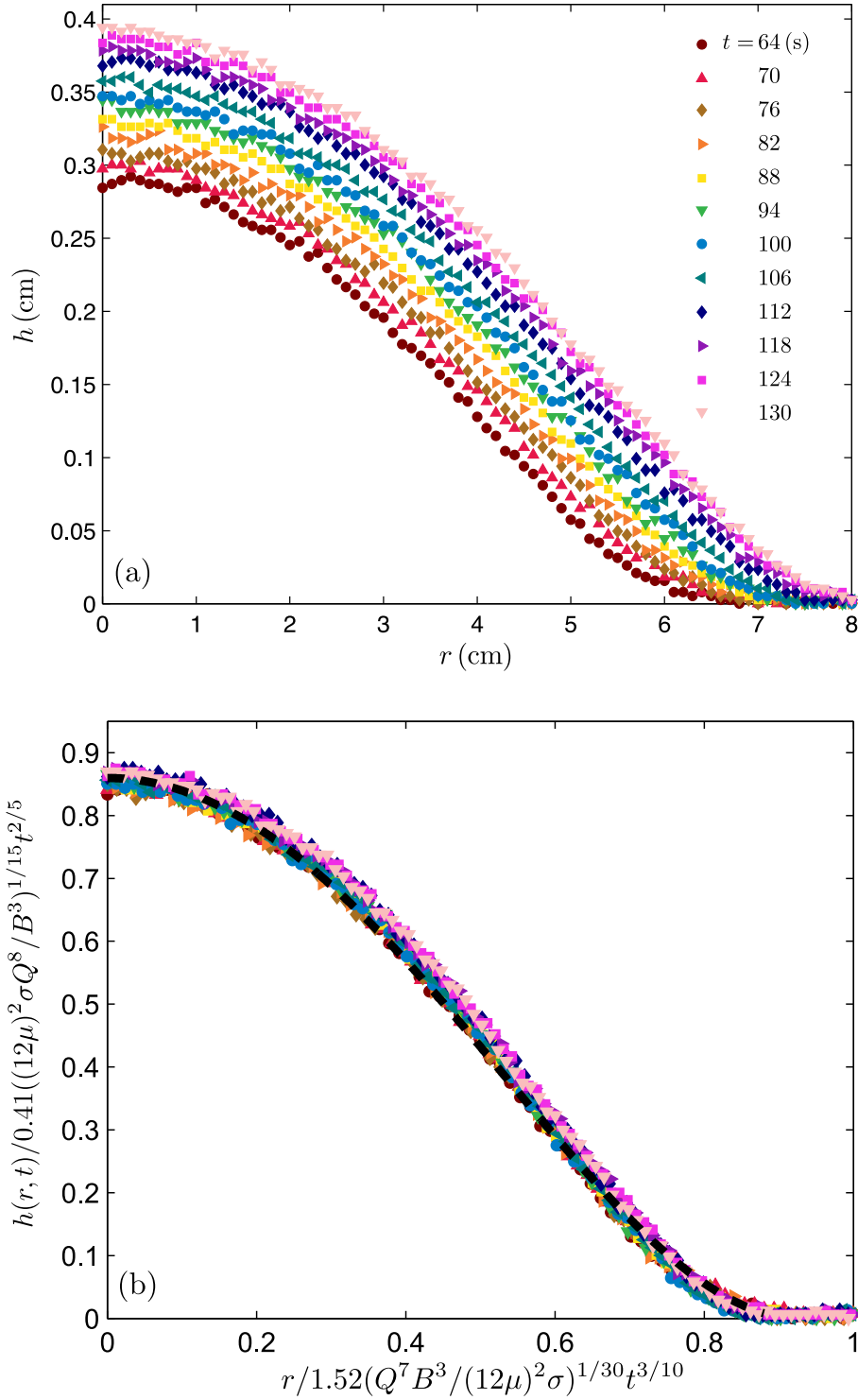


**Figure 3.5: Experimental results of the cross-section.** Deflection profiles for an experiment in the viscosity dominant regime with viscosity  $\mu = 2.12$  Pa s, volume flux  $Q = 3.09 \times 10^{-7} \text{ m}^3 \text{ s}^{-1}$ ,  $\sigma = 101 \times 10^3$  Pa for  $t = 64 - 130$  s, where  $\Delta t = 6$  s. (a) Measured deflection, and (b) deflection scaled with theoretical expressions (3.14) and (3.15). The black-dashed line shows the theoretical profile (3.4).

a chord taken slightly off-centre. For these reasons, the magnitude of the measured radius and height in figure 3.5a are less than the theoretical prediction for a profile through the origin, i.e. the dimensionless radial extent and central deflection in figure 3.5b are less than 1. However, providing the offset from the origin is sufficiently small, a bell-shaped profile would still be anticipated, given by equation (3.4), as shown in the collapse of profiles in figure 3.5b. Once the injected volume is large enough, the influence of this non-axisymmetry subsides and hence does not influence the dynamics analysed below.

Figure 3.6a shows the radial extent with time for six experiments with different volume fluxes in the viscosity dominant regime. In figure 3.6b the radial extent is scaled with  $(Q^7 B^3 / ((12\mu)^2 \sigma))^{1/30}$  from equation (3.14). This scaling collapses the experimental data after the initial transient close to a common curve with power-law exponent 3/10, in line with the theoretical scaling  $R_F \sim t^{3/10}$  in the viscosity dominant regime. The black-dashed line in figure 3.6b corresponds to the best fit line  $R_F / (Q^7 B^3 / ((12\mu)^2 \sigma))^{1/30} = 1.40 t^{3/10}$ , where the prefactor is within 8% of the theoretical prefactor 1.52.

For the viscosity dominant regime, the lag length is measured manually using the methods described in section 3.3, see figure 3.3c. Figure 3.3d plots the lag length for two experiments with volume fluxes  $Q = (1.43, 2.40) \times 10^{-7} \text{ m}^3 \text{ s}^{-1}$ , where  $L$  is the average of the measured lag lengths and the error bars are one standard deviation above and below the mean. The overlapping error bars for the two experiments suggest there is no measurable difference between the lag lengths which is supported by the negligible dependence on the volume flux,  $Q^{1/30}$ , in equation (3.16). The black dashed and dot-dashed lines in figure 3.3d are equation (3.16) plotted with  $\sigma = 101 \times 10^3, 60 \times 10^3 \text{ Pa}$  respectively. If the vapour tip produces a vacuum pressure at the front the vapour tip pressure would be zero,  $p_T = 0$ , and hence  $\sigma = p_0 + \rho_s g d - p_T \simeq 101 \times 10^3 \text{ Pa}$ . The magnitude of the lag length observed suggests the tip pressure is non-negligible. Some small amount of air may have been trapped when placing the adhesive sheet onto the glass substrate. These bubbles may act to increase the pressure at the tip and hence explain the smaller value of  $\sigma$  required to fit the lag length observed. Alternatively, some of the aqueous glycerine solution may have evaporated into the tip, suggesting that the pressure in the vapour tip is approximately equal to the vapour pressure.

The measured lag length also appears to be smaller at early times, in contrast to the theoretical prediction. However, it should be noted that equation (3.8) has been written in the limit  $R_F \gg L$ , which may be violated at early times. As a result, when fluid is first injected the elastic sheet is clamped at the radius of the injection hole, and the sheet is lifted up by the injection of fluid with a small lag length at the front. As the blister begins to propagate beyond this radius the lag length first increases as it relaxes to the dynamically determined

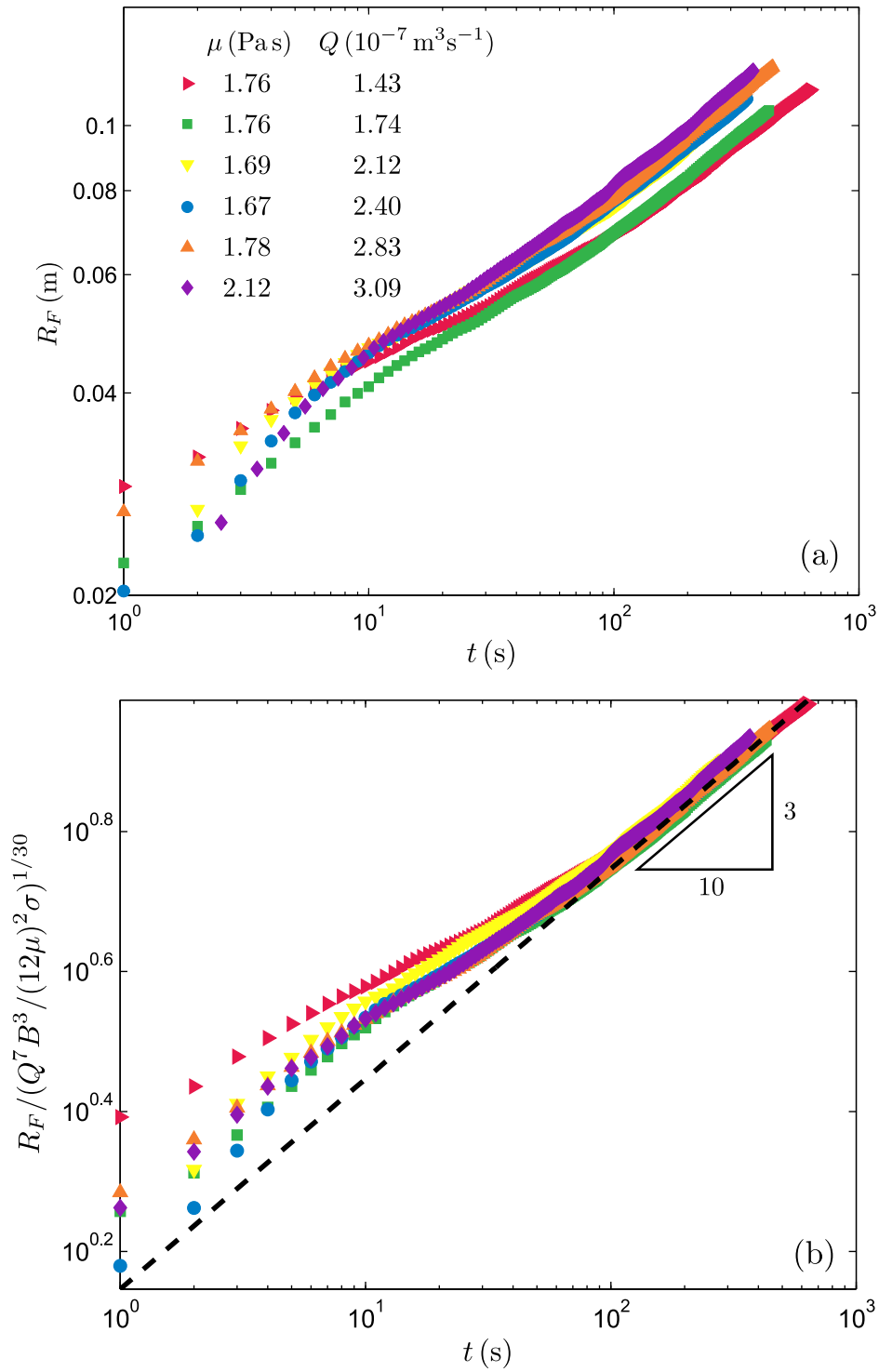


**Figure 3.6: Experimental results for viscosity dominant spreading.** (a) Measured radial extent with time, and (b) radial extent scaled with  $(Q^7 B^3 / ((12\mu)^2 \sigma))^{1/30}$ . Black-dashed line corresponds to best fit  $R_F / ((Q^7 B^3 / ((12\mu)^2 \sigma))^{1/30}) = 1.40 t^{3/10}$ .

extent. This transient behaviour can be seen in figure 3.6b where the radial extent does not collapse at early times and in figure 3.3 where the lag length increases initially, and continues until the pressure decreases to that given by the elastic pressure i.e. until the blister is large enough that the initial pressure build up is negligible. The constant lag length observed at late time during the viscosity dominant spreading is then consistent with the slowly varying lag length  $L \sim t^{-1/10}$  predicted by the theoretical model.

### 3.4.2 Adhesion dominant spreading

Experiments 7–12 (table 3.1) are in the adhesion dominant regime. In these experiments glycerine-water solutions with viscosities  $\mu = 0.03 - 0.17$  Pa s were injected with volume fluxes  $Q = (1.56 - 4.81) \times 10^{-7} \text{ m}^3 \text{ s}^{-1}$ . Figure 3.7a shows the measured radial extent with time. Under the assumption that the adhesion energy is constant and with fracture front curvature given by measured value  $\kappa = 2.94 \pm 0.15 \text{ m}^{-1}$ , the radial extent is scaled by  $Q^{1/4}$  from equation (3.17) and it is found that the prefactor  $c$ , where  $R_F = c(Qt)^{1/4}$ , is dependent on the glycerol-water content of the injected fluid. From equation (3.17),  $c$  is a constant set by the curvature imposed by adhesion at the fracture front. Hence, the curvature at the fracture front, which is constant for any given experiment, is found to differ from the measured static value  $\kappa$  and varies with the fluid viscosity. The curvature, or equivalently the adhesion energy, is therefore a function of the glycerol-water content, with blistering a sensitive measure of the effective surface energy of the adhesive tape in response to interaction with a fluid. The curvature  $\kappa_{adh}$  is independently measured for each experiment by fitting a quadratic to the tip region of the detected deflection profiles, see table 3.1 and figure 3.8a. This demonstrates a decrease in curvature from the static measurement  $\kappa$  with decreasing viscosity. Figure 3.8b plots the measured curvature  $\kappa_{adh}$  against the prefactor  $c$  for the six experiments, where  $R_F = c(Qt)^{1/4}$ ; the error bars are given by one standard deviation above and below the mean. The prefactor is found to be a function of the measured curvature,  $c = c(\kappa_{adh})$  where  $c = 1.45 \kappa_{adh}^{-1/4}$  (black-dashed line). Hence, the exponent of  $\kappa_{adh}$  agrees with the static scaling given by equation (3.17). In figure 3.7b the radial extent is scaled by  $(Q/\kappa_{adh})^{1/4}$  using the measured values of  $\kappa_{adh}$ . This shows a collapse of the experimental data after the initial transient onto a common curve with power-law exponent 1/4, in line with theoretical prediction, where the black-dashed line is best fit  $R_F/(Q/\kappa_{adh})^{1/4} = 1.45 t^{1/4}$ . The prefactor is within 13% of theoretical prefactor 1.66; this discrepancy is largely due to the inherent limitations in the measurement of experimental curvature  $\kappa_{adh}$ .

Unlike the viscosity dominant regime, in the adhesion dominant regime no measurable lag region was observed during experiments. However condensation droplets were seen when pulling off the adhesive tape. This suggests that the vapour tip was present and at low enough

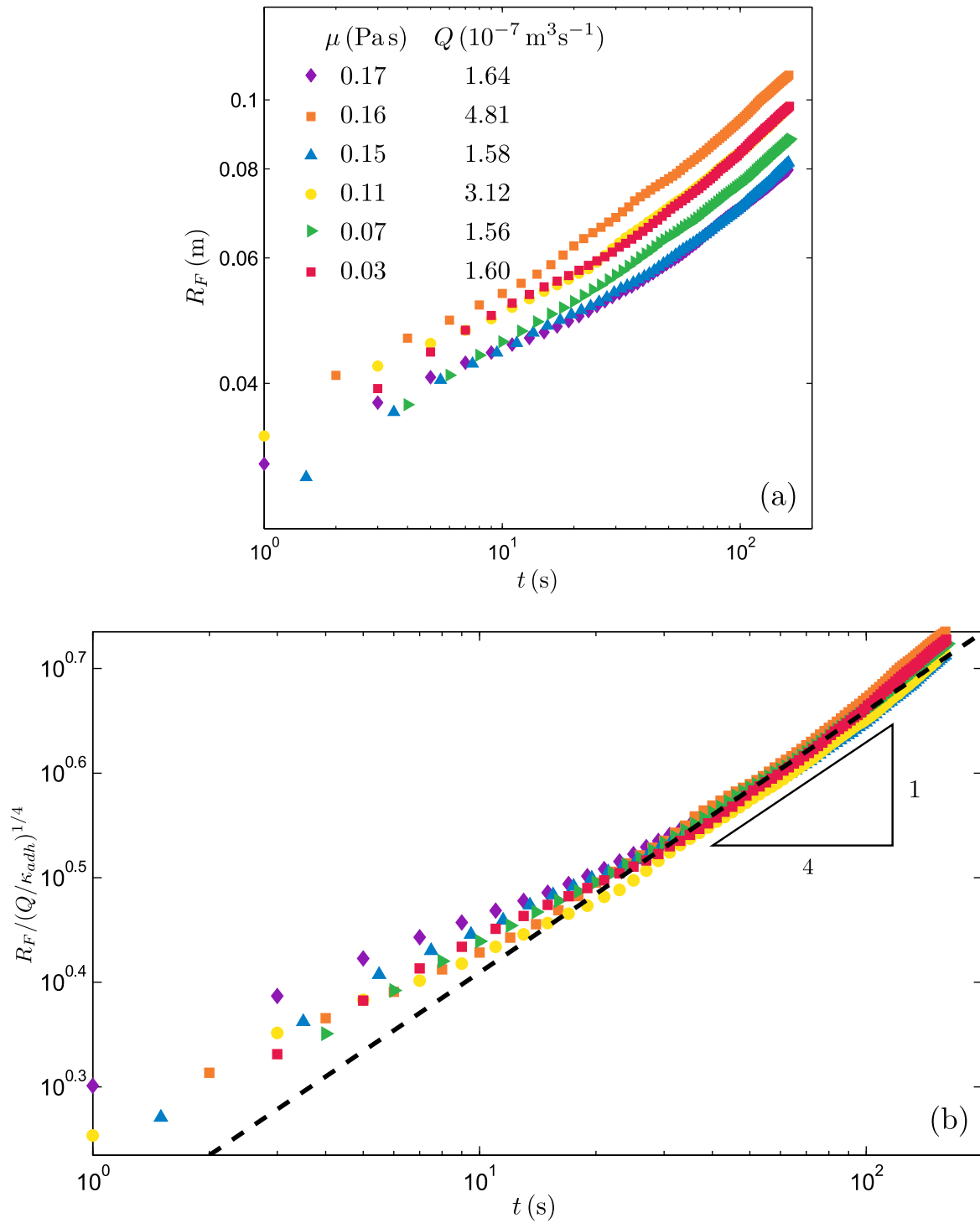


**Figure 3.7: Experimental results for adhesion dominant spreading.** (a) Measured radial extent with time, and (b) radial extent scaled with  $(Q/\kappa_{adh})^{1/4}$ . Black-dashed line corresponds to best fit  $R_F / (Q/\kappa_{adh})^{1/4} = 1.45 t^{1/4}$ .

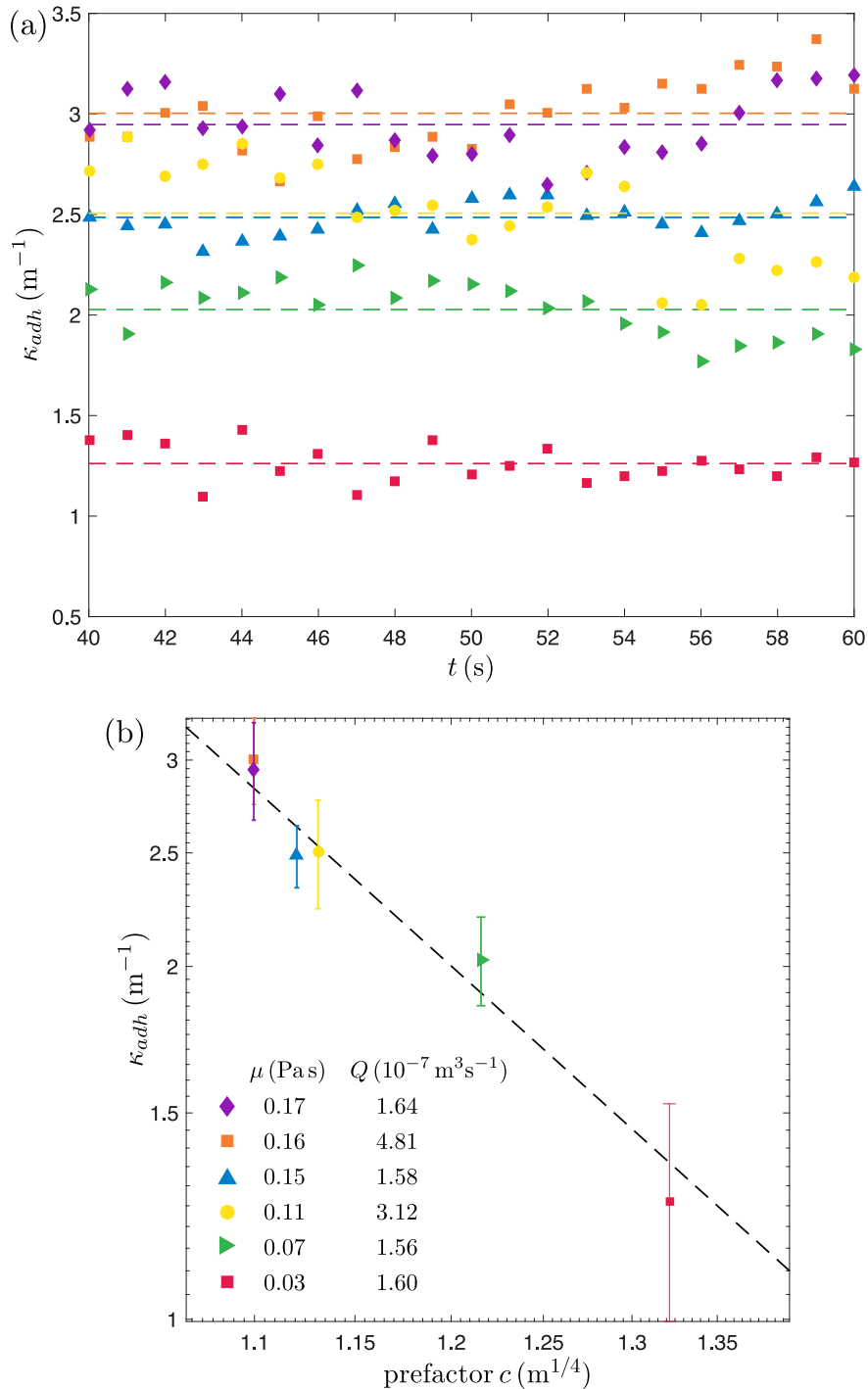


**Figure 3.8: Measured curvature in adhesion dominant regime.** (a) Plot of curvature  $\kappa_{adh}$  with time for six experiments in the adhesion dominant regime, and (b) plot of curvature against prefactor  $c$ , where  $c = R_F/(Qt)^{1/4}$ .

pressures to exsolve gas from the glycerine-water mix but was of sufficiently small scale such that it could not be distinguished from the fluid front during experiments using the optical technique described. Substituting the experimental parameters  $\mu$ ,  $Q$  and  $\kappa_{adh}$ , and taking  $\sigma = 101 \times 10^3$  Pa, into the expression for the lag length in the adhesion dominant regime equation (3.19) gives  $L \simeq 0.8 - 1.2 \times 10^{-3}$  m. This is consistent with a lag length which was below the image resolution as demonstrated in figure 3.3. The decrease in curvature (and hence decrease in adhesion energy  $\Delta\gamma$ ) with viscosity can be explained by a chemical interaction between the fluid and adhesive material when the lag length becomes small. This weakens the adhesive strength, and hence reduces the curvature.

### 3.5 Discussion

Static blister tests have long been used as a measure of the strength of adhesion between two materials (Jensen, 1991; Wagner and Vella, 2011). The coupling of a viscous fluid delaminating adhered elastica has focused attention towards the study of blister dynamics (Hewitt et al., 2015; Lister et al., 2013) with application in a wide range of biological and industrial settings. These include the flow of biofluids through deformable vessels (Grotberg and Jensen, 2004) such as the reopening of the pulmonary airways (Heil and Hazel, 2011); and the manufacturing of stretchable electronics (Sun et al., 2006) made from buckled film on an elastomeric substrate (Khang et al., 2009). The experiments described in section 3.4 have highlighted that blister dynamics could again usefully be applied to understanding the strength of adhesion with blistering providing a sensitive measure of the effective surface energy of the adhesive tape in response to interaction with a fluid. In addition, the treatment of a thin elastica coupled with an adhesive sheet has provided a simple, new approach to understanding fluid-driven fracturing in an experimental setting. Hence, this experimental setup could lend itself to investigating other outstanding problems such as the effect of inhomogeneity in adhesive strength on the dynamics of fluid-driven fractures.

Section 3.2 describes the static shapes for a given volume  $V$  and the dynamic spreading regimes for a constant flux injection,  $V = Qt$ . One can think of connecting these two cases by considering the evolution of a blister once injection has stopped at time  $t = T$ , or equivalently the dynamic spreading of a constant volume  $V = QT$ . As in the constant flux case, spreading can be separated into two regimes: viscosity dominant spreading and adhesion dominant spreading. An evolution equation for the fluid front in the viscosity dominant regime can be found by substituting the interior curvature  $\kappa_{int} = 24QT/\pi R_F^4$  from equation (3.4) into

equation (3.13). Hence the fluid front is given by

$$R_F(t) = 1.68 \left[ \frac{(QT)^7 B^3}{(12\mu)^2 \sigma} \right]^{1/30} t^{1/15}, \quad (3.20)$$

where the lag length decreases more rapidly than in the constant flux case with

$$L(t) = 0.97 \left[ \frac{(12\mu)^4 QT B^9}{\sigma^{13}} \right]^{1/30} t^{-2/15}. \quad (3.21)$$

In the adhesion dominant regime, the blister reaches the static shape (3.4) with constant radial extent and central deflection (3.5), where  $V = QT$ , with no lag between the fluid and fracture fronts. Equating these two expressions gives transitional timescale  $T_{C_V} = 12\mu(QT)^{1/4} \sigma^{1/2} / B^{3/2} \kappa^{15/4}$ . Hence, for a constant flux injection, if the injection is stopped at some time  $t = T < T_{C_V}$  the blister would continue to propagate slowly in the viscosity dominant regime with radial extent (3.20) and decreasing lag length (3.21). When  $t > T_{C_V}$ , there is a transition to adhesion control where the fracture front becomes stationary. Conversely, if  $T > T_{C_V}$  the fracture front would become stationary when the injection is stopped. This provides a mechanism for stopping a fluid-driven fracture, something that is often overlooked when considering the propagation of magmatic intrusions. It is worth noting that, ultimately the static length of the blister is set by adhesion in cases where the fluid properties do not change with time. This ultimate extent of magmatic intrusions must either be set by fracturing at the front, or by properties of the evolving fluid, such as a yield strength or solidification. This will be discussed further in chapter 4 when considering the (thickness versus length) field data for mafic sills.

### 3.6 Concluding remarks

I have presented a theoretical model to describe fluid-driven fracturing of adhered elastica by the introduction of a vapour tip separating the fracture and fluid fronts. Coupled with a fracture criterion imposed at the tip, this leads to the possibility of static shapes where the potential energy of the blister balances the energy required for fracture. For dynamic inflation, spreading can be split into two distinct regimes: viscosity dominant spreading controlled by the pressure gradient driving fluid into the vapour tip, and adhesion dominant spreading controlled by interfacial adhesion. Experiments using thin elastica adhered to a horizontal substrate have yielded consistent comparisons with theoretical predictions in the two regimes. The experimental techniques developed have also provided further evidence for the formation of an experimental vapour tip, again consistent with that proposed by the

theoretical model. However, the nature of the tip region in terms of its small size have made measurement of the time evolution of the vapour tip difficult. In addition, the complexity of the adhesive due to its interaction with the glycerine-water solutions has made it challenging to characterise. This highlights that more work needs to be done to concretely nail down the role the tip plays in the dynamics of spreading fluid-filled fractures. In particular, considering how alternative combinations of the injected fluid and adhesive tape could (a) make the tip easier to measure, and (b) reduce the interaction between the fluid and the adhesive. Nonetheless, these experiments provide a simple setup to investigate fluid-driven fracturing of elastic media and observe the formation of a fluid lag, previously only observed in laboratory experiments on the fracturing of elastic blocks (Bunger et al., 2005, 2013; Medlin and Massé, 1984).

The motivation behind studying fluid-driven fracturing of adhered elastica was to try to build a simplified model for magmatic intrusions that includes the key physical mechanisms such as elastic deformation, viscous flow and fracturing of rock. With this model, I can begin to compare the results (such as aspect ratios) with collated field data (Cruden and McCaffrey, 2006; Cruden et al., 2017). In chapter 4, I explore this comparison, looking at turbulently emplaced mafic sills where a fluid lag is a possible front condition. This study also highlights the intuition that can be gained from laboratory experiments. I explore this further in chapter 5 where I investigate magmatic intrusions associated with a topographic slope theoretically and experimentally.



# Chapter 4

## Turbulent fluid-driven fracturing

---

### 4.1 Introduction

In chapter 3, I studied the fluid-driven fracturing of adhered elastica as a model for shallow magmatic intrusions. Models such as this and those by numerous other authors (e.g. Bungler and Cruden, 2011; Michaut, 2011) aim to explain the key physical mechanisms involved in the emplacement of magmatic intrusions, such as those collated by Cruden and McCaffrey (2006) and Cruden et al. (2017), see figure 4.1 adapted from Cruden et al. (2017). Bungler and Cruden (2011) made good comparisons between the aspect ratios (thickness versus length) of their model and the field data for laccoliths. However, their comparison struggled to reconcile the positive gradient of the thickness versus length dataset for mafic sills,  $T \sim L^m$  where  $m > 0$ . Note, for the remainder of this chapter I write the thickness versus horizontal length relationship as  $h \sim R^m$  to be consistent with notation. Bungler and Cruden (2011) argue that this discrepancy could be due to an increasing fracture toughness (adhesion energy) and/or a decreasing Young's modulus  $E$  with intrusion size. This would lead to a positive relationship between thickness and length of mafic sills, a hypothesis that is supported in part by small scale laboratory experiments that show smaller fracture toughnesses and larger elastic moduli compared with in the field (e.g. Olson, 2003). However, applying this model would require a trend in material properties with intrusion site, and hence would be a challenging model to implement with the data available. Moreover, their comparison with the two diverging strands of intrusions (laccoliths and mafic sills) after lengths of  $L \sim 1$  km relies on taking a smaller fracture toughness for mafic sills compared with laccoliths. They attribute the discrepancy here with an increase in fracture toughness with the blunting of the fracture front due to magma solidification, as supported by field evidence of bulbous terminations (Johnson and Pollard, 1973; Morgan et al., 2008).

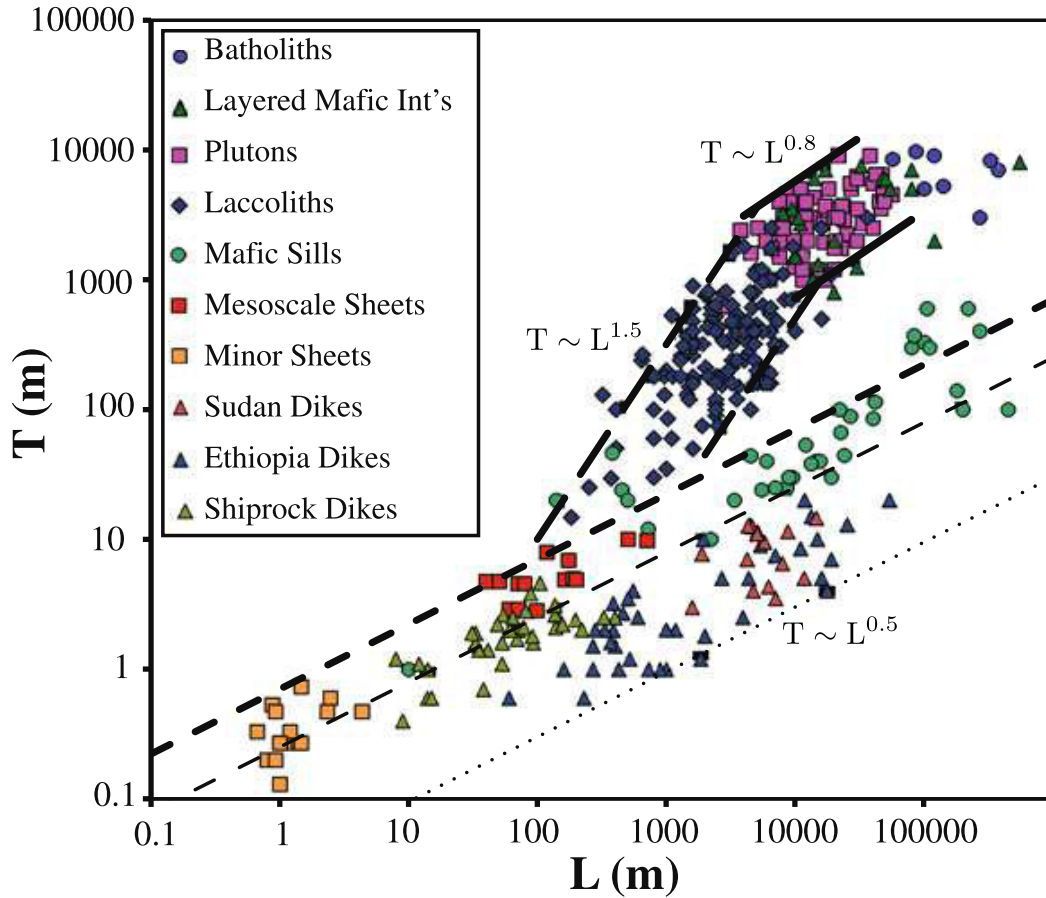


**Figure 4.1:** Figure adapted from Cruden et al. (2017) (their figure 1a). Log-log plot of the thickness  $T$  against length  $L$  for a range of magmatic intrusions, see legend. Lines indicate approximate power-law relationships: minor sheets, mesoscale sheets, sills and dykes are given by scaling  $T \sim L^{0.5}$ , laccoliths by  $T \sim L^{1.5}$ , and plutons by  $T \sim L^{0.8}$ .

In addition to these trends in aspect ratios of magmatic intrusions, field evidence has shown that mafic sills may exhibit evidence of turbulent flow. Kille et al. (1986) describe how a lack of chilled margin and a wide contact aureole around an intrusion indicates a high heat flux into the surrounding rock. Together with a coarser grain size, Kille et al. (1986) suggest these observations imply the flow was turbulent. Holness and Humphreys (2003) argue that these features could also be explained by a prolonged laminar flow, which would also result in considerable heating of the surrounding rock. Another measure of whether the emplacement is turbulent is to calculate the Reynolds number,

$$Re = \frac{\rho U H}{\mu}, \quad (4.1)$$

which is the ratio of inertial forces to viscous forces, where  $\rho$  is the density,  $\mu$  the viscosity,  $U$  is a characteristic velocity, and  $H$  is a characteristic length scale. Taking typical values of a

magma density  $\rho = 2800 \text{ kg m}^{-3}$ , viscosity  $\mu = 10^2 \text{ Pa s}$  and velocity  $U \sim 1 \text{ m s}^{-1}$ , mafic sills with thicknesses between 1 and 100's m would be expected to be between transitional and fully turbulent flow,  $Re \sim 28 - 2800$ , (Holness and Humphreys, 2003; Kavanagh et al., 2006). However, the models considered thus far for magmatic intrusions have assumed laminar flow dominated by viscous dissipation or fracture toughness at the tip. The introduction of turbulent flow would both reduce the emplacement duration and allow propagation to be controlled by the dynamics of the turbulent interior rather than the physics at the fracture front. A simple turbulent–laminar hybrid model has been considered previously for the tip structure of hydraulic fractures and subglacial drainage (Dontsov, 2016; Hewitt et al., 2018). I build on this work here for magmatic intrusions with the aim of trying to understand the aspect ratios of mafic sills, in particular the positive trend in the collated field data (Cruden and McCaffrey, 2006; Cruden et al., 2017). In my analysis I aim to assess the controlling physical processes during the emplacement of magmatic intrusions.

Near the front of the fracture where the aperture tends to zero it is anticipated that eventually viscous dissipation dominates over turbulent dissipation. In this limit, I define the local Reynolds number as  $Re = \rho \dot{R} \delta / \mu$ , where  $\dot{R}$  is the velocity of the front of the intrusion and  $\delta$  is a characteristic height scale of the front. As the height goes to zero at the fracture front,  $\delta \rightarrow 0$ , the local Reynolds number must also go to zero. Hence there must be a region of laminar flow near the fracture front, with a transition to turbulent flow away from the fracture front. The dominant control on the intrusion depends on where the most dissipation is found: either throughout the interior of the intrusion or in the laminar region at the front. As the speed of propagation decreases and the laminar region grows, the majority of dissipation is made up of viscous dissipation at the front. Hence the flow transitions from turbulent interior (or bulk) control to control by the laminar physics at the tip.

The aim of this chapter is to understand the aspect ratio data for mafic sills from Cruden et al. (2017). Motivated by evidence that mafic sills may exhibit turbulent flow, I first build a model to include both turbulent and laminar flow, assessing the transition between these two regimes when different physical processes are considered at the fracture front. In particular, this highlights when the flow is interior or front controlled, with the majority of the viscous dissipation occurring throughout the interior or at the front, respectively. Given this model, I then evaluate the aspect ratios from the turbulent regimes together with those from laminar propagation. This then provides a suite of models to compare with the field data on mafic sills.

This chapter is laid out as follows. In section 4.2.1, I recap the turbulent–laminar model from Hewitt et al. (2018). In section 4.2.3, I outline new similarity solutions for the turbulent model when gravity begins to play a role. In sections 4.3.1–4.3.3, I summarise the different

laminar flow regimes at the fracture front with either a pre-wetted film or a fluid lag. I calculate the aspect ratios of intrusions in these regimes and timescales for the transition from interior, turbulent control to tip, laminar controlled propagation. Finally, in section 4.4, I discuss the implications for the aspect ratios of turbulently emplaced intrusions such as mafic sills.

## 4.2 Model setup

### 4.2.1 Turbulent–laminar model recap

To examine the influence of turbulence, consider the deformation of an elastic sheet of thickness  $d$ , bending stiffness  $B$  and density  $\rho_s$  due to the injection of fluid beneath at the origin  $r = 0$  of density  $\rho$  and viscosity  $\mu$ . As in chapter 3, axisymmetric spreading and elastic deformation of a thin-elastic sheet are assumed, with deformation in the bending limit such that  $h \ll d$ , where  $h$  is the height of the intrusion.

Following Hewitt et al. (2018), in the case of turbulent flow, the radial flow can be related to radial pressure gradients in terms of a Darcy-Weisbach friction factor,  $f_D(Re)$ , such that

$$\frac{\partial p}{\partial r} = -f_D(Re) \frac{\rho U^2}{4h}, \quad (4.2)$$

where  $U$  is the mean radial flow. This formulation is typically used to calculate the pressure drop during turbulent flow down a pipe. Here, the friction factor  $f_D$  is written as a function of the local Reynolds number  $Re \equiv \rho U h / \mu$ . In section 3.2, the flux for laminar radial flow is given by

$$q = -\frac{r h^3}{12\mu} \frac{\partial p}{\partial r} \equiv U r h. \quad (4.3)$$

Rearranging and comparing with equation (4.2) gives  $f_D(Re) = 48/Re$  in the laminar limit.

In the turbulent limit, Hewitt et al. (2018) give a physical picture of the flow by suggesting that turbulent flow in the fracture is bounded by viscous shear layers of thickness  $\delta_b \ll h$ . By fixing the boundary layer Reynolds number at a critical value  $Re_c \equiv \rho U \delta_b / \mu$ , and balancing the pressure gradient with viscous stresses across this boundary, they write

$$\frac{\partial p}{\partial r} h \simeq \frac{2\mu U}{\delta_b} \simeq 2\mu U \frac{\rho U}{\mu Re_c}. \quad (4.4)$$

Again, rearranging and comparing with equation (4.2) gives a constant friction factor  $f_D(Re) = 8/Re_c$  in the turbulent limit.

A simple combination of the turbulent and laminar regimes is achieved by adding the two Darcy-Weisbach factors to get a composite pressure gradient,

$$\frac{\partial p}{\partial r} = -\frac{\rho U^2}{4h} \left( \frac{48}{Re} + \frac{8}{Re_c} \right), \quad (4.5)$$

which recovers the correct laminar and turbulent limits for  $Re \ll 1$  and  $Re \gg 1$  respectively. Rearranging this quadratic equation then gives an expression for the mean radial flux,

$$Uh = \frac{3\mu Re_c}{\rho} \operatorname{sgn} \left( \frac{\partial p}{\partial r} \right) \left[ -1 + \sqrt{1 + \frac{\rho h^3}{18\mu^2 Re_c} \left| \frac{\partial p}{\partial r} \right|} \right]. \quad (4.6)$$

Substituting the mean radial flux into a statement of local mass conservation,

$$\frac{\partial h}{\partial t} + \frac{1}{r} \frac{\partial}{\partial r} (rUh) = 0, \quad (4.7)$$

then gives an evolution equation for the height of the blister

$$\frac{\partial h}{\partial t} + \operatorname{sgn} \left( \frac{\partial p}{\partial r} \right) \frac{1}{r} \frac{\partial}{\partial r} \left( \frac{3\mu Re_c r}{\rho} \left[ -1 + \sqrt{1 + \frac{\rho h^3}{18\mu^2 Re_c} \left| \frac{\partial p}{\partial r} \right|} \right] \right) = 0. \quad (4.8)$$

In the laminar limit, with  $Re \rightarrow 0$ , this reduces to equation (3.2). Here the pressure gradient is given by terms due to elasticity of the overlying sheet and gravity,

$$\frac{\partial p}{\partial r} = \frac{\partial}{\partial r} (B\nabla^4 h + \rho gh). \quad (4.9)$$

The next two sections describe the transition from interior (bulk), turbulent control to front, laminar controlled propagation and similarity solutions in the turbulent regime.

### 4.2.2 Transition to laminar control

The turbulent-laminar hybrid model described in section 4.2.1 is constructed so as to recover the correct laminar and turbulent limits as a function of the Reynolds number,  $Re = \rho Uh/\mu$ . This is demonstrated by balancing the two terms underneath the square root of equation (4.8). When there is a transition from turbulent to laminar flow, the following inequality is satisfied

$$\left| \frac{\partial p}{\partial r} \right| < \frac{18\mu^2 Re_c}{\rho h^3}. \quad (4.10)$$

The scaling for the radial pressure gradient will be dominated by where the majority of the dissipation in the fluid is found, and hence the location of the largest pressure drop. For radial

extents less than the elastogravity length scale, when bending is dominant, laminar flow is controlled by processes at the front, dominated by the pressure drop there. Provided the flow is laminar in this region at the front, the overall propagation can be laminar, independent of what the flow looks like in the interior (either turbulent or laminar). To evaluate the transition to laminar flow when bending is dominant, only the local Reynolds number for height and length scales at the tip need to be considered. Hence, inequality (4.10) can be evaluated over the height and length scales of the tip.

When gravity begins to play a role, the interior pressure gradient within the intrusion may be dominated by gravity, with bending important at the front over length scales of  $\mathcal{O}(l_{eg})$ . If the majority of the viscous dissipation, and hence pressure drop, occurs over a bending boundary layer at the front then the intrusion is tip controlled. As in the pure bending case, the overall rate of propagation can be determined by laminar flow in this boundary layer, and is independent of what the flow looks like in the interior (either turbulent or laminar). Again, to evaluate the transition to laminar flow, only the height and length scales at the tip need to be considered.

For intrusions whose radial extent is much greater than the elastogravity length scale, bending can be neglected, and hence the majority of the pressure drop occurs over the whole intrusion so that propagation is controlled by the interior processes. The intrusion behaves as a viscous gravity current (Huppert, 1982) with scales

$$\frac{h}{t} \sim \frac{\rho g h^3}{\mu r^2}, \quad Qt \sim hr^2 \quad \Rightarrow \quad h \sim \left( \frac{\mu Q}{\rho g} \right)^{1/4}, \quad r \sim \left( \frac{\rho g Q^3}{\mu} \right)^{1/8} t^{1/2}. \quad (4.11)$$

Given that the pressure drop occurs over the whole intrusion, substituting these scales for height and length into inequality (4.10) gives

$$Re(r) = \frac{\rho Q}{\mu r} < Re_c. \quad (4.12)$$

This inequality states that for there to be a transition to laminar flow when gravity is dominant, and bending can be neglected everywhere, the Reynolds number at each radius  $r$  is required to be less than the critical Reynolds number  $Re_c$ .

The remainder of the chapter will focus on when the flow is controlled by laminar processes at the front, in cases where (i) bending is important over the whole intrusion or (ii) in a boundary layer at the front. To do so, height  $\delta$  and length  $\varepsilon$  scales for the laminar flow at the front are derived, which are dependent on the physical processes at the front, either a pre-wetting film or fluid lag. These height and length scales are also a function of the front velocity  $\dot{R}$ . In order to determine the transition from turbulent, bulk control to laminar, front

controlled propagation, inequality (4.10), or equivalently the local Reynolds number, needs to be evaluated at the tip. By assuming the front velocity is given by the turbulent model, equations (4.25a) or (4.25b) for the bending and gravity regimes respectively, a consistency argument is used to check whether the local Reynolds number is low enough for laminar dominated flow to exist.

In the next section the front velocity  $\dot{R}$  is calculated in the turbulent regime when either bending or gravity is important. In section 4.3, the height and length scales,  $\delta$  and  $\varepsilon$  are calculated for different physics at the fracture front. In particular, either a pre-wetted film (Lister et al., 2013) or a fluid lag (chapter 3; Hewitt et al., 2015) is considered. Both these height and length scales in the different regimes and the front velocities are then used to evaluate the transition from turbulent to laminar flow.

### 4.2.3 Similarity solutions for turbulent flow

When turbulence is dominant, the flow is controlled by dissipation in the interior, and the physics at the front does not impact the propagation. The propagation can then be split into two regimes depending on the radial extent of the flow. When the radius is less than the elastogravity length scale,  $R \ll l_{eg}$ , the length scale at which gravity starts to play a role, then the pressure gradient is dominantly elastic. As the radius becomes greater than the elastogravity length scale,  $R \gg l_{eg}$ , hydrostatic pressure gradients dominate. Hewitt et al. (2018) outlined the similarity solution for the bending regime. Their solution is recapped here and then the similarity solution in the gravity regime is outlined.

In the turbulent regime, equation (4.8) reduces to

$$\frac{\partial h}{\partial t} = -\frac{Re_c^{1/2}}{2^{1/2}\rho^{1/2}} \operatorname{sgn}\left(\frac{\partial p}{\partial r}\right) \frac{1}{r} \frac{\partial}{\partial r} \left( r \sqrt{h^3 \left| \frac{\partial p}{\partial r} \right|} \right), \quad \text{where} \quad \frac{\partial p}{\partial r} = \frac{\partial}{\partial r} (B\nabla^4 h + \rho gh). \quad (4.13)$$

This statement of local mass conservation, along with a statement of global conservation of mass for a constant flux with volume flux  $Q$ ,

$$Qt = 2\pi \int_0^R hr \, dr, \quad (4.14)$$

defines the turbulent flow case, together with boundary conditions at the origin and fracture front. At the origin, boundary conditions that the height  $h$  and its derivatives do not diverge as  $r \rightarrow 0$  are applied. At the fracture front, zero height and no flux through the nose give boundary conditions on  $h$  and  $\nabla h$ . Note, that when gravity is dominant, the reduced order of the equations means fewer boundary conditions are required.

### Bending regime

In the bending regime when the radial extents are much less than the elastogravity length scale,  $R \ll l_{eg} = (B/\rho g)^{1/4}$ , Hewitt et al. (2018) showed there exists a similarity solution with scales

$$R(t) = 1.70 \left( \frac{Re_c B Q^2}{\rho} \right)^{1/11} t^{4/11}, \quad h(0, t) = 0.39 \left( \frac{\rho^2 Q^7}{Re_c^2 B^2} \right)^{1/11} t^{3/11}. \quad (4.15)$$

The data of mafic sills from Cruden et al. (2017) suggests a relationship between the thickness and length of intrusions. In order to compare with the theoretical models described in this chapter, the aspect ratios of different models are computed. Hence for this turbulent model

$$h = 0.26 \left( \frac{\rho Q^2}{Re_c B} \right)^{1/4} R^{3/4}. \quad (4.16)$$

### Gravity regime

For radial extents much greater than the elastogravity length scale,  $R \gg l_{eg}$ , there is a transition to gravity control. Equations (4.13) and (4.14) give the following two scalings

$$\frac{h}{t} \sim \frac{Re_c^{1/2} g^{1/2} h^2}{2^{1/2} r^{3/2}}, \quad Qt \sim hr^2, \quad (4.17)$$

respectively, and suggest one should look for similarity solutions of the form

$$h = \left( \frac{4Q^3}{Re_c^2 g^2} \right)^{1/7} t^{-1/7} f(\eta) \quad \text{where} \quad \eta = \frac{r}{\left( \frac{Re_c g Q^2}{2} \right)^{1/7} t^{4/7}}. \quad (4.18)$$

In the laminar model described in chapter 3, the divergence of viscous stresses at the tip mean a form of regularisation is required to construct solutions that have a contact line which advances at a finite speed (Huh and Scriven, 1971). To check that this is not the case here, steady solutions are sought in the frame of reference of the nose. By writing  $h = H(\zeta \equiv r - R)$ , equation (4.13) becomes

$$-\dot{R}H' = -\frac{Re_c^{1/2} g^{1/2}}{2^{1/2}} \text{sgn}(H') \left( \sqrt{H^3 |H'|} \right)', \quad (4.19)$$

where the prime denotes differentiation with respect to  $\zeta$ . Integrating and imposing zero height at the fracture front,  $H(0) = 0$ , gives

$$\left( \frac{2^{1/2} \dot{R}}{Re_c^{1/2} g^{1/2}} \right)^2 = H|H'| \quad \Rightarrow \quad H = \frac{2\dot{R}}{Re_c^{1/2} g^{1/2}} (R-r)^{1/2}. \quad (4.20)$$

The constant at the front of the expression for  $H$  is positive suggesting that a similarity solution for the whole intrusion exists, with a contact line that advances such that  $H \sim (R-r)^{1/2}$ . Substituting in ansatz (4.18) into the evolution equation for the height of the intrusion in the turbulent regime (4.13),  $f(\eta)$  must satisfy

$$-\left( \frac{1}{7}f + \frac{4}{7}\eta f_\eta \right) = -\text{sgn}(f_\eta) \frac{1}{\eta} \frac{\partial}{\partial \eta} \left( \eta \sqrt{f^3 |f_\eta|} \right) \quad \text{and} \quad 2\pi \int_0^{\eta_N} f \eta \, d\eta = 1, \quad (4.21)$$

where  $\eta(r=R) = \eta_N$ . To solve (4.21) numerically, function  $f(\eta)$  is rewritten as  $f = \eta_N^a \phi(\xi \equiv \frac{\eta}{\eta_N})$ . Substituting into the governing equation for  $f$  gives  $a = 3/2$  and hence

$$\eta_N = \left( 2\pi \int_0^1 \phi \xi \, d\xi \right)^{-2/7}. \quad (4.22)$$

Two boundary conditions from the shape of the nose impose that the height is zero,  $\phi(1) = 0$ , and that there is no flux through the nose. This gives

$$\phi = \frac{4\sqrt{2}}{7}(1-\xi)^{1/2}, \quad \phi_\xi = -\frac{2\sqrt{2}}{7}(1-\xi)^{-1/2} \quad \text{as} \quad \xi \rightarrow 1, \quad (4.23)$$

respectively. The system is solved numerically using MATLAB's BVP4c solver. The numerical solution gives  $\eta_N = 0.889$ . Figure 4.2 plots the similarity solution for the turbulent model where either (a) bending or (b) gravity is dominant. Figure 4.2b suggests there is a singularity at the origin, with  $\phi$  diverging at  $\xi \rightarrow 0$ . In practice this singularity is resolved by the importance of bending in a boundary layer near the origin. This can be seen by comparing the two contributions to the pressure gradient in equation (4.13). For radial extents  $r \leq l_{eg}$ ,  $\xi \leq l_{eg}/R(t)$ , the contribution to the pressure gradient due to elasticity becomes comparable to the hydrostatic pressure gradient, and hence the gravity similarity solution is no longer valid. This is shown schematically by the vertical dashed line on figure 4.2b for some time  $t = t_b$ .

The similarity solution gives aspect ratio for this turbulent model when gravity is dominant

$$h \sim \left( \frac{Q^2}{Re_c g} \right)^{1/4} R^{-1/4}, \quad (4.24)$$

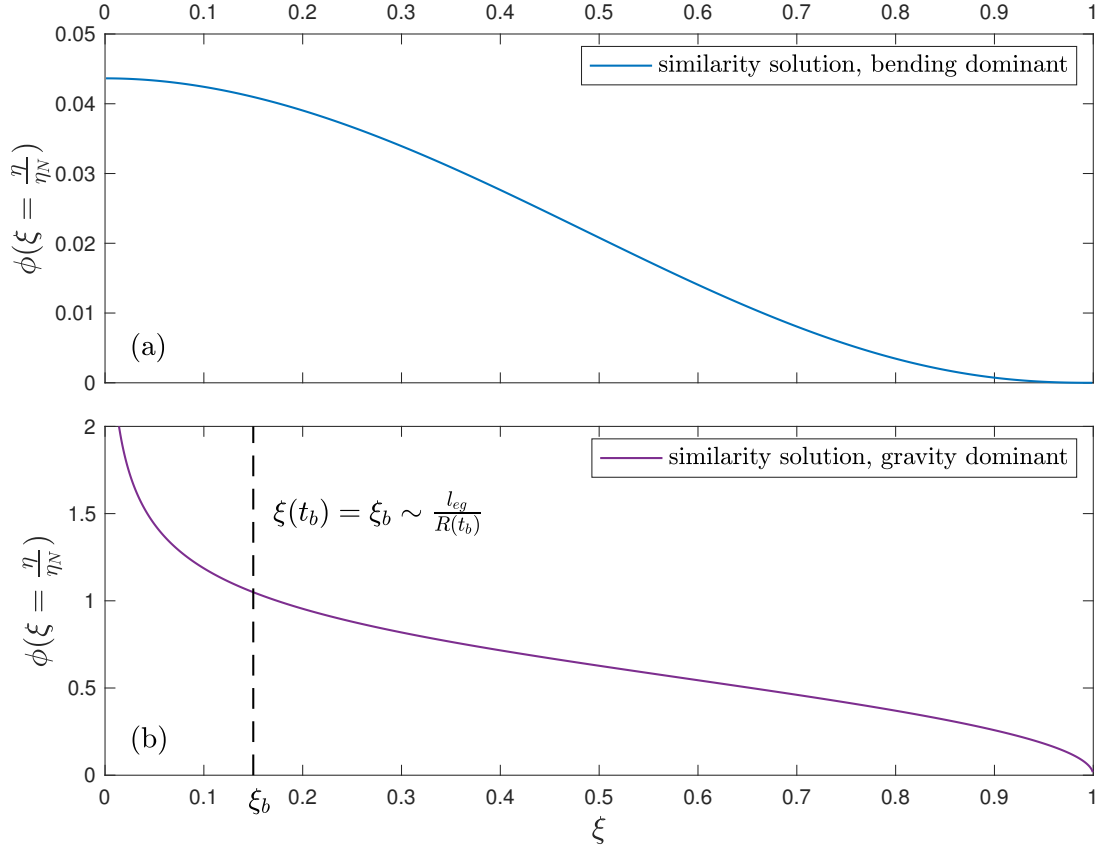


**Figure 4.2: Similarity solutions for the turbulent model.** Plot of scaled height  $\phi$  against scaled extent  $\xi$  in (a) the bending and (b) the gravity dominant regimes. Vertical dashed line in (b) denotes the bending boundary layer near the origin,  $\xi \leq \xi_b$ , at some time  $t = t_b$ .

where the prefactor here may be determined by considering the bending boundary layer at the origin, as mentioned above.

### 4.3 Laminar control

The transition from turbulent to laminar flow depends on the physics at the front. In particular, the physical processes of a pre-wetted film (Lister et al., 2013), or a fluid lag when either viscosity or adhesion (fracture toughness) are dominant (chapter 3; Hewitt et al., 2015) are considered at the front. For each of the three different laminar regimes, the transition from turbulent to laminar propagation is assessed and the resulting aspect ratio when the intrusion is laminar controlled.

To assess the transition from turbulent, bulk control to laminar, front controlled propagation, the height and length scales at the front are considered. First suppose there is a laminar region at the front of the intrusion with height and length scales,  $\delta$  and  $\varepsilon$  respectively, governed by the physics at the front, either a pre-wetted film or a fluid lag. These height and length scales are functions of the speed of the front  $\dot{R}$ . Using the height scale  $\delta$  and the speed of the front, a local Reynolds number can be constructed,  $Re = \rho\dot{R}\delta/\mu$ , which may be compared with the critical Reynolds number  $Re_c$ . This is equivalent to evaluating the inequality (4.10), where the dominant pressure drop is examined. To determine the local Reynolds number, an expression for  $\dot{R}$  needs to be chosen. The analysis proceeds as follows. If the front velocity  $\dot{R}$  is given by the turbulent solution, and as a consequence the tip region is found to be laminar,  $Re \ll Re_c$ , then this is inconsistent. Hence, there is a transition to laminar control. Alternatively, if as a consequence  $Re \gg Re_c$  then the flow is, self consistently, turbulence controlled. Note, however, if the front velocity is given by the laminar solution, this would give a laminar tip by construction.

For all three physical processes at the front, the height  $\delta$  and length  $\varepsilon$  scales of the laminar front region are determined where viscous dissipation is greatest. The timescale  $t_c$  is calculated when the local Reynolds number is equal to the critical Reynolds number  $Re_c$  at the front, and the power-law approach of the Reynolds number at the front is derived. Finally, in each case the aspect ratio of the intrusion when it is laminar controlled is determined.

Section 4.2.3 describes the turbulent model in both the bending and gravity regimes. By differentiating the radius as a function of time, expressions for the front speed  $\dot{R}$  can be found,

$$\dot{R} = 0.62 \left( \frac{Re_c B Q^2}{\rho} \right)^{1/11} t^{-7/11} \quad \text{for } R \ll l_{eg}, \quad (4.25a)$$

$$\dot{R} \sim (Re_c g Q^2)^{1/7} t^{-3/7} \quad \text{for } R \gg l_{eg}. \quad (4.25b)$$

These velocities are used in the following sections when calculating the local Reynolds number at the front.

When the majority of viscous dissipation occurs over a laminar region at the front, the remainder of the intrusion can be assumed to be quasi-static with negligible horizontal pressure gradients (either with turbulent or laminar flow). When bending is dominant, this gives  $p = B\nabla^4 h = \text{const}$ , and hence interior curvature

$$\kappa_{int} = \frac{24Qt}{\pi R^4} \quad \text{for } R \ll l_{eg}. \quad (4.26)$$

To calculate the rate of front propagation, as in section 3.2.2, the curvature of the nose region,  $\delta/\varepsilon^2$ , is then matched onto this interior curvature to give expressions for the radial extent and vertical height of the intrusion.

In a similar manner, when gravity begins to play a role, the pressure is given by  $p = B\nabla^4 h + \rho gh = \text{const}$ . This gives a flat topped profile with region of  $\mathcal{O}(l_{eg})$  where bending and gravity balance. The interior curvature is given by assuming a disc of uniform height,

$$\kappa_{int} = \frac{Qt}{\pi l_{eg}^2 R^2} \quad \text{for } R \gg l_{eg}. \quad (4.27)$$

This interior curvature is then matched onto the curvature from the pure bending region at the tip.

To assess the aspect ratio for each laminar regime, the expressions for the bulk radius and height of the intrusion are rearranged to eliminate time, and hence get an expression of the form  $h \sim R^m$ .

### 4.3.1 Pre-wetted film model

Following Lister et al. (2013) and Hewitt et al. (2015), consider a pre-wetted film of thickness  $h_0$  in the far field. This serves as a good example to demonstrate the methodology used in considering the transition from turbulent to laminar flow as the equations are continuous at the fracture front, unlike a fluid lag where a jump in physics needs to be carefully considered. In the laminar regime, for  $Re \rightarrow 0$ , equation (4.8) reduces to equation (3.2),

$$\frac{\partial h}{\partial t} = \frac{1}{12\mu} \frac{1}{r} \frac{\partial}{\partial r} \left( r h^3 \frac{\partial p}{\partial r} \right) \quad \text{where} \quad \frac{\partial p}{\partial r} = \frac{\partial}{\partial r} (B\nabla^4 h + \rho gh). \quad (4.28)$$

Height and length scales at the front are found by moving into the steady reference frame  $h = \delta F[\xi \equiv (r - R)/\varepsilon]$ . When bending is dominant this gives

$$- \dot{R} F' = \frac{B\delta^3}{12\mu\varepsilon^5} (F^3 F^V)', \quad (4.29)$$

where prime denotes differentiation with respect to  $\xi$ . A natural height scale at the tip is the height of the pre-wetting film,  $\delta = h_0$ . The horizontal peeling length scale is therefore

$$\varepsilon = \left( \frac{Bh_0^3}{12\mu\dot{R}} \right)^{1/5}, \quad (4.30)$$

the viscous length scale over which the pre-wetted film in the far field can be felt (Lister et al., 2013). In the bending regime, taking pressure gradient scaling  $\frac{\partial p}{\partial r} \sim \frac{B\delta}{\varepsilon^5}$ , inequality (4.10) becomes

$$\frac{\rho B \delta^4}{18 \mu^2 \varepsilon^5} < \mathcal{O}(Re_c), \quad (4.31)$$

which after substituting in the height and length scales  $\delta$  and  $\varepsilon$  defined above, where  $\dot{R}$  is given by turbulent flow when bending is dominant (equation 4.25a), gives timescale

$$t_c = \left( \frac{\rho^{10} B h_0^{11} Q^2}{\mu^{11} Re_c^{10}} \right)^{1/7}. \quad (4.32)$$

This timescale  $t_c$  defines when the Reynolds number at the front, in terms of the laminar height and length scales, is equal to the critical Reynolds number  $Re_c$ . For times  $t > t_c$  there is a transition to front, laminar controlled propagation. To demonstrate, the local Reynolds number  $Re = \rho \dot{R} \delta / \mu$  can be evaluated and compared with the critical Reynolds number,

$$\frac{Re}{Re_c} = \frac{\rho \dot{R} \delta}{\mu Re_c} \sim \frac{\rho h_0}{\mu Re_c} \left( \frac{Re_c B Q^2}{\rho} \right)^{1/11} t^{-7/11} = \left( \frac{\rho^{10} B h_0^{11} Q^2}{\mu^{11} Re_c^{10}} \right)^{1/11} t^{-7/11} = \left( \frac{t}{t_c} \right)^{-7/11}. \quad (4.33)$$

As in Lister et al. (2013), matching the interior curvature, (4.26), onto the curvature at the nose,  $\delta/\varepsilon^2 \sim (\mu \dot{R}/B h_0^{1/2})^{2/5}$ , gives expressions for radial extent and vertical height,

$$R(t) = 1.31 \left( \frac{B^2 h_0 Q^5}{\mu^2} \right)^{1/22} t^{7/22}, \quad h(0, t) = 0.55 \left( \frac{\mu^2 Q^6}{B^2 h_0} \right)^{2/22} t^{8/22}, \quad (4.34)$$

where prefactors are determined numerically (for details see Lister et al., 2013). Rearranging gives aspect ratio

$$h = 0.40 \left( \frac{\mu^2 Q^2}{B^2 h_0} \right)^{1/7} R^{8/7}. \quad (4.35)$$

If the radial extent of the blister is greater than the elastogravity length scale, in a region of  $\mathcal{O}(l_{eg})$  from the front there is a balance between bending and gravity. Right at the fracture front, there is a bending boundary layer where the majority of the viscous dissipation occurs. Hence the height and length scales over which to evaluate the laminar flow are the same as in the bending dominant case,

$$\delta = h_0, \quad \varepsilon = \left( \frac{B h_0^{1/2}}{12 \mu \dot{R}} \right)^{1/5}. \quad (4.36)$$

As gravity becomes important in the interior, turbulent flow in the interior is dominated by gravity with front velocity given by equation (4.25b). Substituting these height and length

scales and front velocity into inequality (4.10) gives timescale

$$t_c = \left( \frac{\rho^7 g h_0^7 Q^2}{\mu^7 Re_c^6} \right)^{1/3}. \quad (4.37)$$

Evaluating the local Reynolds number compared with the critical Reynolds number gives a power-law approach to laminar flow at the front,

$$\frac{Re}{Re_c} \equiv \frac{\rho \dot{R} \delta}{\mu Re_c} \sim \frac{\rho h_0}{\mu Re_c} (Re_c g Q^2)^{1/7} t^{-3/7} = \left( \frac{\rho^7 g h_0^7 Q^2}{\mu^7 Re_c^6} \right)^{1/7} t^{-3/7} = \left( \frac{t}{t_c} \right)^{-3/7}. \quad (4.38)$$

The bulk radial extent and vertical height scales are found by matching the interior curvature for the gravity dominant regime, (4.27), onto the curvature at the nose,  $\delta/\varepsilon^2 \sim (\mu \dot{R}/B h_0^{1/2})^{2/5}$ , and imply

$$R(t) = 0.40 \left( \frac{\rho g}{B} \right)^{5/24} \left( \frac{B^2 h_0 Q^5}{\mu^2} \right)^{1/12} t^{7/12}, \quad h(0, t) = 2.02 \left( \frac{B}{\rho g} \right)^{5/12} \left( \frac{\mu^2 Q}{B^2 h_0} \right)^{1/6} t^{-1/6}, \quad (4.39)$$

with aspect ratio,

$$h = 1.55 \left( \frac{\mu^4 B Q^4}{(\rho g)^5 h_0^2} \right)^{1/14} R^{-2/7}, \quad (4.40)$$

where  $\mathcal{O}(1)$  prefactors are determined by numerically solving the boundary layer problem at the nose (Lister et al., 2013).

### 4.3.2 Fluid lag model, viscosity dominant

In chapter 3, an alternative regularisation of a fluid lag, or vapour tip, between the fluid front and fracture front is discussed (Hewitt et al., 2015). As the aperture of the fracture decreases to zero at the fracture front, viscous stresses diverge. The resulting large negative pressure gradient at the tip is limited by the vapour pressure of the fluid, and hence the fracture travels faster (at the elastic wave speed in the solid) while the fluid lags behind. This physical process leads to the emergence of a fluid lag that regularises the dynamics at the tip. The fluid lag has a reduced pressure  $\sigma$  and length  $L = R_N - R_F$ , where  $R_F$ ,  $R_N$  are the fluid and fracture fronts respectively. For the remainder of this chapter, the fluid front is written as  $R \equiv R_F$  to be consistent with notation.

Height and length scales at the front are found by moving into the steady reference frame  $h = \delta F[\xi \equiv (r - R)/\varepsilon]$ , giving the first balance at the front. A second balance at the tip comes from matching the curvature at the fluid-vapour interface (see section 3.2.2). These

scales give

$$\dot{R} \simeq \frac{B\delta^3}{\mu\varepsilon^5}, \quad \frac{\delta}{\varepsilon^2} \simeq \frac{\sigma\varepsilon^2}{B} \quad \Rightarrow \quad \varepsilon = \left( \frac{\mu B^2 \dot{R}}{\sigma^3} \right)^{1/7}, \quad \delta = \left( \frac{\mu^4 B \dot{R}^4}{\sigma^5} \right)^{1/7}. \quad (4.41)$$

The height and length scales  $\delta$  and  $\varepsilon$  give the region over which matching to the reduced pressure  $\sigma$  in the vapour tip is felt, and hence the length scales over which viscous dissipation is dominant and limits the propagation.

Substituting these height and length scales into inequality (4.10), with pressure gradient scaling  $\frac{\partial p}{\partial r} \sim \frac{B\delta}{\varepsilon^5}$  and front velocity (4.25a), gives a timescale for transition to laminar control

$$t_c = \left( \frac{\rho^6 B^2 Q^2}{\mu^3 Re_c^6 \sigma^5} \right)^{1/7}. \quad (4.42)$$

Equivalently, writing the local Reynolds number as  $Re = \rho \dot{R} \delta / \mu$  and comparing with critical Reynolds number,  $Re_c$ , gives

$$\frac{Re}{Re_c} \equiv \frac{\rho \dot{R} \delta}{\mu Re_c} \sim \frac{\rho}{\mu Re_c} \left( \frac{\mu^4 B}{\sigma^5} \right)^{1/7} \left( \frac{Re_c B Q^2}{\rho} \right)^{1/7} t^{-1} = \left( \frac{t}{t_c} \right)^{-1}. \quad (4.43)$$

Matching the interior curvature for the bending dominant regime (4.26) onto the curvature at the fluid-vapour interface ( $\delta/\varepsilon^2 \sim \sigma\varepsilon^2/B$ ; equation (3.14)), gives expressions for the bulk radial extent and vertical height for the the fluid lag regime when viscosity is dominant,

$$R(t) = 1.29 \left( \frac{B^3 Q^7}{\mu^2 \sigma} \right)^{1/30} t^{3/10}, \quad h(0, t) = 0.57 \left( \frac{\mu^2 \sigma Q^8}{B^3} \right)^{1/15} t^{2/5}, \quad (4.44)$$

with, after some rearrangement, an aspect ratio given by

$$h = 0.40 \left( \frac{\mu^2 \sigma Q^2}{B^3} \right)^{1/9} R^{4/3}. \quad (4.45)$$

The prefactors in these relationships are determined numerically by using a travelling wave solution at the nose, as described in section 3.2.2.

In the gravity regime, when the radial extent of the intrusion is much greater than the elastogravity length scale, there is a balance between bending and gravity over a region of  $\mathcal{O}(l_{eg})$  near the front. As in the case with the pre-wetted film, the majority of the dissipation occurs over the bending boundary at the fracture front. Hence the height and length scales over which to evaluate the local Reynolds number are same as in the bending dominant case,

given by equation (4.41). As gravity is dominant in the interior, the front velocity is now given by turbulent model (4.25b). Substituting these height and length scales, together with the front velocity, into inequality (4.10) gives a timescale for transition to laminar flow at the front,

$$t_c = \left( \frac{\rho^{49} g^{11} B^7 Q^{22}}{\mu^{21} Re_c^{38} \sigma^{35}} \right)^{1/33}. \quad (4.46)$$

Equivalently, writing the local Reynolds number as  $Re = \rho \dot{R} \delta / \mu$  and comparing with critical Reynolds number  $Re_c$  gives

$$\frac{Re}{Re_c} \equiv \frac{\rho \dot{R} \delta}{\mu Re_c} \sim \frac{\rho}{\mu Re_c} \left( \frac{\mu^4 B}{\sigma^5} \right)^{1/7} (Re_c g Q^2)^{11/49} t^{-33/49} = \left( \frac{t}{t_c} \right)^{-33/49}. \quad (4.47)$$

To get an expression for the radial extent and vertical height of the intrusion, the interior curvature for the gravity dominant regime (4.27) is matched onto the curvature at the fluid-vapour interface ( $\delta/\varepsilon^2 \sim (\mu^2 \dot{R}^2 \sigma / B^3)^{1/7}$ ; equation (3.14)) to give

$$R(t) = 0.37 \left( \frac{\rho g}{B} \right)^{7/32} \left( \frac{B^3 Q^7}{\mu^2 \sigma} \right)^{1/16} t^{9/16}, \quad h(0, t) = 2.33 \left( \frac{B}{\rho g} \right)^{7/16} \left( \frac{\mu^2 \sigma Q}{B^3} \right)^{1/8} t^{-1/8}, \quad (4.48)$$

with aspect ratio

$$h = 1.87 \left( \frac{\mu^4 \sigma^2 B Q^4}{(\rho g)^7} \right)^{1/18} R^{-2/9}, \quad (4.49)$$

where the calculation of the prefactors is described in section 3.2.2.

### 4.3.3 Fluid lag model, adhesion dominant

When the peeling length scale of the nose region is much smaller than a critical length scale  $L_C = (B\kappa/\sigma)^{1/2}$ , where  $\kappa$  is the constant curvature at the fracture front imposed by adhesion (3.1), the adhesion energy begins to dominate, as described in section 3.2.2. There is a transition to adhesion dominant spreading where the curvature at the front is set by the fracture curvature. This is equivalent to the ‘toughness dominant’ regime as described by Bungler and Cruden (2011).

Moving into a steady reference frame with the front,  $h = \delta F[\varepsilon \equiv (r - R)/\varepsilon]$ , where the pressure gradient now scales with the jump in pressure  $\mathcal{O}(\sigma)$  across the fluid-vapour interface. This, along with the curvature set by adhesion, gives two scalings for the height and length

scales of the laminar tip region dominated by adhesion,

$$\dot{R} \simeq \frac{\delta^2 \sigma}{\mu \varepsilon}, \quad \frac{\delta}{\varepsilon^2} \simeq \kappa \quad \Rightarrow \quad \varepsilon = \left( \frac{\mu \dot{R}}{\sigma \kappa^2} \right)^{1/3}, \quad \delta = \left( \frac{\mu^2 \dot{R}^2}{\sigma^2 \kappa} \right)^{1/3}. \quad (4.50)$$

These length scales describe the region over which the pinning by adhesion at the fracture front is felt. Substituting these height and length scales into inequality (4.10), with pressure gradient scale  $\frac{\partial p}{\partial r} \sim \frac{\sigma}{\varepsilon}$  and front velocity (4.25a), gives

$$t_c = \left( \frac{\rho^{28} B^5 Q^{10}}{\mu^{11} Re_c^{28} \sigma^{22} \kappa^{11}} \right)^{1/35}. \quad (4.51)$$

Equivalently, writing the local Reynolds number  $Re = \rho \dot{R} \delta / \mu$  and comparing with the critical Reynolds number gives

$$\frac{Re}{Re_c} \equiv \frac{\rho \dot{R} \delta}{\mu Re_c} \sim \frac{\rho}{\mu Re_c} \left( \frac{\mu^2}{\sigma^2 \kappa} \right)^{1/3} \left( \frac{Re_c B Q^2}{\rho} \right)^{5/33} t^{-35/33} = \left( \frac{t}{t_c} \right)^{-35/33}. \quad (4.52)$$

Matching the interior curvature for the bending dominant regime (4.26) onto the fracture curvature ( $\delta/\varepsilon^2 \sim \kappa$ ), gives

$$R(t) = 1.66 \left( \frac{Q}{\kappa} \right)^{1/4} t^{1/4}, \quad h(0, t) = 0.35 (\kappa Q)^{1/2} t^{1/2}, \quad (4.53)$$

with aspect ratio

$$h = 0.125 \kappa R^2. \quad (4.54)$$

If the radial extent is greater than the elastogravity length scale, gravity becomes dominant in the interior. On length scales of  $\mathcal{O}(l_{eg})$  at the tip, there is a balance between bending and gravity with curvature imposed by the fracture condition at the front. As in the bending dominant case, the majority of the viscous dissipation occurs over the bending boundary layer at the fracture front, with scales given by equation (4.50). Gravity is dominant in the interior, hence the front velocity is given by the turbulent model in the gravity regime (4.27). Substituting these height and length scales, and front velocity into inequality (4.10), gives a timescale for transition to laminar control,

$$t_c = \left( \frac{\rho^{21} g^5 Q^{10}}{\mu^7 Re_c^{16} \sigma^{14} \kappa^7} \right)^{1/15}. \quad (4.55)$$

Equivalently, writing the local Reynolds number  $Re = \rho \dot{R} \delta / \mu$  and comparing with the critical Reynolds number gives

$$\frac{Re}{Re_c} \equiv \frac{\rho \dot{R} \delta}{\mu Re_c} \sim \frac{\rho}{\mu Re_c} \left( \frac{\mu^2}{\sigma^2 \kappa} \right)^{1/3} (Re_c g Q^2)^{5/21} t^{-5/7} = \left( \frac{t}{t_c} \right)^{-5/7}. \quad (4.56)$$

Finally, the radial extent and vertical height scales of the flow are found by matching the interior curvature for the gravity dominant regime (4.26) onto the fracture curvature, giving

$$R(t) = 0.56 \left( \frac{\rho g}{B} \right)^{1/4} \left( \frac{Q t}{\kappa} \right)^{1/2}, \quad h(t) = \left( \frac{B \kappa^2}{\rho g} \right)^{1/2} = \text{constant}. \quad (4.57)$$

## 4.4 Discussion

### 4.4.1 Summary of models

Table 4.1 summarises the timescale  $t_c$  for transition from turbulent, bulk control to laminar, front controlled propagation for the series of models discussed in 4.3.1–4.3.3. In addition it gives the power-law approach of the local Reynolds number, showing that when gravity begins to play a role, the rate of approach decreases, i.e. the magnitude of the exponents decrease.

Table 4.1 also summarises the aspect ratios in both the turbulent (section 4.2.3) and laminar regimes, when either bending or gravity are important. In particular it demonstrates that in the bending regime (column 1) the aspect ratios show a positive correlation. However, when gravity begins to play a role (column 2) the aspect ratios show a negative correlation (with the exception of the adhesion dominant or toughness model which gives a constant thickness; Bungler and Cruden, 2011). Taking representative values for the Young's modulus  $E = 10^{11}$  Pa, Poisson's ratio  $\nu = 0.25$ , and density of the intruded magma  $\rho = 2800 \text{ kg m}^{-3}$ , together with the depth of intrusion  $d = 50 - 2000$  m (Bunger and Cruden, 2011), gives a wide range of elastogravity length scales,  $l_{eg} \sim 0.45 - 7.1$  km. For the large mafic sills shown in figure 4.1 the length of  $L \sim 1-10$ 's km suggests that both bending and gravity are comparable, and play a role in the propagation.

If gravity were the dominant mechanism for spreading, the models considered thus far all give a negative correlation in the aspect ratios (with the exception of the toughness regime where the height is constant), see table 4.1, column 2. As noted by Bungler and Cruden (2011), one of the key assumptions in these models is that all parameters (volume flux, density,

	bending	gravity
turbulent (sec. 4.2.3)	a) $h = 0.26 \left( \frac{\rho Q^2}{Re_c B} \right)^{1/4} R^{3/4}$	$h \sim \left( \frac{Q^2}{Re_c g} \right)^{1/4} R^{-1/4}$
pre-wetting (sec. 4.3.1)	a) $h = 0.40 \left( \frac{\mu^2 Q^2}{B^2 h_0} \right)^{1/7} R^{8/7}$ b) $t_c = \left( \frac{\rho^{10} B h_0^{11} Q^2}{\mu^{11} Re_c^{10}} \right)^{1/7}$ c) $Re/Re_c \sim (t/t_c)^{-7/11}$	$h = 1.55 \left( \frac{\mu^4 B Q^4}{(\rho g)^5 h_0^2} \right)^{1/14} R^{-2/7}$ $t_c = \left( \frac{\rho^7 g h_0^7 Q^2}{\mu^7 Re_c^6} \right)^{1/3}$ $Re/Re_c \sim (t/t_c)^{-3/7}$
fluid lag (sec. 4.3.2)	a) $h = 0.40 \left( \frac{\mu^2 \sigma Q^2}{B^3} \right)^{1/9} R^{4/3}$ b) $t_c = \left( \frac{\rho^6 B^2 Q^2}{\mu^3 Re_c^6 \sigma^5} \right)^{1/7}$ c) $Re/Re_c \sim (t/t_c)^{-1}$	$h = 1.87 \left( \frac{\mu^4 \sigma^2 B Q^4}{(\rho g)^7} \right)^{1/18} R^{-2/9}$ $t_c = \left( \frac{\rho^{49} g^{11} B^7 Q^{22}}{\mu^{21} Re_c^{38} \sigma^{35}} \right)^{1/33}$ $Re/Re_c \sim (t/t_c)^{-33/49}$
toughness (sec. 4.3.3)	a) $h = 0.125 \kappa R^2$ b) $t_c = \left( \frac{\rho^{28} B^5 Q^{10}}{\mu^{11} Re_c^{28} \sigma^{22} \kappa^{11}} \right)^{1/35}$ c) $Re/Re_c \sim (t/t_c)^{-35/33}$	$h = \left( \frac{B \kappa^2}{\rho g} \right)^{1/2} = \text{constant}$ $t_c = \left( \frac{\rho^{21} g^5 Q^{10}}{\mu^7 Re_c^{16} \sigma^{14} \kappa^7} \right)^{1/15}$ $Re/Re_c \sim (t/t_c)^{-5/7}$

**Table 4.1: Aspect ratios and timescale for transition to laminar flow.** Row 1: Turbulent flow when bending (column 1) or gravity (column 2) is dominant. Row 2: Viscous laminar flow with a pre-wetting film when bending (column 1) or gravity (with a bending nose region; column 2) is dominant. Rows 3–4: as in Row 2 but for either a fluid lag dominated by viscosity or toughness, respectively. In each regime, if applicable, a) the aspect ratio for a constant flux  $Q$ , b) the timescale for transition to laminar control, and c) the power-law approach of the local Reynolds number at the front.

viscosity, bending stiffness and fracture toughness) remain constant in time. However, this is not necessarily likely in many geological settings. For example, consider the volume flux into an intrusion. Although direct measurements of volume flux into an ongoing intrusion are difficult to obtain, there are some studies that indirectly measure the volume flux by post processing. A recent study by Smittarello et al. (2019) used continuous Global Navigation Satellite System (cGNSS) data to model the deformation at Piton de la Fournaise. By looking at the best fit deformation pattern, they obtained a volume flux curve which showed an initially high flux of  $Q \sim 900 \pm 100 \text{ m}^3 \text{ s}^{-1}$  decreasing to  $Q \sim 30 \pm 10 \text{ m}^3 \text{ s}^{-1}$  over the course of a couple of hours. This typifies the large temporal variation in volume flux possible. Another obvious variation in volume flux to consider is with the final emplaced volume, reflecting that larger intrusions typically have larger input fluxes.

To quantitatively consider the change to the aspect ratios if the input flux can vary in time or vary with final emplaced volume, the volume flux may be written as

$$Q = Q_0(t/T_0)^a(V_f/V_0)^b, \quad (4.58)$$

where  $V_f$  is the final emplaced volume,  $Q_0$ ,  $T_0$  and  $V_0$  are constants with dimensions of flux, time and volume respectively, and  $a$  and  $b$  are constant exponents. The aim is to investigate whether a positive correlation in the aspect ratios, e.g.  $h \sim R^m$  where  $m > 0$ , can be found for coefficients  $-1 < a \leq 0$  and  $0 \leq b < 1$ . To do so first  $b = 0$  is assumed with  $a$  varying. The aspect ratio is then taken to be either  $h = \text{constant}$ ,  $h \sim R^{1/2}$  (motivated by mafic sills data; figure 4.1) or  $h \sim R$ . The resulting value of  $a$  then determines if a varying flux is sufficient to explain the trend in the data. The same method is then repeated taking  $a = 0$  and letting  $b$  vary.

To demonstrate, consider the case of the turbulent flow when gravity is dominant, see table 4.2, row 1, column 2. The flux is written as in equation (4.58), where the final volume scales as  $V_f \sim hR^2$ . Substituting these expressions for  $Q$  and  $V_f$  into the height and length scales given by (4.18), and rearranging gives an aspect ratio in terms of parameters  $a$  and  $b$ ,

$$h \sim \left[ \left( \frac{1}{Re_{cg}} \right)^{a+1} \frac{Q_0^2}{T_0^{2a} V_0^{2b}} \right]^{\frac{1}{2(a-b+2)}} R^{\frac{3a+4b-1}{2(a-b+2)}}. \quad (4.59)$$

When the flux is only a function of time,  $b = 0$ , setting the exponent to be  $m = \left[ 0, \frac{1}{2}, 1 \right]$  gives  $a_{b=0} = \left[ \frac{1}{3}, \frac{3}{2}, 5 \right]$ . In the same vein, when the flux is only a function of final emplaced volume  $V_f$ ,  $a = 0$ , comparing the exponents gives  $b_{a=0} = \left[ \frac{1}{4}, \frac{3}{5}, \frac{5}{6} \right]$ . These values of  $a$  and  $b$  suggest that a volume (or, equally, size) dependent flux is required to achieve a positive correlation between thickness and extent. The same procedure is repeated when the propagation is

	bending	gravity
turbulent (sec. 4.2.3)	$h \sim \left[ \left( \frac{\rho}{RecB} \right)^{a+1} \frac{Q_0^2}{T_0^{2a} V_0^{2b}} \right]^{\frac{1}{2(a-b+2)}} R^{\frac{7a+4b+3}{2(a-b+2)}}$ $a_{b=0} = \left[ -\frac{3}{7}, -\frac{1}{6}, \frac{1}{5} \right] \quad \checkmark$ $b_{a=0} = \left[ -\frac{3}{4}, -\frac{1}{5}, \frac{1}{6} \right] \quad \checkmark$	$h \sim \left[ \left( \frac{1}{Recg} \right)^{a+1} \frac{Q_0^2}{T_0^{2a} V_0^{2b}} \right]^{\frac{1}{2(a-b+2)}} R^{\frac{3a+4b-1}{2(a-b+2)}}$ $a_{b=0} = \left[ \frac{1}{3}, \frac{3}{2}, 5 \right]$ $b_{a=0} = \left[ \frac{1}{4}, \frac{3}{5}, \frac{5}{6} \right] \quad \checkmark$
pre-wetting (sec. 4.3.1)	$h \sim \left[ \left( \frac{\mu^2}{B^2 h_0} \right)^{a+1} \frac{Q_0^2}{T_0^{2a} V_0^{2b}} \right]^{\frac{1}{5a-2b+7}} R^{\frac{4(3a+b+2)}{5a-2b+7}}$ $a_{b=0} = \left[ -\frac{2}{3}, -\frac{9}{19}, -\frac{1}{7} \right] \quad \checkmark$ $b_{a=0} = \left[ -2, -\frac{9}{10}, -\frac{1}{6} \right]$	$h \sim \left[ \left( \frac{\mu^4 B}{(\rho g)^5 h_0^2} \right)^{a+1} \frac{Q_0^4}{T_0^{4a} V_0^{4b}} \right]^{\frac{1}{2(5a-2b+7)}} R^{\frac{2(a+2b-1)}{5a-2b+7}}$ $a_{b=0} = [1, -11, -3]$ $b_{a=0} = \left[ \frac{1}{2}, \frac{11}{10}, \frac{3}{2} \right] \quad \checkmark$
fluid lag (sec. 4.3.2)	$h \sim \left[ \left( \frac{\mu^2 \sigma}{B^3} \right)^{a+1} \frac{Q_0^2}{T_0^{2a} V_0^{2b}} \right]^{\frac{1}{7a-2b+9}} R^{\frac{4(4a+b+3)}{7a-2b+9}}$ $a_{b=0} = \left[ -\frac{3}{4}, -\frac{3}{5}, -\frac{1}{3} \right] \quad \checkmark$ $b_{a=0} = \left[ -3, -\frac{3}{2}, -\frac{1}{2} \right]$	$h \sim \left[ \left( \frac{\mu^4 \sigma^2 B}{(\rho g)^7} \right)^{a+1} \frac{Q_0^4}{T_0^{4a} V_0^{4b}} \right]^{\frac{1}{2(7a-2b+9)}} R^{\frac{2(a+2b-1)}{7a-2b+9}}$ $a_{b=0} = \left[ 1, -\frac{13}{3}, -\frac{11}{5} \right]$ $b_{a=0} = \left[ \frac{1}{2}, \frac{13}{10}, \frac{11}{6} \right] \quad \checkmark$
toughness (sec. 4.3.3)	$h = 0.125 \kappa R^2$	$h = \left( \frac{B \kappa^2}{\rho g} \right)^{1/2} = \text{constant}$

**Table 4.2: Aspect ratios for varying flux**  $Q = Q_0(t/T_0)^a(V_f/V_0)^b$ . Row 1: Turbulent flow when bending (column 1) or gravity (column 2) is dominant. Row 2: Viscous laminar flow with a pre-wetting film when bending (column 1) or gravity (with a bending nose region; column 2) is dominant. Rows 3–4: as in Row 2 but for either a fluid lag dominated by viscosity or toughness, respectively. Each regime gives the aspect ratio for varying flux  $Q = Q_0(t/T_0)^a(V_f/V_0)^b$ , the exponents  $a$  when  $b = 0$ , and the exponents  $b$  when  $a = 0$ ,  $h \sim R^m$  where  $m = \left[ 0, \frac{1}{2}, 1 \right]$ .

laminar with either a pre-wetting film or a fluid lag, table 4.2, columns 1 and 2, rows 2 and 3. When imposing the varying flux, it is assumed that  $-1 < a \leq 0$  and  $0 \leq b < 1$ ; where this is the case the exponent is in bold and marked with a tick.

#### 4.4.2 Mafic sills comparison

Thus far the analysis has focused on building a set of models that span a range of different regimes: turbulent or laminar flow; bending or gravity driven; pre-wetting, viscosity or toughness front conditions. The analysis in section 4.4.1 suggests that only a bending dominant model, or a gravity dominant model with input flux varying with the final emplaced volume gives an aspect ratio with a positive correlation, such that  $h \sim R^m$  where  $m > 0$ . The prefactors of these models are now compared with the mafic sills data to try to understand the physical mechanisms that play a role.

Bunger and Cruden (2011) compared the uniform thickness toughness model, section 4.3.3, with the mafic sills data and found the magnitude could be reproduced but not the general trend. However, in order to fit the data they required a fracture toughness for sills that was lower than that for laccoliths. In a similar manner, the models considered here are compared with the mafic sills data. The pre-wetting film model is neglected as, although it provides a useful mathematical example of how to treat elastic-plated gravity currents, there is no physical analogue in the case of magmatic intrusions. The viscosity dominated fluid lag model requires a characterisation of the reduced pressure  $\sigma$  at the front. This parameter is not well constrained and therefore the remainder of the discussion focuses on the turbulent model.

On figures 4.3a–b, the mafic sills data from figure 4.1 have been replotted. The different markers distinguish between the different lengths of intrusions as shown by the legend, with the dashed line showing the fit to all the mafic sills data and the dot-dashed line showing a fit to mafic sills with lengths  $1 \text{ km} < L < 110 \text{ km}$  only. Note, this intermediate range is chosen to ensure the intrusion lengths are large enough to feel the free surface (the thickness of the overburden is much smaller than the intrusion extent) but small enough to be considered as one connected intrusion. On figure 4.3c the final emplaced volume, assuming a disc-shaped geometry, is plotted against length. The solid black line shows the line of best fit  $V_f = 0.50 L^{2.5}$ , where the trend appears clearer than the  $T(L)$  data due to the larger weighting on the length  $L$  in the volume scaling,  $V_f \sim hL^2$ . For these lengths, the estimated final emplaced volumes span the range  $V_f \sim 10^7 - 10^{13} \text{ m}^3$  (see figure 4.3c).

The turbulent model in the bending dominant regime, with a constant volume flux, is first compared with the height and length scale data for the mafic sills. Physical parameters of

density  $\rho = 2800 \text{ kg m}^{-3}$ , viscosity  $\mu = 10^2 \text{ Pa s}$ , Young's modulus  $E = 10^{11} \text{ Pa}$  and Poisson's ratio  $\nu = 0.25$  are taken (Bunger and Cruden, 2011). For the other parameters a range of values are considered. As a range of sills are considered in the dataset, the depth of emplacement varies such that  $d = 50 - 2000 \text{ m}$ . For the critical Reynolds number a range  $Re_c = 10^2 - 10^3$  (Kavanagh et al., 2006) is also considered, however this range is due to uncertainty in the value of the Reynolds number when the transition to laminar flow occurs. Determining a volume flux is complicated by the lack of available measurements. Bunger and Cruden (2011) take a low estimate of  $Q \sim 1 \text{ m}^3 \text{ s}^{-1}$ , however fluxes as high as  $Q \sim 400 \text{ m}^3 \text{ s}^{-1}$  have been measured for dyke intrusions (Ágústsdóttir et al., 2016), with higher estimates of  $Q \sim 900 \text{ m}^3 \text{ s}^{-1}$  from modelling deformation due to sill emplacements (Smittarello et al., 2019). An estimate of  $Q = 10^2 \text{ m}^3 \text{ s}^{-1}$  is therefore taken. These input parameters give a range of aspect ratios. The turbulent model in the bending regime is shown by the green shaded region on figure 4.3a and demonstrates that this vastly underestimates the thickness of the sills in the data set. By increasing the flux to  $Q = 10^6 \text{ m}^3 \text{ s}^{-1}$ , shown by the yellow shaded region, with a low critical Reynolds number, the thickness versus length of the mafic sills data can be reproduced. For this higher value of the volume flux, the largest intrusions in the range  $1 \text{ km} < L < 110 \text{ km}$  with a volume of  $V \sim 10^{13} \text{ m}^3$  give an emplacement duration of  $t \sim 120$  days.

Table 4.2 suggests that a turbulent-gravity model with a volume flux varying with final emplaced volume,  $Q = Q_0(V_f/V_0)^{3/5}$ , also produces a positive correlation in the aspect ratio. However, a value of the prefactor  $Q_0V_0^{-3/5}$  needs to be chosen. Motivated by the volume flux required to reproduce the magnitude of the mafic sills data in the bending regime, a prefactor of  $Q_0V_0^{-3/5} = 0.016$  is chosen such that for the largest volume,  $V_f \sim 10^{13} \text{ m}^3$ , the flux is  $Q \sim 10^6 \text{ m}^3 \text{ s}^{-1}$ . For the smallest volume,  $V_f \sim 10^7 \text{ m}^3$ , this gives a flux of  $Q \sim 250 \text{ m}^3 \text{ s}^{-1}$ . Hence this gives an emplacement duration of between  $t \sim 10 \text{ hrs} - 120$  days. All other parameters are the same as in the constant volume flux case described above. Figure 4.3b plots this turbulent-gravity model with a varying volume flux against the mafic sills data, shown by the green shaded region, which again vastly underestimates the thickness of the intrusions. Increasing the volume flux by a factor of 10, shown by the yellow shaded region, does not reproduce the magnitude of the thickness. Note there is an unknown prefactor of  $\mathcal{O}(1)$  which may change this comparison slightly but not the conclusions drawn. Hence, from these two comparisons only the turbulent-bending model with a high volume flux and low critical Reynolds number can reproduce the thickness versus length mafic sills data set.

Cawthorn (2012) states that large igneous provinces typically accrue a volume of 1 million  $\text{km}^3$  in 1 million years, equivalently  $Q \sim 30 \text{ m}^3 \text{ s}^{-1}$ . However, there is much evidence to suggest that the volume flux may not be uniform but instead have periods of heightened activity. Using paleomagnetism, Moulin et al. (2011) showed that magmatic pulses in the

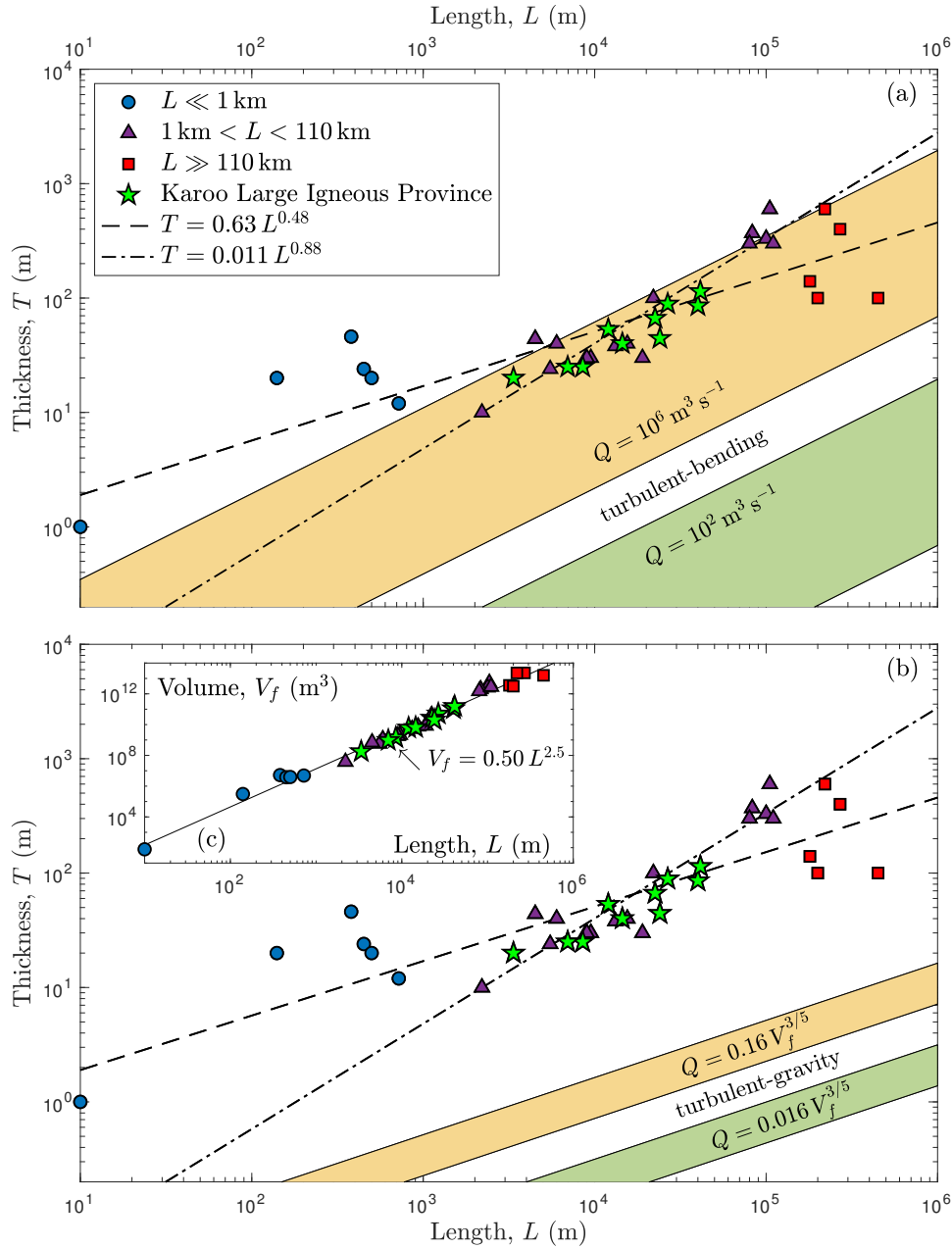


**Figure 4.3: Turbulent model plotted against mafic sills data from figure 4.1 (green circles).** Different symbols denote different lengths of intrusions. Dashed line denotes best fit to all data. Dot-dashed lines denote fit to data with lengths  $1 \text{ km} < L < 110 \text{ km}$ . Field data from the Karoo Large Igneous Province (South Africa) is marked by green stars. (a) The turbulent model in the bending regime for volume fluxes  $Q = (10^2, 10^6) \text{ m}^3 \text{ s}^{-1}$  is shown by the green and yellow shaded regions respectively. (b) The turbulent model in the gravity regime for volume fluxes varying with final emplaced volume  $Q = (0.016, 0.16) V_f^{3/5}$  is shown by the green and yellow shaded regions respectively. (c) Estimated final emplaced volume  $V_f$  against length  $L$  assuming a disc-shaped geometry. Line of best fit,  $V_f = 0.50 L^{2.5}$ , shown by the solid black line.

Karoo sills from the Karoo Large Igneous Province in South Africa may have exceeded the average eruption rates by three orders of magnitude. Measurements from this province are included in the mafic sills data set and are marked by the green stars on figures 4.3a–b. This evidence of intense activity is supported by studies of the Deccan traps (Chenet et al., 2009) that show a periodic increase in eruption rates above the average for the entire province by two orders of magnitude. Both of these observations support the comparison here that a volume flux several orders of magnitude higher than the average is required to reproduce the mafic sills data.

This analysis relies on comparing purely the maximum height and length scales of the intrusions and not the geometry. However, geological mapping of mafic sills often reveals disc shaped geometries (Chevallier and Woodford, 1999), suggesting gravity may be playing a role. The large discrepancy, therefore, between the turbulent model and the mafic sills data may point towards other physical mechanisms playing an important role. One possible factor may be that these measurements of mafic sills could be composite (one or more sills inside one another) or multiple (discrete and stacked) sills. The Karoo Large Igneous Province is known to be associated with multiple and composite sills (Cawthorn, 2012). Slement (2010) used borehole measurements from the Karoo sills to show that numerous thick sills have been inflated further by thinner sills, as seen from the distinct cores and quenched margins. In general, however, field evidence such as this is difficult to obtain meaning the thickness of single events is often overestimated, which may contribute towards reconciling the discrepancies between the turbulent model explored here and the field data for mafic sills.

One of the aims of the study in this chapter on turbulent emplacement, and the work in chapter 3, is to consider the dynamic emplacement of magmatic intrusions. The models considered thus far for a constant flux assume that the intrusion does not stop spreading, and that the aspect ratios given are for some time  $t$  rather than a final emplaced geometry. The introduction of an adhesion energy at the fracture front (or fracture toughness) is one way to reconcile this. At the end of chapter 3, section 3.5, the problem of when the volume flux ceases, and the intrusion spreads with a constant volume, is discussed. Here, the adhesion energy (or fracture toughness) stops the intrusion, with the same aspect ratio as for the dynamic case propagating in the adhesion dominant regime. Hence, comparing with the dynamic model in this case is justified as it is the same as the static, constant volume geometry.

Another way to reconcile this problem is to consider solidification processes. Thorey and Michaut (2016) modelled magmatic intrusions with a temperature dependent viscosity, where the temperature evolved from a hot to a cold viscosity as boundary layers between the surrounding rock and the flowing intrusion grew due to conductive cooling. The introduction

of solidification to a model with a fluid lag and a fracture criterion at the fracture front would lead to a set of physical processes that are capable of stopping an intrusion. Either the geometry would be determined by solidification processes or the fracture toughness at the front. This is analogous to the freezing of a viscous droplet, where either surface tension or solidification governs the final geometry of the droplet as a function of the volume of the droplet.

## 4.5 Concluding remarks

In this chapter, motivated by field evidence, I have outlined a simplified model to include both turbulent and laminar flow in an intrusion. This formulation allows the transition between these two regimes to be estimated for different physical processes at the front: a pre-wetted film or a fluid lag dominated by either viscosity or adhesion. This formulation also provides a wealth of propagation regimes and highlights how to transition between these regimes depending on where the majority of the viscous dissipation (or pressure drop) is found in the fluid. As a result, the intrusion may exhibit both turbulent flow in the interior and viscous flow at the tip, but the propagation may only be controlled by either turbulent or laminar processes depending on the the height and length scales of the laminar region at the front.

The extensive collection of models allowed comparisons to be made with field data for mafic sills from Cruden and McCaffrey (2006) and Cruden et al. (2017). In comparisons with the turbulent model I found that a volume flux several orders of magnitude higher than the average is required to reproduce the thickness of these intrusions, which may be supported by evidence of periods of intense volcanic activity leading to vast underestimates of the volume flux. An alternative explanation for the discrepancy in the comparison may be due to the formation of composite sill structures. However, there are many other factors which have been neglected from the study including the effects of solidification (Chanceaux and Menand, 2016) and inelastic deformation of the overburden (Scheibert et al., 2017), both of which may explain the final emplaced geometries seen in the field.

# Chapter 5

## Influence of topographic gradients on shallow magmatic intrusions: downslope evolution of an adhered, elastic-plated gravity current

---

### 5.1 Introduction

In chapter 3, I outlined a model of an idealised magmatic intrusion incorporating the requirement to fracture rock layers at the front of the intrusion in order for propagation to occur. Building on this work, in chapter 4, I considered the additional complexity of turbulent emplacement. In both cases the aim is to distil the various physical mechanisms at play to find the dominant contribution in the formation of magmatic intrusions seen in the field.

The models considered thus far assume that the geological strata, such as sedimentary bedding planes, or pre-existing weaknesses, into which the magma intrudes are horizontal and the topographic variation is negligible (that is, the thickness  $d$  of the overburden is uniform). However, this is often not the case; two recent examples demonstrate the influence of topographic gradients on shallow magmatic intrusions. In 2014 a dyke intruded from the Bárðabunga volcanic system in Iceland. Bárðabunga is a subglacial, basaltic volcano located in the northwestern corner of the Vatnajökull ice cap. Sigmundsson et al. (2014) showed that the dyke propagated laterally for  $\sim 45$  km along a path driven by pressure gradients, initially predominantly associated with the overlying topography. As the dyke moved away from the volcano towards more level topography, it began to propagate in a direction dictated by

the local stress field due to plate spreading. A second example is the 2007 eruption of the Piton de la Fournaise volcano, which forms the southeast part of La Réunion in the Indian Ocean. This eruption resulted in a large sill intrusion along the eastern flank of the volcano. The intrusion is proposed to have followed the topographic gradient of the flank along a parallel sloping pre-existing weakness or structural discontinuity (Froger et al., 2015). Both of these examples demonstrate how topographic gradients can influence the flow path and flow structure of intrusions. Previous modelling of the influence of topography on propagation has focused on specific events (e.g. Urbani et al., 2017) with the aim of replicating the known extent of the intrusion. In contrast, I take a more general approach and try to understand the effect of a linear topographic gradient, or sloping bedding plane, in order to develop a theoretical framework that is applicable to a broader range of geophysical locations.

To understand the influence of topographic gradients on the propagation of shallow magmatic intrusions, I first simplify the geometry. Consider a horizontal bedding plane where the overlying sedimentary strata thickness varies linearly, such that

$$d = d_0 - x \sin \theta, \quad (5.1)$$

where  $d_0$  is the thickness at the inlet at  $x = 0$ ,  $x$  denotes the coordinate in the direction of the topographic gradient, and  $\theta$  is a measure of the angle of inclination of the topography. To calculate the pressure  $p$ , I make the assumption that over the length of the intrusion, with characteristic length  $L$ , the change in thickness of the overburden is small compared with its thickness at any point,  $\sin \theta L/d, \sin^2 \theta L^2/d^2 \ll 1$ . This means that terms proportional to  $\partial B/\partial x, \partial^2 B/\partial x^2$ , where  $B$  is the bending stiffness, can be neglected, and the influence of topographic gradients only comes into driving the intrusion preferentially in the  $x$  direction,

$$p \simeq \frac{Ed_0^3}{12(1-\nu^2)} \nabla^4 h + \rho g(h-z) - \rho_s g x \sin \theta, \quad (5.2)$$

where, without loss of generality, I have neglected any constant pressure offsets. To investigate this problem is challenging experimentally as it requires creating different overburdens with varying thicknesses.

An alternative but related problem is that of a shallow magmatic intrusion propagating along a sloping bedding plane, with a parallel overburden of uniform thickness  $d$ . From Lister (1992), the pressure in this case is given by

$$p = B \nabla^4 h + \rho g(h-z) \cos \theta - \rho g x \sin \theta, \quad (5.3)$$

where bending stiffness  $B$  is constant, and  $\theta$  is the inclination of the bedding plane to the horizontal in the coordinate direction  $x$ , with axes aligned parallel and perpendicular to

the plane. Hence, under the assumptions that intrusions are sufficiently small that pressure gradients in the cross-slope direction are dominated by bending, and that  $\rho_s \sim \rho$ , then these two expressions for the pressure have the same structure: in both situations the main influence of the topographic gradient or sloping bedding plane is in the additional downslope component of gravity,  $g \sin \theta$ .

In this chapter, for simplicity, I will focus on this second problem, however, as shown above, this will also allow conclusions to be drawn on the influence of topographic gradients on shallow magmatic intrusions. I consider the evolution of an adhered, elastic-plated gravity current, where the substrate is inclined at a uniform angle  $\theta$  and the elastic sheet has uniform thickness  $d$ . This chapter is laid out as follows. In section 5.2, I describe the theoretical model. In section 5.3, I describe the results of the laboratory experiments conducted. And finally, in section 5.4, I discuss these results and the implications for the influence of topographic gradients, and sloping bedding planes, on shallow magmatic intrusions.

## 5.2 Theoretical model

### 5.2.1 Model setup

Following on from chapter 3, consider an elastic sheet of uniform thickness  $d$ , bending stiffness  $B = d^3 E / [12(1 - \nu^2)]$ , where  $E$  is Young's modulus, and  $\nu$  is Poisson's ratio. The elastic sheet is adhered to the plane with adhesion energy  $\Delta\gamma$  (see equation (3.1)), inclined at an angle  $\theta$  to the horizontal. Let  $x$  denote the downslope coordinate,  $y$  the cross-slope coordinate, and  $z$  the coordinate normal to the plane. The thickness of the fluid layer at time  $t$  is given by  $h(x, y, t)$ . Figure 5.1 shows the parameters of the model and the orientation of the axes parallel and perpendicular to the inclined plane.

In the lubrication approximation, the extent of the flow is assumed to be much larger than its thickness, and hence  $\nabla h \ll 1$ . The pressure and the velocity in the current are given by a balance between elastic and hydrostatic forces,

$$p = B\nabla^4 h + \rho g(h - z) \cos \theta - \rho g x \sin \theta, \quad (5.4)$$

$$\mathbf{u} = -\frac{1}{2\mu} z(h - z) \nabla p, \quad (5.5)$$

where  $\nabla = (\partial_x, \partial_y)$  (Lister, 1992). This is the same model setup as in section 3.2 with an additional term in the pressure due to the downslope component of gravity.

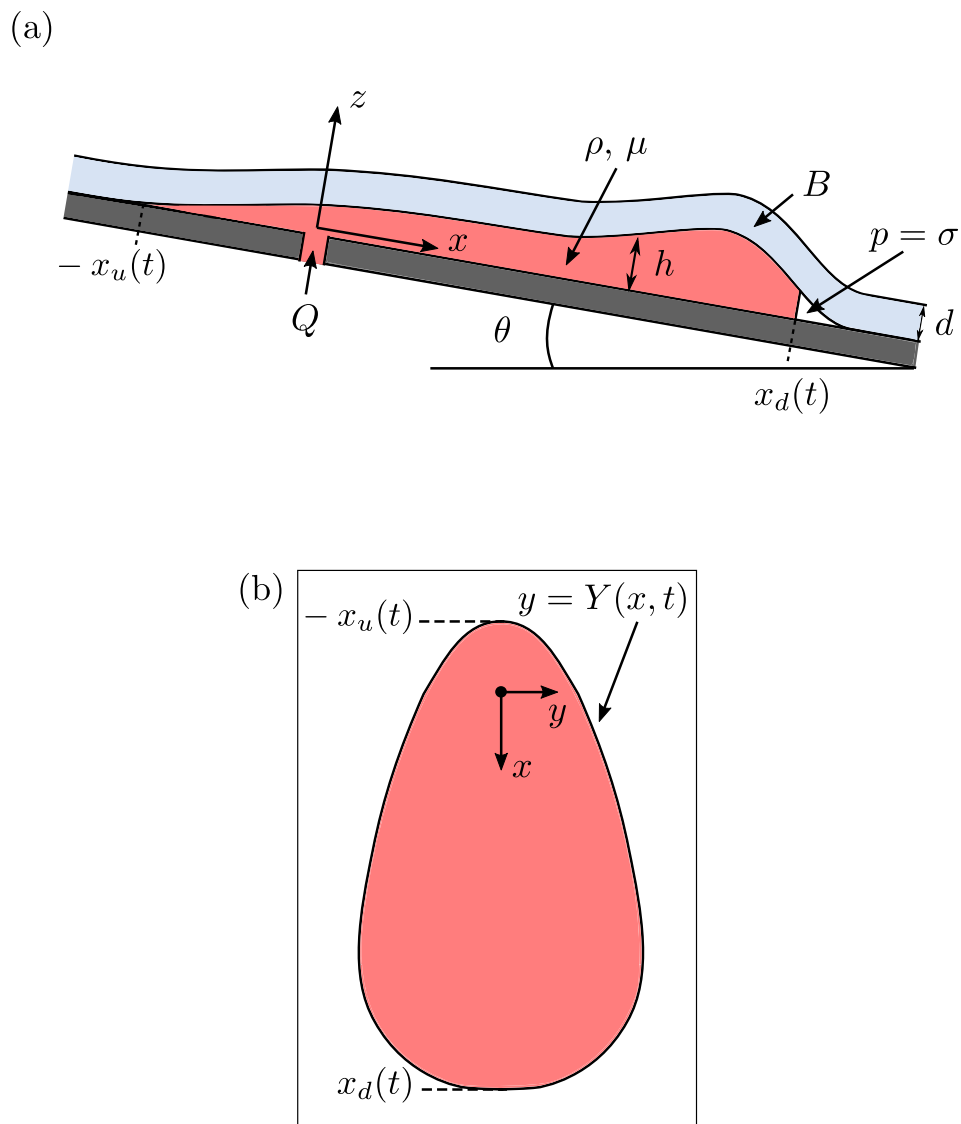


**Figure 5.1: Diagram of the theoretical and experimental setup with the parameters in the problem.** (a) Side view, and (b) plan view.

Depth integrating equation (5.5) and applying local mass conservation gives the governing equation for the rate of change of the height of the current  $h(x, y, t)$ ,

$$\frac{\partial h}{\partial t} = \frac{1}{12\mu} \left[ \nabla \cdot (h^3 \nabla (B \nabla^4 h)) + \rho g \cos \theta \nabla \cdot (h^3 \nabla h) - \rho g \sin \theta \frac{\partial h^3}{\partial x} \right], \quad (5.6)$$

along with global mass conservation

$$Qt = \int_{-x_u}^{x_d} \int_{-Y}^Y h \, dx dy, \quad (5.7)$$

where the perimeter of the flow is given by  $y = Y(x, t)$ , and  $Q$  is a constant volume flux. At the edge, boundary conditions of zero height and slope give

$$h = \mathbf{n} \cdot \nabla h = 0 \quad \text{at} \quad y = Y(x, t), \quad (5.8)$$

with symmetry conditions along the centerline

$$h_y = h_{yyy} = h_{yyyy} = 0 \quad \text{at} \quad y = 0. \quad (5.9)$$

In the case of a downslope gravity current, the status of the contact line, i.e. whether it is advancing, stationary or receding, depends on the position around the current (upslope or downslope of the injection hole) and on the volume constraint (constant, increasing or waning volume flux; Lister, 1992). In this problem of an adhered, elastic-plated gravity current, the elastic sheet cannot re-adhere once fractured. This is motivated by fractured bedding planes that provide pre-existing weaknesses or structural discontinuities for preferential magma propagation. As a result, in this model, receding contact lines cannot exist, instead all contact lines are either advancing or stationary. A curvature condition is imposed at the front due to the adhesion energy between the sheet and the plane, below which the contact line is stationary, above which the contact line is advancing. From section 3.2.2, the curvature condition at the fluid front is given by

$$\nabla^2 h \Big|_{y=Y(x,t)} = \begin{cases} \left[ \frac{2^3 (12\mu)^2 \sigma}{B^3} \right]^{1/7} (\mathbf{n} \cdot \dot{\mathbf{x}})^{2/7} \Big|_{y=Y(x,t)}, & \text{viscosity dominant,} \\ \kappa, & \text{adhesion dominant,} \end{cases} \quad (5.10)$$

where  $\dot{\mathbf{x}} = (\dot{x}, \dot{y})$ . Note, the second radius of curvature does not play a role in fracturing as the tip may be considered roughly two-dimensional for  $Y \gg h, d$ . At a stationary contact line, if the current begins to recede from the front, it leaves a fluid film behind. There are two types of film. If the extent of the film beyond the fluid front is large compared with the current size then it is effectively infinite. If, however, the extent of the film is small compared

with the size of the current, then it can be considered finite with compact support provided by the adhesion at the fracture front. This range of different contact line conditions leads to different dynamics at the front.

Initially, when the current is small, the downslope component of gravity is negligible and the problem reduces to that of an adhered, elastic-plated gravity current on a horizontal plane as discussed in chapter 3. Eventually the downslope component of gravity dominates the flow and hence propagation is predominantly downslope. The transition between axisymmetric, elasticity-dominant pressure-gradient control and downslope propagation occurs when these two contributions are comparable. Balancing these terms, a length scale over which the transition from horizontal to downslope flow occurs can be predicted. Taking the vertical, horizontal and time scales to be  $H$ ,  $L_d$  and  $T$ , and balancing the first and final terms on the right-hand side of equation (5.6), along with a scaling of global mass conservation (equation (5.7)), gives

$$\frac{BH^4}{12\mu L_d^6} \sim \frac{\rho g \sin \theta H^3}{12\mu L_d} \quad \text{and} \quad QT \sim HL_d^2. \quad (5.11)$$

The radial extent in the viscosity (equation (3.14)) and adhesion (equation (3.17)) dominant regimes gives a third scaling,

$$L_d \sim \begin{cases} \left[ \frac{Q^7 B^3}{(12\mu)^2 \sigma} \right]^{1/30} T^{3/10}, & \text{viscosity dominant,} \\ \left( \frac{24Q}{\pi\kappa} \right)^{1/4} T^{1/4}, & \text{adhesion dominant.} \end{cases} \quad (5.12)$$

Rearranging the three expressions gives a length scale for transition from axisymmetric to downslope propagation

$$L_d \sim \begin{cases} \left[ \frac{(12\mu)^2 \sigma B^6 Q^2}{(\rho g \sin \theta)^9} \right]^{1/33} & \text{for } \frac{R_C}{L_d} \equiv \left[ \frac{(12\mu)^2 \sigma Q^2 (\rho g \sin \theta)^2}{B^5 \kappa^{11}} \right]^{3/22} > 1 \quad (\text{viscosity dominant}), \\ \left( \frac{\kappa B}{\rho g \sin \theta} \right)^{1/3} & \text{for } \frac{R_C}{L_d} \equiv \left[ \frac{(12\mu)^2 \sigma Q^2 (\rho g \sin \theta)^2}{B^5 \kappa^{11}} \right]^{1/3} < 1 \quad (\text{adhesion dominant}). \end{cases} \quad (5.13)$$

The length scale  $R_C$  is the radial scale at which axisymmetric spreading transitions from viscosity dominant to adhesion dominant spreading, see section 3.2.2. When  $L_d < R_C$ , the transition from horizontal to downslope flow occurs when the axisymmetric spreading is controlled by viscous dissipation at the front (viscosity dominant spreading). When  $L_d > R_C$ , the transition from horizontal to downslope flow occurs when axisymmetric spreading is controlled by the adhesion energy at the front (adhesion dominant spreading).

### 5.2.2 Transient dynamics

Once the downslope component of gravity begins to take effect, a head forms at the nose of the current, migrating the initial volume downslope. Hewitt et al. (2015) investigated an elastic-plated gravity current from a line source (two-dimensional) with either a pre-wetting film or a fluid lag (zero adhesion energy at the fracture front). They showed that the front behaves as a travelling wave. Far from the injection point, the wave travels at a constant speed with a tail of uniform height behind. The study in this chapter considers an elastic-plated gravity current from a point source (three dimensional) with a fluid lag and a fracture criterion at the front. For the three-dimensional problem, the addition of cross-slope spreading and the fracture criterion at the front make the analysis complex. As such, laboratory experiments are utilised to map out the transient dynamics of the head, see section 5.3.3.

### 5.2.3 Steady state

The initial transient head fractures out to a distance  $y = \pm \max_t Y(x, t)$  as it travels downslope, dependent on the dynamics of the head. Once fractured, the contact line cannot retreat and hence leaves behind a fluid film. The continuing flux behind the transient head then flows into this film to form a steady-state channel. If the fluid spreads out to the fracture front, the extent is determined by the dynamics of the transient head, and hence is history dependent. The curvature at the fracture front is then between the fracture criterion and zero,  $0 < \nabla^2 h|_{y=\pm \max_t Y(x, t)} < \kappa$ . If, however, the flux behind the transient head is focused in some channel much smaller than the fracture front, then the extent is determined by the steady state, with a fluid film boundary condition at the front, and adhesion providing compact support in the far field. The curvature at the edge of the steady-state channel behind the transient head is zero due to the fluid film boundary condition there. In the following analysis the fracture front extent, determined by the transient head, is defined as  $Y_f(x) \equiv \max_t Y(x, t)$ , and the fluid front in the fluid film as  $Y_p = Y_p(x) < Y_f(x)$ .

Figures 5.2a–b shows two sample images from a constant flux experiment demonstrating the difference between fracture front  $Y_f$  and fluid film front  $Y_p$ . In figure 5.2a the current spreads axisymmetrically causing the fracture front to propagate out, indicated by the solid black line. In figure 5.2b the initial current begins to travel downslope to form the transient head. Behind the head, surrounding the injection point, there remains the fracture front from the initial axisymmetric spreading given by the solid black line. This marks out the extent of the fractured region. In this region there is the fluid-film front, given by the black dashed line, which indicates the front of the current, where between these two fronts there is a fluid film.

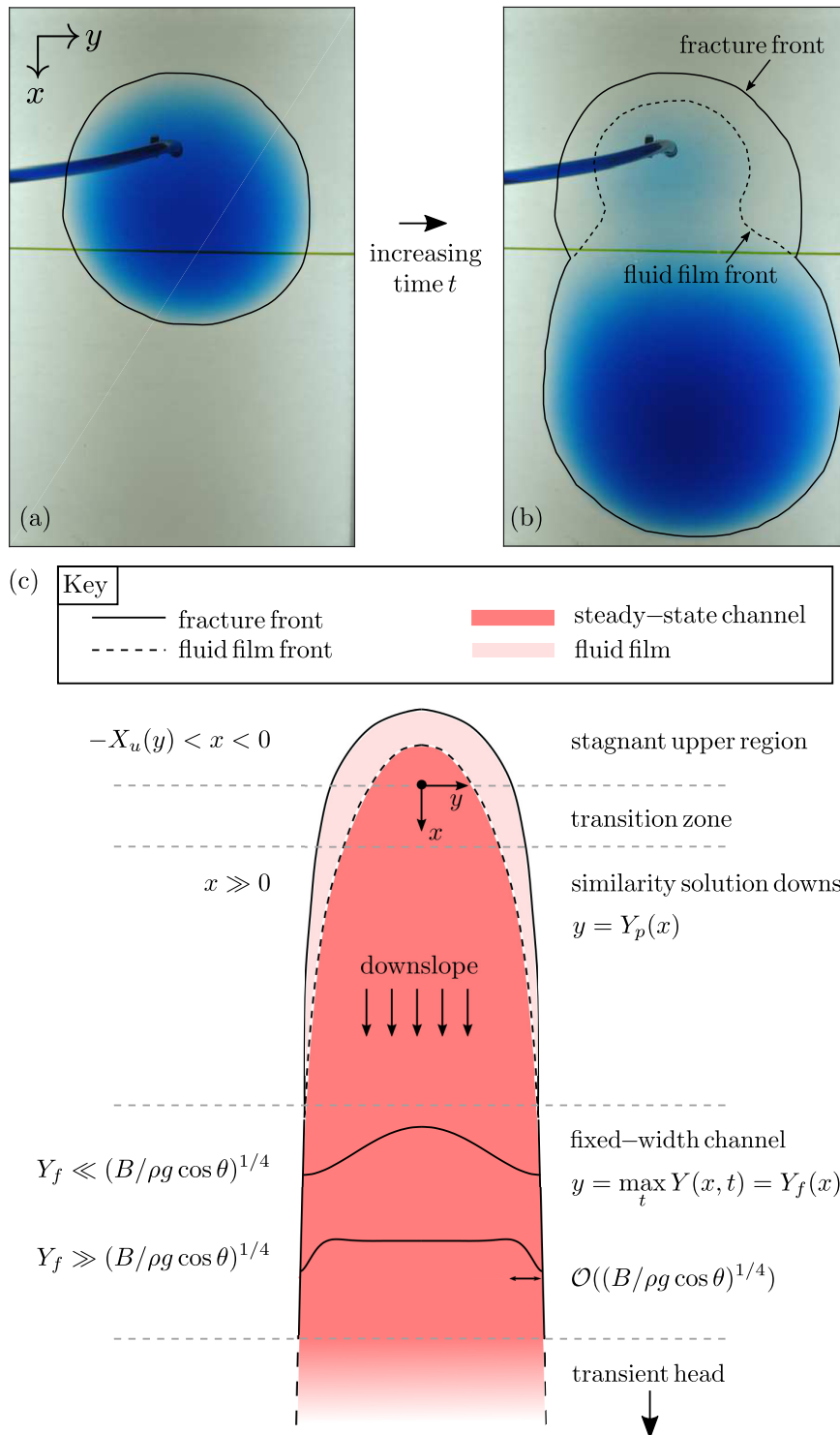


**Figure 5.2: Schematic of the transient head and the steady-state channel.** (a–b) Sample images from experiments showing the evolution of the fracture front and fluid-film front with increasing time  $t$ . (c) Schematic of the steady-state channel.

Motivated by the experimental results in section 5.3, the steady state behind the transient head can be split into three regions, see figure 5.2c. Upstream of the injection point, there is a stagnant region where the flux is zero. Here, there is a balance between elasticity and the downslope component of gravity, which determines the geometry. If the extent of the stagnant region is much smaller than the fracture front, then a fluid film boundary condition can be assumed with a fracture criterion providing compact support in the far field. However, if the stagnant region spreads out to the fracture front then it is pinned by the adhesion energy there. Hence, the boundary conditions depend on the transient head dynamics. Experimentally, this could also depend on any initial offset from the injection hole due to inhomogeneity in the adhesion energy. Downslope of the injection point, and away from the transient head, there is a balance between the flux cross-slope, dominated by pressure gradients due to elasticity, and the flux downslope, dominated by gravity. When the steady-state channel is smaller than the fracture front, this leads to a similarity solution downstream, independent of the transient head. When the steady-state channel reaches the fracture front, the extent is determined by the transient head dynamics with geometry due to inflation of a channel as a function of unknown extent  $y = \pm \max_t Y(x, t) = Y_f(x)$ . The rest of this section describes these three regions, separately, and introduces the boundary conditions which set the problem in detail.

### Upstream profile

The shape of the current upstream of the injection point tends to a steady state and so the flux is zero,  $q_x = q_y = 0$ . This steady state is given by a balance between elasticity and the downstream component of gravity (Hewitt et al., 2015; Lister, 1992). The steady profile is the solution to

$$B \frac{\partial}{\partial x} \nabla^4 h = \rho g \sin \theta \quad \text{for} \quad -X_u(y) < x < 0, \quad (5.14)$$

where  $X_u(y)$  is the upstream extent, with  $X_u(0) = x_u$  (see figure 5.1). This fifth-order equation and unknown upstream extent  $X_u$  is subject to boundary conditions at the front and along the centreline. At the front, if the current has receded from the fracture front, the film gives zero gradient perpendicular to the front and zero curvature. Note, the thickness of the film is assumed negligible when considering the steady state. If, however, the current remains at the fracture front, the gradient is zero but the curvature is between the fracture criterion and zero. This gives

$$h = \mathbf{n} \cdot \nabla h = 0, \quad 0 \leq \nabla^2 h < \kappa \quad \text{at} \quad x = -X_u(y). \quad (5.15)$$

Along the centreline, the current is symmetric in the cross-slope coordinate  $y$ ,

$$h_y = h_{yyy} \quad \text{at} \quad y = 0. \quad (5.16)$$

Finally, the upstream stagnant profile is matched onto the rest of the current at  $x = 0$  with continuity of  $h$  and its first four derivatives.

Immediately downstream of the injection point, there is a steady-state transition zone. Here the flux is constant,

$$\int_{-Y_{p,f}(x)}^{Y_{p,f}(x)} \mathbf{q} \cdot \hat{\mathbf{x}} \, dy = \text{const}, \quad \text{where} \quad \mathbf{q} = \frac{h^3}{12\mu} \left[ \rho g \cos \theta \nabla h + \nabla (B \nabla^4 h) \right] - \frac{\rho g \sin \theta}{12\mu} h^3 \hat{\mathbf{x}}, \quad (5.17)$$

where  $Y_{p,f}(x)$  is either the fluid front in the film, or the fracture front. Boundary conditions are then given by (5.15) and (5.16), and matching onto the upstream stagnant region. These equations need to be solved numerically to give a steady-state region around the injection point. In this model setup, the transient head is assumed to be in the far-field downslope.

### Similarity solution downstream

Far downstream from the injection point, with  $x$  large, and away from the head, there is a balance between the flux cross-slope dominated by pressure gradients due to elasticity and the flux downslope dominated by gravity. When the steady-state channel is smaller than the fracture front, boundary conditions of a film with compact support in the far field can be applied. Equation (5.6) then reduces to

$$B \frac{\partial}{\partial y} \left( h^3 h_{yyyyy} \right) - \rho g \sin \theta \frac{\partial}{\partial x} (h^3) = 0. \quad (5.18)$$

The flux is directed downslope, and by integrating equation (5.6) in  $x$  and  $y$ , the statement for global mass conservation can be approximated as a flux condition (Lister, 1992; Smith, 1973)

$$Q = \frac{\rho g \sin \theta}{12\mu} \int_{-Y_p(x)}^{Y_p(x)} h^3 \, dy. \quad (5.19)$$

This gives rise to a similarity solution of the form

$$h = \left[ \frac{(12\mu Q)^6}{B(\rho g \sin \theta)^5} \right]^{1/19} x^{-1/19} f(\eta) \quad \text{where} \quad \eta = \frac{y}{\left[ \frac{12\mu Q B^3}{(\rho g \sin \theta)^4} \right]^{1/19} x^{3/19}}. \quad (5.20)$$

Substituting into equation (5.18) gives an ordinary differential equation for  $f(\eta)$

$$\left(f^3 f_{\eta\eta\eta\eta}\right)_\eta = -\frac{3}{19}f^3 - \frac{3}{19}\eta(f^3)_\eta \quad \Rightarrow \quad \left(f^3 f_{\eta\eta\eta\eta}\right)_\eta = -\frac{3}{19}(\eta f^3)_\eta, \quad (5.21)$$

where subscripts denote differentiation with respect to  $\eta$ . Boundary conditions due to symmetry along the centreline and matching onto the film at the front give

$$f_\eta(0) = f_{\eta\eta}(0) = 0, \quad f(\eta_N) = f_\eta(\eta_N) = f_{\eta\eta}(\eta_N) = 0, \quad (5.22)$$

where  $\eta_N = y/Y_p(x)$ . Hence, equation (5.21) can be integrated to give the following profile in similarity space

$$f = \frac{1}{4560}(\eta_N^2 - \eta^2)^3 \quad \text{with} \quad \eta_N = \left(4560^3 \times \frac{230945}{131072}\right)^{1/19} \simeq 3.897, \quad (5.23)$$

where  $\eta_N$  is calculated by using the integral flux condition, equation (5.19). Dimensionally,  $h$  is therefore

$$h = \frac{1}{4560} \left[ \frac{(12\mu Q)^6}{B(\rho g \sin \theta)^5} \right]^{1/19} x^{-1/19} \left( \eta_N^2 - \frac{y^2}{Y_p^2} \right)^3, \quad (5.24)$$

with cross-slope extent

$$Y_p(x) \simeq 3.897 \left[ \frac{12\mu Q B^3}{(\rho g \sin \theta)^4} \right]^{1/19} x^{3/19}. \quad (5.25)$$

In this analysis, elasticity is assumed to dominate the pressure gradient in the cross-slope. However, for widths  $Y_p(x) \gg (B/\rho g \cos \theta)^{1/4}$  gravity begins to play a role. As elasticity becomes negligible, the problem reduces to the flow of a viscous gravity current down an inclined plane, with similarity solution described by Lister (1992).

### Fixed-width channel

If the flow spreads out to the fracture front, the extent is determined by the dynamics of the transient head, with  $y = \max_t Y(x, t) \equiv Y_f(x)$ . Assuming that  $h_{yy}|_{Y_f(x)} < \kappa$ , the front is pinned at the fracture front. Inflated by the downslope flux, a lateral balance between elastic and gravitational stress determines the geometry of the channel at each  $x$  for fixed channel width  $Y_f(x)$ . Assuming negligible pressure variation in the cross-slope, the geometry of the channel is a solution to the fourth-order equation

$$p(x) = \rho g x \sin \theta = B h_{yyyy} + \rho g \cos \theta h, \quad (5.26)$$

with downslope flux and boundary conditions along the centreline and fracture front

$$\frac{12\mu Q}{\rho g \sin \theta} = \int_{-Y_f(x)}^{Y_f(x)} h^3 dy, \quad (5.27)$$

$$h = h_y = 0 \quad \text{at} \quad y = \pm Y_f(x), \quad h_y = h_{yyy} = 0 \quad \text{at} \quad y = 0. \quad (5.28)$$

Again, although the flow spreads out to the fracture front set by the transient dynamics, the curvature is not necessarily at the fracture criterion. In the bending limit with  $Y_f \ll (B/\rho g \cos \theta)^{1/4}$ , solving the fourth-order equation gives the cross-slope height as a function width  $Y_f(x)$  set by the transient head,

$$h = \left( \frac{9009\mu Q}{512\rho g \sin \theta} \right)^{1/3} Y_f^{-1/3} \left( 1 - \frac{y^2}{Y_f^2} \right)^2. \quad (5.29)$$

If the fracture front continues to propagate cross-slope, gravity begins to play a role. The profile then has a flat-topped structure where bending is only important in a boundary layer at the front of  $\mathcal{O}((B/\rho g \cos \theta)^{1/4})$ . Figure 5.2c summarises these regions of the steady-state flow: stagnant upper region with a transition zone, the similarity solution downstream, and the fixed-width channel. A fluid film is shown in the case where the current recedes away from the fracture front.

## 5.3 Experiments

### 5.3.1 Experimental setup

A set of experiments, conducted to investigate the downslope fluid-driven fracturing of adhered elastica, consisted of injecting a viscous fluid beneath an elastic sheet adhered to a rigid substrate (see figure 5.1). These experiments were carried out in a similar manner to those reported in section 3.3, save that the substrate and sheet were inclined at angles  $\theta$  to the horizontal. Elastic sheets of polydimethylsiloxane (PDMS) were used with thicknesses  $d = 2.0 \pm 0.02 - 9.8 \pm 0.3$  mm, and bending stiffnesses  $B = 3.81 \times 10^{-2} - 1.80 \times 10^{-1}$  Pa m<sup>3</sup>. The PDMS sheet was manually adhered to a glass table using TUFFBond™ Adhesive Mount Film of thickness  $0.15 \pm 0.01$  mm. Vegetable oil was injected between the glass table and the composite PDMS and adhesive sheet. Injection was through a 5.5 mm diameter aperture and the flux was determined by measuring the mass of the injection reservoir using a mass balance. This section describes 12 experiments conducted in which the volume flux  $Q$ , angle of inclination  $\theta$ , and thickness of the elastic sheet  $d$  were varied.

Experiment (marker)	$Q$ ( $10^{-7} \text{ m}^3 \text{ s}^{-1}$ )	$\theta$ ( $\pm 0.1^\circ$ )	$d$ ( $10^{-3} \text{ m}$ )	$B$ ( $\text{Pa m}^3$ )	$T_C$ (s)
1 ●	1.83	26.7	$5.5 \pm 0.02$	$3.81 \times 10^{-2}$	0.65
2 ●	3.65	26.7	$5.5 \pm 0.02$	$3.81 \times 10^{-2}$	0.82
3 ●	7.12	26.7	$5.5 \pm 0.02$	$3.81 \times 10^{-2}$	1.02
4 ●	1.83	20.3	$5.5 \pm 0.02$	$3.81 \times 10^{-2}$	0.65
5 ●	3.57	20.3	$5.5 \pm 0.02$	$3.81 \times 10^{-2}$	0.81
6 ●	7.02	20.3	$5.5 \pm 0.02$	$3.81 \times 10^{-2}$	1.02
7 ●	1.79	15.4	$5.5 \pm 0.02$	$3.81 \times 10^{-2}$	0.78
8 ●	3.59	15.4	$5.5 \pm 0.02$	$3.81 \times 10^{-2}$	0.95
9 ●	7.00	15.4	$5.5 \pm 0.02$	$3.81 \times 10^{-2}$	1.19
10 ●	1.78	26.7	$9.8 \pm 0.3$	$1.80 \times 10^{-1}$	1.64
11 ●	1.77	26.7	$2.0 \pm 0.02$	$1.83 \times 10^{-3}$	0.17
12 n/a	1.76–13.1	26.7	$5.5 \pm 0.02$	$3.81 \times 10^{-2}$	n/a

**Table 5.1: Table of experimental parameters varied in experiments.** All other parameters remained fixed  $\rho = 920 \text{ kg m}^{-3}$ ,  $\mu = 0.072 - 0.083 \pm 0.004 \text{ Pa s}$ , where variation in viscosity is due to small temperature variations in the ambient temperature.

### 5.3.2 Calibration

To measure the lateral extent and topography of the blister, photographs were taken from below, perpendicular to the inclined glass sheet. To measure the vertical thickness of the blister, the dye attenuation technique was used. This technique uses the intensity of images, i.e. the amount of light that can pass through the dyed oil, to convert intensity to thickness measurements (e.g O’Keeffe et al., 2018). To do so, the experiments were calibrated against known thicknesses from a wedge with a linear taper filled with dyed oil, as shown in figures 5.3a–b. Plotting the intensity against thickness, figure 5.3c, then gives a calibration curve that can be used to calculate the thickness of the blister during the experiments. The error in the conducted experiments is characterised by the standard deviation of intensity measurements through the wedge at different points on the plane. Due to the saturation in light intensity with increasing thickness across the light sheet, the error in measurement increases for larger blister thicknesses. This is reflected in the uncertainties shown in the experimental results, which are discussed further in sections 5.3.3 and 5.4.

### 5.3.3 Results

Table 5.1 summarises the physical parameters in the experiments. In experiments 1–11, the volume flux  $Q$ , angle of inclination  $\theta$  and sheet thickness  $d$  were varied to investigate the transient head. In experiment 12, the volume flux was varied incrementally throughout the experiment to investigate the steady-state channel behind the transient head. For each

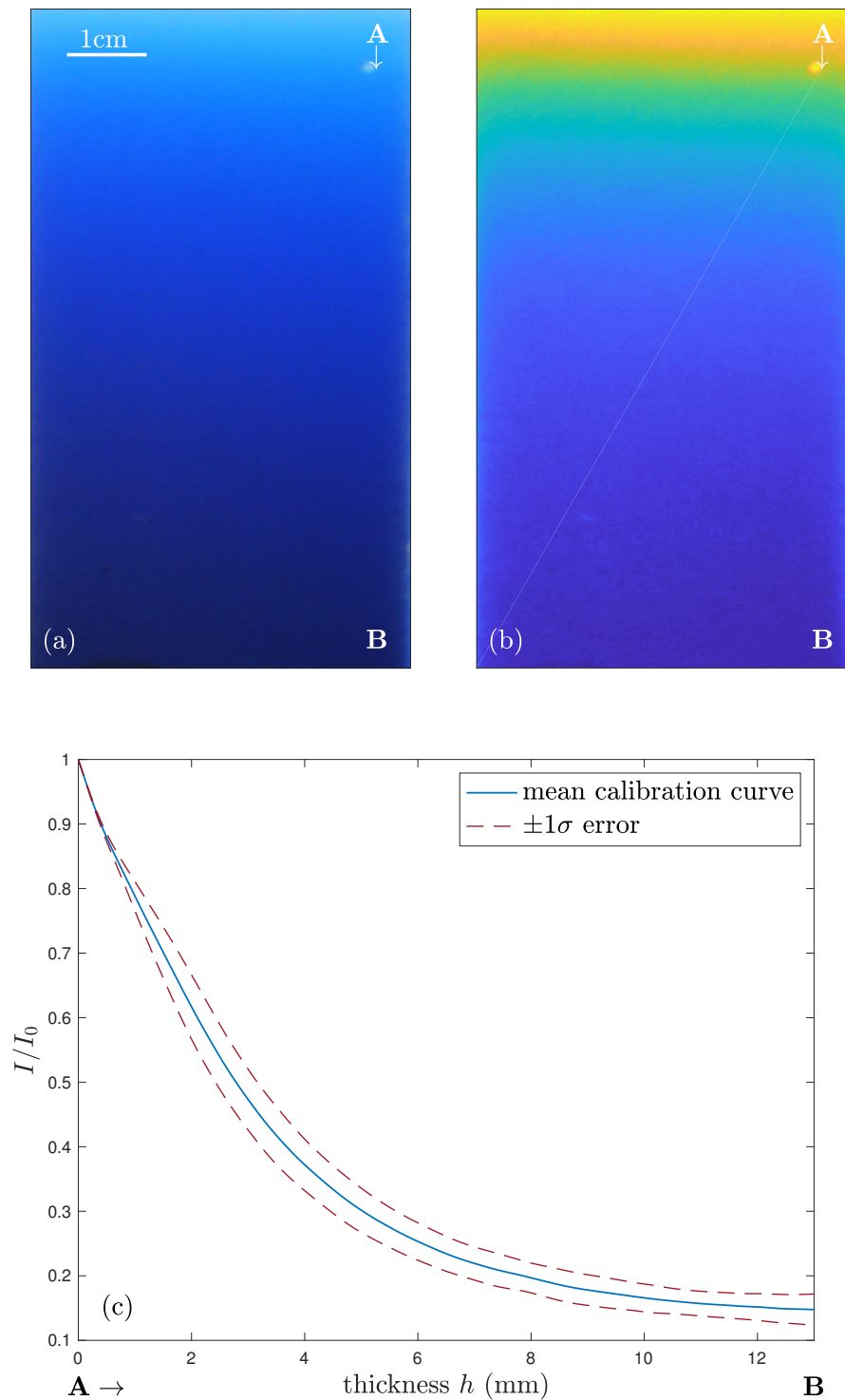


**Figure 5.3: Calibrating dye attenuation.** Image of calibration wedge; (a) raw image, (b) green channel isolated. (c) Graph of light intensity of the green channel scaled by the background intensity  $I/I_0$  against wedge thickness giving error bars due to variations in calibration curve across the inclined plane.

experiment the blister first spreads axisymmetrically until the effects of the downslope component of gravity become important. During this initial axisymmetric phase the experiments rapidly transition from viscosity to adhesion dominant spreading, with a transition timescale  $T_C \simeq 0.6 - 1.7$  s. This can equivalently be written as a length scale  $R_C \simeq 0.5 - 1.9$  cm. The length scale for transition from axisymmetric to downslope propagation is  $L_d \simeq 2.4 - 5.1$  cm, giving ratio  $R_C/L_d \simeq 0.2 - 0.5$ , see equation (5.13). Hence the experiments are anticipated to be in the adhesion dominant spreading regime when the transition to downslope propagation occurs.

Figure 5.4 plots images from experiment 1 (table 5.1) at uniform time intervals showing the injection and evolution of a downslope blister. Note that the feeder pipe and fluorescent line were removed during image processing and do not interfere with the results. Initially the spreading is axisymmetric (a–b) and can be described by the equations governing an adhered, elastic-plated gravity current on a horizontal plane (see chapter 3). When the extent of the current is large enough,  $x_d \gg L_d$ , the downslope component of gravity begins to dominate and an asymmetry emerges as there is a migration downslope (c–f). Eventually, this initial transient detaches from the injection position and travels downslope (g–h) leaving a fluid film which is re-inflated to form a steady-state channel (i). Figure 5.5a–i shows surface plots for this experiment (experiment 1, table 5.1) at the same time intervals. The surface is projected to show the cross-slope and downslope evolution of the blister. The analysis to follow will focus on the dynamics of the head structure and the static geometry of the steady-state channel behind.

### Transient head

As seen in figures 5.4 and 5.5, after the initial axisymmetric spreading, a transient head is formed that travels downslope and dominates the subsequent blister evolution. Figure 5.6a plots the downslope extent as a function of time for experiments 1–11 (table 5.1). Further downslope, the head reaches a constant velocity, shown by the dashed lines which demonstrate a linear fit to the extent versus time at the end of each experiment. Figures 5.6b–c plot this velocity  $\dot{x}_d$  against volume flux  $Q$  and angle of inclination  $\theta$ , respectively. The colours of data points refer to experiments 1–11 in table 5.1, see legend in figure 5.6a. The different symbols collate experiments with the same volume flux or angle of inclination indicated by the dashed lines (see caption for details). As the flux and angle of inclination increase, the downslope velocity increases because the advection downslope increases. As the bending stiffness increases, the downslope velocity decreases, as shown by the arrow on figure 5.6c. This is because as the bending stiffness increases, as in the axisymmetric case, the height

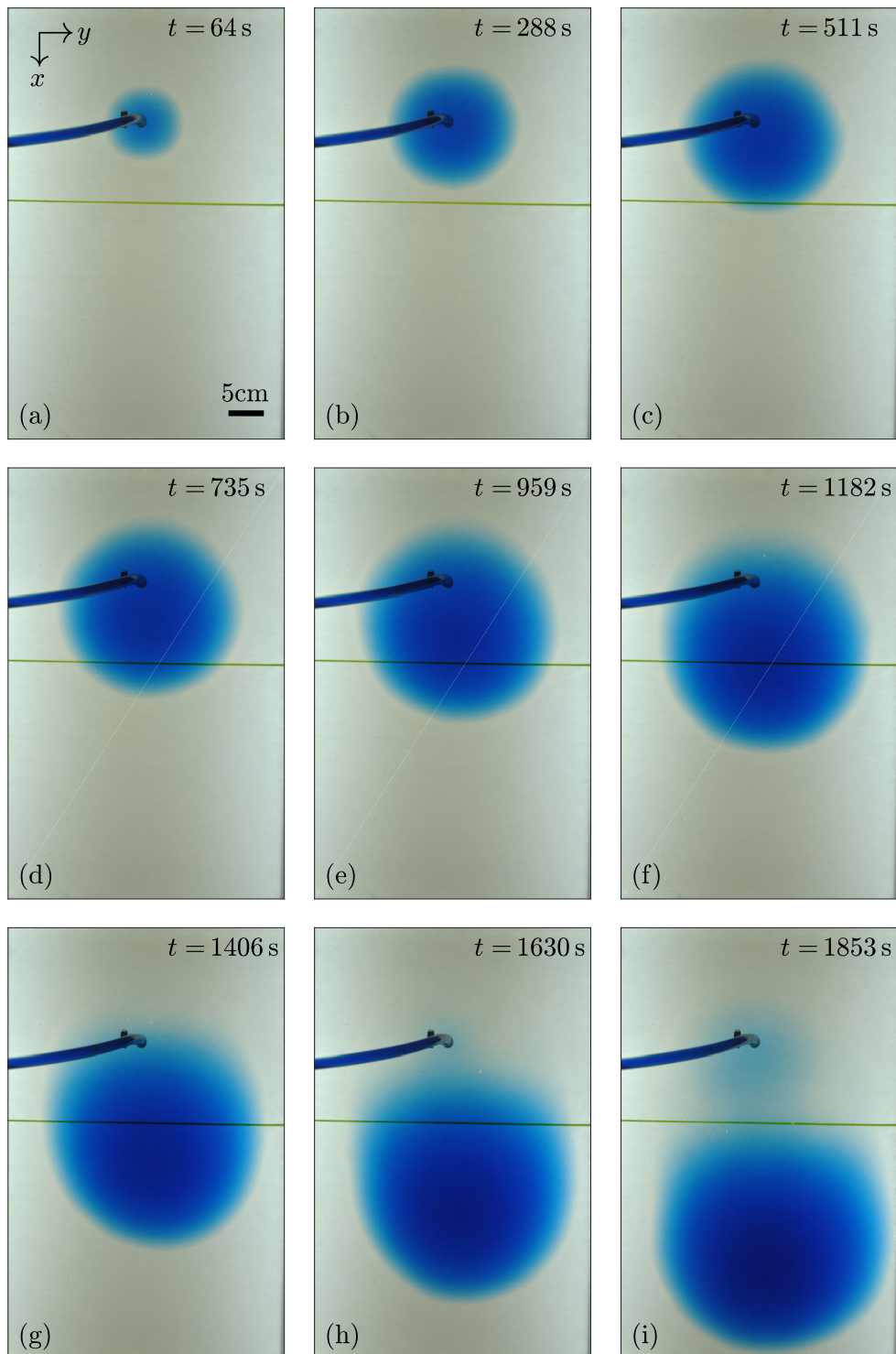


**Figure 5.4:** Images of experiment 1 (table 5.1). Images are at uniform time intervals, see legend.

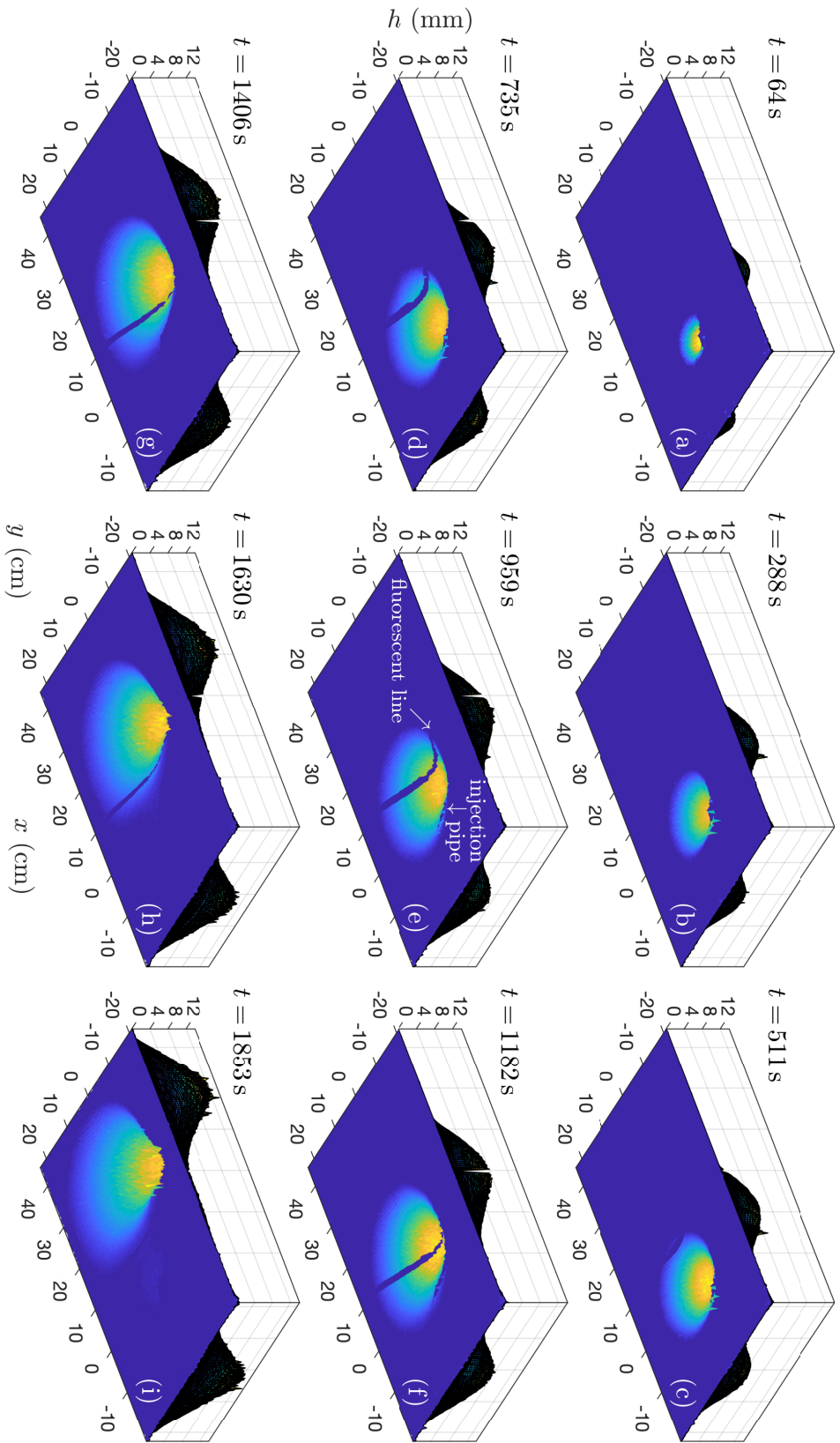


**Figure 5.5: Surface plots of experiment 1 (table 5.1).** Surface plots are at uniform time intervals as in figure 5.4, see legend. The feeder pipe and fluorescent line, highlighted in (e), have been removed from the image processing.

scales decrease and the lateral extents increase. This increases in the aspect ratio of the blister including the length scales at the tip and hence increases the viscous dissipation there.

An estimate of downslope velocity in the steady-state channel behind the transient head can be found dividing the volume flux  $Q$  by the average area of the channel after the transient head has passed through. This gives a range of velocities  $\sim 2.1 - 5.2 \times 10^{-3} \text{ m s}^{-1}$  for experiments 1-11. This velocity is an order of magnitude higher than the downslope velocity  $\dot{x}_d$  suggesting that the transient head is being fed by the channel behind. Crucially, this is the converse of what is found in the two-dimensional case. Hewitt et al. (2015) showed that for two-dimensional systems the depth-averaged speed of the channel and the front speed were equal, with the head represented by a travelling wave.

Figures 5.7a–c shows the geometry of the head. Figure 5.7a plots the downslope evolution of a cross-section at  $y = 0$  for experiment 1, with profiles taken at time intervals of  $\sim 60$  s. As the transient head travels downslope, an asymmetry starts to develop, with a tail emerging behind. The extent of the maximum of the head is denoted as  $x_{max}$ , with height  $h_0$ . The maximum points  $(x, z) = (x_{max}, h_0)$  are marked as black circles with the dashed line showing the linear increase in height downslope, whilst the downslope extent travels at a constant speed.

In figure 5.7b the downslope profiles for times  $t > 1500$  s are translated into the travelling reference frame of the front, with the blister thickness scaled by  $h_0$  and the downslope extent scaled by  $x_d - x_{max}$ , the distance between the front and maximum of the head. The profiles collapse well onto a universal curve for late times, or equivalently large distances away from the injection point. To compare different experiments, this final collapsed profile is plotted for experiments 1-6, 10 and 11 on figure 5.7c, with colours defined in table 5.1. Note, experiments 8, 9 and 10 have been omitted as the dye saturated the oil before the end of the experiment so maximum point  $(x_{max}, h_0)$  could not be identified. For all of the experiments with bending stiffness  $B = 3.81 \times 10^{-2} \text{ Pa m}^3$ , the downslope profiles collapse onto a universal curve, shown by the central curve. The two profiles that do not collapse are for an increased and decreased bending stiffness, experiments 10 and 11 respectively. They suggest a transition between bending and tensional regimes where the inflation geometry moves from a quartic to quadratic profile.

Figure 5.8a plots the evolution of the outline of experiment 1, cross-section through  $z = 0$ , showing the migration cross-slope and downslope. The fluorescent line and injection pipe were removed from the images before processing. In the experiments the injected dye concentration was tuned to optimise measurement of the transient head evolution, therefore the detection of the upslope extent was difficult due to the low dye intensity. Hence, at late times there is a lot of scatter in detection of the blister outline for  $x < 0$  so we focus on the downslope extent

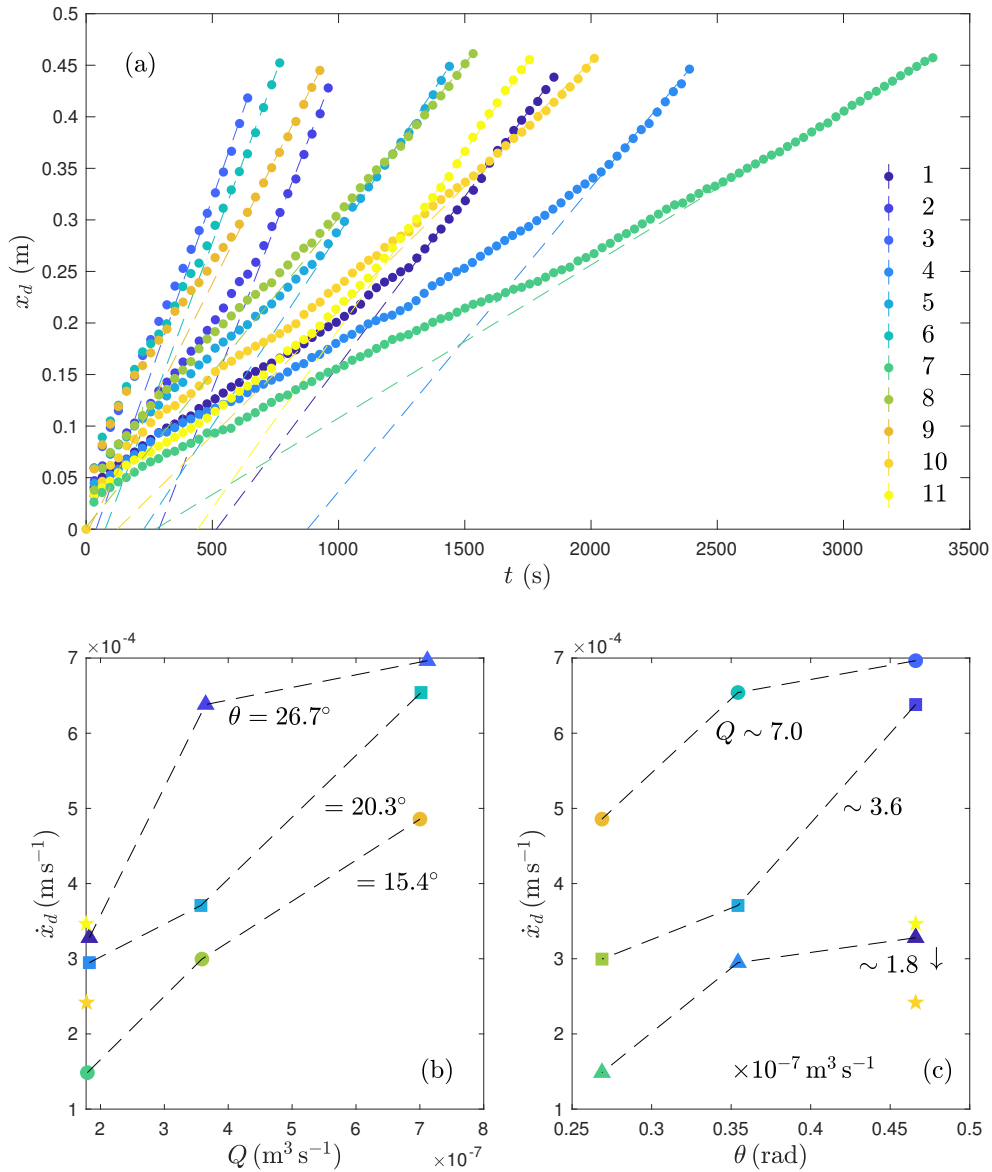


**Figure 5.6: Downslope extent of the transient head.** (a) Plot of the downslope extent  $x_d$  against time. Dashed lines show linear fit to calculate final velocity. The colours indicate different experiments 1-11 as shown in the legend and table 5.1. (b) Plot of final velocity  $\dot{x}_d$  as a function of volume flux  $Q$ . Different symbols refer to different angles of inclination:  $\theta = 26.7^\circ$ ,  $20.3^\circ$  and  $15.4^\circ$  given by triangles, squares and circles, respectively, indicated by the dashed lines. Stars denote changing the bending stiffness. (c) Plot of final velocity against the angle of inclination  $\theta$ . Different symbols refer to different approximate volume fluxes:  $Q \sim 1.8$ ,  $3.6$  and  $7.0 \times 10^{-7} \text{ m}^3 \text{ s}^{-1}$  given by triangles, squares and circles, respectively, indicated by the dashed lines. Stars denote changing the bending stiffness. The arrow shows increasing bending stiffness  $B$ .

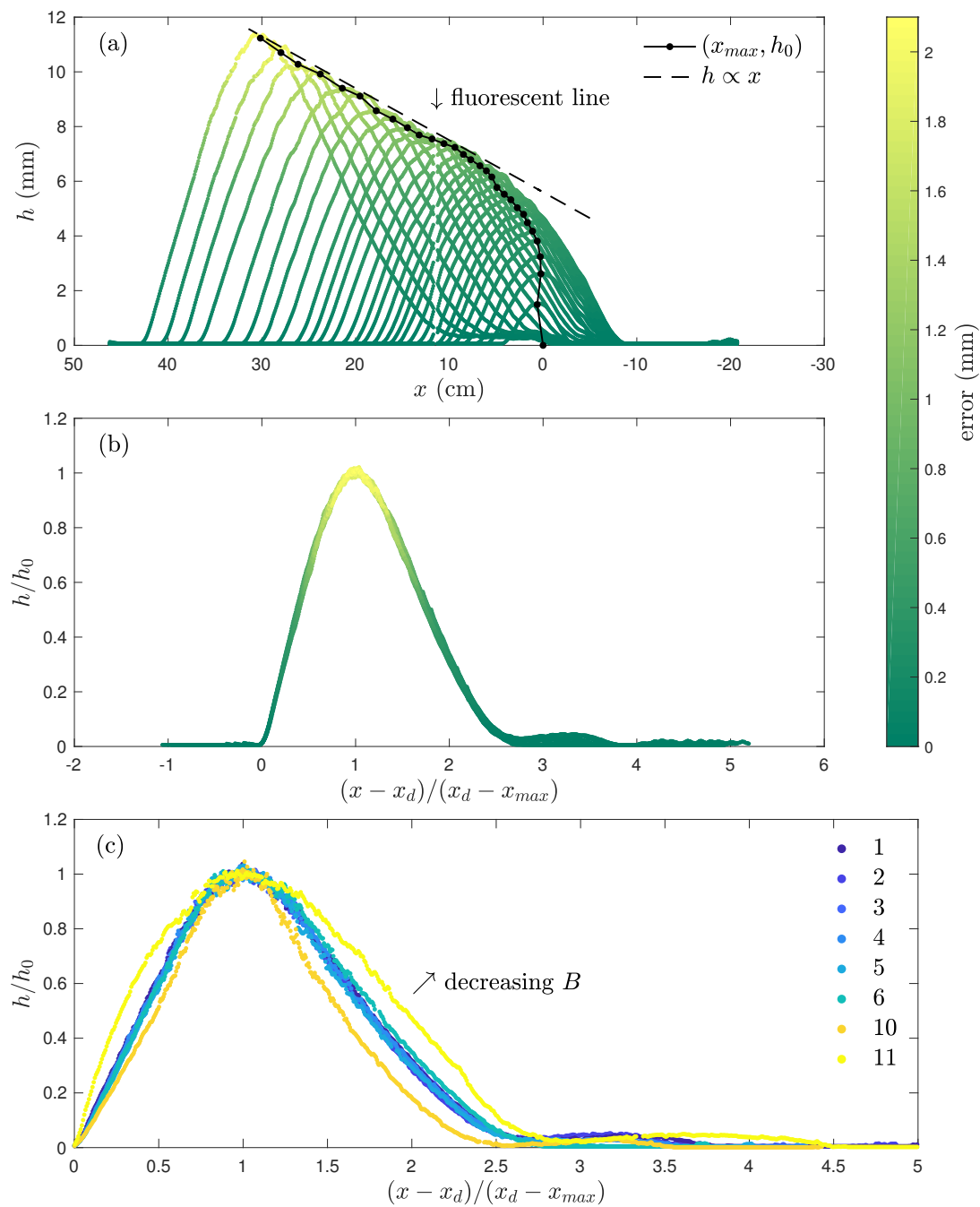


**Figure 5.7: Downslope geometry of the transient head.** (a) Downslope profiles at cross-section  $y = 0$  of experiment 1. The maximum points  $(x_{max}, h_0)$  are marked as black circles with the dashed line showing the linear increase in height downslope. Note, the break in profiles around  $x \sim 10$  cm is where the fluorescent line has been removed. (b) Downslope profiles translated into a travelling reference frame of the front  $x_d$  and collapsed by  $h_0$  in the vertical and  $x_d - x_{max}$  in the horizontal for  $t > 1500$  s. (c) Collation of final downslope profiles for experiments 1-6, 10 and 11.

in figures 5.8b–c. For times  $t > 1500$  s in figure 5.8b, the outlines are scaled by  $x_d - x_{max}$  in the downslope direction and  $\max_x Y(x, t)$  in the cross-slope direction showing a transition to a universal transient head shape. Finally, figure 5.8c shows a collation of final outlines from experiments 1-6, 10 and 11. Note, experiments 8, 9 and 10 are omitted as the maximum point  $(x_{max}, h_0)$ , needed to scale the outlines, could not be identified. For  $y / \max_x Y(x, t) > 0$  there is a good collapse of the outlines seen by the overlapping curves, showing that bending stiffness has less of an effect on the collapse of the head outline. Note for  $y / \max_x Y(x, t) < 0$  the spread in the outlines is due to the blister reaching the edge of imageable region, seen by the linear features (labelled) at  $y / \max_x Y(x, t) = 1$  in some of the experiments.

Figures 5.7 and 5.8 demonstrate that the transient head geometry can be collapsed onto a universal shape. This suggests that power-law scalings exist for the maximum cross-slope width  $\max_x Y(x, t)$ , the maximum height  $h_0$  and the downslope length scale  $x_d - x_{max}$ . Figure 5.9 shows the evolution of length scales of the transient head against time. In figure 5.9a the maximum extent of the head,  $\max_x Y(x, t)$ , is plotted against time and demonstrates that changing the volume flux  $Q$  has a stronger control on the evolving profile than changing the inclination  $\theta$ . To collapse the experimental data, the cross-slope extent  $\max_x Y(x, t)$  is scaled by the viscosity dominant scaling for the radial extent of an axisymmetric blister,  $Q^{7/30} B^{1/10}$ . Note the adhesion dominant regime has a very similar dependence on the volume flux and bending stiffness,  $Q^{1/4} B^{1/8}$ . The comparison with dashed lines  $\sim t^{3/10}$  and  $\sim t^{1/4}$  suggest that there is a transition from viscosity dominant to adhesion dominant spreading in the cross-slope direction.

The length and time scales  $R_C$  and  $T_C$  evaluated at the start of this section and shown in table 5.1 show that initially the axisymmetric spreading is dominated by the requirement to overcome the adhesion energy at the front, hence the curvature is constant value  $\kappa$  given by the fracture criterion. For length scales  $L_d \sim 2.4 - 5.1$  cm the downslope component of gravity begins to play a role in the dynamics. This is clearly demonstrated in figure 5.10. Figure 5.10a shows the migration upslope, the receding of the front leaving a film behind, and the final re-inflation around the injection hole. Note, as in figure 5.8, the dye concentration was tuned to measure the transient head evolution, therefore detection of the upslope extent after the transient has passed through is not accurate. Figure 5.10b plots the ratio of the upslope to downslope extent  $x_u/x_d$  and hence shows that the asymmetry about the injection point begins almost immediately,  $x_u/x_d < 1$ , causing the blister to migrate downslope. The speed of the front, and hence the curvature at the edge of the transient head, now depends on the position around the head, with the curvature decreasing from a maximum at the downslope extent to a minimum at the upslope extent.

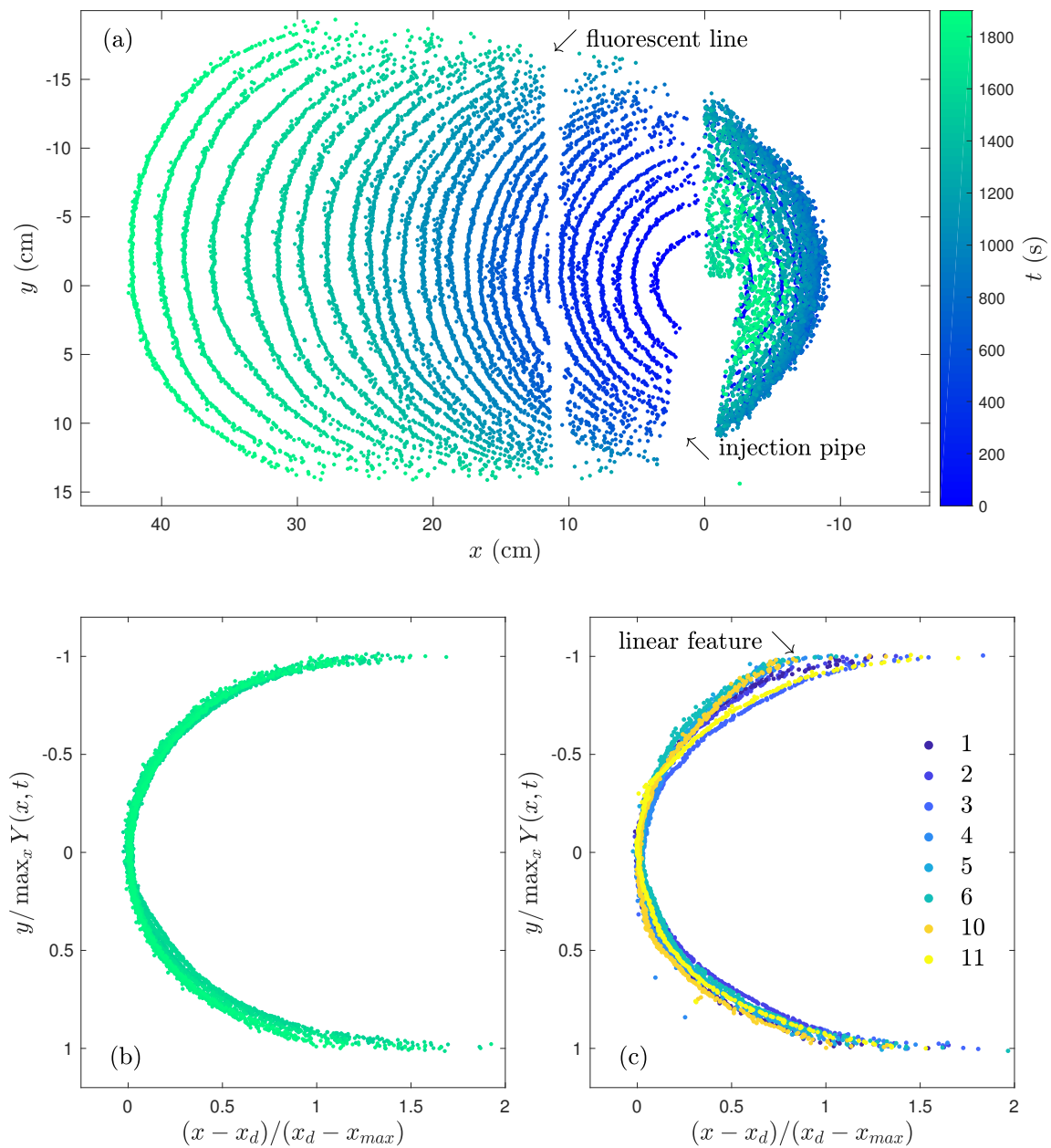


**Figure 5.8: Extent of the transient head.** (a) Evolution of outline of experiment 1. Colourbar indicates time  $t$ . (b) Outline collapsed by  $x_d - x_{max}$  in the downslope and  $\max_x Y(x, t)$  in the cross-slope for  $t > 1500$  s. (c) Collation of final outlines for experiments 1-6, 10 and 11, see table 5.1.

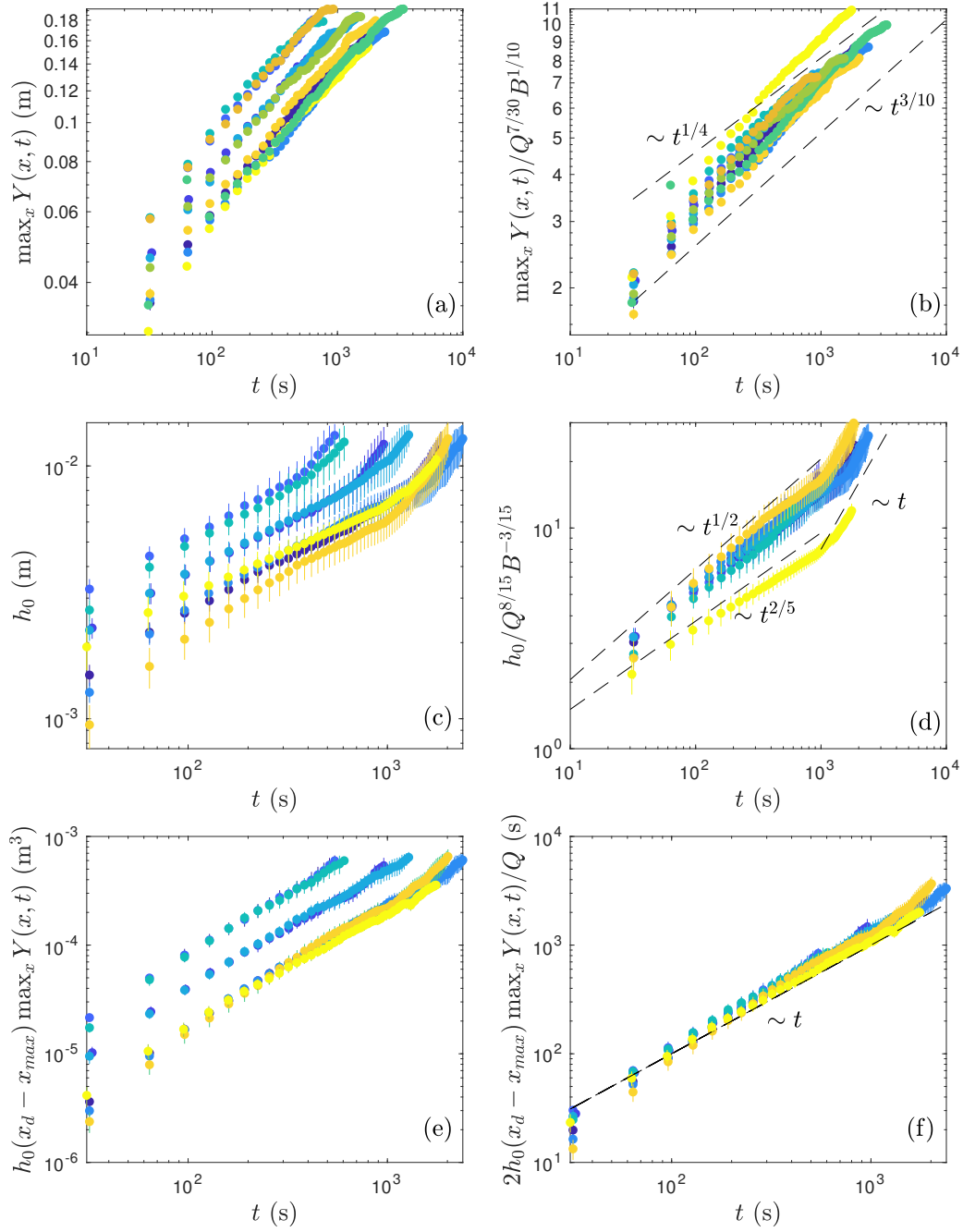


**Figure 5.9: Evolution of length scales of the transient head.** (a) Cross-slope width  $\max_x Y(x, t)$  with time, (b) scaled by viscosity dominant scaling. Dashed lines indicate scalings from viscosity and adhesion dominant regimes. (c) Maximum height with time, (d) scaled by viscosity dominant scaling. Dashed lines indicate scalings from viscosity and adhesion dominant regimes and proposed linear scaling at late times. (e) Volume of transient head with time, (d) scaled with volume flux  $Q$ . Dashed line indicates linear trend showing a constant flux into the transient head.

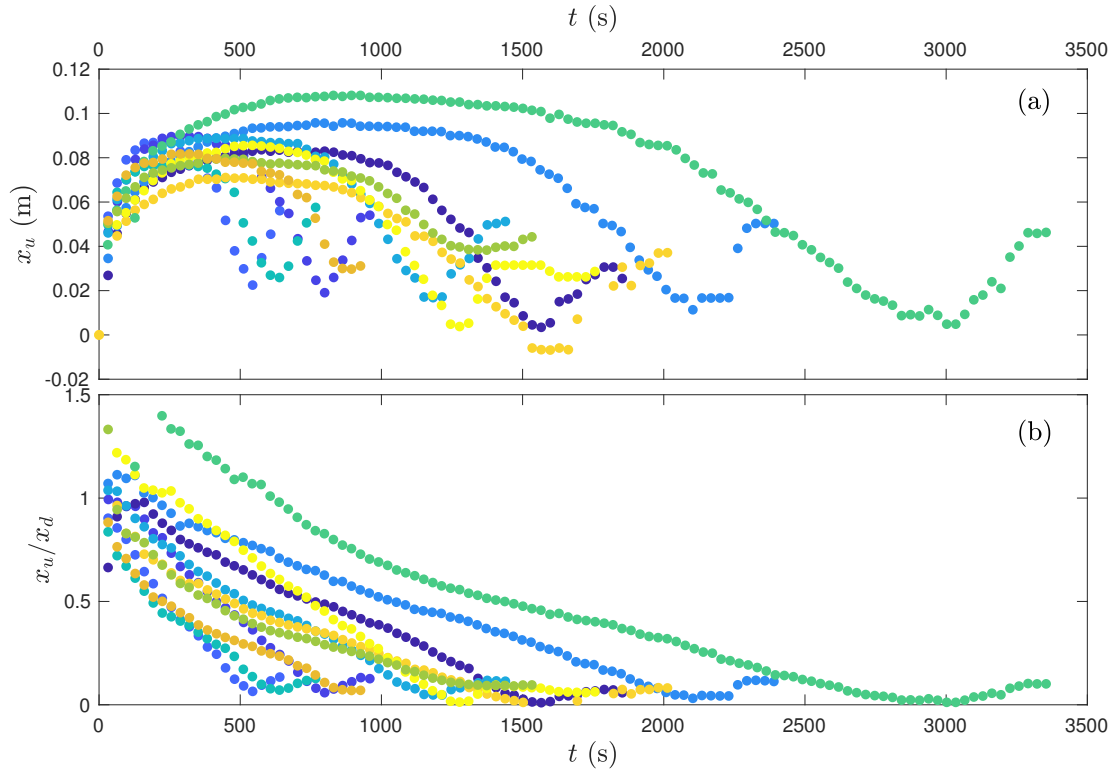


**Figure 5.10: Upslope extent.** (a) Upslope extent  $x_u$  against time. (b) Ratio of the upslope extent to downslope extent  $x_u/x_d$  against time showing the influence of the downslope component of gravity.

Parallels can be drawn with a droplet of constant volume sliding down an inclined plane. In this case, instead of the curvature at the front the contact angle at the front determines whether the contact line advances or recedes. Brown et al. (1980) show that for different inclinations, there is a smooth transition between advancing and receding contact lines moving from the front (furthest downslope) to the back of the droplet. Hence, in the experiments described here, as there is a change in speed or equally curvature, there must be a transition between viscosity dominant and adhesion dominant spreading moving around the fracture front of the blister. As in the axisymmetric case, for a constant flux, the curvature at the front decreases in time  $t$ . Hence, for a given position around the transient head, there is always a transition from viscosity dominant to adhesion dominant spreading. Figure 5.9a demonstrates this transition for cross-slope extent  $\max_x Y(x, t)$  and suggests that the inclination of the substrate increases the length scale of transition to adhesion dominant spreading at this point around the transient head.

Figure 5.9c plots the maximum height  $h_0$  of the transient head against time and again shows that the influence of the volume flux  $Q$  dominates that of the angle of inclination  $\theta$ . Motivated by the cross-slope extent  $\max_x Y(x, t)$ , the maximum height is scaled by the viscosity dominant

scaling  $Q^{8/15}B^{-3/15}$ , although note that again the adhesion dominant scaling is very similar,  $Q^{1/4}B^{-1/4}$ . The scaling collapses the maximum height well, showing a trend consistent with the viscosity dominant scaling  $\sim t^{2/5}$ . There is then a sharp increase where the maximum height begins to increase rapidly, where on figure 5.9d there is a comparison with a linear slope  $\sim t$ . This rapid change in height coincides with the detachment of the transient head from the injection point. On figure 5.9e an estimate of the volume of the transient head  $h_0(x_d - x_{max}) \max_x Y(x, t)$  is plotted, with the volume scaled by volume flux  $Q$  in figure 5.9f. This suggests the volume of the transient head grows linearly in time. Note, the deviation away from linearity at large  $t$  suggests an overestimation of one of the parameters (as at most the transient head volume can increase linearly). The biggest errors come from the measuring the maximum height due to dye saturation for large thicknesses, hence this may be the cause of the overestimation.

Initially the blister spreads axisymmetrically. The downslope component of gravity causes the blister to migrate downslope. Analogous to a drop sliding down an incline, the curvature around the blister smoothly transitions from a maximum at the downslope extent to a minimum at the upslope extent. Eventually, the blister detaches from the injection point forming a transient head. This detachment coincides with a rapid increase in the height of the head, which propagates at constant speed downslope. As the transient head travels downslope it fractures a region leaving a fluid film after it has passed through. The continuing volume flux forms a channel in the film which feeds the transient head with a constant volume flux. The next section describes the results of experiment 12 designed to investigate the steady-state channel behind the transient head.

### Steady-state channel

As the transient head travels downslope, it leaves behind a fluid film. The continuing volume flux then re-inflates this region to form a channel of a given geometry. If the channel width is smaller than the fracture width (or film extent) due to the head, then the boundary conditions in the cross-slope direction are given by matching onto a film with the fracture front providing compact support in the far field. In this case the channel can be described by the similarity solution outlined in section 5.2.3. If, however, the channel inflates up to the fracture front, then the width  $y = \max_t Y(x, t) \equiv Y_f(x)$  is set by the transient dynamics and the geometry is given by steady-state solution described in section 5.2.3.

Experiment 12 focuses on looking at the steady-state channel, with an initial constant volume flux  $Q = 1.76 \times 10^{-7} \text{ m}^3 \text{ s}^{-1}$ . After the transient head had passed through, the same flux was maintained for  $\sim 15$  mins to ensure a steady state had been reached. The flux was

then increased to  $Q = 3.49, 6.81, 10.0, 13.2 \times 10^{-7} \text{ m}^3 \text{ s}^{-1}$ , waiting for  $\sim 15$  mins after each increase to ensure a steady-state channel had been reached. The aim of the experiment was to look at the geometry of the channel as a function of the volume flux  $Q$ . Figure 5.11 plots the results from this experiment where profiles are taken at the end of each interval. Figure 5.11a plots the cross-slope profile at  $x = 9.5 \text{ cm}$ . Each profile is for an increase in the flux and shows that the edge of the channel remains pinned as it is continually inflated. Hence, the theory for the fixed width channel in section 5.2.3 should provide the best description with cross-slope extent  $y = \max_t Y(x, t) \equiv Y_f(x)$ . Figure 5.11b plots the cross-slope profiles collapsed by  $h_0$  in the vertical and  $Y_f$  in the horizontal. The dashed line plots bell-shaped profile  $h/h_0 = (1 - y^2/Y_f^2)^2$  from equation (5.29). This gives a range of curvatures less than the fracture criterion,  $h'' = 8h_0/Y_f^2 = 0.27 - 0.52 \text{ m}^{-1} < \kappa = 6.4 \text{ m}^{-1}$ . This is consistent with the channel being fixed at the fracture front determined by the transient head dynamics.

Figure 5.11c plots the downslope profile at  $y = 0$  for increasing volume flux  $Q$ , where the dashed lines indicate the region over which the cross-slope profile in  $y$  is averaged. As the flux is increased, the upslope extent  $x = -x_u$  remains constant suggesting it is fixed by the fracture front. The upslope extent is governed by a balance between pressure due to elasticity and gravity, with zero incoming flux, i.e. a constant volume at each flux, see section 5.2.3. If it was surrounded by a fluid film,  $x_u$  would migrate upslope with increasing flux. However, if the upslope extent is pinned at the fracture front, the curvature needs to overcome the fracture criterion in order to propagate. Hence, this experiment shows an example of when there is no extensive fluid film around the stagnant upper region. Travelling downslope, the channel height decreases slightly. This is to accommodate the increasing width of the channel (due to the increasing width transient head fracturing a larger area) and the predominantly downslope volume flux. Note, the bulge seen in figure 5.11c at the largest  $x$  values is a build-up of a oil at the end of the table after the transient head has drained upon reaching the end of the table. Finally, figure 5.11d plots the maximum height  $h_0$  as a function of volume flux  $Q$ , with equation (5.29) given by the dashed line. Error bars here are due to the uncertainty in height measurements from the dye attenuation technique. Hence, both the collapsed profiles and the maximum height  $h_0$  as a function of the volume flux demonstrate that the tail of the current is well described by a steady-state channel where the width  $Y_f$  is fixed by the fracture front of the transient head.

## 5.4 Discussion and future work

The experiments described in section 5.3.3 map out the evolution of an adhered, elastic-plated gravity current. The steady-state channel is described successfully by the theory outlined in

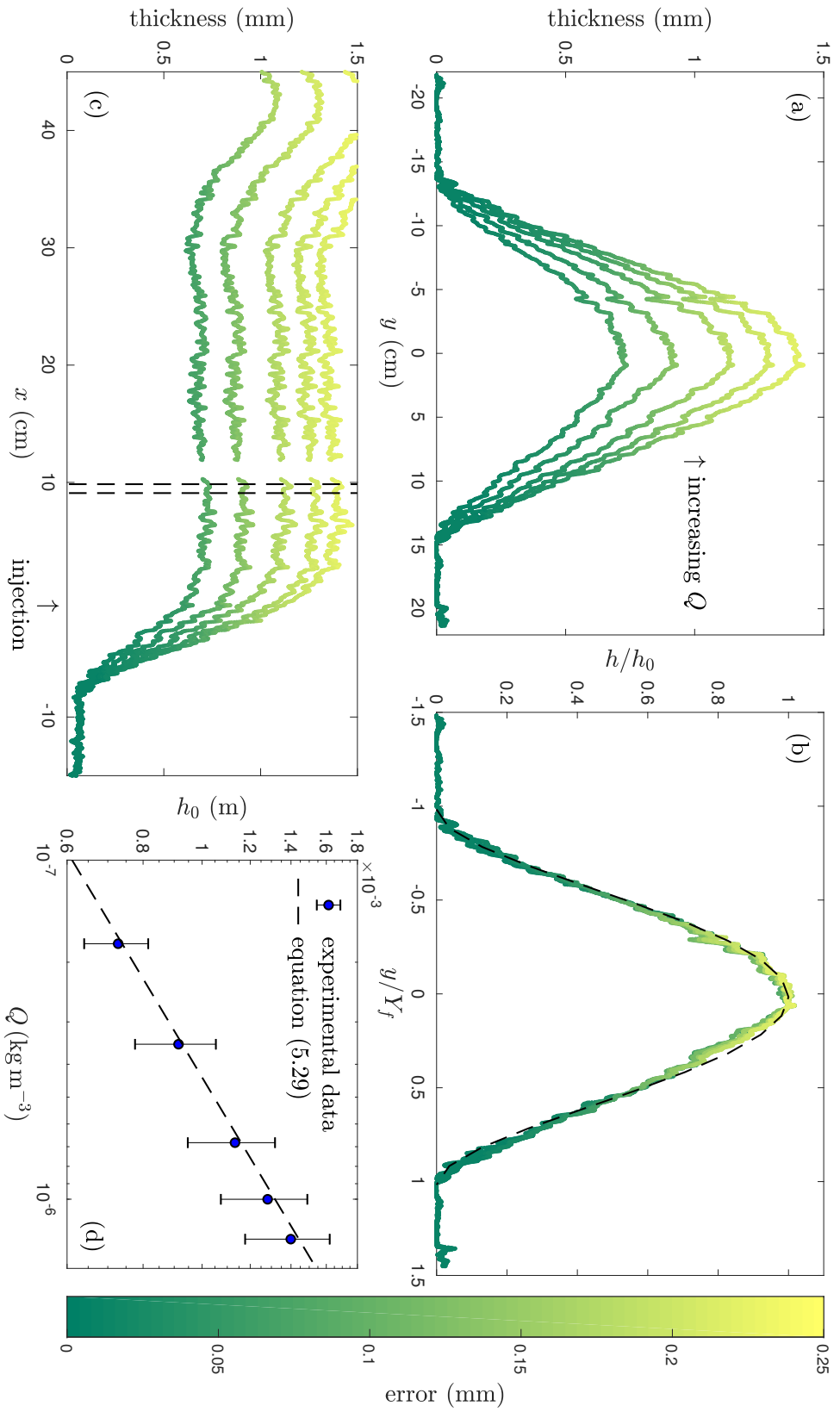


**Figure 5.11: Steady-state experiment (table 5.1; experiment 12).** (a) Cross-slope profiles for increasing flux and (b) collapsed profiles. Dashed line given by  $h/h_0 = (1 - y^2/Y_f^2)^2$  from equation (5.29). (c) Downslope profiles for increasing flux. Dashed lines mark the region over which the cross-slope profile is averaged. (d) Maximum height  $h_0$  as a function of volume flux  $Q$ . Dashed line from equation (5.29).

section 5.2.3. However the dynamics of the transient head are complex and remain poorly understood. This is largely due to the asymmetry in contact lines. Due to the type of adhesion used in the experiments described, only advancing, not receding, contact lines are possible. As a result there is a history dependence where the dynamics of the transient head can play a leading-order role in the late-time steady-state channel, in contrast to the study of inclined viscous gravity currents (Lister, 1992).

To explore this further, additional laboratory experiments need to be carried out. Firstly, I plan to carry out a series of experiments with a different viscosity fluid. This would establish the extent to which the viscosity of the fluid is having an influence on the spreading of the transient head, and hence where the spreading is viscosity dominant or adhesion dominant. Secondly, I plan to adapt the current experimental setup to carry out longer experiments. Currently, the distance between the injection input and the end of the table limits the downslope extent measurable before the transient head reaches the end, see figure 5.4i where the head has almost reached the end. Ideally, the table would be long enough to measure the dynamics of the transient head far away from the injection, such that there is a developed steady-state channel in between. Finally, although the dye attenuation technique has many benefits over measuring the deflection of a fluorescent line, as used in chapter 3, the errors are significantly larger. This is primarily due to the variation in light sheet intensity across the experimental region meaning the calibration curves vary considerably. To tackle this problem, I plan to use a more homogeneous light sheet and use a separate calibration curve (with a transition section in between) for different sections of the experimental region to reduce the error.

The motivation behind looking at the downslope evolution of adhered, elastic-plated gravity currents is to consider the influence of topographic gradients (or sloping bedding planes) on shallow magmatic intrusions. However, as described, the dynamics of the transient head are complex and require further laboratory experiments to fully characterise. Despite this, comparisons with first-order features of the flow can be made with shallow magmatic intrusions seen in the field. A good example is the Piton de la Fournaise flank sill intrusion, La Réunion Island, in 2007, (Froger et al., 2015), however there are numerous other similar examples of flank intrusions here and elsewhere (e.g. Froger et al., 2004; Fukushima et al., 2010; Jónsson et al., 1999; Sigmundsson et al., 1999; Smittarello et al., 2019).

For the 2007 eruption at Piton de la Fournaise, observations using Interferometric Synthetic Aperture Radar (InSAR) data reveal distinct deformation patterns as a result of the intrusion. InSAR uses the differences in the phase of waves back to the satellite from two or more Synthetic Aperture Radar images to map changes in the surface elevation. Figure 5.12 shows two interferograms obtained by Froger et al. (2015) spanning the period of volcanic activity.

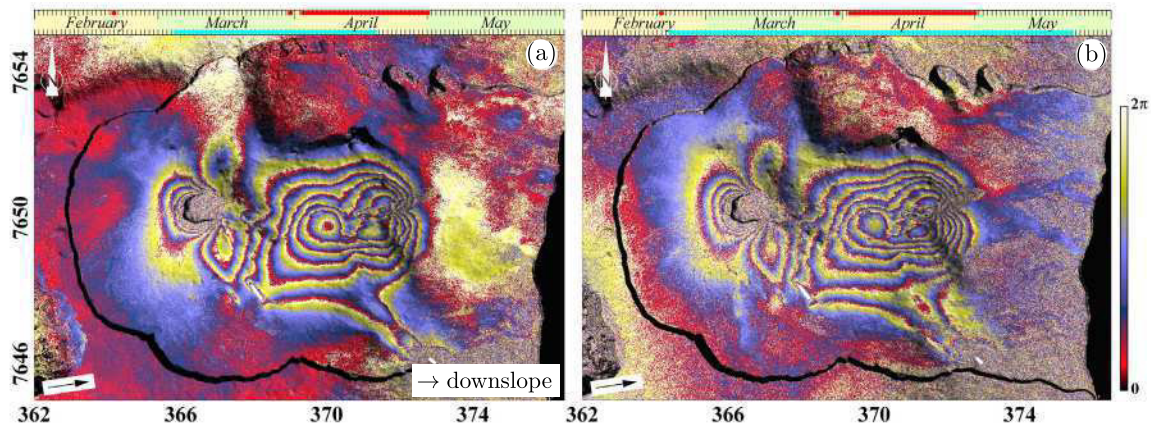


**Figure 5.12:** Figure adapted from Froger et al. (2015) (their figure 2). (a) Interferogram of Piton de la Fournaise from 4th March to 19th April, 2007, and (b) from 20th February to 23rd May, 2007, as shown by the cyan bars on the time scale at the top of each figure. Red bars show the periods of volcanic activity. The axes are given in km. The interferogram is projected onto a digital elevation map. The fringes indicate displacement in the line-of-sight direction, shown by the black arrow. One fringe (red-blue-yellow) is equal to a line-of-sight displacement of 11.8 cm.

These interferograms are then processed using standard techniques to construct displacement maps in the East-West and vertical directions (for more details of the techniques used see Froger et al., 2015). Figure 5.13 shows these displacements in the form of contour maps in the two directions. The deformation patterns exhibit several key features similar to observations from the experiments described above. In particular, the deformation patterns exhibit a rounded deformation front furthest downslope with a linear structure of deformation aligned across the slope, upslope of the largest deformation. These features are consistent with the transient head structure shown particularly in figure 5.4i. In addition, the displacement maps show a positive line-of-sight deformation around the central cone, marked CC on figure 5.13, the suggested inlet to the intrusion. The experiments described above would support the idea that this is a re-inflation of a pre-existing fractured structure after the dominant transient head has migrated downslope. Finally, the flank intrusion clearly demonstrates a characteristic length scale of propagation cross-slope, similar to the experiments. Further insight into the dynamics of the transient head from future experiments will better constrain what sets this length scale.

## 5.5 Concluding remarks

In this chapter I have described a theoretical and experimental model of the downslope evolution of an adhered, elastic-plated gravity current. I have constructed a theoretical model,

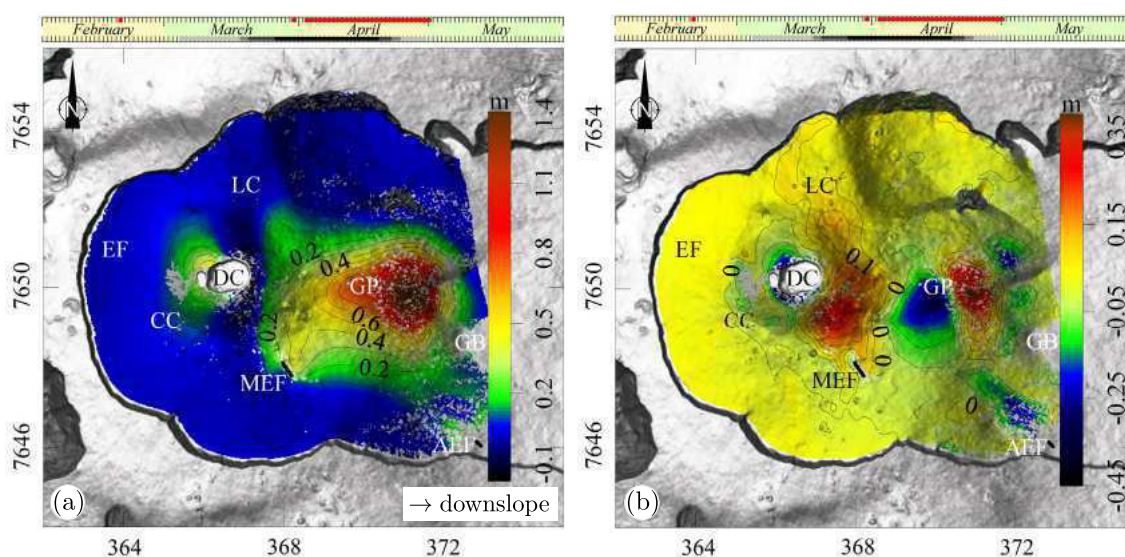


**Figure 5.13:** Figure adapted from Froger et al. (2015) (their figure 4). Computed displacements at Piton de la Fournaise for the period shown by the black bar on the time scale at the top of each figure (red bars show periods of volcanic activity). The axes are given in km. (a) East-West component of displacement with contour level 0.1 m, and (b) the vertical component of displacement with contour level 0.05 m.

building upon my analysis in chapter 3 and the work of Hewitt et al. (2015) and Lister (1992), with analytical results for the geometry of the steady-state channel. I have described a series of experiments aimed at looking at the dynamics of the transient head and the geometry of the steady-state channel. The geometry of the head can be collapsed onto universal curves evolving with a power-law behaviour. However, to understand the details of the transient head's evolution, further experiments need to be carried out. Solving the system numerically is another avenue that could be explored. The steady-state channel exhibits a geometry that is accurately described by analytical results for inflation of a fixed-width channel. First-order features of these experiments resonate with flank intrusions seen at Piton de la Fournaise, highlighting the benefit of considering a distilled model to understand the key physical mechanisms underlying shallow magmatic intrusions.

# Chapter 6

## Conclusions and future work

---

### 6.1 Conclusions

This dissertation has explored the formation of fold-thrust belts and the emplacement of magmatic intrusions through theoretical, numerical and experimental studies. In both cases simplified models have been built to describe the first-order processes, in particular the interplay between viscous flow and elastic deformation. I discuss the conclusions of these studies below.

#### 6.1.1 Fold-thrust belts

In chapter 2 a new, dynamic model was proposed to describe the evolution and geometry of fold-thrust belts. This model couples a viscously deforming sediment wedge with an underthrusting plate which flexurally subsides in response. Analytical and numerical results demonstrate the existence of two regimes of wedge growth: either growth is dominated by gravitational spreading of the sediment due to topographic gradients, or growth is dominated by vertical thickening due to the advection of sediment on the subducting plate. A critical non-dimensional parameter  $\Lambda_C = \pi^{1/2} T_s^3 \rho g / [3\mu U l_{eg} (1 + \rho/\Delta\rho)]$  defines these two regimes. When  $\Lambda_C \gg 1$ , the wedge grows predominantly through gravitational spreading; whereas when  $\Lambda_C \ll 1$  the wedge grows predominantly through vertical thickening.

The model is applied to observations of the topography and sediment-basement interface in the Makran accretionary prism and the Indo-Burman Ranges. In the Makran, the comparison shows that flexure in the underthrusting plate is required to explain the geometry of the sediment-basement interface from seismic reflection profiles. In the Indo-Burman Ranges,

the comparison suggests that the change in sediment thickness from north to south of the Shillong Plateau played a leading order role in determining the style of topography observed.

### 6.1.2 Magmatic intrusions

In chapter 3 the emplacement of magmatic intrusions was investigated analytically and experimentally. I extended the model for an elastic-plated gravity current to include the requirement to fracture adhered layers at the front. The analysis, conducted for an axisymmetric geometry, demonstrated that there are two regimes of spreading: either spreading is viscosity dominant and limited by the viscous dissipation at the front, or the spreading is adhesion dominant and limited by the requirement to overcome the fracture energy at the front. An experimental setup in which a viscous fluid was injected underneath an elastic sheet, adhered to a horizontal substrate, confirmed the existence of these two regimes. In addition, the experiments enabled observation of the evolution of the vapour tip at the front.

In chapter 4 the additional complexity of turbulent flow was considered, motivated by field evidence that suggests that mafic sills exhibit turbulent flow. Following the analysis of Hewitt et al. (2018), I built a turbulent-laminar hybrid model. By considering different physical processes at the front, a pre-wetting film or a fluid lag, the transition from turbulent flow to laminar flow was determined. Comparisons to field data of the thickness versus length of mafic sills suggests an input volume flux several orders of magnitude higher than the average is required to reproduce the thickness of these intrusions. This finding may be supported by evidence of periods of intense volcanic activity leading to vast underestimates of the volume flux. An alternative explanation for the discrepancy in the comparison may be due to the formation of composite sill structures overestimating the thickness of individual intrusions.

In chapter 5 the influence of topographic gradients on the propagation of magmatic intrusions was investigated by studying the downslope evolution of an adhered, elastic-plated gravity current. I conducted experiments using an extended setup from chapter 3, where a viscous fluid is injected beneath an elastic sheet adhered to a substrate, with both the elastic sheet and substrate inclined at an angle to the horizontal. The experiments demonstrated the formation of a transient head structure that travels downslope, fracturing a region in which a steady-state channel is formed behind. Analytical results building on the work of Lister (1992) agree well with the geometry of the steady-state channel formed. First-order comparisons with the flank intrusions at Piton de la Fournaise support the idea that gravity was playing a key role in the propagation.

## 6.2 Future work

The problems described in this dissertation open up many further avenues to the formation of fold-thrust belts and the emplacement of magmatic intrusions. I discuss future work in both of these studies below.

### 6.2.1 Fold-thrust belts

The study described in chapter 2 focuses on analytical and numerical techniques to understand the formation of fold-thrust belts. An alternative method would be to consider analogue modelling. Experimental analogue modelling has largely relied on sandbox models (Graveleau et al., 2012). These models use either cohesive or non-cohesive rheologies to compare with Coulomb wedge theory on a large scale, and the processes of folding and faulting on a smaller scale. In contrast, experiments assuming a fluid rheology for the sediment in the wedge are yet lacking. I plan to carry out future experiments using Carbopol as a sedimentary analogue. Carbopol is a polymer fluid with a non-Newtonian rheology, that exhibits visco-elasto-plastic properties. In the experiments, a uniform layer of Carbopol would be scraped along a horizontal base by a rigid backstop, modelling a fold-thrust belt in a travelling reference frame. These experiments would have many benefits over the current sandbox standard. Firstly, the polymer content of the Carbopol could be altered to give different rheological properties for the sediment (Di Giuseppe et al., 2015), which can be measured accurately using a rheometer. These properties would then be scalable to the bulk effective properties of the sediment in the wedge. In addition, as Carbopol is transparent, deformation within the wedge could be measured by tracking the motion of passive tracers. The aim of the experiments would be to examine the observable features of the flow, i.e. the surface velocities and strain rate, and relate them to more complex rheologies than can easily be considered analytically. In addition, these experiments would give a better understanding of deformation within the wedge and away from the side walls, which cannot easily be done in experiments with sand.

### 6.2.2 Magmatic intrusions

As mentioned in section 4.4.2, the effect of the process of solidification on the geometry of magmatic intrusions seen in the field is poorly understood. Theoretical and experimental studies have looked at solidification and temperature-dependent viscosities in a constant flux intrusion (e.g. Chanceaux and Menand, 2016; Thorey and Michaut, 2016) and a constant

volume intrusion (Roman and Jaupart, 2017). An interesting extension of these previous studies would examine how solidification can act as a stopping mechanism, or equivalently, for a given volume when does an intrusion stop spreading? Together with the fluid lag and a fracture criterion at the fracture front introduced in chapter 3, the geometry would either be determined by solidification processes or the fracture toughness at the front. At the end of chapter 4, the volumetric flux of magmatic intrusions is discussed, suggesting that there are periods of intense volcanic activity which wane dramatically. This would support the idea of examining a constant volume emplacement, as the solidification effects during the initial transient would be negligible for sufficiently high fluxes.

This problem of solidification could be investigated analytically by looking at the growth of boundary layers by conductive cooling in an elastic-plated gravity current. By comparing the thickness of the boundary layer with the height scale of the current, assuming no solidification, an estimate of when solidification begins to play a role could be made. The effects of solidification could be explored further by carrying out experiments where an elastic sheet sits on a cold plate. A hot viscous fluid, such as golden syrup, could then be pumped in between the two layers, which would eventually solidify. The radius at which the intrusion solidifies would then either be determined by solidification or by the adhesion between the plate and elastic sheet. This would be analogous to freezing a droplet where either the radius is determined by freezing or surface tension.

Finally, in section 5.4, further experiments are discussed for the downslope evolution of an adhered, elastic-plated gravity current. These experiments are aimed at further understanding the transient head dynamics. By improving the current setup to a longer experimental region, the transient head can be observed for a longer period away from the injection point. In addition, adjusting the viscosity of the fluid used will allow the dependence on viscosity to be determined. Finally, future experiments would aim to improve the imaging technique in order to reduce the large errors in thickness measurements.

The work reported in this dissertation highlights the utility of constructing simplified theoretical and experimental models of complex geophysical systems. In both studies the models developed have provided further understanding of the geophysical observations. Comparisons with topographic data have demonstrated the importance of sediment thickness and flexure of the underthrusting plate in fold-thrust belts. The models described for magmatic intrusions have supported the idea of pulsed, heightened volcanic activity in mafic sills instead of a uniform volume flux, and demonstrated the control of topographic gradients on the geometry of shallow magmatic intrusions. These studies also underline the importance of considering the complex rheologies of geophysical materials over different length and time scales, in particular the interplay between elastic deformation and viscous flow.

# References

---

- Ágústsdóttir, T., Woods, J., Greenfield, T., Green, R. G., White, R. S., Winder, T., Brandsdóttir, B., Steinthórsson, S., and Soosalu, H. (2016). Strike-slip faulting during the 2014 Bárðarbunga-Holuhraun dike intrusion, central Iceland. *Geophys. Res. Lett.*, 43:1495–1503.
- Alam, M., Alam, M. M., Curray, J. R., Chowdhury, M. L. R., and Gani, M. R. (2003). An overview of the sedimentary geology of the Bengal Basin in relation to the regional tectonic framework and basin-fill history. *Sediment. Geol.*, 155(3-4):179–208.
- Anderson, E. M. (1951). *The dynamics of faulting and dyke formation with applications to Britain*. Hafner Pub. Co., second edition.
- Anderson, O. L. (1978). The role of magma vapors in volcanic tremors and rapid eruptions. *Bull. Volcanol.*, 41(4):341–353.
- Ball, T. V., Balmforth, N. J., and Hewitt, I. J. (2019a). Indentation into a plastic fluid layer. *Proc. Roy. Soc. A*, 475:20180747.
- Ball, T. V., Huppert, H. E., Lister, J. R., and Neufeld, J. A. (2017). The relaxation time for viscous and porous gravity currents following a change in flux. *J. Fluid Mech.*, 821:330–342.
- Ball, T. V. and Neufeld, J. A. (2018). Static and dynamic fluid-driven fracturing of adhered elastica. *Phys. Rev. Fluids*, 3(7):074101.
- Ball, T. V., Penney, C. E., Neufeld, J. A., and Copley, A. C. (2019b). Controls on the geometry and evolution of thin-skinned fold-thrust belts, and applications to the Makran accretionary prism and Indo-Burman Ranges. *Geophys. J. Int.*, 218(1):247–267.
- Beaumont, C., Jamieson, R. A., Nguyen, M. H., and Lee, B. (2001). Himalayan tectonics explained by extrusion of a low-viscosity crustal channel coupled to focused surface denudation. *Nature*, 414(6865):738–742.
- Betka, P. M., Seeber, L., Thomson, S. N., Steckler, M. S., Sincavage, R., and Zoramthara, C. (2018). Slip-partitioning above a shallow, weak décollement beneath the Indo-Burman accretionary prism. *Earth Planet. Sci. Lett.*, 503:17–28.
- Borja, R. I. and Dreiss, S. J. (1989). Numerical modeling of accretionary wedge mechanics: Application to the Barbados subduction problem. *J. Geophys. Res.*, 94(B7):9323–9339.
- Brace, W. F. and Kohlstedt, D. L. (1980). Limits on lithospheric stress imposed by laboratory experiments. *J. Geophys. Res.*, 85(B11):6248–6252.

- Brown, R. A., Orr Jr, F. M., and Scriven, L. E. (1980). Static drop on an inclined plate: Analysis by the finite element method. *J. Colloid Interface Sci.*, 73(1):76–87.
- Brunnschweiler, R. O. (1966). On the geology of the Indo-Burman Ranges (Arakan coast and Yoma, Chin Hills, Naga Hills). *Geol. Soc. Aust. Bull.*, 13:137–194.
- Brunnschweiler, R. O. (1974). Indo-Burman Ranges. *Geol. Soc. London, Spec. Publ.*, 4(1):279–299.
- Bry, M. and White, N. (2007). Reappraising elastic thickness variation at oceanic trenches. *J. Geophys. Res.*, 112:B08414.
- Bunger, A. P. and Cruden, A. R. (2011). Modeling the growth of laccoliths and large mafic sills: Role of magma body forces. *J. Geophys. Res.*, 116:B02203.
- Bunger, A. P., Detournay, E., and Jeffrey, R. G. (2005). Crack tip behavior in near-surface fluid-driven fracture experiments. *C. R. Mecanique*, 333(4):299–304.
- Bunger, A. P., Gordeliy, E., and Detournay, E. (2013). Comparison between laboratory experiments and coupled simulations of saucer-shaped hydraulic fractures in homogeneous brittle-elastic solids. *J. Mech. Phys. Solids*, 61(7):1636–1654.
- Burov, E., Kogan, M. G., Lyon-Caen, H., and Molnar, P. (1990). Gravity anomalies, the deep structure, and dynamic processes beneath the Tien Shan. *Earth Planet. Sci. Lett.*, 96(3-4):367–383.
- Byrne, D. E., Sykes, L. R., and Davis, D. M. (1992). Great thrust earthquakes and aseismic slip along the plate boundary of the Makran subduction zone. *J. Geophys. Res.*, 97(B1):449–478.
- Carey, S. W. (1962). *Scale of geotectonic phenomena*. Government Printer, University of Tasmania.
- Cawthorn, R. G. (2012). Multiple sills or a layered intrusion? Time to decide. *S. Afr. J. Geol.*, 115(3):283–290.
- Chanceaux, L. and Menand, T. (2016). The effects of solidification on sill propagation dynamics and morphology. *Earth Planet. Sci. Lett.*, 442:39–50.
- Chapple, W. M. (1978). Mechanics of thin-skinned fold-and-thrust belts. *Geol. Soc. Am. Bull.*, 89(8):1189–1198.
- Chen, B., Kaban, M. K., Khrepy, S. E., and Al-Arifi, N. (2015). Effective elastic thickness of the Arabian plate: Weak shield versus strong platform. *Geophys. Res. Lett.*, 42(2):3298–3304.
- Chen, W.-P. and Molnar, P. (1983). Focal depths of intracontinental and intraplate earthquakes and their implications for the thermal and mechanical properties of the lithosphere. *J. Geophys. Res.*, 88(B5):4183–4214.
- Chenet, A.-L., Courtillot, V., Fluteau, F., Gérard, M., Quidelleur, X., Khadri, S. F. R., Subbarao, K. V., and Thordarson, T. (2009). Determination of rapid Deccan eruptions across the Cretaceous-Tertiary boundary using paleomagnetic secular variation: 2. Constraints from analysis of eight new sections and synthesis for a 3500-m-thick composite section. *J. Geophys. Res.*, 114:B06103.

- Chevallier, L. and Woodford, A. (1999). Morpho-tectonics and mechanism of emplacement of the dolerite rings and sills of the western Karoo, South Africa. *S. Afr. J. Geol.*, 102(1):43–54.
- Connolly, J. A. D. and Podladchikov, Y. Y. (2000). Temperature-dependent viscoelastic compaction and compartmentalization in sedimentary basins. *Tectonophysics*, 324(3):137–168.
- Copley, A. and McKenzie, D. (2007). Models of crustal flow in the India-Asia collision zone. *Geophys. J. Int.*, 169(2):683–698.
- Corry, C. E. (1988). Laccoliths: Mechanics of emplacement and growth. *Geol. Soc. Am. Spec. Pap.*, 220.
- Craig, T. J. and Copley, A. (2014). An explanation for the age independence of oceanic elastic thickness estimates from flexural profiles at subduction zones, and implications for continental rheology. *Earth Planet. Sci. Lett.*, 392:207–216.
- Crisp, J. A. (1984). Rates of magma emplacement and volcanic output. *J. Volcanol. Geotherm. Res.*, 20(3-4):177–211.
- Cruden, A. R. and McCaffrey, K. J. W. (2001). Growth of plutons by floor-subsidence: Implications for rates of emplacement, intrusion spacing and melt-extraction mechanisms. *Phys. Chem. Earth (A)*, 26(4-5):303–315.
- Cruden, A. R. and McCaffrey, K. J. W. (2006). Dimensional scaling relationships of tabular igneous intrusions and their implications for a size, depth and compositionally dependent spectrum of emplacement processes in the crust. *Am. Geophys. Union, Fall Meet. 2006, Abstr. id. V12B-06*.
- Cruden, A. R., McCaffrey, K. J. W., and Bungler, A. P. (2017). Geometric scaling of tabular igneous intrusions: Implications for emplacement and growth. In *Physical Geology of Shallow Magmatic Systems*, pages 11–38. Springer.
- Curray, J. R. (1991). Possible greenschist metamorphism at the base of a 22-km sedimentary section, Bay of Bengal. *Geology*, 19(11):1097–1100.
- Dahlen, F. A. (1984). Noncohesive critical Coulomb wedges: An exact solution. *J. Geophys. Res.*, 89(B12):10125–10133.
- Dahlen, F. A. (1990). Critical taper model of fold-and-thrust belts and accretionary wedges. *Annu. Rev. Earth Planet. Sci.*, 18(1):55–99.
- Dahlen, F. A., Suppe, J., and Davis, D. (1984). Mechanics of fold-and-thrust belts and accretionary wedges: Cohesive Coulomb theory. *J. Geophys. Res.*, 89(B12):10087–10101.
- Dasgupta, S., Narula, P. L., Acharyya, S. K., and Banerjee, J. (2000). *Seismotectonic atlas of India and its environs*. Geological Survey of India.
- Davis, D., Suppe, J., and Dahlen, F. A. (1983). Mechanics of fold-and-thrust belts and accretionary wedges. *J. Geophys. Res.*, 88(B2):1153–1172.
- Detournay, E. (2016). Mechanics of hydraulic fractures. *Annu. Rev. Fluid Mech.*, 48:311–339.
- Di Giuseppe, E., Corbi, F., Funicello, F., Massmeyer, A., Santimano, T. N., Rosenau, M., and Davaille, A. (2015). Characterization of Carbopol® hydrogel rheology for experimental tectonics and geodynamics. *Tectonophysics*, 642(1):29–45.

- Dolati, A. (2010). *Stratigraphy, structural geology and low-temperature thermochronology across the Makran accretionary wedge in Iran*. PhD thesis, ETH Zurich.
- Dontsov, E. V. (2016). Tip region of a hydraulic fracture driven by a laminar-to-turbulent fluid flow. *J. Fluid Mech.*, 797:R2.
- Elliot, D. (1976). The motion of thrust sheets. *J. Geophys. Res.*, 81(5):949–963.
- Ellis, S., Fullsack, P., and Beaumont, C. (1995). Oblique convergence of the crust driven by basal forcing: Implications for length-scales of deformation and strain partitioning in orogens. *Geophys. J. Int.*, 120(1):24–44.
- Emerman, S. H. and Turcotte, D. L. (1983). A fluid model for the shape of accretionary wedges. *Earth Planet. Sci. Lett.*, 63(3):379–384.
- England, P. and McKenzie, D. (1982). A thin viscous sheet model for continental deformation. *Geophys. J. R. astr. Soc.*, 70(2):295–321.
- Eres, M. H., Schwartz, L. W., and Roy, R. V. (2000). Fingering phenomena for driven coating films. *Phys. Fluids*, 12(6):1278–1295.
- Flesch, L., Bendick, R., and Bischoff, S. (2018). Limitations on inferring 3D architecture and dynamics from surface velocities in the India-Eurasia collision zone. *Geophys. Res. Lett.*, 45(3):1379–1386.
- Flitton, J. C. and King, J. R. (2004). Moving-boundary and fixed-domain problems for a sixth-order thin-film equation. *Eur. J. Appl. Math.*, 15(6):713–754.
- Forsyth, D. W. (1985). Subsurface loading and estimates of the flexural rigidity of continental lithosphere. *J. Geophys. Res.*, 90(B14):12623–12632.
- Froger, J.-L., Famin, V., Cayol, V., Augier, A., Michon, L., and Lénat, J.-F. (2015). Time-dependent displacements during and after the April 2007 eruption of Piton de la Fournaise, revealed by interferometric data. *J. Volcanol. Geotherm. Res.*, 296:55–68.
- Froger, J.-L., Fukushima, Y., Briole, P., Staudacher, T., Souriot, T., and Villeneuve, N. (2004). The deformation field of the August 2003 eruption at Piton de la Fournaise, Reunion Island, mapped by ASAR interferometry. *Geophys. Res. Lett.*, 31:L14601.
- Fukushima, Y., Cayol, V., Durand, P., and Massonnet, D. (2010). Evolution of magma conduits during the 1998–2000 eruptions of Piton de la Fournaise volcano, Réunion Island. *J. Geophys. Res.*, 115:B10204.
- Garagash, D. and Detournay, E. (1999). The tip region of a fluid-driven fracture in an elastic medium. *J. Appl. Mech.*, 67(1):183–192.
- Ghose, N. C. and Singh, R. N. (1980). Occurrence of blueschist facies in the ophiolite belt of Naga Hills, east of Kiphire, N. E. India. *Geol. Rundschau*, 69:41–48.
- Gilbert, G. K. (1877). *Geology of the Henry Mountains, Utah*. US Government Printing Office.
- Glassmaker, N. J. and Hui, C. Y. (2004). Elastica solution for a nanotube formed by self-adhesion of a folded thin film. *J. Appl. Phys.*, 96(6):3429–3434.

- Glazner, A. F., Bartley, J. M., Coleman, D. S., Gray, W., and Taylor, R. Z. (2004). Are plutons assembled over millions of years by amalgamation from small magma chambers? *GSA today*, 14(4-5):4–12.
- Govin, G., Najman, Y., Copley, A., Millar, I., van der Beek, P., Huyghe, P., Grujic, D., and Davenport, J. (2018). Timing and mechanism of the rise of the Shillong Plateau in the Himalayan foreland. *Geology*, 46(3):279–282.
- Gratier, J.-P., Renard, F., and Labaume, P. (1999). How pressure solution creep and fracturing processes interact in the upper crust to make it behave in both a brittle and viscous manner. *J. Struct. Geol.*, 21(8-9):1189–1197.
- Gratton, J. and Perazzo, C. A. (2009). Self-similar asymptotics in convergent viscous gravity currents of non-Newtonian liquids. *J. Phys. Conf. Ser.*, 166:012011.
- Graveleau, F., Malavieille, J., and Dominguez, S. (2012). Experimental modelling of orogenic wedges: A review. *Tectonophysics*, 538:1–66.
- Grotberg, J. B. and Jensen, O. E. (2004). Biofluid mechanics in flexible tubes. *Annu. Rev. Fluid Mech.*, 36:121–147.
- Haddad, D. and Watts, A. B. (1999). Subsidence history, gravity anomalies, and flexure of the northeast Australian margin in Papua New Guinea. *Tectonics*, 18(5):827–842.
- Heil, M. and Hazel, A. L. (2011). Fluid-structure interaction in internal physiological flows. *Ann. Rev. Fluid Mech.*, 43(1):141–162.
- Hewitt, D. R., Chini, G. P., and Neufeld, J. A. (2018). The influence of a poroelastic till on rapid subglacial flooding and cavity formation. *J. Fluid Mech.*, 855:1170–1207.
- Hewitt, I. J., Balmforth, N. J., and De Bruyn, J. R. (2015). Elastic-plated gravity currents. *Eur. J. Appl. Math.*, 26(1):1–31.
- Holness, M. B. and Humphreys, M. C. S. (2003). The Traigh Bhàn na Sgùrra Sill, Isle of Mull: Flow localization in a major magma conduit. *J. Petrol.*, 44(11):1961–1976.
- Huh, C. and Scriven, L. E. (1971). Hydrodynamic model of steady movement of a solid/liquid/fluid contact line. *J. Colloid. Interf. Sci.*, 35(1):85–101.
- Huppert, H. E. (1982). Propagation of two-dimensional and axisymmetric viscous gravity currents over a rigid horizontal surface. *J. Fluid Mech.*, 121:43–58.
- Jackson, M. D. and Pollard, D. D. (1988). The laccolith-stock controversy: New results from the southern Henry Mountains, Utah. *Geol. Soc. Am. Bull.*, 100(10):117–139.
- Jensen, H. M. (1991). The blister test for interface toughness measurement. *Eng. Fract. Mech.*, 40(3):475–486.
- Johnson, A. M. and Pollard, D. D. (1973). Mechanics of growth of some laccolithic intrusions in the Henry mountains, Utah, I. Field observations, Gilbert’s model, physical properties and flow of the magma. *Tectonophysics*, 18(3-4):261–309.
- Jónsson, S., Zebker, H., Cervelli, P., Segall, P., Garbeil, H., Mouginiis-Mark, P., and Rowland, S. (1999). A shallow-dipping dike fed the 1995 flank eruption at Fernandina volcano, Galpagos, observed by satellite radar interferometry. *Geophys. Res. Lett.*, 26(8):1077–1080.

- Jordan, T. A. and Watts, A. B. (2005). Gravity anomalies, flexure and the elastic thickness structure of the India-Eurasia collisional system. *Earth Planet. Sci. Lett.*, 236(3-4):732–750.
- Karner, G. D. and Watts, A. B. (1983). Gravity anomalies and flexure of the lithosphere at mountain ranges. *J. Geophys. Res.*, 88(B12):10449–10477.
- Kavanagh, J. L., Menand, T., and Daniels, K. A. (2013). Gelatine as a crustal analogue: Determining elastic properties for modelling magmatic intrusions. *Tectonophysics*, 582:101–111.
- Kavanagh, J. L., Menand, T., and Sparks, R. S. J. (2006). An experimental investigation of sill formation and propagation in layered elastic media. *Earth Planet. Sci. Lett.*, 245(3-4):799–813.
- Khang, D.-Y., Rogers, J. A., and Lee, H. H. (2009). Mechanical buckling: Mechanics, metrology, and stretchable electronics. *Adv. Funct. Mater.*, 19(10):1526–1536.
- Khin, K., Sakai, T., and Zaw, K. (2014). Neogene syn-tectonic sedimentation in the eastern margin of Arakan-Bengal basins, and its implications on for the Indian-Asian collision in western Myanmar. *Gondwana Res.*, 26(1):89–111.
- Khin, K., Sakai, T., and Zaw, K. (2017). Arakan coastal ranges in western Myanmar, geology and provenance of Neogene siliciclastic sequences: Implications for the tectonic evolution of the Himalaya-Bengal system. *Geol. Soc. London, Mem.*, 48(1):81–116.
- Kille, I. C., Thompson, R. N., Morrison, M. A., and Thompson, R. F. (1986). Field evidence for turbulence during flow of basalt magma through conduits from southwest Mull. *Geol. Mag.*, 123(6):693–697.
- Kopp, C., Fruehn, J., Flueh, E. R., Reichert, C., Kukowski, N., Bialas, J., and Klaeschen, D. (2000). Structure of the Makran subduction zone from wide-angle and reflection seismic data. *Tectonophysics*, 329(1-4):171–191.
- Kuenen, P. H. (1937). Intrusion of cone-sheets. *Geol. Mag.*, 74(4):177–183.
- Lister, J. R. (1990). Buoyancy-driven fluid fracture: The effects of material toughness and of low-viscosity precursors. *J. Fluid Mech.*, 210:263–280.
- Lister, J. R. (1992). Viscous flows down an inclined plane from point and line sources. *J. Fluid Mech.*, 242:631–653.
- Lister, J. R., Peng, G. G., and Neufeld, J. A. (2013). Viscous control of peeling an elastic sheet by bending and pulling. *Phys. Rev. Lett.*, 111:154501.
- Lyon-Caen, H. and Molnar, P. (1983). Constraints on the structure of the Himalaya from an analysis of gravity anomalies and a flexural model of the lithosphere. *J. Geophys. Res.*, 88(B10):8171–8191.
- Malyshev, B. M. and Salganik, R. L. (1965). The strength of adhesive joints using the theory of cracks. *Int. J. Fract. Mech.*, 1(2):114–128.
- Mandl, G. (1988). Mechanics of tectonic faulting: Models and basic concepts. In *Developments in Structural Geology, 1*. Elsevier Amsterdam.
- McKenzie, D. and Fairhead, D. (1997). Estimates of the effective elastic thickness of the continental lithosphere from Bouguer and free air gravity anomalies. *J. Geophys. Res.*, 102(B12):27523–27552.

- Meade, B. J. (2007). Present-day kinematics at the India-Asia collision zone. *Geology*, 35(1):81–84.
- Medlin, W. L. and Massé, L. (1984). Laboratory experiments in fracture propagation. *Soc. Petrol. Eng. J.*, 24(03):256–268.
- Medvedev, S. (2002). Mechanics of viscous wedges: Modeling by analytical and numerical approaches. *J. Geophys. Res.*, 107(B6):2123.
- Menand, T. (2011). Physical controls and depth of emplacement of igneous bodies: A review. *Tectonophysics*, 500(1-4):11–19.
- Michaut, C. (2011). Dynamics of magmatic intrusions in the upper crust: Theory and applications to laccoliths on Earth and the Moon. *J. Geophys. Res.*, 116:B05205.
- Mitchell, A. H. G. (1993). Cretaceous-Cenozoic tectonic events in the western Myanmar (Burma)-Assam region. *J. Geol. Soc. London.*, 150(6):1089–1102.
- Mitra, S., Priestley, K., Bhattacharyya, A. K., and Gaur, V. K. (2005). Crustal structure and earthquake focal depths beneath northeastern India and southern Tibet. *Geophys. J. Int.*, 160(1):227–248.
- Molnar, P. and Tapponnier, P. (1975). Cenozoic tectonics of Asia: Effects of a continental collision. *Science*, 189(4201):419–426.
- Morgan, S., Stanik, A., Horsman, E., Tikoff, B., de Saint Blanquat, M., and Habert, G. (2008). Emplacement of multiple magma sheets and wall rock deformation: Trachyte Mesa intrusion, Henry Mountains, Utah. *J. Struct. Geol.*, 30(4):491–512.
- Moulin, M., Fluteau, F., Courtillot, V., Marsh, J., Delpech, G., Quidelleur, X., Gérard, M., and Jay, A. E. (2011). An attempt to constrain the age, duration, and eruptive history of the Karoo flood basalt: Naude’s Nek section (South Africa). *J. Geophys. Res.*, 116:B07403.
- Ni, J. F., Guzman-Speziale, M., Bevis, M., Holt, W. E., Wallace, T. C., and Seager, W. R. (1989). Accretionary tectonics of Burma and the three-dimensional geometry of the Burma subduction zone. *Geology*, 17(1):68–71.
- Niño, F., Chéry, J., and Gratier, J.-P. (1998). Mechanical modeling of compressional basins: Origin and interaction of faults, erosion, and subsidence in the Ventura basin, California. *Tectonics*, 17(6):955–972.
- O’Keeffe, N. J., Huppert, H. E., and Linden, P. F. (2018). Experimental exploration of fluid-driven cracks in brittle hydrogels. *J. Fluid Mech.*, 844:435–458.
- Olson, J. E. (2003). Sublinear scaling of fracture aperture versus length: An exception or the rule? *J. Geophys. Res.*, 108(B9):2413.
- Pansino, S. and Taisne, B. (2019). How magmatic storage regions attract and repel propagating dikes. *J. Geophys. Res. Solid Earth*, 124(1):274–290.
- Parsons, T., Sleep, N. H., and Thompson, G. A. (1992). Host rock rheology controls on the emplacement of tabular intrusions: Implications for underplating of extending crust. *Tectonics*, 11(6):1348–1356.

- Penney, C., Tavakoli, F., Saadat, A., Nankali, H. R., Sedighi, M., Khorrami, F., Sobouti, F., Rafi, Z., Copley, A., Jackson, J., and Priestley, K. (2017). Megathrust and accretionary wedge properties and behaviour in the Makran subduction zone. *Geophys. J. Int.*, 209(3):1800–1830.
- Perazzo, C. A. and Gratton, J. (2008). Asymptotic regimes of ridge and rift formation in a thin viscous sheet model. *Phys. Fluids*, 20:043103.
- Perazzo, C. A. and Gratton, J. (2010). Convergent flow in a two-layer system and mountain building. *Phys. Fluids*, 22:056603.
- Pollard, D. D. and Johnson, A. M. (1973). Mechanics of growth of some laccolithic intrusions in the Henry Mountains, Utah, II. Bending and failure of the overburden layers and sill formation. *Tectonophysics*, 18(3-4):311–354.
- Price, R. A. (1973). Large-scale gravitational flow of supra-crustal rocks, southern Canadian Rockies. In De Jong, K. A. and Scholten, R., editors, *Gravity and Tectonics*, pages 491–502. New York, Wiley.
- Roman, A. and Jaupart, C. (2017). Postemplacement dynamics of basaltic intrusions in the continental crust. *J. Geophys. Res. Solid Earth*, 122(2):966–987.
- Rubin, A. M. (1995). Propagation of magma-filled cracks. *Annu. Rev. Earth Planet. Sci.*, 23:287–336.
- Ruh, J. B., Kaus, B. J. P., and Burg, J.-P. (2012). Numerical investigation of deformation mechanics in fold-and-thrust belts: Influence of rheology of single and multiple décollements. *Tectonics*, 31:TC3005.
- Rutter, E. H. (1983). Pressure solution in nature, theory and experiment. *J. Geol. Soc. London.*, 140(5):725–740.
- Scheibert, J., Galland, O., and Hafver, A. (2017). Inelastic deformation during sill and laccolith emplacement: Insights from an analytic elastoplastic model. *J. Geophys. Res. Solid Earth*, 122(2):923–945.
- Schlichting, H. (1979). *Boundary-layer theory 7th ed.* Springer.
- Shreve, R. L. and Cloos, M. (1986). Dynamics of sediment subduction, melange formation, and prism accretion. *J. Geophys. Res.*, 91(B10):10229–10245.
- Sigmundsson, F., Durand, P., and Massonnet, D. (1999). Opening of an eruptive fissure and seaward displacement at Piton de la Fournaise volcano measured by RADARSAT satellite radar interferometry. *Geophys. Res. Lett.*, 26(5):533–536.
- Sigmundsson, F., Hooper, A., Hreinsdóttir, S., Vogfjörð, K. S., Feiggsson, B. G., Heimisson, E. R., Dumont, S., Parks, M., Spaans, K., Gudmundsson, G. B., Drouin, V., Rnadóttir, T., Jónsdóttir, K., Gudmundsson, M. T., Högnadóttir, T., Fridriksdóttir, H. M., Hensch, M., Einarsson, P., Magnússon, E., Samsonov, S., Brandsdóttir, B., White, R. S., Gústsdóttir, T., Greenfield, T., Green, R. G., Hjartardóttir, R., Pedersen, R., Bennett, R. A., Geirsson, H., Femina, P. C. L., Björnsson, H., Pálsson, F., Sturkell, E., Bean, C. J., Möllhoff, M., Braidon, A. K., and Eibl, E. P. S. (2014). Segmented lateral dyke growth in a rifting event at Bárðarbunga volcanic system, Iceland. *Nature*, 517(7533):191–195.

- Sikder, A. M. and Alam, M. M. (2003). 2-D modelling of the anticlinal structures and structural development of the eastern fold belt of the Bengal Basin, Bangladesh. *Sediment. Geol.*, 155(3-4):209–226.
- Simpson, G. (2011). Mechanics of non-critical fold-thrust belts based on finite element models. *Tectonophysics*, 499(1-4):142–155.
- Simpson, G. D. H. (2006). Modelling interactions between fold-thrust belt deformation, foreland flexure and surface mass transport. *Basin Res.*, 18(2):125–143.
- Simpson, G. D. H. (2010). Influence of the mechanical behaviour of brittle-ductile fold-thrust belts on the development of foreland basins. *Basin Res.*, 22(2):139–156.
- Slement, C. (2010). The extent of fractionation and mineral accumulation in a 190 m thick karoo sill, near the gariiep dam. *Unpublished Honours project University of the Witwatersrand South Africa.*
- Smith, P. C. (1973). A similarity solution for slow viscous flow down an inclined plane. *J. Fluid Mech.*, 58(2):275–288.
- Smittarello, D., Cayol, V., Pinel, V., Peltier, A., Froger, J.-L., and Ferrazzini, V. (2019). Magma propagation at Piton de la Fournaise from joint inversion of InSAR and GNSS. *J. Geophys. Res. Solid Earth*, 124:1361–1387.
- Snyder, D. B. and Barazangi, M. (1986). Deep crustal structure and flexure of the Arabian plate beneath the Zagros collisional mountain belt as inferred from gravity observations. *Tectonics*, 5(3):361–373.
- Soibam, I., Khuman, M. C., and Subhamenon, S. S. (2015). Ophiolitic rocks of the Indo-Myanmar Ranges, NE India: Relicts of an inverted and tectonically imbricated hyper-extended continental margin basin? *Geol. Soc. London, Spec. Publ.*, 413:301–331.
- Steckler, M. S., Akhter, S. H., and Seeber, L. (2008). Collision of the Ganges-Brahmaputra Delta with the Burma Arc: Implications for earthquake hazard. *Earth Planet. Sci. Lett.*, 273(3-4):367–378.
- Steckler, M. S., Mondal, D. R., Akhter, S. H., Seeber, L., Feng, L., Gale, J., Hill, E. M., and Howe, M. (2016). Locked and loading megathrust linked to active subduction beneath the Indo-Burman Ranges. *Nat. Geosci.*, 9(8):615–618.
- Stockmal, G. S. (1983). Modeling of large-scale accretionary wedge deformation. *J. Geophys. Res.*, 88(B10):8271–8287.
- Stockmal, G. S., Beaumont, C., Nguyen, M. H., and Lee, B. (2007). Mechanics of thin-skinned fold-and-thrust belts: Insights from numerical models. *Geol. Soc. Am. Spec. Pap.*, 433:63–98.
- Stork, A. L., Selby, N. D., Heyburn, R., and Searle, M. P. (2008). Accurate relative earthquake hypocenters reveal structure of the Burma subduction zone. *Bull. Seismol. Soc. Am.*, 98(6):2815–2827.
- Stuart, I. M. (1966). A loop test for bending length and rigidity. *Brit. J. Appl. Phys.*, 17(9):1215–1220.
- Sun, Y., Choi, W. M., Jiang, H., Huang, Y. Y., and Rogers, J. A. (2006). Controlled buckling of semiconductor nanoribbons for stretchable electronics. *Nat. Nanotechnol.*, 1(3):201–207.

- Suppe, J. (1980). A retrodeformable cross section of northern Taiwan. *Proc. Geol. Soc. China*, 23:46–55.
- Tanaka, Y., Fukao, K., and Miyamoto, Y. (2000). Fracture energy of gels. *Eur. Phys. J. E*, 3(4):395–401.
- Tanner, L. H. (1979). The spreading of silicone oil drops on horizontal surfaces. *J. Phys. D Appl. Phys.*, 12(9):1473–1484.
- Thorey, C. and Michaut, C. (2016). Elastic-plated gravity currents with a temperature-dependent viscosity. *J. Fluid Mech.*, 805:88–117.
- Timoshenko, S. and Woinowsky-Krieger, S. (1959). *Theory of Plates and Shells*. McGraw-Hill.
- Townsend, M. R., Pollard, D. D., and Smith, R. P. (2017). Mechanical models for dikes: A third school of thought. *Tectonophysics*, 703-704:98–118.
- Tsai, V. C. and Rice, J. R. (2010). A model for turbulent hydraulic fracture and application to crack propagation at glacier beds. *J. Geophys. Res.*, 115:F03007.
- Urbani, S., Acocella, V., Rivalta, E., and Corbi, F. (2017). Propagation and arrest of dikes under topography: Models applied to the 2014 Bárðarbunga (Iceland) rifting event. *Geophys. Res. Lett.*, 44(13):6692–6701.
- Vernant, P., Nilforoushan, F., Hatzfeld, D., Abbassi, M. R., Vigny, C., Masson, F., Nankali, H., Martinod, J., Ashtiani, A., Bayer, R., Tavakoli, F., and Chéry, J. (2004). Present-day crustal deformation and plate kinematics in the Middle East constrained by GPS measurements in Iran and northern Oman. *Geophys. J. Int.*, 157(1):381–398.
- Wagner, T. J. W. and Vella, D. (2011). Floating carpets and the delamination of elastic sheets. *Phys. Rev. Lett.*, 107:044301.
- Wagner, T. J. W. and Vella, D. (2013). The ‘Sticky Elastica’: Delamination blisters beyond small deformations. *Soft Matter*, 9(4):1025–1030.
- Walcott, R. I. (1970). Flexural rigidity, thickness, and viscosity of the lithosphere. *J. Geophys. Res.*, 75(20):3941–3954.
- Wang, K. and Hu, Y. (2006). Accretionary prisms in subduction earthquake cycles: The theory of dynamic Coulomb wedge. *J. Geophys. Res.*, 111:B06410.
- Wang, W.-H. (2001). Lithospheric flexure under a critically tapered mountain belt: A new technique to study the evolution of the Tertiary Taiwan orogeny. *Earth Planet. Sci. Lett.*, 192(4):571–581.
- Wang, Z.-Q. and Detournay, E. (2018). The tip region of a near-surface hydraulic fracture. *J. Appl. Mech.*, 85(4):041010.
- Watts, A. B., Lamb, S. H., Fairhead, J. D., and Dewey, J. F. (1995). Lithospheric flexure and bending of the Central Andes. *Earth Planet. Sci. Lett.*, 134(1-2):9–21.
- Watts, A. B., Zhong, S. J., and Hunter, J. (2013). The behavior of the lithosphere on seismic to geologic timescales. *Annu. Rev. Earth Planet. Sci.*, 41:443–468.
- White, R. S. (1982). Deformation of the Makran accretionary sediment prism in the Gulf of Oman (north-west Indian Ocean). *Geol. Soc. London, Spec. Publ.*, 10:357–372.

- 
- Willett, S. D. (1992). Dynamic and kinematic growth and change of a Coulomb wedge. In *Thrust Tectonics*, pages 19–31. Springer.
- Zhao, W.-L., Davis, D. M., Dahlen, F. A., and Suppe, J. (1986). Origin of convex accretionary wedges: Evidence from Barbados. *J. Geophys. Res.*, 91(B10):10246–10258.



# Appendix A

## Numerical methods

---

In chapter 2, the coupled system of non-dimensional equations for the evolution of the topographic height and the flexural subsidence of the underthrusting plate, given by equations (2.11) and (2.12), is solved numerically, along with boundary conditions at the backstop and in the far field (equations (2.13) and (2.14)), and global mass conservation (equation (2.15)). The numerical scheme uses a finite difference Crank-Nicolson algorithm with an adaptive time and spatial step, and a predictor-corrector scheme to handle the non-linearities (effectively the non-linear diffusivity proportional to the sedimentary depth cubed). This scheme is based on the code written by Lister (1992) to model viscous flow down an inclined plane.

The numerical scheme calculates the height of the wedge,  $h$ , at the next time-step, solving equation (2.11), using information about the height of the wedge at the current time-step, and the depth of the sediment-basement interface,  $s$ , at the current and previous time-step. The depth of the sediment-basement interface at the next time-step is then updated, solving equation (2.12), using height at the next time-step. This process is repeated twice in the form of a predictor step and a corrector step, as defined below.

In the numerical scheme, equation (2.11), writing  $q$  as the flux, is discretised as follows,

$$\frac{(h_i^{n+1} - s_i^n) - (h_i^n - s_i^{n-1})}{\Delta t} = \frac{q_{i-\frac{1}{2}}^{n,n+1} - q_{i+\frac{1}{2}}^{n,n+1}}{\Delta x}, \quad (\text{A.1})$$

where  $h_i^n$  and  $s_i^n$  are the height of the wedge and depth of the sediment-basement interface at grid cell  $i$  and time-step  $n$ ,  $\Delta x$  is the grid spacing, and  $\Delta t$  is the time-step. The Crank-Nicolson algorithm is centred in space and time. Hence the flux out of cell  $i$ , second term on

the right-hand side of equation (A.1), is given by

$$q_{i+\frac{1}{2}}^{n,n+1} = - \left[ \frac{(h_{i+1}^m - s_{i+1}^m) + (h_i^m - s_i^m)}{2\Delta x} \right]^3 \frac{h_{i+1}^{n,n+1} - h_i^{n,n+1}}{\Delta x} - \left[ \frac{(h_{i+1}^{n,n+1} - s_{i+1}^n) - (h_i^{n,n+1} - s_i^n)}{\Delta x} \right], \quad (\text{A.2})$$

where

$$h_i^{n,n+1} = \frac{h_i^{n+1} + h_i^n}{2} \quad \text{and} \quad h_i^m = \begin{cases} h_i^n, & \text{predictor step,} \\ h_i^{n,n+1}, & \text{corrector step.} \end{cases} \quad (\text{A.3})$$

By writing the flux into cell  $i$ ,  $q_{i-\frac{1}{2}}^{n,n+1}$ , in a similar way to (A.2), equation (2.11), after some rearrangement, can be written as

$$C_{u,i}h_{i+1}^{n+1} + C_{d,i}h_i^{n+1} + C_{l,i}h_{i-1}^{n+1} = d_i, \quad (\text{A.4})$$

where  $C_{u,i}$ ,  $C_{d,i}$  and  $C_{l,i}$  are the coefficients of the new wedge height  $\mathbf{h}^{n+1}$ , and  $\mathbf{d}$  is a vector dependent on information at the  $n$ th time-step.  $C$  is a tridiagonal matrix such that  $C\mathbf{h}^{n+1} = \mathbf{d}$ , which can be solved using the tridiagonal matrix algorithm.

The depth of the sediment-basement interface,  $s$ , is then updated using equation (2.12), which can be discretised using central differences,

$$\frac{s_{i+2}^{n+1} - 4s_{i+1}^{n+1} + 6s_i^{n+1} - 4s_{i-1}^{n+1} + s_{i-2}^{n+1}}{\Delta x^4} + s_i^{n+1} = -\lambda h_i^{n+1}, \quad (\text{A.5})$$

where  $\lambda = \Delta\rho/\rho$ . After rearrangement, this gives

$$A_{u_2,i}s_{i+2}^{n+1} + A_{u_1,i}s_{i+1}^{n+1} + A_{d,i}s_i^{n+1} + A_{l_1,i}s_{i-1}^{n+1} + A_{l_2,i}s_{i-2}^{n+1} = b_i. \quad (\text{A.6})$$

In a similar manner,  $A_{u_2,i}$ ,  $A_{u_1,i}$ ,  $A_{d,i}$ ,  $A_{l_1,i}$  and  $A_{l_2,i}$  are coefficients of the new sediment-basement depth  $\mathbf{s}^{n+1}$ , and  $\mathbf{b}$  is a vector dependent on the wedge height  $\mathbf{h}^{n+1}$ .  $A$  is a band-diagonal matrix such that  $A\mathbf{s}^{n+1} = \mathbf{b}$ , which can be solved using LU decomposition.

# Appendix B

## Optimisation method

---

### Makran

For the comparison with the Makran accretionary prism, given values of the incoming sediment thickness  $T_s$ , convergence velocity  $U$  and sediment and mantle densities,  $\rho$  and  $\rho_m$ , the optimisation method described below aimed at finding the age  $t$ , the elastic thickness  $T_e$  and the viscosity  $\mu$  that best reproduced the datasets.

First the datasets for the topography in the Makran and the sediment-basement interface are made non-dimensional using the scalings described in (2.10). The non-dimensional datasets are then compared with the numerical solutions for different values of the non-dimensional age  $t$  and parameter  $H_\infty$ . To make this comparison, three known parameters need to be specified:  $H$ ,  $l_{eg}$  and  $H_\infty$ . By scaling the vertical distances by  $T_s/H$ , this eliminates  $H$  from the comparison leaving the remaining two parameters,  $l_{eg}$  and  $H_\infty$ . An optimisation is performed over the non-dimensional age, the elastogravity length scale  $l_{eg}$  and the parameter  $H_\infty$ , minimising the residual misfit between the numerical solutions and the non-dimensional datasets. The residual is weighted (3/4) on the topography comparison, and (1/8) on each of the seismic reflection profile and earthquake location dataset comparisons. This is chosen due to the smaller uncertainties in the topographic dataset. For given sediment thickness  $T_s$ , convergence velocity  $U$  and sediment and mantle densities,  $\rho$  and  $\rho_m$ , the resulting values of non-dimensional time  $t$ , elastogravity length scale  $l_{eg}$  and  $H_\infty$  can then be rearranged to give a dimensional age, elastic thickness  $T_e$  and viscosity  $\mu$ . The range of values given section 2.4.1 is due to variations in the input values of the sediment thickness  $T_s$  and convergence velocity  $U$ .

## Indo-Burman Ranges

For the comparison with the Indo-Burman Ranges, a purely isostatic model is considered with  $s = -\lambda h$ . For given values of age and sediment and mantle densities,  $\rho$  and  $\rho_m$ , the optimisation method described below aimed at finding the sediment thickness in the north  $T_{s(north)}$  and south  $T_{s(south)}$ , with the same viscosity  $\mu$  and convergence velocity  $U$ , that best reproduced the datasets.

Without the elasticity of the plate, the variables can be made non-dimensional such that there are no parameters in the system, with scalings

$$H = h_\infty, \quad X = \frac{\rho g (1 + \lambda)^2 h_\infty^3}{3\mu U} \quad \text{and} \quad T = \frac{X}{U} \equiv \frac{\rho g (1 + \lambda)^2 h_\infty^3}{3\mu U^2}. \quad (\text{B.1})$$

The datasets for the topography in the north and south of the Indo-Burman Ranges are made non-dimensional by using the scalings given above. The non-dimensional datasets are then compared with the one numerical solution (as there are no parameters in the system). To make the comparison, three unknown parameters need to be specified:  $H$ ,  $X$  and  $T$ . An optimisation is performed over these three parameters, minimising the residual fit between the numerical solutions and the non-dimensional datasets. Initially an optimisation is performed over the datasets in the north and south separately, for different values of the viscosity, convergence velocity and sediment thickness, and hence  $H$ ,  $X$  and  $T$ . The residuals are then summed (weighted evenly in the north and south) for each set of values for the viscosity and convergence velocity. For given values of the age  $t$  and sediment and mantle densities  $\rho$  and  $\rho_m$ , the sediment thickness in the north  $T_{s(north)}$  and south  $T_{s(south)}$ , with the same viscosity  $\mu$  and convergence velocity  $U$ , is then found. The range of values given in section 2.4.2 is due to variations in the input values of the sediment density  $\rho$  and age.